Open Research Online

The Open University's repository of research publications
and other research outputs

Theoretical studies of low energy electron collisions with small molecular clusters

Thesis

How to cite:

Caprasecca, Stefano (2010). Theoretical studies of low energy electron collisions with small molecular clusters. PhD thesis The Open University.

For guidance on citations see FAQs.

© 2010 The Author


https://creativecommons.org/licenses/by-nc-nd/4.0/

Version: Version of Record

Link(s) to article on publisher's website:
http://dx.doi.org/doi:10.21954/ou.ro.0000ed45

Copyright and Moral Rights for the articles on this site are retained by the individual authors and/or other copyright owners. For more information on Open Research Online's data policy on reuse of materials please consult the policies page.

oro.open.ac.uk

31 0341434 1
UNRESTRICTED

The Open University

Stefano Caprasecca

Theoretical studies of low energy electron collisions with small molecular clusters

A Thesis submitted for the degree of Doctor of Philosophy

Department of Physics & Astronomy

September 2010

DATE OF SUBMISSION: 17 MAY 2010
DATE OF AWARD: 31 AUG 2010

I have seen all the works that are done under the sun; and, behold, all is vanity and vexation of spirit.

That which is crooked cannot be made straight: and that which is wanting cannot be numbered.

I communed with mine own heart, saying, Lo, I am come to great estate, and have gotten more wisdom than all they that have been before me in Jerusalem: yea, my heart had great experience of wisdom and knowledge.

And I gave my heart to know wisdom, and to know madness and folly: I perceived that this also is vexation of spirit.

For in much wisdom is much grief: and he that increaseth knowledge increaseth sorrow.

Ecclesiastes I 14–18

« O frati, » dissi « che per cento milia	« Brothers, » I said, « o you, who having crossed
perigli siete giunti a l'occidente,	a hundred thousand dangers, reach the west,
a questa tanto picciola vigilia	to this brief waking-time that still is left
d'i nostri sensi ch'è del rimanente,	unto your senses, you must not deny
non vogliate negar l'esperienza,	experience of that which lies beyond
di retro al sol, del mondo sanza gente.	the sun, and of the world that is unpeopled.
Considerate la vostra semenza:	Consider well the seed that gave you birth:
fatti non foste a viver come bruti,	you were not made to live your lives as brutes,
ma per seguir virtute e canoscenza. »	but to be followers of worth and knowledge. »

Dante Alighieri, *Commedia, Inferno* — Canto XXVI vv. 85 – 126

Contents

List of Figures

List of Tables

Abstract

We developed and tested a new approach to treat low energy electron collisions with molecular clusters, called Multiple Scattering, which simplifies the scattering process by dividing the target cluster into molecular sub-units; *ab initio* methods are employed to calculate collisional data for the electron – sub-unit scattering process, which is later combined by the Multiple Scattering method to account for the interference between sub-units. We applied the novel method to the scattering from water and formic acid clusters; the results (cross sections) were compared to other theoretical and experimental results, showing good agreement. The *ab initio* R-matrix method was employed both for producing the collisional information on the sub-units and also for calculating comparison cross sections where previous results were not available.

Chapter 1

Introduction

The present research aims at developing and implementing a fast computational method, based on Multiple Scattering (MS) ideas, to calculate cross sections for the low energy electron collision process with molecular clusters. In order to assess its validity and determine the range of applicability, the method is applied to the study of electron collisions with different types of small clusters. Results are compared, when possible, to more accurate *ab initio* calculations and experiments.

The existing low energy *ab initio* scattering methods (e.g. Kohn variational method, Swinger multichannel method, Rome symmetry-adapted Single Centre Expansion, R-matrix — UK, Bonn and JILA implementations) are generally constrained by the target size and are therefore unable to treat big targets; in most cases, this is not due to the method *per se*, but to its computational requirements, which depend strongly on the number of electrons and spatial extent of the target (Khakoo et al. 2006). Calculations therefore become in practice unfeasible if large targets (either big molecules or molecular aggregates) are chosen. Recent calculations on big targets involve, for instance, the electron scattering from formamide (Goumans et al. 2009), tetrahydrofurane (THF) (Milosavljević et al. 2008), glucose (da Costa et al. 2010), DNA components — sugars (Baccarelli et al. 2009), bases (Gianturco et al. 2008, Blanco & García 2007, Dora et al. 2009), and other constituents (Winstead & McKoy 2008, Winstead et al. 2007). The majority of studies are on isolated (gas phase) molecules, although these may in some cases not be significant models for the simulation of realistic targets. In particular, over the

last years, many attempts have been made to describe the effect that low energy electrons have on biologically relevant molecules, mainly in connection to the radiation damage in biological environments; in this respect, the results for gas phase molecules, although helpful, may sometimes not provide the best starting point for the realistic description of the large scale process. For this reason, being able to study aggregates of these molecules may be very useful.

Non *ab initio* methods are computationally less demanding and hence applicable to the study of larger and more significant targets, although they may lack the accuracy of *ab initio* ones. The development and evaluation of a novel method to treat low energy electron collisions from molecular clusters, with little computational requirements, making use of input obtained from *ab initio* methods, is the main objective of this work.

1.1 Low energy electrons and biological radiation damage

In recent years, many studies have focussed on the damage of nucleic acids (DNA and RNA) caused by the interaction of ionising radiation (e.g. α, β and γ rays, ions, X-rays) with biological tissue, because of its potential mutagenic, recombinagenic and carcinogenic effects. Such effects are initiated by the high energy particle and other fast particles produced by the primary radiation, interacting with cellular constituents and generating different secondary products (excited molecules, radicals, cations, anions and secondary electrons) through ionisation, excitation and energy transfer processes. While the primary energy deposition process and its effects are quite well understood (Inokuti 1971, Mott & Massey 1965), allowing the calculation of energy absorption from different types of ionising radiation, the relationship between absorbed dose and biological effect is still not well defined. Yet, understanding the biological, physical and chemical processes that lead to DNA and RNA damage could be extremely helpful both for cancer prevention and cure.

The majority of the secondary products have energies below 30 eV, and are produced in large quantities ($\sim 10^5$ / MeV); in addition, it has been shown that more energy flows into ionisation than excitation (Inokuti 1971), so that secondary electrons (SE) carry most of the deposited energy. Boudaïffa et al. (2000) have shown that electrons having an energy

below 20 eV play a significant role in the DNA damage, causing single- and double-strand breaks, along with base, sugar and phosphate lesions (Pan et al. 2003, Abdoul-Carime & Sanche 2002, Cai et al. 2006, Pan & Sanche 2005), and base release (Zheng et al. 2005), even when energetically below the DNA ionisation threshold. In the same article, Boudaïffa et al. (2000) also observed a strong energy dependence of the incidence of DNA strand breaks and concluded that the reaction starts with a resonant electron attachment to various DNA components (bases, deoxyribose, phosphate or hydration water molecules) followed by bond dissociation. The fragmentation products may also further react with other DNA components.

Low energy secondary electrons[1] also initiate several other processes when interacting with molecules surrounding DNA and RNA, leading to the production of radicals and ions which can in turn interact to produce new species or damage biomolecules. Such reactions usually proceed through the resonant attachment of an electron to the target, forming temporary negative ions (TNI), which may later fragment either decaying into dissociative electronically excited states or dissociating into a stable anion and a neutral radical (Sanche 2005). The latter process is referred to as *dissociative electron attachment* (DEA).

It is crucial to understand how the mechanism of DNA damage is affected by the presence of cellular components (e.g. H_2O, O_2, proteins). Of particular importance for clarifying the radiation damage processes is the interaction of secondary electrons with water molecules, in various aggregation states, because water is widely present in all biological environments and forms hydration layers around biomolecules; the latter are essential for structural stabilisation (see e.g. the works of Kabeláč & Hobza (2007), Saenger (1984) on DNA, and those of Rueda et al. (2003) and Rueda et al. (2006) showing that the helical form is unstable in the gas phase or in non polar solvents) and activity (influencing the affinities with which DNA is bound by proteins and drugs (Privalov et al. 2007)). Due to its large dipole moment, water tends to trap low energy electrons and plays an important role in electron induced processes (Garrett et al. 2005) and in the induction of DNA damage (e.g. Ptasińska &

[1] We define *low energy electrons* (LEEs) as those whose energy is below the ionisation threshold of the target.

Sanche 2007, Yokoya et al. 2009), for instance by generating OH radicals, which later interact with DNA causing considerable damage (Chatgilialoglu & O'Neill 2001, Ward et al. 1985). In general, when TNIs are formed, the presence of solvation water (often arranged in clusters) around molecules allows various mechanisms to occurr, depending on the way the extra energy is dissipated in the clusters (Balog et al. 2004); various experimental studies are focussing on the effect of hydration on nucleic acids and proteins (see for instance Kim et al. 1996, on nucleic bases).

The damage of other macromolecules present in the cellular environment can also have effects on the nucleic acids. All DNA and RNA functions depend on their interaction with proteins, which are also responsible for damage repair (along with transcription, translation and replication). Damage of such proteins may impair their functioning, as many recent studies have demonstrated; for example Daly (2009) showed that the radiation resistance of some bacteria (particularly *deinococcus radiodurans*) is related to their ability to protect DNA repair enzymes.

1.2 Molecular clusters

Clusters are ensembles of atoms or molecules which are not bonded by covalent bonds, and whose character may be regarded as between that of a bulk and that of a gas. The interaction between the atoms or molecules forming a cluster (also called *monomers*), is limited to the usual intermolecular forces (e.g. dispersion, dipole – dipole interaction, hydrogen bonding).

Clusters are important because they behave differently form either isolated molecules and liquid- or solid-phase, as it has been observed in many different fields, where they play significant roles. Here we firstly give an overview of the environments where molecular clusters have been observed, and some example of their reactions; we then focus briefly on the clusters which are studied in this work — water and formic acid ones. Finally we present the two main reasons why small clusters have been chosen as targets in this thesis.

Although a vast literature is available on atomic clusters, we will not address them, since our method has been particularly developed to treat molecular ones.

1.2.1 Clusters in different environments

Molecular clusters are present in *interstellar clouds*, where they form in the rapid ejection of molecules from solid surfaces during electron or ion impacts (Duley 1996). Clusters of H_2, H_2O, CO and hydrocarbons have been observed; an extensive literature exists on the formation and properties of neutral and ionic clusters (Sugano 1991, Haberland 1994).

In the *earth's atmosphere*, cosmic rays generate ions which then stabilise by reacting with other atmospheric molecules and through charge-driven clustering with polar molecules (H_2O, NH_3) (Harrison & Carslaw 2003, Aplin & McPheat 2005); such clusters grow to form ultrafine aerosols which are responsible for starting the nucleation into water droplets (Morrell & Shields 2010); the effects are different at different altitudes (formation of clouds, fog, deposition of nitrogen, acidification of precipitations, formation of potentially dangerous aerosols, Castleman & Jena 2006). Various molecular cluster structures have been detected — $NH_4^+ (H_2O)_n$, $HSO_4^- (H_2SO_4)_n (HNO_3)_m$, $NO_3^- (HNO_3)_n$ — and atmospheric abundances calculated, particularly for $N_2O (H_2O)_n$, $CO_2 (H_2O)_n$, $(H_2O)_n$ (Lemke & Seward 2008). Of particular importance are clusters of hydrated acids, whose growth is faster than that of clusters made of water only, and which may then become stable nuclei (Aloisio et al. 2002). The formation of clouds has effects both on the soil and for the albedo, which is critical for the temperature of the planet (Charlson et al. 2001).

Clusters of small and large molecules have also been observed in *biological environments*: the interaction of the former ones with biomolecules is important for structural stabilisation and reactions; they also play a role in the radiation damage processes. Clusters of biomolecules are also being studied, often showing a markedly different behaviour from the isolated molecules (see e.g., among many others, the experimental results of Nam et al. (2007) and Schlathölter et al. (2006) on dimers of DNA bases). There is a much smaller number of theoretical studies (e.g. Gianturco et al. (2005) on formic acid dimer, Freitas et al. (2009) on $(CH_2O) (H_2O)$ complex).

In general, clusters are also present in a variety of *dense gaseous media* (Kreil et al. 1998), where they form spontaneously; in this environment, many studies analysed the interaction between electrons and clusters, particularly focussing on the effect clusters have in electron

transport and electron attachment processes (Kreil et al. 1998). In particular, a vast literature is available on electron capture in molecular clusters, which may differ markedly from the same process in isolated molecules; H_2O clusters, for instance, can capture LEEs forming $(H_2O)_n^-$ (Dixon-Warren et al. (1991) studied clusters with $n \geqslant 11$); this ion may be viewed as an excess electron trapped in the field of oriented H_2O dipoles (Landman et al. 1987, Coe et al. 1990, Haberland 1994). There are studies on electron attachment to $(NO)_n$, $(CO)_n$ (Senn et al. 1999), O_2 clusters (Matejcik et al. 1996, Kreil et al. 1998) and N_2O clusters (Hanel et al. 2001); the presence of zero energy resonances characterises the anion formation in clusters but it is absent from the same process on isolated molecules (Märk 1991, Stamatovic 1988).

1.2.2 Water and formic acid clusters

In this work, we have studied electron collisions with different water and formic acid clusters; the former have been observed to constitute some hydration layers around biomolecules; studies on the structure of DNA revealed that, while the first layer is characterised by water molecules forming well-ordered bridges between two acceptor atoms, often belonging to different strands (Kosztin et al. 1999, Arai et al. 2005, Yonetani et al. 2008), the outer layers have a less ordered structure. However, such structure cannot be explained in terms of bulk water, as showed comparing simulation and time-resolved Stokes-Shift experiments (Sen et al. 2009) and from microcalorimetric analysis (Arai et al. 2005, Dragan et al. 2008); particularly, the density is higher than that of bulk water. These outer layers may be then explained in terms of clustered water, as it is denser than liquid water or ice but still structured by hydrogen bonds with the neighbouring water molecules (as shown by Yonetani et al. (2008) for the second hydration layer of DNA).

Water clusters (homogeneous, but especially heterogeneous, with other atmospheric species) may play an important role in the radiative balance (Kjaergaard et al. 2003), in the oxydation of trace gases and in other atmospheric processes (Sennikov et al. 2006).

As for the clusters of formic acid, they are also of importance both in biological environments and in the interstellar medium, where they are expected to play a role in the formation of more complex molecules (Irvine et al. 1989). Moreover, formic acid generally represents

a good model for the study of larger carboxylic acids, which usually arrange themselves in very stable dimers through the formation of two hydrogen bonds (the carboxyl group functions as both a hydrogen bond acceptor and donor). Both HCOOH and $(HCOOH)_2$ are viewed as potential key components in the formation of small biomolecules in the interstellar medium (Ban et al. 2000).

1.2.3 Small molecular clusters and present research

The present research is focussed on the study of electron collisions with molecular clusters; the Multiple Scattering method, under implementation and testing, has been developed in such a way as to be applicable to the most general cases: firstly, it can treat heterogeneous clusters, so that its application can easily be extended to other relevant systems other than those illustrated in this work. Moreover, although this research is focussed on the scattering process with *small* clusters made up by no more than five monomers, the method is in principle applicable to larger systems.

Apart from their intrinsic interest, molecular clusters have been chosen as targets of this research for two reasons; the first is of a *methodological kind*: the testing process of the method, as well as the assessment of its applicability range, is based on a comparison between the results it provides and other results, either experimental or theoretical. In most cases, particularly for water clusters, no electron scattering results are available that could be used as a reference, with the exception of Gorfinkiel et al. (2002) on $(H_2O)_2$. It was therefore necessary to perform parallel calculations with a more accurate scattering programme. The UK R-matrix suite of codes has been chosen to perform these calculations; as will be better explained later, this code, being *ab initio*, suffers from limitations on the target size, mainly due to high computational requirements, and cannot be applied to the study of electron scattering from large molecules.[2] For this reason there has been the need to choose targets that could be treated both with a Multiple Scattering approach and with an R-matrix one, and molecular clusters made up by a small number of monomers represent

[2]Work is at present under way to re-engineer the suite so that it can effectively make use of current computational capabilities, thus enabling the study of more complex collisional processes with larger targets.

an ideal compromise. In fact, very small clusters (typically consisting of two or three small monomers) can be studied easily with both methods, providing enough data to perform an accurate comparison and to test the new Multiple Scattering (MS) approach. Afterwards, the number of monomers forming the cluster has been increased, and the electron scattering study with these targets has been continued with the MS code only.

Finally, the choice of molecular clusters is also justified by *practical reasons*, which are related to the applicability of the Multiple Scattering technique. The underpinning idea, more extensively presented later, is to divide the target into parts (henceforth called *sub-units*), and to combine scattering information on each of these in order to obtain collisional data relative to the target as a whole. A requirement for the combination to be performed correctly is that the sub-units forming the target should be as independent as possible, avoiding for instance significant electron sharing. It is then clear that having a molecular cluster as target makes it possible to partition it into its molecular constituents, so that each monomer is considered as a separate sub-unit. Such choice is ideal for applying the Multiple Scattering technique since, according to the definition of cluster, the interaction between monomers is never strong and no intramolecular covalent bonds are present (the formation of hydrogen bonds is possibly the most common way of formation of molecular clusters — both homogeneous and heterogeneous — between biologically relevant species).

1.3 Presentation of the methods used

As mentioned above, two methods have been applied to the study of LEE interaction with small molecular clusters. The R-matrix method (Burke & Berrington 1993), well established and widely used for this type of calculations, has been employed to provide input collisional data relative to the sub-units independently, which is required by the MS code to run. It has also been used for comparison purposes, in order to provide results (cross sections) that could be compared with those obtained with the MS method, under development and test.

An overview of both methods is introduced here, stressing the main differences between them; a more in-depth explanation of their theoretical functioning is presented later.

1.3.1 R-matrix method

The R-matrix is an *ab initio* method based on the idea that, since the scattering process between two generic particles is driven by their interaction potential, and since such potential is different when the particles are far away and when they are closer, it is possible to separate the relative coordinate space into an inner and an outer region. In the spherical inner region, short-range interactions dominate, so exchange and correlation effects are explicitly taken into account. In the outer region only long-range interactions are relevant and hence included, while exchange and correlation are neglected.

The inner region calculation is the most computationally demanding, due to the inclusion of short range interactions; the memory and time requirements depend strongly on the size of the region itself and on the number of target electrons, as it will be shown in chapter 2. The inner region should always be large enough to contain most of the target electronic density, so that the latter is negligible outside it and short range interactions may be safely disregarded. When large targets are being studied, the choice of a small inner region could cause exchange and correlation to be excluded from the calculation in regions of space where they are not negligible.

The UK polyatomic R-matrix suite (Morgan et al. 1997) has not only been used alongside the Multiple Scattering to perform parallel calculations for comparison purposes, but has also served as a generator of the input required by the Multiple Scattering code to work. In fact, the MS code simply combines the sub-units' scattering data; such data has to be generated independently and input. In principle, any method able to provide scattering information (i.e. to compute T-matrices for the electron – sub-unit scattering process) could be used, but the R-matrix has been chosen for two important reasons. Firstly, the MS division of the target into sub-units (initially treated independently and later allowed to interact) for all practical purposes is achieved dividing the coordinate space into spherical regions, each of which contains one sub-unit (in the present research one molecular monomer). When the regions are initially considered as independent scatterers, the idea of applying the R-matrix method for this looks quite natural, because it is based on an analogous spherical division (between inner and outer regions). Moreover, it will be also shown later that

two T-matrices are actually needed by the MS code for each monomer: one comes from a standard scattering calculation, while the other must be obtained including only the short-range interaction between the monomer and the scattering electron. This "modified" data can be easily obtained with the R-matrix code, where the long-range interaction can be easily "switched off" in the outer region part of the calculation.

A second reason for choosing the R-matrix method is for consistency's sake. Since the MS results will often be compared with cluster results obtained with the R-matrix code, it is reasonable to use the same programme for the input required on the sub-units. It is then possible to perform calculations of consistent complexity and accuracy, so that the eventual differences between the final MS and R-matrix cross sections may only be attributed to the Multiple Scattering treatment.

1.3.2 The Multiple Scattering method

The Multiple Scattering method is based on the assumption that the sub-units forming the target are independent and non interacting. Any form of bonding between them is completely disregarded and, if eventually present, should be artificially included, although this is not always possible. The only interaction which is accounted for is the interference effect (the *multiple scattering*) of the scattering electron wavefunction.

This method, firstly employed in the study of scattering processes in the 1970s, was originally applied to the electron – molecule collisions, where atomic sub-units were defined (Dill & Dehmer 1974). Notwithstanding the good outcomes, the definition of atomic sub-units for molecules clashes with the assumptions underpinning the method, whose use for electron scattering with molecules was later dropped when more refined quantum chemistry techniques became available. The Multiple Scattering method has been reactivated recently by Caron and co-workers, who applied it to the electron collisions with the water dimer and DNA models (where the sub-units consisted of bases, sugars and phosphates, Caron et al. 2008, Caron et al. 2009), and also to study the band structure of water ice.

In this thesis, we follow their approach in the study of low energy electron collisions with molecular clusters; as specified before, these clusters represent ideal targets for the MS

method, because the inter-monomer interaction is very weak. Therefore, to a first approximation, the scattering process may be described as a series of collisions with independent molecules; interference effects are considered at a later stage. As introduced in the presentation of the R-matrix method, the Multiple Scattering code we have developed only accounts for such interference effects, by combining collisional information on each monomer treated as an independent scatterer. This information is not calculated by the code itself, and needs to be provided by other means. In this respect, we also followed the approach of Caron and co-workers, who firstly employed the R-matrix method for this scope.

Although several recent studies made use of the MS method, among which a work on electron scattering with $(H_2O)_2$ (Bouchiha et al. 2008), it has never been methodically employed in the low energy electron collisions with molecular clusters; in our research we have therefore tried to clarify the range of applicability of the Multiple Scattering approach in the study of such process, and to determine the limitations and issues related to it.

1.4 Outline of the thesis

A more detailed description of the theoretical methods employed is given in chapters 2 (R-matrix) and 3 (Multiple Scattering), with particular stress on the versions used in this research (UK R-matrix suite of codes and the MS code developed at the Open University).

The results are described and analysed in the following chapters. The study on water clusters is presented in chapter 4; different water dimer geometries, mainly differing by their dipole moment, have been studied, corresponding to various relative minima of the potential energy surface (PES). Particular attention has been focussed on the effect of the dipole moment on the agreement between the well established R-matrix method's results and the Multiple Scattering ones. A non-equilibrium water trimer geometry has also been studied with both methods. As for larger water clusters, calculations of cross section for $(H_2O)_4$ and $(H_2O)_5$ have been performed using the MS approach only.

In chapter 5 the results obtained for HCOOH are presented. The formic acid dimer has been studied with the MS code and the results have been compared to earlier theoretical and experimental ones available.

Our attempts to further modify the MS treatment in order to perform calculations for inelastic collisions and its application to the $(H_2O)_2$ cluster at equilibrium geometry are presented in chapter 6.

The final conclusions and remarks are reported in chapter 7.

Chapter 2

R-matrix Theory

The R-matrix is a close-coupling expansion method based on the division of the coordinate space into two regions: an inner region, where the modelling of the scattering particle – target interaction is complex, and an outer region, where the equations describing such interaction may be simplified (Burke & Berrington 1993). It was originally introduced by Wigner (1946) and Wigner & Eisenbud (1947) to study nuclear reactions, and later developed for electron – atom collisions by Burke and collaborators (Burke et al. (1971), Burke & Robb (1975) and Burke (1976)). The electron – molecule collision treatment was later implemented by Schneider and collaborators (Schneider (1975), Schneider & Hay (1976)), Burke et al. (1977) for diatomic molecules, and Nestmann et al. (1991) and Morgan et al. (1997) for polyatomic molecules.

The mentioned division of the space is performed by means of a spherical boundary centred on the centre of mass of the target. It is justified by the assumption that the interaction between the electron and the target molecule shows different features when the radial coordinate of the scattering electron lies in different regions. If the boundary is constructed so that the density corresponding to the electronic states included in the close-coupling expansion is entirely contained inside the sphere (or, more precisely, is negligible ouside it), then only the scattering electron can be found in the outer region. The most important consequence is that the Pauli exclusion principle needs to be taken into account in the inner region only; outside it, the scattering electron is virtually distinguishable from the target ones, with a

consequent simplification of the physics, and it moves in a local potential arising from the long range interaction with the target. A single centre expansion of the potential and of the wavefunction may then be used.

For such assumption to be valid, the boundary radius must be large enough to contain all the target electronic wavefunctions. This may cause problems when such wavefunctions are very extended, which happens both when the molecule is spatially large and when the wavefunctions themselves are diffuse, for instance when Rydberg states are included in the calculation.

In the inner region, the interaction potential is strong, non-local, dominated by short range interactions, and multicentred. The wavefunctions may be found using *ab initio* quantum chemistry methods, as initially formulated for the R-matrix approach by Burke and collaborators (Burke et al. (1971) and Burke & Robb (1975)). As a consequence, modelling the scattering problem in the inner region is generally the most demanding step from a computational perspective. However, provided the continuum basis spans the appropriate energy range, the inner region problem is energy-independent and is solved only once; the energy dependence is obtained from the outer region part of the calculation.

R-matrix calculations consist of three fundamental parts: the description of the target (presented in section 2.2), the inner region calculation (section 2.3), and the outer region calculation (section 2.4). In the following sections, the theory will be presented as it is implemented for polyatomic molecules in the UK polyatomic R-matrix suite. Section 2.1 will introduce the notation and the approximations used; sections 2.5 and 2.6 will respectively discuss practical issues related to the code implementation and give an overview of the types of resonances (or temporary negative ions) that can be encountered in an electron – molecule collision.

2.1 Approximations and notation

Given a system composed by electrons and nuclei, the position of each from the centre of mass will be denoted by r_α where α labels either an electron or a nucleus. When electronic functions are considered, the dependence of spin will be included in the notation defining

a coordinate $x_\alpha = (r_\alpha, \sigma_\alpha)$. Finally, the set of all the electronic and nuclear variables will be collectively indicated as $\boldsymbol{X}$ and $\boldsymbol{R}$ respectively.

Throughout this chapter, attention will be focussed on solving the *electronic* problem only. This semplification is justified by some initial assumptions, which are commonly used in quantum chemistry. The Hamiltonian describing the motion of the system can be generally divided into an electronic and a nuclear part.[1] Since nuclei are much slower than electrons, being heavier, it is a good approximation to neglect the nuclear kinetic energy and consider the nuclear repulsion constant.

The solution of the Schrödinger equation involving the electronic Hamiltonian only is then a function depending explicitly on the electronic coordinates, and parametrically on the nuclear coordinates. This means that the electronic problem can be solved at different nuclear geometries, and different electronic solutions obtained for each of these.

In more mathematical terms, such approximation, called *Born-Oppenheimer approximation* (see, for example Szabo & Ostlund 1996), means that the total wavefunction may be factorised as:

$$\Omega(\boldsymbol{X}, \boldsymbol{R}, t) = \Psi^t(\boldsymbol{X}, t \mid \boldsymbol{R})\, \Xi^t(\boldsymbol{R}, t), \tag{2.1}$$

and the nuclear and electronic motions may be decoupled.

Taking advantage of such approximation, the whole scattering problem can be solved keeping the nuclei fixed at a certain geometry (normally the equilibrium geometry, or that of a local minimum of the potential); this assumption, which, unlike the Born-Oppenheimer, is related to the scattering process, is called *Fixed Nuclei approximation*.

The theory shown in this chapter assumes that both the Born-Oppenheimer and Fixed Nuclei approximations are valid, and therefore refers to the electronic motion only: it is assumed that the nuclear positions are fixed, so that the total Hamiltonian depends on the electronic coordinates only. For simplicity, the parametrical dependence on the nuclear geometry is dropped from the notation throughout the chapter.

Moreover, attention will be focussed on the stationary solutions of the Schrödinger

[1] Or, more precisely, into terms accounting for the nuclear motion (operator ∇^2_R) and terms that do not include it.

equation: assuming that the process is conservative, the energy of the system is conserved in time, and the Hamiltonian does not depend explicitly on it. It is then possible to factorise the electronic wavefunction as:

$$\Psi^{\mathrm{t}}(\boldsymbol{X}, t \mid \boldsymbol{R}) = \Psi(\boldsymbol{X} \mid \boldsymbol{R})\, e^{-\frac{iEt}{\hbar}}, \tag{2.2}$$

so that the time-dependent Schrödinger equation is simplified into its time-independent formulation:

$$\begin{aligned} \widehat{H}\Psi^{\mathrm{t}} &= i\hbar\frac{\partial\Psi^{\mathrm{t}}}{\partial t} = E\Psi^{\mathrm{t}}; \\ \widehat{H}\Psi &= E\Psi. \end{aligned} \tag{2.3}$$

2.2 Description of the target

The electronic states of the target molecule are described by multiconfigurational wavefunctions Φ_i, which are linear combinations of single configurations ϕ_p:

$$\Phi_i(\boldsymbol{x}_1 \ldots \boldsymbol{x}_N) = \sum_p f_{i,p}\phi_p(\boldsymbol{x}_1 \ldots \boldsymbol{x}_N); \tag{2.4}$$

Each configuration is a function of all the electronic space-spin coordinates and can be written more explicitly as:

$$\phi_p(\boldsymbol{x}_1 \ldots \boldsymbol{x}_N) = \phi_p(\widetilde{\chi}_1^{o_1^p}, \widetilde{\chi}_2^{o_2^p}, \ldots \widetilde{\chi}_w^{o_w^p} \mid \boldsymbol{x}_1 \ldots \boldsymbol{x}_N), \tag{2.5}$$

where $\widetilde{\chi}_q$ are monoelectronic functions (molecular spin-orbitals), products of the electronic spatial functions and the spin functions — $\widetilde{\chi}_i(\boldsymbol{x}) = \chi_i(\boldsymbol{r})\sigma_i(\omega)$ — and o_q^p their occupation numbers, satisfying the relation $\sum_q o_q^p = N$ for all p. More explicitly, each configuration ϕ_p is an antisymmetric product of the monoelectronic functions, written as a Slater determinant:

$$\phi_i = \frac{1}{\sqrt{N!}} \begin{vmatrix} \widetilde{\chi}_1(\boldsymbol{x}_1) & \widetilde{\chi}_2(\boldsymbol{x}_1) & \ldots & \widetilde{\chi}_N(\boldsymbol{x}_1) \\ \widetilde{\chi}_1(\boldsymbol{x}_2) & \widetilde{\chi}_2(\boldsymbol{x}_2) & \ldots & \widetilde{\chi}_N(\boldsymbol{x}_2) \\ \vdots & & \ddots & \\ \widetilde{\chi}_1(\boldsymbol{x}_N) & \widetilde{\chi}_2(\boldsymbol{x}_N) & \ldots & \widetilde{\chi}_N(\boldsymbol{x}_N) \end{vmatrix}. \tag{2.6}$$

2.2.1 Molecular orbitals and the Hartree Fock self consistent Field method

The molecular orbitals (MOs) χ_i are expanded as linear combinations of Gaussian type orbitals (GTOs) centred on each nucleus; the GTOs are spatial functions of the form:

$$\Gamma_j(\boldsymbol{r}) = Nre^{-\gamma_j r^2} Y_{l_j,m_j}(\theta,\phi), \tag{2.7}$$

where (r,θ,ϕ) are the polar coordinates of vector $\boldsymbol{r}$, Y_{l_j,m_j} are spherical harmonics, γ_j an exponent determining the extent of the function and N a normalisation constant. Although GTOs do not have a correct cuspidate behaviour to correctly reproduce the electronic distribution very close to the nuclei, they are a very convenient choice for a basis set because multicentre integrals can be easily evaluated analytically.

Molecular orbitals are therefore expanded on the GTO basis as:

$$\chi_i = \sum_{j=1}^{N_i} a_{i,j}\Gamma_j. \tag{2.8}$$

The kind and number of basis functions to include, N_i, are chosen from standard tabulated basis sets, depending on the type of description one requires.

The construction of molecular orbitals proceeds through the solution of the N-electronic problem $\widehat{H}\phi_0 = E_0\phi_0$, where ϕ_0 is a single configuration of the type 2.6 representing the ground state.

The N-electron problem is solved introducing the *Hartree-Fock approximation*, which allows one to write the N-electronic Hamiltonian $\widehat{H}$ as a sum of monoelectronic ones $\widehat{h}_i(\boldsymbol{x}_i)$, where the nonlocal part of the potential — the electron – electron repulsion — is treated in an average way. That is,

$$\widehat{H} = \sum_i \widehat{h}_i(\boldsymbol{x}_i) = \sum_i \left(-\frac{1}{2}\nabla_i^2 - \sum_{P=1}^{M} \frac{Z_P}{r_{i,P}} + v_i^{\mathrm{HF}}(\boldsymbol{x}_i) \right), \tag{2.9}$$

where v_i^{HF} is the average potential experienced by the i-th electron due to the interaction with all the other electrons; the index i runs over the N electrons and the index P over the M nuclei. In this approximation, the molecular orbitals are obtained variationally, as those which minimise the energy $E_0 = \langle\phi_0|\widehat{H}|\phi_0\rangle$; the variational parameters here are in fact the expansion coefficients $a_{i,j}$ of equation (2.8).

By guessing an initial set of molecular orbitals (that is, a set of coefficients $a_{i,j}$), one calculates the average potentials v_i^{HF}, the monoelectronic hamiltonians $\widehat{h}_i$, and solves the eigenvalue problem $\widehat{h}_i\chi_i = \varepsilon_i\chi_i$, from which a new set of orbitals χ_i are obtained. The procedure (called *Hartree-Fock self consistent field* — HF-SCF) is repeated until self-consistency.

In the end each orbital is characterised by an energy ε_i; the ground state configuration is formed by the $N/2$ lowest-energy orbitals (assuming the system is closed-shell). Although the Hartree-Fock orbitals best describe the ground state configuration ϕ_0, they are also used to generate excited configurations simply by promoting electrons to higher-energy orbitals (those not occupied in the ground state configuration, known as *unoccupied* or *virtual* orbitals). A set of configurations ϕ_p may then be obtained by inserting different orbitals into the Slater determinant.

2.2.2 Natural orbitals

It may be convenient in some cases to make use of an alternative orbitals basis, different to that of Hartree-Fock molecular orbitals; in particular, it is possible to define a set of orbitals, called *natural orbitals*, firstly introduced by P.-O. Löwdin (1955), for which a Configuration Interaction (CI) expansion is more rapidly convergent than with the Hartree-Fock ones (Szabo & Ostlund 1996).

Given a normalised N-electron wavefunction $\phi_i(\mathbf{X})$ like that of equation (2.6), it is possible to define a function of two variables called *first-order reduced density matrix* Ω:

$$\Omega(x_1, x_1') = N \int dx_2 \ldots dx_N \; \phi(x_1 \ldots x_N) \; \phi^*(x_1' \ldots x_N), \tag{2.10}$$

which can be expanded on the orthonormal basis of Hartree-Fock spin-orbitals $\widetilde{\chi}_i$ as:

$$\Omega(x_1, x_1') = \sum_{i,j} \Omega_{i,j} \; \widetilde{\chi}_i(x_1) \; \widetilde{\chi}_j^*(x_1'). \tag{2.11}$$

The elements $\Omega_{i,j}$ form a matrix $\mathbf{\Omega}$, which is a discrete representation of $\Omega(x_1, x_1')$; it is Hermitian, its trace equals the number of electrons N and is generally non-diagonal.

It is possible to find a different orbital basis $\{\eta_i\}$ for which the matrix representation of $\Omega(x_1, x_1')$ is diagonal:

$$\Omega(x_1, x_1') = \sum_k o_k \; \eta_k(x_1) \; \eta_k^*(x_1'), \tag{2.12}$$

where o_k is the occupation number of the natural spin-orbital η_k.

The importance of natural orbitals (NOs) is that they give the most rapidly convergent CI expansion, so that fewer configurations are required to obtain the same accuracy given by configurations formed by any other orthonormal basis set. Natural orbitals, particularly state averaged ones, are very useful when several electronic states are included in the expansion, and they have been used for some targets in this research.

2.2.3 Configuration Interaction method

In the R-matrix method, the molecular electronic states are represented by multiconfigurational functions, as expressed in equation (2.4). The number and type of configurations included define the Configuration Interaction (CI) model; even if one is interested in the elastic scattering off a molecule in the ground state, it is always recommended to use a multiconfigurational wavefunction to improve the description. There are different CI models; the most relevant are called full-CI, SDCI and CASCI; the latter has been used in this work.

Full-CI is the most computationally expensive of all models, since it includes all the possible configurations that can be obtained with the N electrons using all the n orbitals obtained from a given HF-SCF calculation. The number of orbitals n depends on the basis set used: in principle n can be infinite, in which case a full-CI would provide the *exact energy* of all the electronic states (neglecting relativistic effects). In practice, the basis set is always finite, and the full-CI energy provides upper bounds to the exact energies. Even when small bases are used, however, the number of configurations generated $\binom{n}{N}$ in a full-CI is in most cases too large to be considered. For this reason, alternative models are preferred, where the CI expansion is truncated and only a fraction of the possible configurations is included.

The SDCI model (Singles-Doubles Configuration Interaction) includes all the single and double excitations, i.e. those configurations where one or two electrons have been promoted from an orbital occupied in the reference configuration to an unoccupied (high-energy) one. All the possible combination thereof are included.

The CASCI model (Complete Active Space Configuration Interaction) relies on more chemically oriented assumptions: while the SDCI includes very unlikely and high-energetic

configurations (such as, for instance, that obtained by promoting a very bound electron from the lowest molecular orbital (MO) to the highest unoccupied MO, which will hardly contribute to the target ground state description) the CASCI model divides the molecular orbital space into a *core space* (the c lowest orbitals), an *active space* (the next a orbitals) and a *virtual space* (the remaining ones). While the n_c electrons in the core space are left "frozen", the n_a active ones are allowed to occupy any orbital in the active space, and all the possible $\binom{n_a}{a}$ configurations are included. The virtual[2] orbitals v are all left unoccupied ($n_v = n - n_c - n_a$).

The more configurations included, the lower is the molecular energy, which is obtained variationally diagonalising the matrix of elements $\langle \phi_i | \widehat{H}^{(N)} | \phi_{i'} \rangle$, where $\widehat{H}^{(N)}$ is the N-electron Born-Oppenheimer Hamiltonian, which can we written, in atomic units, as:

$$\widehat{H}^{(N)} = -\frac{1}{2}\sum_{i=1}^{N} \nabla_i^2 - \sum_{i=1}^{N}\sum_{P=1}^{M} \frac{Z_P}{r_{P,i}} + \frac{1}{2}\sum_{\substack{i,j=1 \\ i\neq j}}^{N} \frac{1}{r_{i,j}} + \frac{1}{2}\sum_{\substack{P,Q=1 \\ P\neq Q}}^{M} \frac{Z_P Z_Q}{r_{P,Q}}, \tag{2.13}$$

so that the multi-configurational functions of equation (2.4):

$$\Phi_i(x_1 \ldots x_N) = \sum_p f_{i,p}\phi_p(x_1 \ldots x_N)$$

are eigenfunction of $\widehat{H}^{(N)}$. In equation (2.13) the indices i and j run over the N target electrons and the indices P and Q run over the M nuclei; Z_P is the charge of the P-th nucleus and $r_{a,b}$ is the distance between particles a and b.

The target properties that will be later used in the outer region are calculated using the target wavefunctions thus obtained. These are multipole moments for the differest states $|\Phi_i\rangle$ and are calculated as:

$$\begin{aligned} \mu_{v,w} = Q^{(1)}_{v,w} &= \langle \Phi_v | -\sum_{i=1}^{N} r_i |\Phi_w\rangle + \sum_{P=1}^{M} Z_P r_P; \\ Q^{(2)}_{v,w} &= \langle \Phi_v | -\sum_{i} r_i \otimes r_i |\Phi_k\rangle + \sum_{P} Z_P (r_P \otimes r_P); \\ &\ldots \end{aligned} \tag{2.14}$$

where indices i and P run over the N electrons and M nuclei respectively, and $r_q = (x_q, y_q, z_q)$

[2]Note that *virtual orbitals* are here defined as those contained in the virtual space, i.e. those not taking part in the CI model, always left unoccupied. In section 2.2.1, on the other hand, they were defined as the orbitals which are not occupied when the molecule is in the ground state.

is the coordinate vector of particle q. The term $r \otimes r'$ is the short for all the possible couples $(xx', xy', xz', yx'...)$ and can be intuitively extended to the product of more than two vectors.

2.3 Inner region

In the inner region calculation, the scattering electron is added to the system. The $(N+1)$-electronic wavefunctions[3] are built using the close-coupling approximation as:

$$\widetilde{\psi}_k(x_1 \dots x_{N+1}) = \widehat{A} \sum_{i,j} c_{i,j,k} \Phi_i(x_1 \dots x_N) \left[\frac{u_{i,j}(r_{N+1})}{r_{N+1}} Y_{l_i,m_i}(\hat{r}_{N+1}) \sigma_i(\omega_{N+1}) \right] + \sum_j d_{j,k} \widetilde{\phi}_j(x_1 \dots x_{N+1}), \tag{2.15}$$

where the scattering electron is labelled $(N+1)$ and σ_i are spin functions. The functions Φ_i are the multi-configurational wavefunctions from equation (2.2.3), describing target states involving the N target electrons. The set of orbitals $u_{i,j}$, which do not vanish at the R-matrix boundary unlike those describing the target, is introduced to describe the scattering electron; these orbitals are referred to as *continuum* orbitals.

Particular care must be put in the coupling between the target states Φ_i and the continuum functions shown in brackets: each contribution must have the correct spatial and spin symmetry of the total $(N+1)$-electron wavefunction $\widetilde{\psi}_k$ (for this reason the spin functions of the scattering electron are explicitly indicated). Besides, the Pauli principle has to be taken into account by means of the anti-symmetrisation operator $\widehat{A}$.

The continuum orbitals $u_{i,j}$ are built from GTOs centred on the target centre of mass; again, the choice of GTOs is very convenient when multicentral integrals are calculated. The continuum GTO basis set is constructed by fitting a set of Bessel functions within a finite region of space, whose extent depends on the radius defining the R-matrix boundary. The Bessel functions included in the construction are those with eigenenergies up to a certain value, which is chosen taking into account the energy range of the scattering process to be studied, so that the same basis for the continuum orbitals may be used for all energies of interest. Although nodeless gaussian functions are used to fit Bessel functions, which

[3]From now on, the $(N+1)$-electron functions will be denoted by a $\sim$ for clarity, in order to distinguish them from the N-electron functions shown so far.

have many nodes at high values of l, the fitting procedure developed by Faure et al. (2002), based on a minimisation suggested by Nestmann & Peyerimhoff (1990), gives good results (provided the energy range of the scattering electron and the spatial extention of the inner region are correctly taken into account).

The continuum orbitals are orthogonalised with respect to the target orbitals and successively among themselves. Issues arise when a large R-matrix boundary is chosen: many GTOs must then be included for a good continuum description, and this may lead to linear dependence with the target orbitals.

The second summation on the right hand side of equation (2.15) includes $(N + 1)$-electron configurations $\widetilde{\phi}_j(x_1 \ldots x_{N+1})$ which are analogous to the N-electron configurations $\phi_p(x_1 \ldots x_N)$ of equation (2.5), and which vanish at the R-matrix boundary since all the electrons occupy target molecular orbitals. They are also referred to as L^2 *terms*, because they are square integrable.

The inclusion of this second term in the expansion (2.15) is necessary to account for important regions of configurational space that would be otherwise omitted because of the orthogonality between molecular and continuum orbitals (occupied respectively by N electrons and one electron). In the $(N + 1)$-electron configurations $\widetilde{\phi}_j$ all electrons occupy target molecular orbitals, so correlation effects, including virtual excitation to higher electronic states, are accounted for.

The $(N+1)$-electron Hamiltonian $\widehat{H}^{(N+1)}$ is identical to the N-electron one, $\widehat{H}^{(N)}$, of equation (2.13), with the only difference that the electron indices i and j run from 1 to $N + 1$.

When solving the Schrödinger equation in the inner region, it must be taken into account that, unlike the corresponding target wavefunctions Φ_i in equation (2.5), the $(N + 1)$ wavefunctions $\widetilde{\psi}_k$ in equation (2.15) are not negligible at or outside the boundary. The usual Hamiltonian is not convenient for a problem in a finite region (Shimamura 1977) since it is not Hermitian because of non-zero surface contributions. An operator, $\widehat{L}$, called *Bloch operator* (Bloch 1957) is introduced to eliminate such contributions:

$$\widehat{L}^{(N+1)} = \frac{1}{2} \sum_{i=1}^{N+1} \sum_{c} \left|\Phi_{i_c} Y_{l_c,m_c}(\hat{r}_i)\right\rangle \delta(r_i - a) \left(\frac{d}{dr_i} - \frac{b-1}{r_i}\right) \left\langle \Phi_{i_c} Y_{l_c,m_c}(\hat{r}_i)\right| . \tag{2.16}$$

Here a is the radius of the boundary sphere and b an arbitrary constant, often set to zero.

The inner region functions $\widetilde{\psi}_k$ are obtained by diagonalising the matrix of elements $\langle\widetilde{\psi}_k|\widehat{H}^{(N+1)}+\widehat{L}^{(N+1)}|\widetilde{\psi}_{k'}\rangle$ and are therefore eigenfunctions of the $(\widehat{H}^{(N+1)}+\widehat{L}^{(N+1)})$ operator with eigenvalues E_k; they form an orthonormal set which is a complete basis for $(N+1)$-electron functions in the inner region (within the basis used). The total wavefunction, $\widetilde{\Psi}$, which depends on the coordinates of the $(N+1)$ electrons and on the energy of the system, can be expanded (in the internal region only) as:

$$\widetilde{\Psi}(x_1 \ldots x_{N+1}, E) = \sum_k A_k(E)\widetilde{\psi}_k(x_1 \ldots x_{N+1}). \tag{2.17}$$

This wavefunction satisfies the Schrödinger equation:

$$\widehat{H}^{(N+1)}\widetilde{\Psi} = E\widetilde{\Psi}, \tag{2.18}$$

which can be then modified to include the Bloch operator:

$$\left(\widehat{H}^{(N+1)}-E\right)\widetilde{\Psi} = \left(\widehat{H}^{(N+1)}+\widehat{L}^{(N+1)}-\widehat{L}^{(N+1)}-E\right)\widetilde{\Psi} = 0; \tag{2.19}$$

$$\left(\widehat{H}^{(N+1)}+\widehat{L}^{(N+1)}-E\right)\widetilde{\Psi} = \widehat{L}^{(N+1)}\widetilde{\Psi}, \tag{2.20}$$

whose formal solution is

$$\widetilde{\Psi} = \left(\widehat{H}^{(N+1)}+\widehat{L}^{(N+1)}-E\right)^{-1}\widehat{L}^{(N+1)}\widetilde{\Psi}. \tag{2.21}$$

Expanding on the $\{|\widetilde{\psi}_k\rangle\}$ basis, defined by equation (2.15), using the projector operator $\widehat{1} = \sum_k |\widetilde{\psi}_k\rangle\langle\widetilde{\psi}_k|$ and considering that the functions $|\widetilde{\psi}_k\rangle$ are eigenfunctions of the $\left(\widehat{H}^{(N+1)}+\widehat{L}^{(N+1)}-E\right)^{-1}$ operator with eigenvalues $\frac{1}{(E_k-E)}$, we obtain:

$$|\widetilde{\Psi}\rangle = \sum_k \frac{|\widetilde{\psi}_k\rangle\langle\widetilde{\psi}_k|\widehat{L}^{(N+1)}|\widetilde{\Psi}\rangle}{E_k-E}. \tag{2.22}$$

Now we can substitute the expression (2.16) for the Bloch operator and project onto the states $\left|\Phi_{i_c}Y_{l_c,m_c}(\hat{r}_i)\frac{1}{r_{N+1}}\right\rangle$, obtaining:

$$\left\langle\Phi_{i_c}Y_{l_c,m_c}\frac{1}{r_{N+1}}\middle|\widetilde{\Psi}\right\rangle = \frac{1}{2}\sum_k \frac{\left\langle\Phi_{i_c}Y_{l_c,m_c}\frac{1}{r_{N+1}}\middle|\widetilde{\psi}_k\right\rangle}{E_k-E}\sum_{i=1}^{N+1}\sum_{c'}\left\langle\widetilde{\psi}_k|\Phi_{i_{c'}}Y_{l_{c'},m_{c'}}\right\rangle\delta(r_i-a)\left(\frac{d}{dr_i}-\frac{b-1}{r_i}\right)\left\langle\Phi_{c'}Y_{l_{c'},m_{c'}}|\widetilde{\Psi}\right\rangle \tag{2.23}$$

All the radial integrals in (2.22) and (2.22) are limited to the inner region, so the radial parts run from $r_i = 0$ to $r_i = a$.

Defining the reduced radial functions as:

$$F_c(r=a) = \left\langle \Phi_c Y_{l_c,m_c} \frac{1}{r_{N+1}} \middle| \widetilde{\Psi} \right\rangle_{r=a} \tag{2.24}$$

and the surface amplitudes as:

$$f_{c,k}(a) = \left\langle \Phi_c Y_{l_c,m_c} \frac{1}{r_{N+1}} \middle| \widetilde{\psi}_k \right\rangle_{r=a} \tag{2.25}$$

we can evaluate the functions in equation (2.23) at the boundary $r_{N+1} = a$, obtaining:

$$\begin{aligned} F_c(a) &= \frac{1}{2a} \sum_{c'} \left(\sum_k \frac{f_{c,k}(a) f_{c',k}(a)}{E_k - E} \right) \left(r \frac{dF_{c'}}{dr} - bF_{c'} \right) \Big|_{r=a} = \\ &= \sum_{c'} R_{c,c'}(E,a) \left(a \left. \frac{dF_{c'}}{dr} \right|_a - bF_{c'}(a) \right). \end{aligned} \tag{2.26}$$

Here the R-matrix has been defined as

$$R_{c,c'}(E,a) = \frac{1}{2a} \sum_k \frac{f_{c,k}(a) f_{c',k}(a)}{E_k - E}. \tag{2.27}$$

The R-matrix method is named after function (2.27) because the fundamental idea it is based on is the use of this function to link the scattering solutions in the inner and the outer regions. Writing equation (2.26) in matrix form, one gets:

$$\boldsymbol{R}(E,a) = \frac{\boldsymbol{F}(a)}{a\boldsymbol{F}'(a)}, \tag{2.28}$$

where the arbitrary constant b has been set to zero. It is clear then that the inverse of the R-matrix calculated at the boundary is related to the logarythmic derivative of the scattering radial function:

$$\boldsymbol{R}^{-1}(E,a) = a \left. \frac{\boldsymbol{F}'}{\boldsymbol{F}} \right|_{r=a}. \tag{2.29}$$

The indices c and c' label channels, which may be defined as

$$\Delta_c(\boldsymbol{x}_1 \ldots \boldsymbol{x}_N, \hat{r}_{N+1}, \omega_{N+1}) = \Phi_{i_c}(\boldsymbol{x}_1 \ldots \boldsymbol{x}_N) Y_{l_c,m_c}(\hat{r}_{N+1}) \sigma_c(\omega_{N+1}); \tag{2.30}$$

again, $\sigma_c(\omega_{N+1})$, the spin function of the $(N+1)$-th electron, is included to indicate that the function Δ_c is correctly antisymmetrised and that the total spin symmetry is appropriately accounted for. The index c is just a numbering index and refers to sets of indices defining the channel $\left(c = (i_c, \sigma_c^{\mathrm{TOT}}, l_c, m_c)\right)$, so that for each value of c a target state and the scattering electron's angular and spin components are specified.

A channel may be seen as a possible outcome of the collision process, which is uniquely defined by a specific target state and by the angular momentum of the scattering electron and the spin of the $(N+1)$ system.

The propagation described in the next section is carried out on the R-matrix (which contains the radial function) because its numerical properties make it a more appropriate function to deal with in the outer region than the radial function F_c itself or its derivative (Light & Walker 1976).

The aim of the inner region calculation, then, is only to compute $R(E,a)$ at the boundary; to do so, it is sufficient to know the $\left(\widehat{H}^{(N+1)} + \widehat{L}^{(N+1)}\right)$ eigenfunctions $\widetilde{\psi}_k$, their eigenvalues E_k and to compute the surface amplitudes $f_{c,k}(r)$. The energy dependent coefficients $A_k(E)$ of the expansion (2.17) do not need to be computed.

2.4 Outer region

In the outer region, the wavefunction may be written in terms of channels as:

$$\widetilde{\Psi}(x_1 \ldots x_{N+1}) = \sum_c \Delta_c(x_1 \ldots x_N, \hat{r}_{N+1}, \omega_{N+1}) \frac{F_c(r_{N+1})}{r_{N+1}}, \tag{2.31}$$

where $F_c(r)$ is the reduced radial function defined in equation (2.24).

Applying the Schrödinger equation to $\widetilde{\Psi}$ and projecting it onto the channel functions $\left(\left\langle \Delta_{c'} \frac{1}{r_{N+1}} \right|\right)$, it can be shown that the radial functions $F_c(r)$ must satisfy the set of coupled equations:

$$\left(\frac{d^2}{dr^2} - \frac{l_c(l_c+1)}{r^2} + k_c^2\right) F_c(r) = 2 \sum_{c'} V_{c,c'}(r) F_{c'}(r), \tag{2.32}$$

where $k_c^2 = 2(E - E_{i_c})$ and E_{i_c} is the energy of the i_c-th state of the target that defines channels.

This set of equations can be solved by propagating the R-matrix from the boundary a to a larger distance a_{out} where the interaction with the target is negligible (usually $a_{\text{out}} \approx 50 - 200\ a_0$) (Baluja et al. 1982, Morgan 1984). A Gailitis expansion method (Gailitis 1976, Noble & Nesbet 1984) is then used to solve the outer region problem.

The potential in the outer region may be written as a local potential accounting for the

long range interaction only using the multipole expansion:

$$V_{c,c'}(r) = \sum_{\gamma=0} \frac{\alpha^{(\gamma)}_{c,c'}}{r^{\gamma+1}} \tag{2.33}$$

where the coefficients are defined as:

$$\alpha^{(\gamma)}_{c,c'} = \sqrt{\frac{2l_c+1}{2l_{c'}+1}} C(l_c, \gamma, l_{c'} \mid m_c, m_\gamma, m_{c'}) C(l_c, \gamma, l_{c'} \mid 0,0,0) Q^{(\gamma)}_{c,c'} \tag{2.34}$$

where $C(l_1, l_2, l_3 \mid m_1, m_2, m_3)$ is a Clebsch-Gordan coefficient and $Q^{(\gamma)}_{c,c'}$ the target transition moments (the Coulomb potential when $\gamma = 0$, the dipole moment when $\gamma = 1$, the quadrupole moment when $\gamma = 2$, etc., as shown in equation (2.14)). $Q^{(\gamma)}_{c,c}$ represents a permanent moment of the c-th target state and $Q^{(\gamma)}_{c,c'\neq c}$ the transition moments responsible for the coupling between channels.

It is possible that a calculation is needed where the interaction is set to zero in the whole outer region; this may be required, for instance, to provide input T-matrices for the Multiple Scattering code where the long range interaction needs to be completely neglected. In such a case, the solutions are matched to Bessel functions instead of Gailitis ones.

Each equation of the set (2.32) has n_{open} linearly independent solutions, where n_{open} is the number of open channels, i.e. those channels whose threshold energy E_c is below the scattering electron kinetic energy (E). These solutions will be referred to using a second index ($F_{c,c'}$) and at an asymptotic distance have the form:

$$F_{c,c'}(r) \overset{r\to\infty}{\sim} \begin{cases} \frac{1}{\sqrt{k_c}} \left[\sin\left(k_c r - \frac{\pi}{2} l_c\right) \delta_{c,c'} + \cos\left(k_c r - \frac{\pi}{2} l_c\right) K_{c,c'}\right]; & \text{[open channels]} \\ e^{-|k_c| r} \sim 0. & \text{[closed channels]} \end{cases} \tag{2.35}$$

The diagonal term on the left hand side of the open channel expression is the solution of the homogeneous equations (i.e. absence of interaction), while the nondiagonal term accounts for all the interaction.

All the information on the collision process can be obtained from the matrix $\boldsymbol{K}$, of elements $K_{c,c'}$, called *reaction matrix*. The S-matrix is defined as:

$$\boldsymbol{S} = (\mathbf{1} + i\boldsymbol{K})(\mathbf{1} - i\boldsymbol{K})^{-1} \tag{2.36}$$

and the eigenphase sum, which is a useful analytical tool, especially to identify resonances, may be calculated from:

$$\delta = \sum_c \arctan(K^{\mathrm{d}}_{c,c}), \tag{2.37}$$

where $\boldsymbol{K}^{\mathrm{d}}$ is the diagonalised reaction matrix.

Finally, matrix $\boldsymbol{T}$, from which the cross section is determined, is calculated as:

$$\boldsymbol{T} = \boldsymbol{S} - \boldsymbol{1} \tag{2.38}$$

The general expression to compute the cross section of a process $\sigma(c_{\mathrm{fin}} \leftarrow c_{\mathrm{ini}})$ is proportional to the element $\left|T_{c_{\mathrm{fin}},c_{\mathrm{ini}}}\right|^2$, where the process itself is identified by the initial and final channels c_{ini} and c_{fin}. Since each channel specifies the state of the target, the total spin and the angular components of the scattering electron $\left(c = (i_c, \sigma_c^{\mathrm{TOT}}, l_c, m_c)\right)$, and since this work aims to study the more general process $(i_{c_{\mathrm{fin}}} \leftarrow i_{c_{\mathrm{ini}}})$ with focus on the initial and final states of the target only, it is necessary to sum over all the T-matrix elements including the same initial and final target states (as well as over the partial waves and total spin) to obtain the desired cross section (Taylor 2006):

$$\sigma(i_{c_{\mathrm{fin}}} \leftarrow i_{c_{\mathrm{ini}}}) = \frac{\pi}{k^2_{i_{c_{\mathrm{ini}}}}} \sum_{\Gamma} \sum_{\sigma_c^{\mathrm{TOT}}} \sum_{l_{c_{\mathrm{ini}}}, l_{c_{\mathrm{fin}}}} \sum_{m_{c_{\mathrm{ini}}}, m_{c_{\mathrm{fin}}}} \frac{2\sigma_c^{\mathrm{TOT}} + 1}{2(2\sigma_{c_{\mathrm{ini}}} + 1)} \left|T^{[\Gamma]}_{c_{\mathrm{fin}},c_{\mathrm{ini}}}\right|^2, \tag{2.39}$$

where $\sigma_{c_{\mathrm{ini}}}$ is the spin angular momentum of the $i_{c_{\mathrm{ini}}}$ state, σ_c^{TOT} the total spin angular momentum of the system and Γ denotes the irreducible representation, whose role will be clarified in section 2.5.4.

2.5 Computational implementation and practical issues

There are various issues arising when the theory explained above is implemented computationally. The most important will be presented here, after an overview of the calculation steps in the UK R-matrix polyatomic code.

2.5.1 UK R-matrix polyatomic suite

A schematic overview of the input required and the stages involved in the scattering calculations performed with the UK R-matrix suite, as implemented to treat the collision

from polyatomic molecules, is provided below; the calculations consist of three parts: the target (table 2.1), inner region (table 2.2) and outer region (table 2.3) calculations. A detailed description of the programmes may be found in Tennyson (2010).

INPUT	CALCULATIONS	REFs
• **geometry** (nuclear coordinates), **point group & atomic orbitals** are chosen		
	– atomic integrals are calculated	
	– Hartree Fock Self Consistent Field calculation; orthogonal target orbitals obtained (alternatively NOs can be provided)	§2.2.1 [§2.2.2]
• **CI model** is chosen		
	– configurations are generated with the appropriate spin and space symmetry	§2.2.3
	– Hamiltonian matrix for the N-electron calculation is built; eigenvalues and eigenvectors are calculated (only the first few are normally needed)	eq. (2.13)
	– the target properties are calculated	eq. (2.14)

Table 2.1: *Stages of the target calculation. Under 'REFs', references to the relevant equations and sections of the thesis, illustrating the corresponding stage, are indicated.*

2.5.2 Partial wave expansion

The decomposition of the scattering functions in partial waves, as implicitly effected in equation (2.15), is exact if all the values of l are included; in practice the functions are expanded up to a certain value l_{max}, because the inclusion of a very large number of partial waves increases the computational requirements and makes the solution of the problem impractical. In the UK polyatomic R-matrix suite, only partial waves up to $l = 5$ can be included; $l_{max} = 4$ is mostly used.

Sometimes the number of partial waves required for convergence is higher than $l_{max} = 5$, especially when the interaction potential includes long range terms (targets with a significant

INPUT	CALCULATIONS	REFs
• **continuum orbital basis set** input • **R-matrix radius** a **& deletion threshold** for orthogonalisation set		
	– integrals are calculated *– continuum orbitals are orthogonalised to target orbitals and then among themselves* *– continuum orbitals with overlap less than the deletion threshold are discarded*	
• **CI model** is chosen (consistently with target calculation)		
	– configurations are generated *– Hamiltonian matrix for the* $(N+1)$*-electron calculation is built; all eigenvalues are calculated*	eq. (2.15)

Table 2.2: *Stages of the inner region scattering calculation. Under 'REFs', references to the relevant equations and sections of the thesis, illustrating the corresponding stage, are indicated.*

dipole moment are a case in point). The remaining terms can be included using the first Born approximation (Chu & Dalgarno 1974, Gibson et al. 1987), and can be obtained in a closed form without passing through a partial wave expansion. This correction includes contributions from all angular momenta (Watson & McKoy 1979, Fliflet & McKoy 1980).

In the calculations presented in this thesis, the use of the Born approximation will be discussed in each case; it will be clear that sometimes it is not needed, especially when comparing theoretical results.

2.5.3 Balanced calculations

A balance between the representation of the target wavefunctions — Φ_i in equation (2.4) — and the $(N+1)$ wavefunctions in the inner region — $\widetilde{\psi}_k$ in equation (2.15) — is fundamental in the R-matrix treatment of scattering processes.

INPUT	CALCULATIONS	REFs
	– the R-matrix is built at the boundary using the $(N+1)$ eigenvalues and boundary amplitudes	eq. (2.27)
• a_{out} is set • **target states** to be included in the outer region set		
	– the R-matrix is propagated from a to a_{out} using target properties (transition moments)	
	– K-matrix, S-matrix & T-matrix calculated	eqs. (2.35), (2.36), (2.38)
	– cross section & eigenphase sum calculated	eqs. (2.39), (2.37)
	– (Time delay/eigenphase sum analysis of resonances, bound states)	§2.6

Table 2.3: *Stages of the outer region scattering calculation. Under 'REFs', references to the relevant equations and sections in the thesis, illustrating the corresponding stage, are indicated.*

The ability to identify the position of resonances depends mainly on the relationship between the eigenenergies of the target and the eigenenergies of the confined $(N+1)$ system. Improving the description of one of the two systems without improving the other has the effect of increasing or decreasing the differences between these two sets of energies, with a corresponding shift in the resonance energies.

For example, if the $(N+1)$ description is improved, the E_k energies of equation (2.27) will be lowered, and the resonance features potentially associated with them will be lowered too and could become bound.

It is not always easy to carry out balanced calculations for the target and for the $(N+1)$-electron systems. In this thesis, the Complete Active Space Configuration Interaction model (CAS-CI) has been used for all calculations. If N is the total number of electrons, and n_{core} is the number of frozen ones, the model for the target calculation may be written as $(\text{core})^{n_{\text{core}}}\ (\text{CAS})^{N-n_{\text{core}}}$. It is then easy to define a model of comparable complexity for the L^2 configurations included in the expansion of the $\widetilde{\psi}_k$ $(N+1)$ wavefunctions: these should be of the form $(\text{core})^{n_{\text{core}}}\ (\text{CAS})^{N-n_{\text{core}}+1}$.

When other models different from CAS-CI are used, the correct choice of configurations to include may not be trivial (Tennyson 1996) and achieving a balance between the N and $(N+1)$ calculations very difficult.

2.5.4 Symmetry properties

Symmetry properties may be extensively used to reduce the computational requirements of the calculations; for this reason, the higher the symmetry of the target, the lighter the calculation.

Given a molecule belonging to a certain point group, its molecular orbitals and electronic wavefunctions are associated with the different irreducible representations (IRs) of that group. This means that they transform like the IRs under the symmetry elements defining the group. Since the integral of a product of two functions belonging to different IRs is zero, it is possible to reduce the number of operations required with a consequent decrease in calculation complexity. A direct consequence of this is that the Hamiltonian and the K, S and T matrices assume a block-diagonal form, so that it is possible to define different matrices (e.g. $T^{[\Gamma]}$, where Γ identifies the IR). The block-diagonal form of the Hamiltonian matrix, in particular, reduces significantly the inner region calculation, as each block can be diagonalised independently.

It is for this reason that equation (2.39) includes a sum over the irreducible representations Γ: the T-matrix elements are in fact calculated separately for each IR.

2.6 Resonances

In electron collisions, a resonance is the temporary trapping of the scattering electron to form a quasi-bound, short lived, state whose lifetime is however much longer than the usual collision time. Many reactions triggered by low-energy electron scattering pass through such a metastable state $(AB^-)^\dagger$ which later decays through different pathways.

The presence of a resonance leads to a sharp rise of the eigenphase sum (which usually varies slowly as a function of the energy) and it can usually also be seen as a peak in the

cross section centred at E^R, the resonance energy (Taylor 2006). The resonance parameters (position and width) can be obtained by fitting the eigenphase sum to the Breit-Wigner formula (Atkins & Friedman 1997):

$$\delta(E) = \sum_i \arctan\left(\frac{\Gamma_i^R}{E - E_i^R}\right) + \sum_j \delta_j^{nR}(E)E_j, \tag{2.40}$$

where the indices i and j run over the resonant and non resonant channels respectively, δ_j^{nR} is the background eigenphase (the eigenphase of the non resonant channels) and Γ^R the width of the resonance, from which it is possible to extract the resonance lifetime:

$$\tau^R \simeq \frac{\hbar}{\Gamma^R}. \tag{2.41}$$

There are also other ways of obtaining resonance patameters; for instance by analysing the time-delay matrix Q, defined as:

$$Q = -i\hbar S^* \frac{dS}{dE}, \tag{2.42}$$

whose largest eigenvalue q represents the longest time delay of the incident particle and has a Lorentzian form close to a resonance (Stibbe & Tennyson 1998):

$$q(E) = \frac{\Gamma^R}{\left((E - E^R)^2 + \left(\frac{\Gamma^R}{2}\right)^2\right)}. \tag{2.43}$$

There are different types of resonances; the simplest one is called *shape resonance*, which can be viewed in a chemical way as caused by the scattering electron temporarily occupying an unoccupied molecular orbital of the target (often the LUMO). The energy of such orbital must not be negative, otherwise it would be a bound state, which some systems may support (particularly cations). Shape resonances can be explained in terms of a trapping behind the centrifugal barrier caused by the angular momentum of the scattering electron in the electron – molecule potential. Such resonances often decay through dissociative electron attachment and are rather broad and short lived.

Feshbach resonances are caused by the excitation of the target which then causes trapping of the scattering electron; they are usually narrower than shape resonances and particularly important when the target is a cation, in which case they usually decay through dissociative recombiniation. Due to their nature, Feshbach resonances cannot be obtained from calculations where the target is frozen in its ground state.

Core-excited shape resonances are a combination of shape and Feshbach resonances; firstly the target is electronically excited, and then the electron is trapped in a metastable state by a potential barrier. Both Feshbach and core-excited shape resonances belong to the *core-excited* type resonances, since they involve target excited states. They can decay into all lower target states, but normally core-excited shape resonances decay into the parent excited state.

Other resonances involving vibrational excitation of the nuclear motion are called *nuclear-excited resonances*, and they cannot be studied within the fixed-nuclei approximation. In this work we have encountered both shape resonances (in the collisions with formic acid and its dimer) and Feshbach resonances (in the collision with the water dimer).

Chapter 3

Multiple Scattering theory

The Multiple Scattering (MS) method has been developed over the years, firstly in solid state physics to calculate the electronic properties of solids (Korringa 1947, Kohn & Rostoker 1954, Mores 1956), in nuclear physics to compute nuclear scattering cross sections (Agassi & Gal 1973) and in molecular physics. Its first implementation to treat electron – molecule scattering and photoionization was developed by Dill, Dehmer and collaborators (Dill & Dehmer 1974, Dehmer & Dill 1975, Siegel et al. 1976, Dehmer et al. 1979, Siegel et al. 1980, Siegel et al. 1981); at that time it was impossible to realistically describe the noncentral molecular core region of a polyatomic molecule due to the limited computational resources available. A way to circumvent the problem was found in using jointly two well known techniques: Multiple Scattering for treating nonseparable eigenvalue problems and the electron scattering theory.

The basic idea in the Dill & Dehmer's 1974 paper was to model the multicentred molecular potential as a set of non overlapping atomic potentials immersed in an interstitial region of constant potential. The partitioning of the coordinate space is shown in figure 3.1: non overlapping spherical regions I_i contain one atom; the model atomic spherical potential is summed to the monopole terms due to the surrounding atoms, re-expanded about the sphere centre. The potential in the interstitial region II, bound by regions I_i and a larger spherical boundary, is constant, while in the outmost region III it is spherical, and calculated summing the monopole terms from all the atoms.

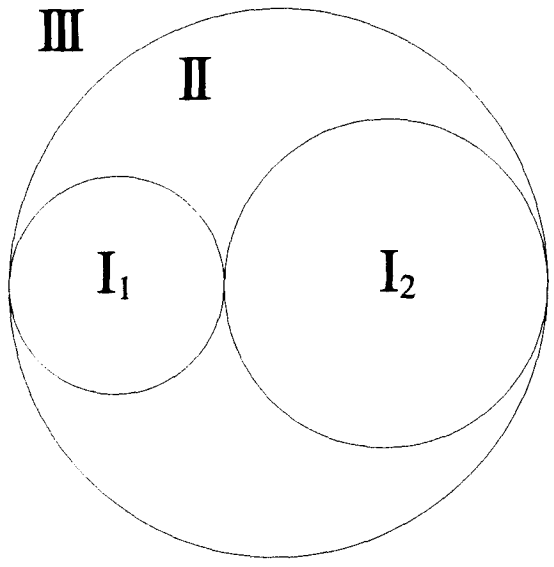

Figure 3.1: *Schematic representation of the space partition in the Multiple Scattering method for a heteronuclear diatomic molecule, as in Dill & Dehmer (1974). In this example, the target has been divided into two sub-units. The spheres I_i are centred on the centre of mass of each sub-unit.*

The assumption that the molecular potential may be approximated in this way is referred to as *muffin-tin approximation*. Williams & Morgan (1974) and Siegel et al. (1976) relaxed the hypothesis that potentials in regions I and III must be spherically symmetric, in order to attempt a more complete description of the target which could better represent effects due to charge density sitting between two atomic centres.

Later, it was also demonstrated that the Multiple Scattering theory (in all its applications, including electron – molecule scattering) allowed the possibility for the spheres defining the regions I_i, which enclosed the atomic potential, to have an arbitrary shape and even to overlap (Butler & Nesbet 1990, Butler et al. 1992, Butler et al. 1993), and that no field corrections were needed, as originally supposed by Ziesche (1974) and Faulkner (1979), as long as the potential range of the atoms did not overlap.

In later years, electron – molecule collision studies with Multiple Scattering technique dropped significantly, because of the drastic improvement of *ab initio* implementations that used quantum chemistry techniques, which allowed a more accurate description of the multicentred molecular potential using, among other things, Configuration Interaction methods.

Only recently, Caron and co-workers resumed the use of the MS method for electron

scattering, adapting it to the treatment of targets too large to be studied with standard *ab initio* techniques. Their approach, which has been followed in this research, is to partition the target into molecules whose size allows to perform *ab initio* calculations, thus defining molecular sub-units instead of atomic ones. The Multiple Scattering treatment is applied to model the collision process with the whole target.

Initially their applications made use of atomic scattering data (from argon and krypton) to model the electron collision process with DNA pseudomolecules (rungs, backbone and base pairs) (Caron & Sanche 2003, Caron & Sanche 2004, Caron & Sanche 2005, Caron & Sanche 2006). The work of Bouchiha et al. (2008) on the water dimer was the first theoretical study to make use of collision data on molecules, obtained with R-matrix calculations; the sub-units consisted of single water molecules. It was one of the first realistic attempts to investigate the behaviour of a molecular cluster under LEE impact, in order to bridge gas-phase and solid-state results. The choice to use the R-matrix method to provide the sub-units' information proved particularly good, for reasons discussed below, and was therefore applied to studies on the band structure of water ice (Caron et al. 2007) and on LEE scattering by DNA, where the sub-units consisted of single bases, sugars and phosphates (Caron et al. 2008, Caron et al. 2009).

Makochekanwa et al. (2005) applied the Multiple Scattering method to the study of the vibrational excitation of water, but their approach is consistently different to that of Caron and co-workers.

In this chapter, the Multiple Scattering technique is presented; the theory is introduced in a general way in section 3.1 for elastic collisions, then the application to the particular case of scattering from molecular clusters and the computational implementation are discussed in section 3.2.

The theoretical treatment for elastic scattering from clusters, introduced below, is substantially similar to that presented in Bouchiha et al. (2008); the computational implementations, though, differ in several points. Some bugs in the code have been corrected and it has been proven that some procedures employed in that work were not needed, or, in one case, incorrect. Finally, the Multiple Scattering code used in this work has been rewritten and

developed to solve more general cases: besides the introduction of the inelastic procedure (see chapter 6), it is now possible to treat heterogeneous clusters made up by any number of sub-units, which may be different in size, number of atoms, geometrical parameters and symmetry properties. Such generalisation has allowed us to study a wider range of targets and has also been useful to check and confirm some results.

3.1 Elastic treatment

As when it was first used, the Multiple Scattering goal is to simplify a problem otherwise too computationally costly to be performed, by dividing it into smaller and more easily solved problems. In its application to low energy electron scattering with molecular clusters, where the "cost" of an *ab initio* calculation depends upon the size of the target (in terms of extension in space and number of electrons), the approach is to partition the coordinate space occupied by the target into volumes (or *sub-regions*) containing single molecules. *Ab initio* methods are then employed to treat the collision process with each sub-unit independently, and the results are finally combined in order to retrieve scattering information relative to the cluster as a whole.

The Multiple Scattering method only deals with the "combination" step; it is assumed that scattering data on the sub-units has already been calculated by other means. In this thesis, the general expression *scattering data* refers to quantities that contain information on the collision process, and may be therefore used to calculate several observables. In particular, our treatment makes use of the sub-units' T-matrices.

In this section, the treatment of elastic scattering will be presented. It is then assumed that the cluster only undergoes elastic collisions, and no excitations are included; the same applies to the electron collision with each sub-unit.

The asymptotic form of the total wavefunction $\psi(\boldsymbol{r})$, describing the electron scattered from the whole cluster, may be written as:

$$\psi(\boldsymbol{r}) = \sum_{L,L'} Y_{L'}(\hat{r}) \left[j_{l'}(kr)\delta_{L,L'} + \frac{1}{2} h^{+}_{l'}(kr) T^{G}_{L',L} \right] \widehat{f_L} \ , \tag{3.1}$$

where the first term in the square brackets represents the incident plane wave of momentum

$k = \sqrt{E}$ and the second term the scattered wave having the same energy (because the process is elastic); E is the kinetic energy of the scattering electron. The index L indicates collectively (l, m), $Y_L(\hat{r})$ are spherical harmonics and j_l and h_l^+ are the spherical Bessel and Hankel functions of the first kind respectively; the coordinates are referred to the centre of mass of the cluster. The matrix $\boldsymbol{T}^{\mathrm{G}}$ (where G stands for *global*) contains the information of the scattering process with the whole target, whence the cross section or the eigenphase sum can be obtained.

Expansion (3.1) should include an infinite number of partial waves to be complete; in practice, the expansion is carried out up to a certain value of l, indicated as $l_{\max}$.

The intrinsic purpose of the Multiple Scattering treatment presented here is to express the unknown global matrix $\boldsymbol{T}^{\mathrm{G}}$ in terms of the sub-units T-matrices $\{\boldsymbol{T}^n\}$; the derivation of such relation will proceed through four steps:

1 — the incoming wavefunction on each sub-unit is written, as a function of the quantities g;

2 — the scattered wavefunction from each sub-unit is calculated;

3 — all the wavefunctions scattered by neighbouring sub-units, together with the incident plane wave, are summed to obtain the total incoming wave on each sub-unit, allowing the calculation of g;

4 — the total scattered wavefunction is calculated and matched with expression (3.1) to obtain an expression for $\boldsymbol{T}^{\mathrm{G}}$ in terms of $\{\boldsymbol{T}^n\}$.

The vector notation used throughout is represented in figure 3.2, where n and n' label two generic molecular sub-units.

The following re-expansion formula (Dill & Dehmer 1974, Danos & Maximon 1965) for the spherical harmonics defined by Messiah (1962) will be used:

$$Y_{L'}(\hat{r}_1)h_{l'}^{\pm}(kr_1) = \sum_{L_1,L_2} \mathrm{i}^{l_1+l_2-l'}(-)^{m'} F^{l_1,l_2,l'}_{m_1,m_2,-m'} Y_{L_1}(\hat{r}_2)Y_{L_2}(\hat{r}_3)h_{l_1}^{\pm}(kr_2)j_{l_2}(kr_3), \qquad (3.2)$$

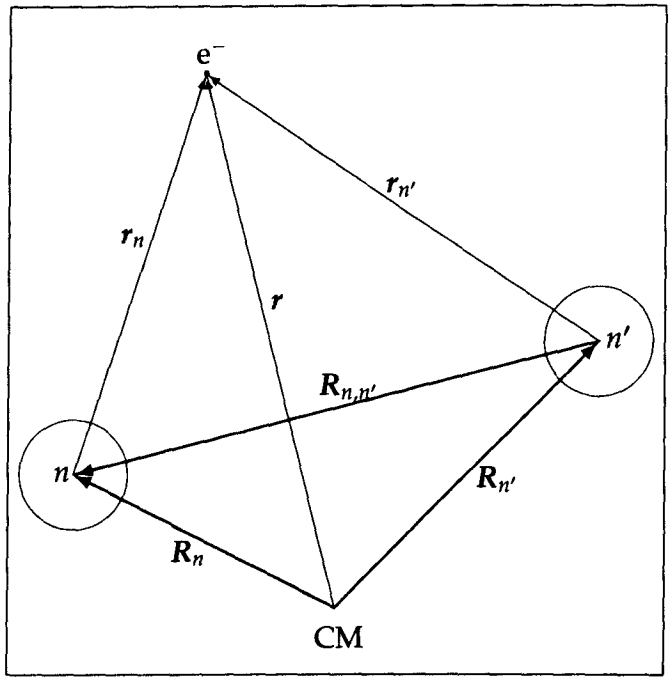

Figure 3.2: *Schematic representation of the vector notation used in the MS treatment. CM indicates the centre of mass of the cluster, the circles labelled n and n′ two generic sub-units, whose centre of mass positions are identified by vectors* $\boldsymbol{R}_n$ *and* $\boldsymbol{R}_{n'}$ *respectively. The position of the scattering electron is* $\boldsymbol{r}$ *from the cluster's centre of mass and* $\boldsymbol{r}_n$ *and* $\boldsymbol{r}_{n'}$ *from those of the sub-units. The figure shows only two sub-units, although the notation and the treatment of this chapter are general for clusters made up by any number of them.*

where

$$F^{l_1,l_2,l_3}_{m_1,m_2,m_3} = \sqrt{4\pi(2l_1+1)(2l_2+1)(2l_3+1)} \begin{pmatrix} l_1 & l_2 & l_3 \\ 0 & 0 & 0 \end{pmatrix} \begin{pmatrix} l_1 & l_2 & l_3 \\ m_1 & m_2 & m_3 \end{pmatrix}, \tag{3.3}$$

and $\begin{pmatrix} l_1 & l_2 & l_3 \\ m_1 & m_2 & m_3 \end{pmatrix}$ is Wigner 3-j symbol (Messiah 1962).

From the definition of spherical Bessel functions, equation (3.2) also holds when the functions $h_l^{\pm}$ are replaced by j_l. The vectors $\boldsymbol{r}_1$ and $\boldsymbol{r}_2$ are related by $\boldsymbol{r}_2 = \boldsymbol{r}_1 - \boldsymbol{r}_3$, with $|\boldsymbol{r}_3| > |\boldsymbol{r}_2|$. Such inequality is very important and will be carefully considered in section 3.2.4.

3.1.1 Step [1]: incoming wavefunction on each monomer

The incident plane wave from equation (3.1) is

$$\psi_{\text{in,PW}}(\boldsymbol{r}) = \sum_{L'} Y_{L'}(\hat{r}) j_{l'}(kr) \widehat{f_{L'}}, \tag{3.4}$$

which can be re-expanded around $\boldsymbol{r}_n$ considering the relation $\boldsymbol{r}_n = \boldsymbol{r} - \boldsymbol{R}_n$:

$$\begin{aligned}\psi_{\text{in,PW}}(\boldsymbol{r}_n) &= \sum_{L'}\sum_{L_1,L_2} \mathrm{i}^{l_1+l_2-l'}(-)^{m'} F^{l_1,l_2,l'}_{m_1,m_2,-m'} Y_{L_1}(\hat{\boldsymbol{r}}_n) j_{l_1}(kr_n) Y_{L_2}(\hat{\boldsymbol{R}}_n) j_{l_2}(kR_n)\widehat{f_{L'}} = \\ &= \sum_{L',L_1} Y_{L_1}(\hat{\boldsymbol{r}}_n) j_{l_1}(kr_n) M^n_{L_1,L'}\widehat{f_{L'}} = \\ &= \sum_{L_1} Y_{L_1}(\hat{\boldsymbol{r}}_n) j_{l_1}(kr_n)\widehat{g^n_{L_1}} \end{aligned} \tag{3.5}$$

where we defined:

$$M^n_{L_1,L'} \equiv \sum_{L_2} \mathrm{i}^{l_1+l_2-l'}(-)^{m'} F^{l_1,l_2,l'}_{m_1,m_2,-m'} Y_{L_2}(\hat{\boldsymbol{R}}_n) j_{l_2}(kr_n); \tag{3.6}$$

and:

$$\widehat{g^n_{L_1}} \equiv \sum_{L'} M^n_{L_1,L'}\widehat{f_{L'}}. \tag{3.7}$$

Equation (3.5) represents the wave incident on the generic sub-unit n due to the incoming plane wave only, expressed as a function of the scattering electron coordinate with respect to the centre of mass of sub-unit n, $\boldsymbol{r}_n$; the total incoming wave, including the contribution of both the plane wave and the waves scattered from the neighbouring sub-units, may be written in a similar form as:

$$\psi_{\text{in},n}(\boldsymbol{r}_n) = \sum_{L_1} Y_{L_1}(\hat{\boldsymbol{r}}_n) j_{l_1}(kr_n) g^n_{L_1} \tag{3.8}$$

where the yet unknown functions $\{g^n\}$ contain all the contributions.

3.1.2 Step [2]: wavefunction scattered from each monomer

Given the incoming wavefunction expressed by (3.8), the scattered wavefunction for sub-unit n can be written making use of the sub-unit T-matrix $\boldsymbol{T}^n$:

$$\psi_{\text{sc},n}(\boldsymbol{r}_n) = \frac{1}{2}\sum_{L,L'} Y_{L'}(\hat{\boldsymbol{r}}_n) h^+_{l'}(kr_n) T^n_{L',L} g^n_L \tag{3.9}$$

which can be re-expanded around the centre of mass of another generic sub-unit n', considering the relation $\boldsymbol{r}_{n'} = \boldsymbol{r}_n - \boldsymbol{R}_{n',n}$:

$$\psi_{\text{sc},n}(\boldsymbol{r}_{n'}) = \sum_{L,L',L_2} Y_{L_2}(\hat{\boldsymbol{r}}_{n'}) j_{l_2}(kr_{n'}) X^{n',n}_{L_2,L'} T^n_{L',L} g^n_L \tag{3.10}$$

where we defined:

$$X^{n',n}_{L_2,L'} \equiv \frac{1}{2}\sum_{L_1} \mathrm{i}^{l_1+l_2-l'}(-)^{m'} F^{l_1,l_2,l'}_{m_1,m_2,-m'} Y_{L_1}(\hat{R}_{n',n}) h^+_{l_1}(kR_{n',n}). \tag{3.11}$$

The definition (3.11) has been written in the assumption that $n \neq n'$, but it can be naturally extended by defining $X^{n,n}_{L_1,L_2} = 0$, since it will be useful later. Equation (3.10) expresses the wave scattered off sub-unit n and incoming onto sub-unit n'.

3.1.3 Step [3]: total incoming wavefunction and derivation of g

The total incoming wavefunction on scatterer n from equation (3.8) can be now re-derived from the obvious relation

$$\psi_{\mathrm{in},n}(\boldsymbol{r}_n) = \psi_{\mathrm{in,PW}}(\boldsymbol{r}_n) + \sum_{n'\neq n} \psi_{\mathrm{sc},n'}(\boldsymbol{r}_n); \tag{3.12}$$

substituting equations (3.5) for $\psi_{\mathrm{in,PW}}(\boldsymbol{r}_n)$ and (3.10) for $\psi_{\mathrm{sc},n'}(\boldsymbol{r}_n)$:

$$\psi_{\mathrm{in},n}(\boldsymbol{r}_n) = \sum_{L_1} Y_{L_1}(\hat{r}_n) j_{l_1}(kr_n) \left[\widehat{g}^n_{L_1} + \sum_{n'\neq n}\sum_{L,L'} X^{n,n'}_{L_1,L'} T^{n'}_{L',L} g^{n'}_L \right]. \tag{3.13}$$

Comparing the two expressions (3.8) and (3.13) for $\psi_{\mathrm{in},n}$, it is possible to obtain the following relation for g:

$$g^n_{L_1} = \widehat{g}^n_{L_1} + \sum_{n'\neq n}\sum_{L,L'} X^{n,n'}_{L_1,L'} T^{n'}_{L',L} g^{n'}_L. \tag{3.14}$$

It is very easy to write this relation in matrix form; to do so, the following vectors and matrices are defined:

$$\widehat{\mathbb{G}} \equiv \begin{bmatrix} \widehat{g}^1 \\ \widehat{g}^2 \\ \vdots \\ \widehat{g}^N \end{bmatrix}; \quad \mathbb{G} \equiv \begin{bmatrix} g^1 \\ g^2 \\ \vdots \\ g^N \end{bmatrix}; \quad \mathbb{T} \equiv \begin{bmatrix} \boldsymbol{T}^1 & \boldsymbol{0} & \cdots & \boldsymbol{0} \\ \boldsymbol{0} & \boldsymbol{T}^2 & & \boldsymbol{0} \\ \vdots & & \ddots & \\ \boldsymbol{0} & \boldsymbol{0} & & \boldsymbol{T}^N \end{bmatrix}; \tag{3.15}$$

$$\mathbb{X} \equiv \begin{bmatrix} \boldsymbol{X}^{1,1} & \boldsymbol{X}^{1,2} & \cdots & \boldsymbol{X}^{1,N} \\ \boldsymbol{X}^{2,1} & \boldsymbol{X}^{2,2} & \cdots & \boldsymbol{X}^{2,N} \\ \vdots & & \ddots & \\ \boldsymbol{X}^{N,1} & \boldsymbol{X}^{N,2} & \cdots & \boldsymbol{X}^{N,N} \end{bmatrix} = \begin{bmatrix} \boldsymbol{0} & \boldsymbol{X}^{1,2} & \cdots & \boldsymbol{X}^{1,N} \\ \boldsymbol{X}^{2,1} & \boldsymbol{0} & \cdots & \boldsymbol{X}^{2,N} \\ \vdots & & \ddots & \\ \boldsymbol{X}^{N,1} & \boldsymbol{X}^{N,2} & \cdots & \boldsymbol{0} \end{bmatrix}. \tag{3.16}$$

Notice that $\boldsymbol{T}^n$ and $\boldsymbol{X}^{n,n'}$ are matrices themselves, and $\widehat{\boldsymbol{g}}^n$ and $\boldsymbol{g}^n$ vectors. They have dimension $(l_{\max}+1)^2$ since the index $L = (l, m)$ runs from $(0, 0)$ to $(l_{\max}, +l_{\max})$; matrices $\boldsymbol{X}^{n,n'}$, $\boldsymbol{T}^n$ and $\mathbf{0}$ have dimensions $\left((l_{\max}+1)^2, (l_{\max}+1)^2\right)$. The final dimension of matrices $\widehat{\mathbb{G}}$ and $\mathbb{G}$ is then $N \times (l_{\max}+1)^2$, where N is the number of sub-units the target has been divided into, and matrices $\mathbb{T}$ and $\mathbb{X}$ have dimension $\left(N \times (l_{\max}+1)^2, N \times (l_{\max}+1)^2\right)$.

Given these definitions, equation (3.14) may be rewritten in a, clearer, matrix form as

$$\mathbb{G} = \widehat{\mathbb{G}} + \mathbb{X}\mathbb{T}\mathbb{G}, \tag{3.17}$$

whose solution is

$$\mathbb{G} = (\mathbb{1} - \mathbb{X}\mathbb{T})^{-1}\,\widehat{\mathbb{G}}, \tag{3.18}$$

where $\mathbb{1}$ is a unit matrix with dimension $\left(N \times (l_{\max}+1)^2, N \times (l_{\max}+1)^2\right)$.

At this point, the unknown vectors introduced in equation (3.8) to include all the terms that contribute to the incoming wave on each sub-unit (i.e. the incoming plane wave plus the waves scattered by neighbouring sub-units) have been expressed, as expected, in terms of the plane wave amplitudes $\widehat{\mathbb{G}}$ multiplied by the multiple scattering term $(\mathbb{1} - \mathbb{X}\mathbb{T})^{-1}$ which will be discussed later.

3.1.4 Step [4]: total scattered wavefunction

Once $\mathbb{G}$ is known, it is possible to add the waves scattered by all the sub-units, given by equation (3.9):

$$\begin{aligned}
\psi_{\text{sc,TOT}} &= \sum_n \psi_{\text{sc},n} = \\
&= \frac{1}{2}\sum_n \sum_{L,L'} Y_{L'}(\hat{r}_n) h^+_{l'}(kr_n) T^n_{L',L} g^n_L = \\
&= \frac{1}{2}\sum_n \sum_{L,L',L_1} Y_{L_1}(\hat{r}) h^+_{l_1}(kr) N^n_{L_1,L'} T^n_{L',L} g^n_L,
\end{aligned} \tag{3.19}$$

where a re-expansion around $\boldsymbol{r}$ has been carried out ($\boldsymbol{r} = \boldsymbol{r}_n - (-\boldsymbol{R}_n)$) and we defined:

$$N^n_{L_1,L'} = \sum_{L_2} \mathrm{i}^{l_1+l_2-l'} (-)^{m'} F^{l_1,l_2,l'}_{m_1,m_2,-m'} Y_{L_2}(-\hat{\boldsymbol{R}}_n) j_{l_2}(kR_n). \tag{3.20}$$

It is then convenient to define matrices

$$\mathbb{M} = \begin{bmatrix} M^1 & M^2 & \cdots & M^N \end{bmatrix}; \quad \mathbb{N} = \begin{bmatrix} N^1 \\ N^2 \\ \vdots \\ N^N \end{bmatrix}; \tag{3.21}$$

where M and N are defined in equations (3.6) and (3.20). Then equation (3.7) can be rewritten in matrix form as $\widehat{\mathbb{G}} = \mathbb{M}\widehat{f}$. Remembering that the scattered wave part in equation (3.1) is

$$\psi_{sc,TOT}(r) = \frac{1}{2}\sum_{L,L'} Y_{L'}(\hat{r}) h_{l'}^{+}(kr) T^{G}_{L',L} \widehat{f}_{L} \ , \tag{3.22}$$

comparing it to equation (3.19), and using equation (3.18), it is possible to write:

$$\mathbb{N}\mathbb{T}\mathbb{G} = \mathbb{N}\mathbb{T}(\mathbb{1} - \mathbb{X}\mathbb{T})^{-1}\widehat{\mathbb{G}} = \mathbb{N}\mathbb{T}(\mathbb{1} - \mathbb{X}\mathbb{T})^{-1}\mathbb{M}\widehat{f} = T^{G}\widehat{f}, \tag{3.23}$$

so that an expression for the global T-matrix T^G can be obtained:

$$T^{G} = \mathbb{N}\mathbb{T}(\mathbb{1} - \mathbb{X}\mathbb{T})^{-1}\mathbb{M}. \tag{3.24}$$

Here, as expected, T^G has the same dimension of T^n (referred to as *(D,D)* for brevity), since matrices $\mathbb{N}$ and $\mathbb{M}$ have dimension *(D,ND)* and *(ND,D)* respectively.

3.1.5 Terms contributing to the global T-matrix T^G

The terms constituting equation (3.24) may be divided into *re-expansion terms* $\mathbb{M}$ (from r to r_n) and $\mathbb{N}$ (from r_n to r), and a *multiple scattering* term $(\mathbb{1} - \mathbb{X}\mathbb{T})^{-1}$. The latter represents the multiple scattering contribution; in fact, the matrix $\mathbb{X}$ includes the "interference" effect due to the presence of waves scattered by the other sub-units. The symmetric blocks $X^{n,n}$ in matrix $\mathbb{X}$ are zero, therefore there is obviously no multiple scattering effect between a sub-unit and itself; moreover, if $\mathbb{X}$ were null, there would be no interference effect at all: the final T-matrix would just be a superposition of sub-units' T-matrices, and the final cross section would simply be $\sigma^G \approx \sum_n \sigma^n \propto \sum_n |T^n|^2$. This indicates that the collision process would be superficially approximated to the sum of independent collisions of the electron with each of the sub-units.

3.2 Discussion and practical application to molecular clusters

Having derived the expression for T^G, the issue remains as to how the T^n should be generated.

3.2.1 T-matrix cutoff

The articles by Caron and co-workers, treating the scattering process with condensed-phase water, DNA and water clusters, have pointed out the need to introduce a modification in equation (3.24), as was also confirmed by our tests. The equation should be rewritten as

$$T^G = \mathbb{N}\mathbb{T}(\mathbb{1} - \mathbb{X}\mathbb{T}_c)^{-1}\mathbb{M}. \tag{3.25}$$

A new T-matrix $\mathbb{T}_c$ is introduced in the multiple scattering term; the label 'c' stands for *cutoff*, since it is necessary to apply two cutoffs to the T-matrices forming it.

The first cutoff is needed when dipolar molecules are treated; due to its long range, the dipole interaction leads to large elastic cross sections at low energies, eventually divergent; however, in the muffin-tin approximation it is assumed that the sub-unit potential is of finite range. Therefore a cutoff must be introduced to limit the range of action of the dipole interaction. This is achieved by including the dipole interaction up to a certain distance a_c from the sub-unit's centre of mass, and neglecting it at larger distances.

The appropriate choice of a_c is not trivial, and must be considered carefully. Although any theoretical method is, in principle, appropriate to obtain the initial sub-units' T-matrices $\{T^n\}$ which are needed to build matrix $\mathbb{T}$ of equation (3.15), it will now become evident that the R-matrix method is particularly fit for this task. The reason is that the partition between inner and outer regions reflects naturally the MS division of space into sub-regions required by the muffin-tin approximation. In the R-matrix technique, the dipole moment cutoff may be easily introduced by modifying the outer region calculation so that the long range potential is neglected.

This can be done in two ways: one is to increase or reduce the R-matrix sphere radius a, and subsequently skip the R-matrix propagation performed in the outer region, matching the scattering wavefunctions with Bessel functions at $r = a$ (see section 2.4; this procedure

implies that $a_c = a$ in all cases, and it is not indicated when very large or very small values of a_c are needed. A large R-matrix radius would cause an unnecessary increase in computational requirements, which would not be justified by geometrical considerations; on the other hand, too small a radius a would introduce errors since a relevant part of the electronic target wavefunctions might then leak outside the boundary and be incorrectly neglected; to avoid this happening, a more compact basis set for the orbitals may be chosen, with a consequent reduction of the quality of the target representation.

A more sensible approach, which has been used in this work, consists in using different values for a and a_c. The choice of a is based on the usual considerations about the spatial extent of the target wavefunctions, for which the use of a large value would be preferable, and is also influenced by the need to minimise the overlap between the spheres containing the sub-units, for which, conversely, a small value of a and more compact orbitals are preferred. The R-matrix calculated at $r = a$ is then propagated with the usual propagation method from a to a_c. This step has the approximate effect of adding (if $a < a_c$) or subtracting (if $a > a_c$) the dipole interaction in the region between a and a_c. Matching with Bessel functions at $r = a_c$ implies that the dipole moment interaction is disregarded between a_c and ∞. The tests that need to be performed to select the correct values of a and a_c will be reported for each type of cluster in the result chapters, where it will be shown that in fact the choice of a and a_c is less critical than initial works implied.

Caron et al. (2007) and Bouchiha et al. (2008) also analysed the need for a second cutoff on the T-matrices forming $\mathbb{T}_c$; this cutoff is applied on the number of partial waves included. The partial wave expansion in the R-matrix calculations is carried out up to $l = 4$ or 5, but it has been observed that the use of the full angular momentum content of the T-matrix at all energies produces an incorrect Multiple Scattering cross section (this was also noticed in the studies on DNA Caron et al. 2008). Such behaviour may be explained in terms of the angular momentum energy barrier $E(l, r) = \frac{l(l+1)}{r^2}$; the electrons scattering from one sub-unit are able to reach another one only if their energy is large enough to overcome the barrier, i.e., only if $E_e > E(l, R_{n,n'})$, where E_e is the electron energy and $R_{n,n'}$ the distance between two generic sub-units. The relevant angular momenta that have to be included in $\mathbb{T}_c$, therefore,

are those for which the following relation (where the energy is in Rydberg) holds:

$$\frac{l(l+1)}{R_{n,n'}^2} \leqslant E_e. \tag{3.26}$$

The same conclusion may be reached with a mathematical reasoning, observing that the elements of matrix $\mathbb{X}$, shown in equation (3.11), include spherical Hankel functions of the first kind $h_l^+(kR_{n,n'})$, which diverge as $(kR_{n,n'})^{-(l+1)}$ when the argument tends to zero; the singularity is dominated by the sub-units distance $R_{n,n'}$. A truncation on the angular momentum expansion is an inexpensive way of getting rid of such behaviour (Caron et al. 2008).

The partial wave cutoff is achieved, in practice, by truncating the T-matrix, including in the matrix $\mathbb{T}_c$ only those elements corresponding to channels associated with partial waves $l \leqslant l_c$; the others are set to zero.[1] So there is no change in the way the T-matrices are generated; the R-matrix calculation is not modified and needs to be run once.

When solving the MS problem in an energy range, different partial wave cutoff values are applied in different energy sub-ranges; problems may then arise due to the discreteness of l, causing discontinuities in the cross section at the "cutoff energies" $E_c^{(l)} = \frac{l(l+1)}{R_{n,n'}^2}$. This issue is circumvented by a two-point interpolation of the cross sections: at any energy E lying between two cutoff energies $\left(E_c^{(l)} < E < E_c^{(l+1)}\right)$ the cross section is a combination of $\sigma^{(l)}(E)$ and $\sigma^{(l+1)}(E)$, weighted according to the differences $\left|E - E_c^{(l)}\right|$ and $\left|E - E_c^{(l+1)}\right|$. Here $\sigma^{(l)}$ indicates the Multiple Scattering cross section, obtained from $\boldsymbol{T}^G$, where $\mathbb{T}_c$ includes partial waves up to l only; these cross sections will be henceforth referred to as *cutoff cross sections*. So the interpolation is not actually performed on the partial waves, but on cross sections including a different number of them.

Bouchiha et al. (2008) also observed that a modification is sometimes needed in equation (3.26) and suggest the introduction of an *ad hoc* energy correction parameter γ to shift the cutoff energies, so that equation (3.26) is rewritten as:

$$\frac{l(l+1)}{R_{n,n'}^2} \leqslant \gamma E_e. \tag{3.27}$$

[1] This procedure is an approximate way to remove contributions from higher partial waves and may introduce errors.

A value of $\gamma = 0.75$ (upwards energy shifting) is used in Bouchiha et al.'s (2008) article on water dimer to get rid of some spurious peaks. The use of such a parameter has been studied in this thesis, in order to determine whether it is actually needed. As will be described in later chapters, we found that in some cases γ is not needed, while in other cases a value of $\gamma < 1$ must be used to ensure a smooth cross section and to eliminate spurious peaks from high partial wave contributions. A more in-depth analysis will be carried out for each system treated.

3.2.2 Rotation of T-matrices

In its application to molecular clusters, the most natural and straightforward interpretation of the target partitioning into sub-units is the definition of each monomer of the cluster as a different sub-unit. This choice turns out to be particularly helpful when homogeneous clusters are treated; in this case, there is no need to run N separate calculations to obtain the N sub-units T-matrices needed in equation (3.15) to build matrix $\mathbb{T}$.[2] If the internal coordinates of the monomers are sufficiently similar, it is possible to calculate only one T-matrix with cutoff and one without, with the monomer in some convenient orientation $O_{\mathrm{R-m}}$, and then apply a rotation to it, in order to account for the various orientations of each monomer in the cluster (O^n_{cls}).

The rotation of the T-matrices is performed by the MS programme, provided the three Euler angles defining it are given. These angles can be found by solving for the *coordinate rotation matrix* $\boldsymbol{R}(\alpha,\beta,\gamma)$, which transforms the orientation of the monomer into that of the cluster — i.e. $\boldsymbol{R}^n(\alpha,\beta,\gamma)\boldsymbol{O}_{\mathrm{R-m}} = \boldsymbol{O}^n_{\mathrm{cls}}$; the index n indicates that one rotation matrix is defined per each monomer forming the cluster. The rotation matrix is constructed according to the formula (Messiah 1962):

$$\boldsymbol{R}(\alpha,\beta,\gamma) = \begin{pmatrix} \cos\gamma\cos\beta\cos\alpha - \sin\gamma\sin\alpha & -\sin\gamma\cos\beta\cos\alpha - \cos\gamma\sin\alpha & \sin\beta\cos\alpha \\ \cos\gamma\cos\beta\sin\alpha + \sin\gamma\cos\alpha & -\sin\gamma\cos\beta\sin\alpha + \cos\gamma\cos\alpha & \sin\beta\sin\alpha \\ -\cos\gamma\sin\beta & \sin\gamma\sin\beta & \cos\beta \end{pmatrix}, \tag{3.28}$$

[2] The computation of the monomer T-matrices is the only preliminary calculation needed, and the most time and computer resource consuming.

where α, β and γ are the Euler angles, and the index n has been dropped for simplicity.[3] Once the Euler angles are known, it is possible to build the matrix which applies the rotation onto the T-matrices; the rotation is actually applied onto the spherical harmonics in whose representation the T-matrix has been originally built (i.e. those defining channels in equation 2.30, from which the K-matrix is constructed as in equation 2.35, and therefore the T-matrix as in equation 2.38). If the spherical harmonics have been defined as those of Messiah (1962),[4] the *spherical harmonics rotation matrix* $W(\alpha,\beta,\gamma)$ is built according to the Wigner formula:

$$W_{L_1,L_2}(\alpha,\beta,\gamma) = \mathrm{e}^{-\mathrm{i}\alpha m_1} w^{(l)}_{m_1,m_2}(\beta) \mathrm{e}^{-\mathrm{i}\gamma m_2}, \tag{3.29}$$

where

$$w^{(l)}_{m_1,m_2}(\beta) = \sum_t (-)^t \frac{\sqrt{(l+m_1)!(l-m_1)!(l+m_2)!(l-m_2)!}}{(l+m_1-t)!(l-m_2-t)!t!(t-m_1+m_2)!} \zeta^{2l+m_1-m_2-2t} \eta^{2t-m_1+m_2}, \tag{3.30}$$

with $\zeta = \cos\left(\frac{\beta}{2}\right)$ and $\eta = \sin\left(\frac{\beta}{2}\right)$. The indices L_1 and L_2 refer collectively to (l_1,m_1) and (l_2,m_2), and $l_1 = l_2 = l$ (the rotation does not mix elements with different total angular momentum).

Once matrix $\boldsymbol{W}$ is built, it is applied onto the T-matrix, obtaining a *rotated T-matrix*:

$$\boldsymbol{T}^{\mathrm{ROT}} = \boldsymbol{W}\boldsymbol{T}\boldsymbol{W}^{-1}. \tag{3.31}$$

The procedure to find the Euler angles is the following: firstly, the orientations of the isolated monomer, $\boldsymbol{O}_{\mathrm{R-m}}$, and of the monomer in the cluster, $\boldsymbol{O}^n_{\mathrm{cls}}$, are obtained. These are calculated choosing three independent geometrical parameters (e.g. position of atoms, direction of bonds, atom – atom vectors) expressed with respect to the coordinate system employed in the respective calculations. The orientation matrices thus obtained, $\boldsymbol{O}_{\mathrm{R-m}}$ and $\boldsymbol{O}^n_{\mathrm{cls}}$, are 3 × 3 matrices. The rotation matrix $\boldsymbol{R}^n$ is such that it transforms $\boldsymbol{O}_{\mathrm{R-m}}$ into $\boldsymbol{O}^n_{\mathrm{cls}}$, i.e. $\boldsymbol{R}^n\,\boldsymbol{O}_{\mathrm{R-m}} = \boldsymbol{O}^n_{\mathrm{cls}}$, and it is therefore obtained with the formula $\boldsymbol{R}^n = \boldsymbol{O}^n_{\mathrm{cls}}\boldsymbol{O}^{-1}_{\mathrm{R-m}}$. Once $\boldsymbol{R}^n$ is known, the Euler angles are calculated using equation (3.28) and input to the programme.

The way to choose an appropriate set of geometrical parameters for the construction of the orientation matrices is not trivial. If the geometries of the isolated and clusterised

[3] If one wants to keep the index n, which labels the N monomers forming the cluster, there would be N Euler angle triplets — $(\alpha^n, \beta^n, \gamma^n)$ — one per monomer.

[4] Otherwise, a further transformation is necessary, in order to account for the different definitions.

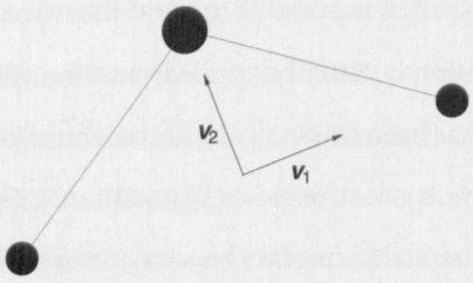

Figure 3.3: *Schematic illustration of the definition of vectors v_1 and v_2 for the water molecule: v_2 identifies the oxygen–CM direction; v_1 lies on the (HOH) plane and is orthogonal to v_2; v_3 is orthogonal to the previous vectors and points out of the plane. All vectors are unitary.*

monomers were identical, the position of three atoms would be sufficient (provided they are independent, i.e. they are not aligned). In practice, the clusterisation often introduces geometrical modifications in the bond lengths and angles, so that building the orientation matrices using the position of three atoms only would cause the solution of the equation $\boldsymbol{R}^n = \boldsymbol{O}^n_{\rm cls}\boldsymbol{O}^{-1}_{\rm R-m}$ to be not unitary; it is therefore safer to employ other geometrical criteria. The one we have been using, and encoded in a small Fortran programme called *eulerrot*, is to define three orthonormal vectors v_1, v_2 and v_3 describing the orientation of the molecule. Their definition is different for each molecule treated. Figure 3.3 shows how the vectors are defined when water clusters are studied: firstly v_2 is defined along the oxygen–CM direction; v_1 is chosen lying on the HOH plane and orthogonal to v_2; v_3 is orthogonal to both of them ($v_3 = v_1 \times v_2$). The vectors are then expressed in terms of the coordinate system employed in the monomer or dimer calculations and the orientation matrices built: $\boldsymbol{O} = \begin{pmatrix} v_1 & v_2 & v_3 \end{pmatrix}$. These definitions are robust with respect to changes of the bond lengths and angles.

3.2.3 Propagation of $T^{\rm G}$

An important difference between our approach and that used in Bouchiha et al. (2008) is in the use of a propagation step which has been abandoned in the present treatment. In their work, the T-matrix $\boldsymbol{T}^{\rm G}$ calculated using equation (3.25) was converted back into an R-matrix at $r = a_{\rm c}$ using an approximate formula, and then propagated to an asymptotic

distance using the standard method employed in the R-matrix code. The cluster's dipole moment was used to build the potential for this propagation. Matching to the asymptotic wavefunctions provided an "asymptotic" T-matrix, that now included the effect of the long-range electron – cluster dipole moment interaction, and which was used to determine the cross section for the cluster.

In the present work, such propagation step has been dropped; firstly because converting a T-matrix into an R-matrix can only be done accurately far away from the target, where the interaction with the scattering electron may be assumed negligible. This is obviously not the case at $r = a_c$. Moreover, it was observed in practice that the extra propagation step was actually not needed, since it worsens the agreement between the MS cross section and the R-matrix one used for comparison in a wide energy range for all the $(H_2O)_2$ geometries.

3.2.4 Geometrical constraints

In the derivation of equation (3.24) in section 3.1, the re-expansion formula (3.2) has been used in three occasion (equations 3.5, 3.10 and 3.19). Such formula may be used if the inequality $|\boldsymbol{R}| > |\boldsymbol{r}'|$ holds, where $\boldsymbol{r}'$ is the coordinate into which the expansion is performed, $\boldsymbol{R} = \boldsymbol{r} - \boldsymbol{r}'$, and $\boldsymbol{r}$ is the original coordinate.

The conditions that must be satisfied when the re-expansion formula is used in section 3.1 may be reduced to:

$$\begin{cases} |\boldsymbol{r}_n| < |\boldsymbol{R}_n|; \\ |\boldsymbol{r}_n| < \left|\boldsymbol{R}_{n,n'}\right|, \end{cases} \tag{3.32}$$

where $\boldsymbol{r}_n$, $\boldsymbol{R}_n$ and $\boldsymbol{R}_{n,n'}$ are defined as in figure 3.2.

While $\boldsymbol{R}_n$ and $\boldsymbol{R}_{n,n'}$ are fixed parameters defined by the geometry of the cluster, vector $\boldsymbol{r}_n$ points to the scattering electron from the centre of mass of sub-unit n, and can in principle assume any value. In practice, however, the re-expansion is performed when the scattering electron is interacting with the sub-unit only, which means that $\boldsymbol{r}_n$ extends up to the distances for which the sub-unit's potential is non-negligible.

The inequalities (3.32) then imply that: the sub-units' potentials must not overlap with the cluster centre of mass (first inequality) or with the centres of mass of the other sub-units

(second one). The second conclusion recalls that of Butler et al. (1993), who relaxed the original constraint of non-overlapping regions, as long as the potentials did not overlap. In order to verify whether we meet these requirements, we must have an idea of the extent of the monomer potentials. In our MS approach, making use of R-matrix data, the molecular potentials considered for the multiple scattering term (i.e. those included in $\mathbb{T}_c$, where the long-range interactions are cut off) are certainly contained inside the sub-region boundaries (because of the constraint imposed by the R-matrix technique on the target electronic density), so it can be assumed that $\max(|\boldsymbol{r}_n|) \leqslant a$. It is less obvious whether a_c could be used instead of a: in principle it is possible to choose $a_c < a$ and remove the long range interactions down to a_c, but this procedure, as stressed in section 3.2.1, is approximate. It is then safer for our purposes to rewrite the inequalities 3.32 as:

$$\begin{cases} a < |\boldsymbol{R}_n| ; \\ a < \left|\boldsymbol{R}_{n,n'}\right| , \end{cases} \tag{3.33}$$

which are easier to verify. Considering also that for all the cluster geometries studied in this thesis the relation $|\boldsymbol{R}_n| < \left|\boldsymbol{R}_{n,n'}\right|$ always holds[5], the inequalities may be reduced to one, i.e. $a < |\boldsymbol{R}_n|$.

Analysing our cluster geometries, it is clear that inequalities (3.33) are not always met: all the clusters studied involve an overlap (of different extent) between the spheres, because the radii of the R-matrix sphere required to achieve a reasonable monomer calculation are bigger than the monomer – CM distances $\boldsymbol{R}_n$ and sometimes even bigger than the monomer – monomer distances $\boldsymbol{R}_{n,n'}$. However, although these conditions are not fulfilled in our calculations, the good results obtained, both for the water and the formic acid clusters, seem to imply that these restrictions are not fundamental. They are not to be underestimated, however: one of the tests carried out on the formic acid dimer, for instance, consisted of varying the inter-monomer distance; when the monomers were brought closer than in the equilibrium geometry, spurious peaks appeared in the cutoff cross sections at higher energies than in the equilibrium case, and were included in the final interpolated cross section. We deemed this effect due to the too large overlap between the sub-units, as it is explained in

[5]The inequality $|\boldsymbol{R}_n| < \left|\boldsymbol{R}_{n,n'}\right|$ holds for most of the small non linear clusters.

section 5.3.2.

3.2.5 Practical computational implementation

An outline of the programme implemented to perform Multiple Scattering calculations (together with the prior steps and calculations) is shown schematically in figure 3.4, where the simplest case of a three-sub-units cluster is considered.

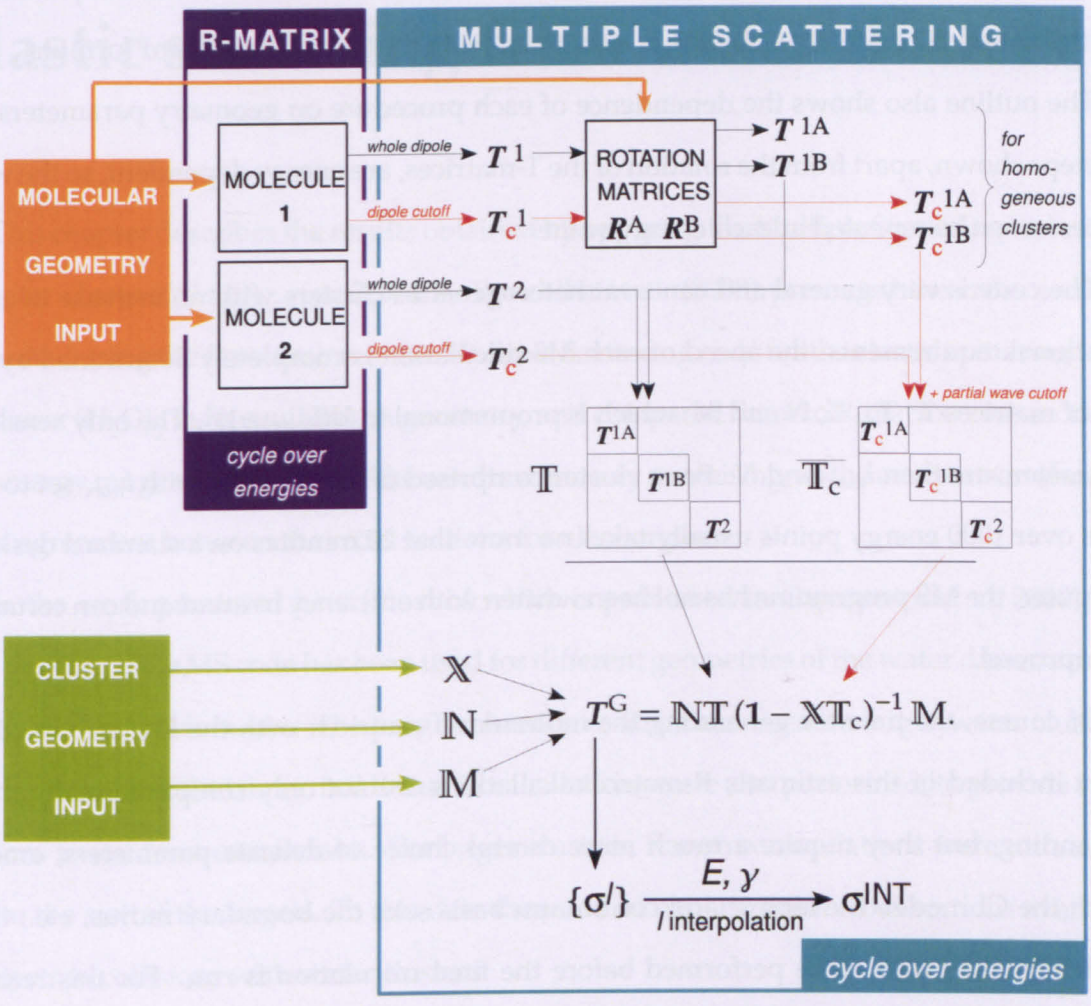

Figure 3.4: *Outline of the code and of the prior calculations needed for a MS calculation. The outline considers a cluster made up by three sub-units, of which two are the same molecule (labelled molecule 1). The rotation matrices are then applied on* T^1 *to account for the different orientations A and B, obtaining matrices* T^{1A} *and* T^{1B}*. No rotation is necessary for molecule 2 with T-matrix* T^2 *if the orientation considered in the R-matrix calculation is the same as that in the cluster; otherwise it should too be rotated.*

The first step is to produce the sub-units T-matrices using the R-matrix suite. Two T-

matrices are calculated for each sub-unit: one considering all the dipole moment interaction, and another including it up to a_c (in the inner region it is automatically taken into account). The inner region calculation needs to be run only once, and the outer region twice. If the cluster is (at least in part) homogeneous, one R-matrix calculation is needed for each different molecule only, and rotation matrices are built to produce rotated T-matrices.

Matrices $\mathbb{T}$ and $\mathbb{T}_c$ are constructed, together with matrices $\mathbb{X}$, $\mathbb{N}$ and $\mathbb{M}$ which depend on the cluster geometry only. The global T-matrix T^G is then obtained from a simple matrix multiplication. The MS cross section is calculated from it, using the standard formula.

The outline also shows the dependence of each procedure on geometry parameters; all the steps shown, apart from the rotation of the T-matrices, are energy dependent, so the wole process must be repeated at each energy value.

The code is very general and can treat heterogeneous clusters with no increase in computational requirements: the speed of each MS calculation is completely determined by the size of matrices $\mathbb{T}$, $\mathbb{T}_c$, $\mathbb{X}$, $\mathbb{N}$ and $\mathbb{M}$, which is proportional to $N(l_{max}+1)^2$. The only sensitive parameters are then l_{max} and N. For a cluster comprised of 3 sub-units, with l_{max} set to 4, a cycle over 1000 energy points usually takes no more that 20 minutes on a standard desktop computer; the MS programme has not been written with efficiency in mind and can certainly be improved.

Of course, the time for generating the molecular T-matrices with the R-matrix method is not included in this estimate; R-matrix calculations are not only computationally more demanding, but they require a much more careful choice of delicate parameters, among which the CI model, the atomic and continuum basis sets, the boundary radius, etc., thus requiring many tests to be performed before the final calculation is run. For this reason, homogeneous cluster calculations are much easier and faster than those for heterogeneous ones.

Chapter 4

Elastic scattering from water clusters

This chapter describes the results obtained by applying the Multiple Scattering technique to water clusters, $(H_2O)_n$, $n = 2,3,4,5$. Bouchiha et al. (2008) presented the cross sections generated using the first version of the Multiple Scattering code for the elastic scattering from the dimer $(H_2O)_2$ in its equilibrium geometry, and compared them to R-matrix cross sections. The energy range was [0 – 10 eV]; the results were very promising, as the comparison showed good agreement between the cross sections for all energies.

In the work presented here (most of which is published in Caprasecca et al. 2009), the new version of the MS code has been used for different geometries of the water dimer, among which the equilibrium one. The programmes have also been used on larger water clusters. For the dimer and the trimer, full R-matrix calculations were also performed, to provide cross sections to use for a comparison. For larger clusters, R-matrix calculations were unfeasible due to the size of the targets. To this date there are no experimental cross sections available for electron collisions with water clusters.

4.1 Water monomer

In order to produce the T-matrices $\boldsymbol{T}$ and $\boldsymbol{T}_c$ required by the MS method to build matrices $\mathbb{T}$ and $\mathbb{T}_c$ of equation (3.25), R-matrix scattering calculations on the isolated water monomer were performed. The equilibrium geometry of water in the ground state has been widely studied, and its geometrical parameters are well known. The two O–H bond lengths are

Figure 4.1: *Ball-and-stick model of H_2O.*

1.808 a_0 and the $\widehat{HOH}$ angle measures 104.52°(Benedict et al. 1956); the molecule therefore belongs to the C_{2v} symmetry point group. Water has a large dipole moment of 1.855 D (Dyke & Muenter 1973), which strongly influences the collision process.

The calculations were performed following the previous work on electron scattering from isolated water by Gorfinkiel et al. (2002); the double-zeta plus polarisation (DZP) Gaussian basis set of Dunning (1970) was used for the oxygen, augmented with 2 *s* and 1 *p* functions (providing 6 *s*-type, 3 *p*-type and 1 *d*-type atomic orbitals), while the triple-zeta (TZ) basis of Dunning (1971) was used for the hydrogens, augmented with 2 *p* functions (3 *s*-type and 2 *p*-type atomic orbitals).

Molecular orbitals (MOs) were obtained from a Hartree-Fock self-consistent field calculation, and then pseudo-natural orbitals (NOs) were generated from Singles-Doubles Configuration Interaction (SDCI) calculations, where approximately 33 000 and 50 000 configurations for singlets and triplets respectively were included in the wavefunctions expansion. A weighted average of the NOs from the ground state $^1A_1$, and the lowest $^1B_1$ and $^3B_1$ states, with weights 4, 3 and 2 respectively, gave a set of NOs providing the best set of threshold energies and dipole moment for the ground state (Gorfinkiel et al. 2002).

These NOs were then used in a CASCI calculation, where two electrons were frozen in the lowest $1a_1$ orbital, and all the possible configurations with the 8 remaining electrons in the active space ($2a_1$—$5a_1$, $1b_1$—$2b_1$, $1b_2$—$2b_2$) were included. Such choice again follows Gorfinkiel et al. (2002), where the same CASCI model was used in order to mantain the balance between the N- and $(N+1)$-electron wavefunctions.

The continuum orbital Gaussian basis was generated (Faure et al. 2002) taking into account both the energy range of the collision process and the R-matrix boundary radius, set

	present	accurate values	
Ground state energy / E_h	−76.0923	−76.2905	(a)
Dipole moment / D	1.8629	1.855	(b)

Table 4.1: *Ground state energy and dipole moment for the water monomer; comparison with:* (a) *van Harrevelt & van Hemert (2000) (MRDCI calculations);* (b) *experiment by Dyke & Muenter (1973).*

to 6 a_0 as described below. The continuum basis set comprised 7 *s*-type, 5 *p*-type, 5 *d*-type, 4 *f*-type and 2 *g*-type GTOs, thus including partial waves from 0 to 4. A test was also carried out including partial waves up to 5 (again, see below); in that case, 2 extra *h*-type orbitals were added.

Only the ground state was included in the target calculation; its calculated energy and dipole moment are listed in table 4.1 and compared with more accurate values.

4.1.1 Choice of a and a_c

The two parameters a and a_c have a different physical meaning and must be chosen upon different considerations.

The R-matrix boundary a, defining the size of the inner region, is chosen considering the spatial extent of the target electronic density, which depends both on the molecular geometry and on the basis set used. Smaller and more compact basis sets are confined inside a smaller region, while the inclusion of diffuse orbitals requires larger radii if the leaking outside the inner region is to be avoided. In general, the choice of the basis set is guided by the characteristics of the molecular electronic states: although the more compact basis sets are more convenient, larger ones may be necessary to ensure a target description of a reasonable quality.

The UK polyatomic R-matrix suite provides two ways to test the appropriateness of a. As a first option, it calculates the approximate amplitudes of the molecular orbitals at the boundary, as a rough way to check that the value of a is appropriate. It is approximate because the amplitudes are calculated centering the orbital wavefunctions on the CM, intstead of on the nuclei. If the amplitudes are bigger than a certain value (typically $\sim 10^{-3}$) a larger a must

be used. A proper check consists in running different calculations with various boundary radii; in principle, the differences in the results should only be due to the exclusion of part of the target electron density from the inner region calculations, thus providing a useful tool to decide whether the value of a is appropriate. In practice, results also depend on the continuum basis set, that is dependent on a (a change in radius leads to a change in all the basis set exponents; hence the difficulty in ensuring that the quality of the continuum description remains the same for all radii).

When an appropriate radius a is found for a particular system, in principle any other larger radius could also be used (provided the continuum bases are generated correctly); such increase would not, however, improve the accuracy of the calculation, while the computational requirements would greatly increase (because of the need for a larger number of continuum functions); therefore, the smallest value of a providing correct results is normally used.

The molecular and continuum basis sets employed in our H_2O calculation were similar to those used by Caron et al. (2007) and Bouchiha et al. (2008), where an R-matrix radius $a = 6\ a_0$ was found to be appropriate; we performed some tests using a smaller ($a = 5\ a_0$) and two larger radii ($a = 10, 14\ a_0$); the cross sections obtained, presented in figure 4.2, confirm that the choice of $a = 6\ a_0$ was correct.

While a is a parameter chosen to ensure the quality of the R-matrix calculation, a_c is related to the Multiple Scattering calculation whose input T-matrices must be provided. It defines the radial limit at which the long-renge interactions are cut off, and it is particularly needed when dipolar molecules are treated. Since such limit has nothing to do with the R-matrix theory, a different parameter, a_c, has been introduced, although, as it will be seen, in many cases it is set equal to a. In the studies carried out by Caron et al. (2007) to find an appropriate value for a_c, whose results we have reproduced and complemented and are plotted in figure 4.3, various cross sections are analysed; these are obtained from R-matrix calculations performed using the same a (here, for H_2O, $a = 6\ a_0$) and introducing different cutoff radii a_c. Some of the cross sections (those with $a_c = 8, 10, 50\ a_0$) show a more or less marked dipole-driven behaviour at low energy, which should be removed in order to

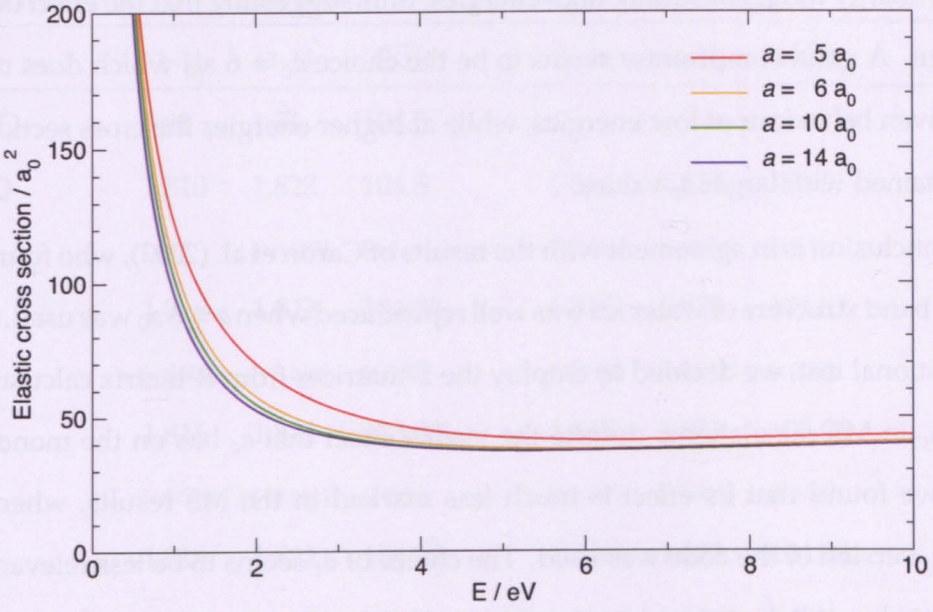

Figure 4.2: *Total elastic cross section for isolated H_2O, from a 1-state R-matrix calculation, with a = 5, 6, 10 and 14 a_0.*

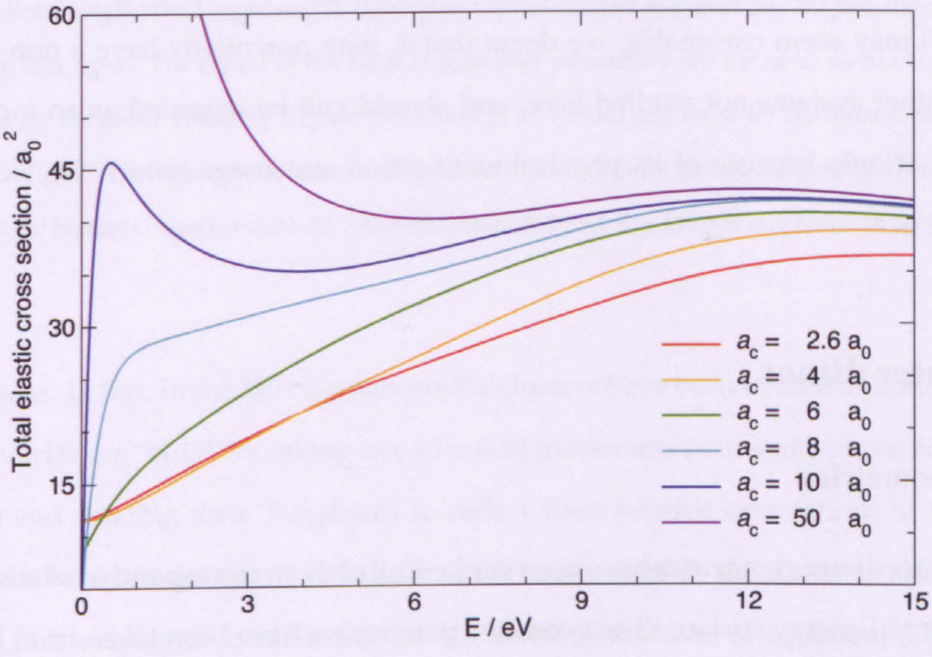

Figure 4.3: *Total elastic cross section for the isolated water molecule, from a 1-state R-matrix calculation with a = 6 a_0 and different values of a_c.*

comply with the Muffin-tin approximation. On the other hand, the very small values (4 and 2.6 a_0) produce cross sections which are appreciably smaller than the abovementioned in

the whole energy range, including high energies, thus suggesting that the effect of the cutoff is too large. A good compromise seems to be the choice $a_c = 6\ a_0$, which does not show a dipole-driven behaviour at low energies, while at higher energies the cross section is closer to that obtained with larger a_c values.

This conclusion is in agreement with the results of Caron et al. (2007), who found that the electronic band structure of water ice was well reproduced when $a = 6\ a_0$ was used. However, as an additional test, we decided to employ the T-matrices from R-matrix calculations with different a_c in MS calculations; despite the visible effect that a_c has on the monomer cross sections, we found that its effect is much less marked in the MS results, when the new, debugged, version of the code was used. The choice of a_c seems to be less relevant than we expected; such result, however, is not striking, as it was also observed by Caron et al. (2008) that the value of a_c is not critical, and previously by Case (1982) that no great differences are encountered for fairly wide variations of the sub-unit sphere radii.

Although setting $a_c = a$ in all calculations (eliminating in actual fact the need for the cutoff parameter) may seem reasonable, we deem that a_c may potentially have a non negligible effect on other systems not studied here, and should still be regarded as an independent parameter, if only because of its physical justification and usage, which are well distinct from those of a.

4.2 Water dimer

4.2.1 Geometries

Five water dimer geometries have been studied; all of them correspond to relative minima of the potential energy surface. The geometry parameters have been taken from Park et al. (2001) (the equilibrium geometry) and Huang et al. (2006) (all the others); some of these are listed in table 4.2.

The geometries studied are characterised by similar parameters, including the inter-monomer distance, and differ mainly for the value of the dipole moment; they were chosen under the constraint that the geometry of the monomers is not heavily distorted from that of

geometry	monomer 1			monomer 2			$R_{1,2}$
	$O-H_1$	$O-H_2$	$\widehat{HOH}$	$O-H_1$	$O-H_2$	$\widehat{HOH}$	
H_2O	1.81	1.81	104.5				
EQ	1.810	1.823	104.5	1.814	1.814	104.6	5.50
	[—]	[+0.013]	[—]	[+0.004]	[+0.004]	[+0.1]	
Z_1	1.816	1.822	104.82	1.816	1.822	104.82	5.37
	[+0.006]	[+0.012]	[+0.32]	[+0.006]	[+0.012]	[+0.32]	
Z_2	1.815	1.821	105.08	1.815	1.821	105.08	5.34
	[+0.005]	[+0.011]	[+0.58]	[+0.005]	[+0.011]	[+0.58]	
S	1.816	1.822	104.95	1.816	1.822	104.95	5.36
	[+0.006]	[+0.012]	[+0.45]	[+0.006]	[+0.012]	[+0.45]	
L	1.818	1.818	101.61	1.818	1.818	104.50	5.70
	[+0.008]	[+0.008]	[-2.82]	[+0.008]	[+0.008]	[—]	

Table 4.2: *Bond lengths (in a_0) and angles (in degrees) of the isolated monomer and the five dimer geometries considered in this work. The values of the isolated monomer parameters are the same as in Gorfinkiel et al. (2002); those for the dimer geometry EQ are from Park et al. (2001) and those for the other dimers are from Huang et al. (2006). The difference between each parameter in the dimer and in the isolated monomer is also shown in square brackets, together with the inter-monomer distance $R_{1,2}$ (also in a_0), listed in the last column.*

isolated water. In fact, in the MS calculations the clusters have been treated as homogeneous: their geometries are "built" by taking two identical monomers (in the gas-phase equilibrium geometry) and rotating their T-matrices to reflect their relative orientations in the dimer. The distance between the centres of mass of the monomers in the dimer is also an input parameter (it is employed to construct the $\mathbb{M}$, $\mathbb{X}$ and $\mathbb{N}$ matrices of equations 3.6, 3.11 and 3.20 used in equation 3.25). When the dimer is made up by monomers whose geometry is different to that of gas-phase water, the geometry of the cluster in the MS calculation is slightly different to that in the R-matrix one, where the parameters listed in table 4.2 are used. In this table, differences between the gas-phase and the dimerised geometries are reported in brackets. The largest difference is found for the geometry labelled L, which also presents a

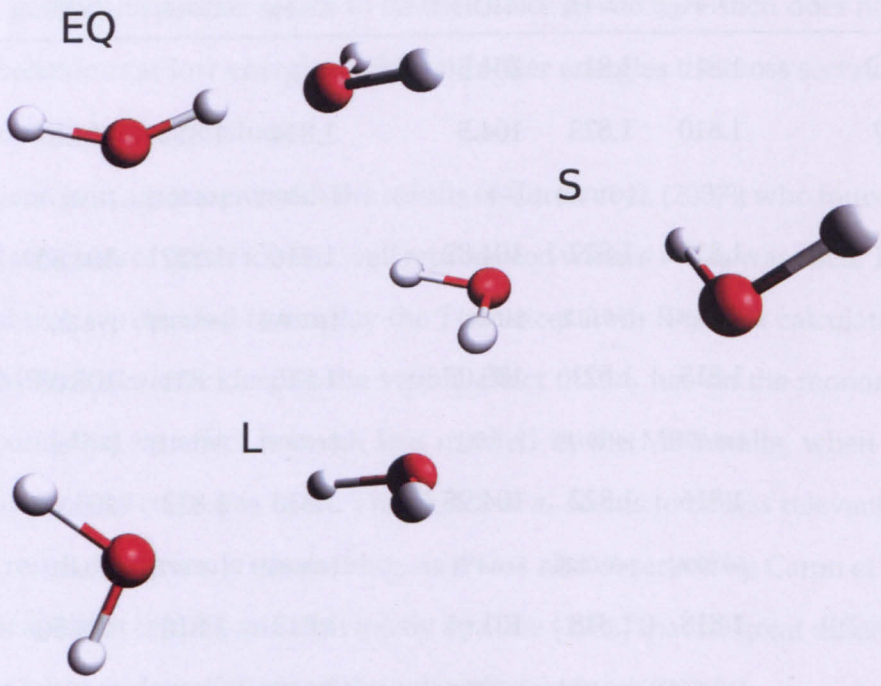

Figure 4.4: *Ball-and-stick models of $(H_2O)_2$, geometries EQ, S and L.*

more marked heterogeneity between the two monomers, having somewhat different angles (the difference is still less than 5% of the total value). In this case, a heterogeneous calculation was also carried out for testing purposes, as explained below.

The MS calculations are mostly influenced by the inter-monomer distance, the monomers' relative orientation and the global dipole moment (i.e. that of the dimer as a whole); it is the latter we are particularly interested in. The global dipole moment is not an input parameter and never explicitly calculated in the MS code; it depends on the monomers' relative orientations, which are input and indirectly determine the global dipole moment. One of the main objects of the work on water dimers was to establish whether the global dipole is intrinsically accounted for in the global T-matrix $\boldsymbol{T}^{\mathrm{G}}$ of equation (3.25). It was to include this interaction that Bouchiha et al. (2008) suggested the use of an extra propagation step, as mentioned in section 3.2.3; our results, though, show that the propagation is not needed.

The dimer geometries are labelled according to their dipole moment magnitude: apart

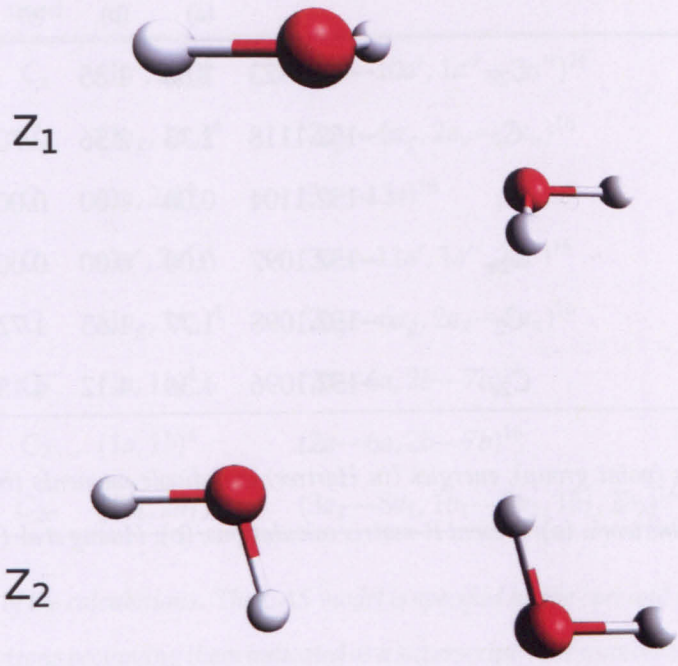

Figure 4.5: *Ball-and-stick models of $(H_2O)_2$, geometries Z_1 and Z_2.*

from the equilibrium dimer EQ, there are two zero-dipole dimers (Z_1 and Z_2), one dimer with a dipole moment smaller than the equilibrium geometry (S) and one with a larger one (L). Table 4.3 lists the dipole moments obtained in the present R-matrix calculations (see next section), compared with those from Huang et al. (2006). Two different zero-dipole geometries have been studied because the comparison between their cross sections, being independent of the dipole interaction, could provide useful information on the effect of the other parameters (mainly the relative orientation, as the inter-monomer distance in very similar in all the dimer geometries).

4.2.2 R-matrix calculations

The R-matrix calculations on the water dimers are also performed following the work of Gorfinkiel et al. (2002) on isolated water, with some minor changes. The double-zeta plus polarisation Gaussian basis set of Dunning (1970) is used for the oxygens and the triple-zeta basis set of Dunning (1971) for the hydrogens, augmented with a diffuse *s*-type and two

geometry	point group	energy / E_h	dipole moment / D		
			(a)	(b)	(c)
H_2O	C_{2v}	−76.0923	1.86	1.85	
EQ	C_s	−152.1118	2.73	2.56	2.70
Z_1	C_i	−152.1104	0.00	0.00	0.00
Z_2	C_{2h}	−152.1097	0.00	0.00	0.00
S	C_2	−152.1098	1.77	1.65	1.72
L	C_{2v}	−152.1096	4.36	4.12	4.15

Table 4.3: *Symmetries (point group), energies (in Hartree) and dipole moments (in Debye) of the dimer geometries considered in this work.* (a): *present R-matrix calculations;* (b): *Huang et al. (2006);* (c): *Tschumper et al. (2002).*

p-type functions extracted from the basis set used by Gil et al. (1994). No natural orbitals are generated and the HF-SCF molecular orbitals are used.

The CASCI model included two forzen core orbitals (occupied by 4 electrons) and 11 active orbitals occupied by the 16 remaining electrons. The symmetry of the core and active orbitals vary throughout the dimer calculations, because the dimer geometries belong to different point groups. In all cases, symmetry properties are used to reduce the computational requirements of the calculations; the real symmetry group of the clusters has always been considered in the calculations, except in one case, for the Z_2 geometry, belonging to the C_{2h} point group, that had not been implemented in the R-matrix code at the time of the calculations. For that geometry, different calculations have been carried out using different subgroups of C_{2h} (C_1, C_i, C_s, C_2); all the results agree, although the C_1 calculation is obviously the slowest and most demanding. Such outcome may seem obvious, but the tests were needed to check the R-matrix results as the UK polyatomic code had problems with combining some target orientations and symmetry groups (some of these are still unsolved). Details on the calculation for each dimer geometry are listed in table 4.4.

The R-matrix radius was set to 13 a_0, following tests performed by Gorfinkiel (2007) on the dimer at the equilibrium geometry; this radius proved valid for the other geometries as well. The continuum orbital basis set, optimised for a = 13 a_0 (Faure et al. 2002), includes 13

geom	symmetry		core orbitals	active orbitals	no. configs	
	orig	used			N	$N+1$
EQ	C_s	C_s	$(1a', 2a')^4$	$(3a'—10a', 1a''—3a'')^{16}$	4 627	23 953
Z_1	C_i	C_i	$(1a_g, 1a_u)^4$	$(2a_g—6a_g, 2a_u—7a_u)^{16}$	4 575	23 745
Z_2	C_{2h}	C_1	$(1a, 2a)^4$	$(3a—13a)^{16}$	9 075	23 595
"	"	C_s	$(1a', 2a')^4$	$(3a'—11a', 1a'', 2a'')^{16}$	4 815	24 705
"	"	C_i	$(1a_g, 1a_u)^4$	$(2a_g—6a_g, 2a_u—7a_u)^{16}$	4 575	23 745
"	"	C_2	$(1a, 1b)^4$	$(2a—6a, 2b—7b)^{16}$	4 575	23 745
S	C_2	C_2	$(1a, 1b)^4$	$(2a—6a, 2b—7b)^{16}$	4 575	23 745
L	C_{2v}	C_{2v}	$(1a_1, 2a_1)^4$	$(3a_1—8a_1, 1b_1—3b_1, 1b_2, 2b_2)^{16}$	2 471	25 213

Table 4.4: *Summary of the calculations. The CAS model is specified by the core and active orbitals in brackets, with the number of electrons occupying them indicated as a superscript. The number of resulting configurations is also indicated, for the N and the (N + 1) calculations. For the latter, the sum of all the configurations from the different calculations performed for each irreducible rappresentation is listed. The reason why the same CI model produces a different number of configurations (see the C_s and C_i calculations for the Z_2 geometry) is due to the different number of combinations resulting from the inclusion of orbitals belonging to different irreducible rappresentation, even if the total number of core and active orbitals is the same; this inequality holds when different subgroups of a larger group are employed.*

s-, 11 *p*-, 10 *d*-, 8 *f*- and 6 *g*-type gaussian functions. Tests with partial waves up to 5 included also 5 *h*-type functions.

The calculated dipole moments differ from those of Huang et al. (2006) by less that 10% for all geometries (see table 4.3); such accuracy is sufficient for the purpose of this work.

4.2.3 Multiple Scattering calculations

The monomer T-matrices T and T_c produced in the R-matrix calculation need to be rotated to account for the relative orientations of the sub-units in the dimer. The Euler angles representing the rotation are obtained comparing the orientation of the water molecule in the R-matrix calculation (where the vector on the molecular plane bisecting the $\widehat{\mathrm{HOH}}$ angle

is placed along $\hat{z}$ and the $\overrightarrow{H-H}$ vector along $\hat{y}$) to that of each monomer in the dimer geometry. Since the dimerised monomers are not identical to the isolated one, no rotation can transform one into the other exactly, so three vectors were chosen instead of the atom positions to identify the orientations. As explained in section 3.2.2, one vector is in the direction $\overrightarrow{O-CM}$, pointing towards O, another lies on the (HOH) plane and is orthogonal to the first, and the third is orthogonal to the previous two. The Euler angles obtained for all the dimers are listed in table 4.5.

geom	α_1	β_1	γ_1	α_2	β_2	γ_2
EQ	90.0	146.95	270.0	90.0	34.90	180.0
Z_1	52.41	90.0	0.0	232.46	90.0	180.0
Z_2	52.65	90.0	180.0	232.65	90.0	0.0
S	52.60	90.0	0.0	252.68	39.68	138.72
L	50.80	90.0	0.0	50.80	90.0	90.0

Table 4.5: *Euler angles for the MS dimer calculations (in degrees).*

In order to test the effect of the small differences in geometry between the MS calculation and the values in table 4.2, a heterogeneous calculation was performed on the dimer labelled L, for which these differences are largest. Two monomer R-matrix calculations were run using the geometry parameters from the dimer, and then rotated; while the second monomer is very similar to the standard gas-phase geometry, the first one differs markedly especially for the narrower $\widehat{HOH}$ angle. The standard (homogeneous) and heterogeneous cross sections are compared in figure 4.6.

The differences in the cross section are minimal, demonstrating that a 5% variation of the bond angles (affecting, for instance, the total dipole moment), does not have a big effect on the total elastic cross section. This justifies our decision to treat the other (less distorted) dimer geometries as if they were completely homogeneous.

The effect of changing the energy correction parameter γ, which has the effect of shifting upwards (when $\gamma < 1$) or downwards (when $\gamma > 1$) the energy cutoff values (see section 3.2.1) was tested. As previously explained, a cutoff must be applied to the number of partial

waves included in the cutoff T-matrix $\boldsymbol{T}_c$ of equation (3.25) (while matrix $\boldsymbol{T}$ includes all of them). The need for it is explained in terms of the energy necessary to overcome the centrifugal barrier, so the number of partial waves to be included in the calculation varies with the scattering energy. We call *cutoff energies* those energies E^{l_c} such that $E^{l_c} = \frac{l_c(l_c+1)}{\gamma R^2}$, for integer values of l_c (R being the inter-monomer distance). When the scattering energy E equals a cutoff energy E^{l_c}, all partial waves up to l_c must be included, while when $E = E^{l_c+1}$ is reached, the contribution from partial wave $l_c + 1$ is added. Instead of calculating a single cross section with a variable number of partial waves, we prefer to compute n cross sections, each of which uses the same number of partial waves in the whole energy range; these cross sections will be referred to as *cutoff cross sections*, σ^{l_c}, and labelled according to the highest partial wave l_c they comprise. Here, the number of cutoff cross sections calculated, n, is equal to $l_{max} + 1$, where l_{max} is the highest partial wave available from the R-matrix input — typically 4 or 5 — (i.e. cross sections σ^0, σ^1... $\sigma^{l_{max}}$ will be computed). Finally, the cross section taken as the result of the Multiple Scattering calculation, referred to as the *interpolated cross section*, σ^{INT} is obtained including each cutoff cross section in the relevant energy range. Because of the discreteness of l_c, this procedure would cause discontinuities at the cutoff

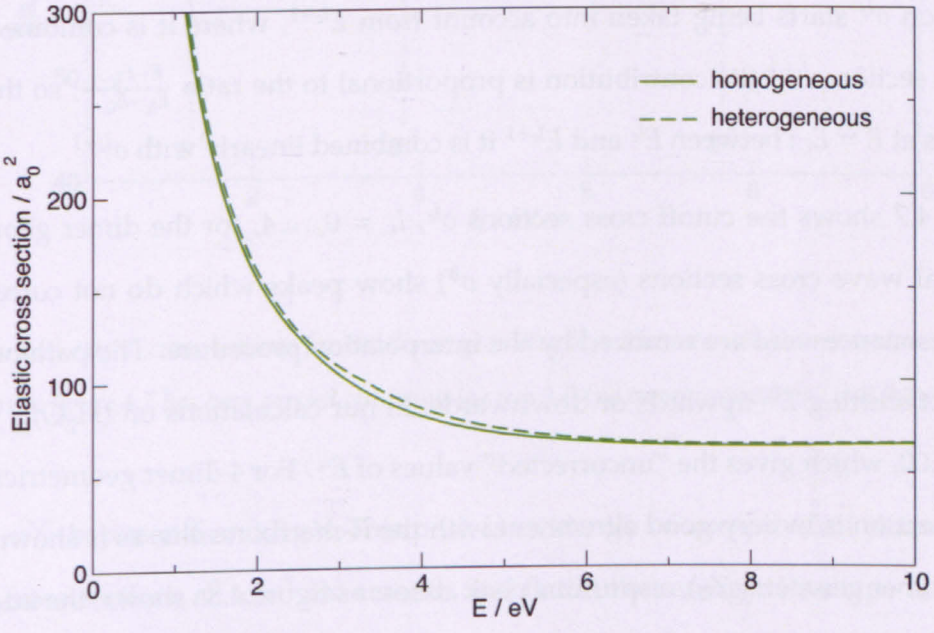

Figure 4.6: *Elastic cross sections for the L dimer geometry, calculated as an heterogeneous and homogeneous cluster, using the MS technique.*

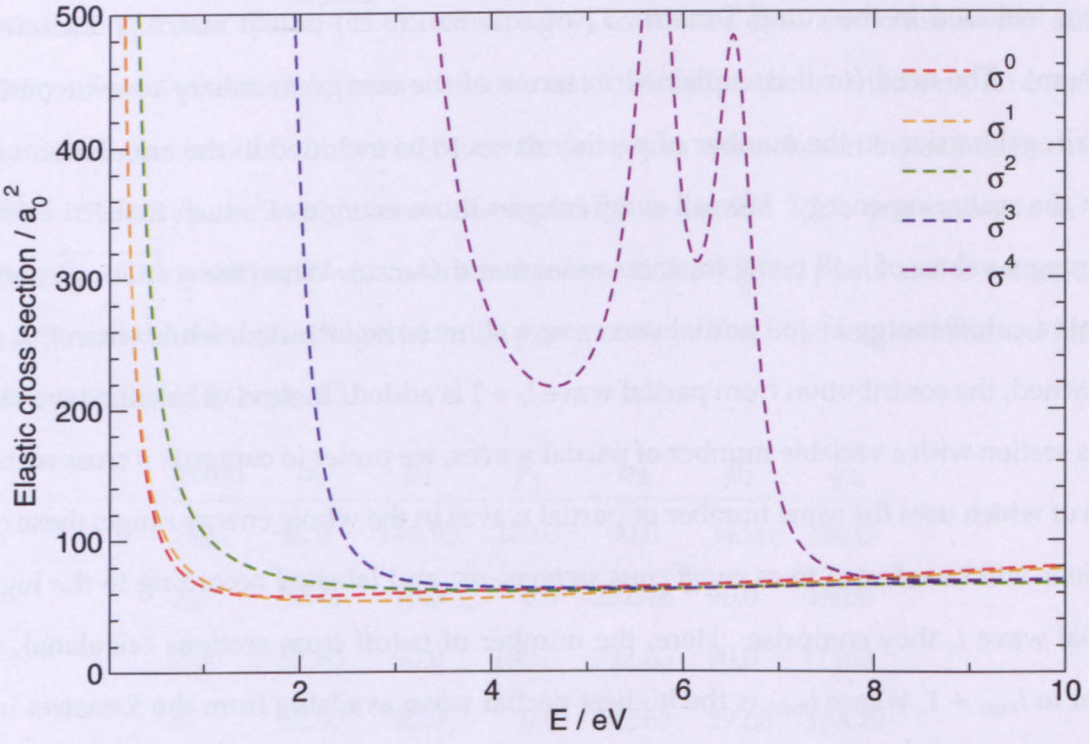

Figure 4.7: *MS elastic cross sections for the dimer geometry Z_2 for different l_{max} values (see text). The peaks appearing when high partial waves contributions are included are not physical. An interpolation procedure is therefore needed.*

energies E^{l_c}; therefore, a two-point interpolation is carried out. This means that each cutoff cross section σ^{l_c} starts being taken into account from E^{l_c-1}, where it is combined linearly with cross section σ^{l_c-1} (its contribution is proportional to the ratio $\frac{E-E_{l_c-1}}{E_{l_c}-E_{l_c-1}}$, so that it fully contributes at $E = E_{l_c}$; between E^{l_c} and E^{l_c+1} it is combined linearly with σ^{l_c+1}.

Figure 4.7 shows the cutoff cross sections σ^{l_c}, $l_c = 0, \ldots 4$, for the dimer geometry Z_2; high partial wave cross sections (especially σ^4) show peaks which do not correspond to physical resonances and are removed by the interpolation procedure. The parameter γ has the effect of shifting E^{l_c} upwards or downwards; in our calculations on $(H_2O)_2$, we firstly tried $\gamma = 1.00$, which gives the "uncorrected" values of E^{l_c}. For 4 dimer geometries out of 5, this cross section is in very good agreement with the R-matrix results, as is shown later. In one case (dimer geometry Z_2), a spurious peak arises: as figure 4.8a shows, the interpolated cross section is smooth until E^3 is reached; at that point, σ^4 starts being included and since it shows tall peaks and is ill-behaved below 8 eV (see figure 4.7) it causes a marked peak to

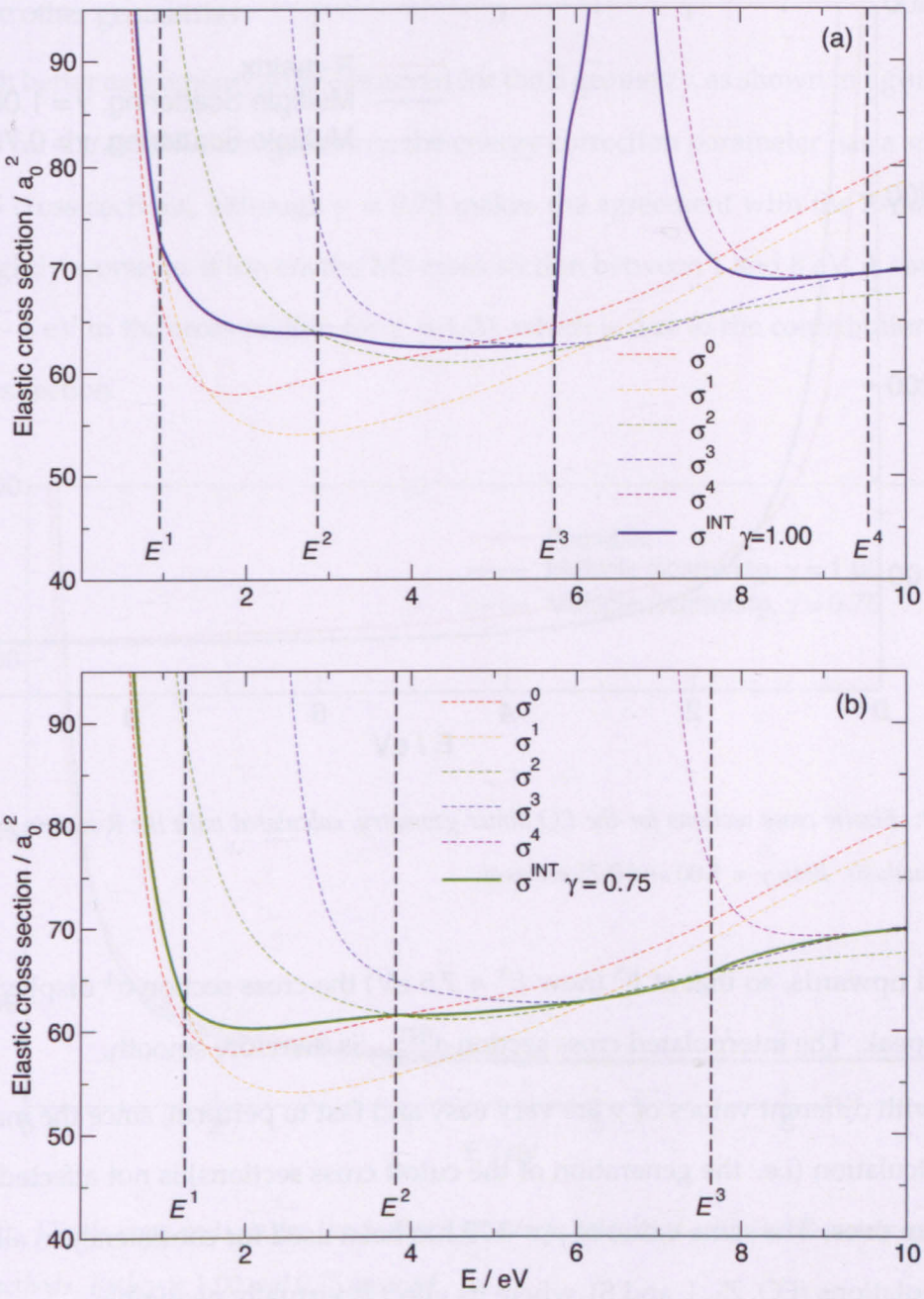

Figure 4.8: *MS elastic cross sections for the dimer geometry Z_2. The interpolation procedure between the cross sections in figure 4.7 has been carried out using* (a) $\gamma = 1.0$ *(no energy correction) and* (b) $\gamma = 0.75$.

appear in σ^{INT} between 6 and 8 eV. This peak is evidently of non-physical character, since the cutoff cross sections σ^0 to σ^3 are smooth and flat at that energy; its shape is also quite unlikely to be that of a physical resonance. We decided to try a different value for γ, setting it to 0.75, as done in Bouchiha et al. (2008). Its effect is clear in figure 4.8b: the cutoff energies

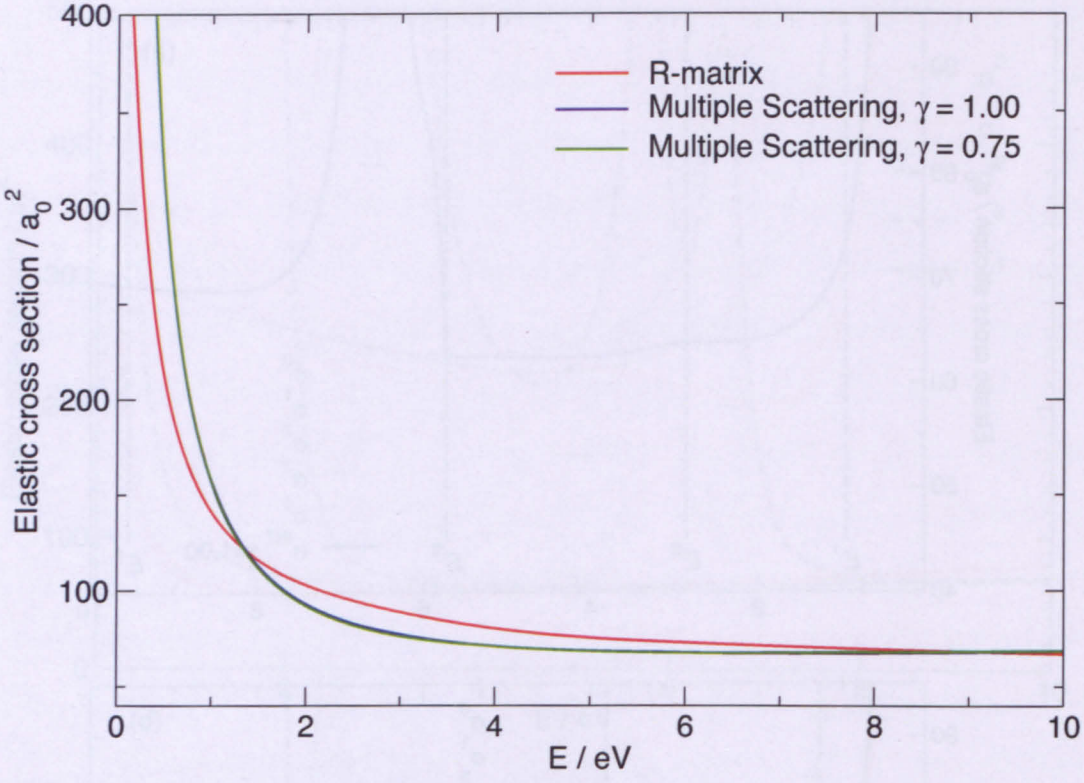

Figure 4.9: *Elastic cross sections for the EQ dimer geometry, calculated with the R-matrix and Multiple Scattering methods. Both $\gamma = 1.00$ and 0.75 are used.*

are shifted upwards, so that at E^3 (now $E^3 \approx 7.5$ eV) the cross section σ^4 displays only the tail of the peak. The interpolated cross section $\sigma^{\mathrm{INT}}_{\gamma=0.75}$ is therefore smooth.

Tests with different values of γ are very easy and fast to perform, since the main part of the MS calculation (i.e. the generation of the cutoff cross sections) is not affected by it and must be run once. The same value of $\gamma = 0.75$ has been used for consistency in all the other dimer calculations (EQ, Z_1, L and S), where its effect is virtually negligible.

4.2.4 Results and comparison with R-matrix calculations

Figure 4.9 shows the comparison between the elastic cross sections obtained with the R-matrix and MS methods at the equilibrium geometry (EQ), as functions of the energy. The agreement between the two is generally good, especially at higher energies, although discrepancies arise at low energy, particularly below 1.5 eV. The two values of $\gamma = 1.00$ and 0.75 produce almost identical Multiple Scattering cross sections, as it is also observed for

most of the other geometries.

A much better agreement can be observed for the S geometry, as shown in figure 4.10. As in the case for the equilibrium geometry, the energy correction parameter has a small effect on the MS cross sections, although $\gamma = 0.75$ makes the agreement with the R-matrix cross section slightly worse, as it lowers the MS cross section between 1 and 8 eV. A small step is visible at ~ 6 eV in the cross section for $\gamma = 1.00$, which is due to the contribution of the σ^4 cutoff cross section.

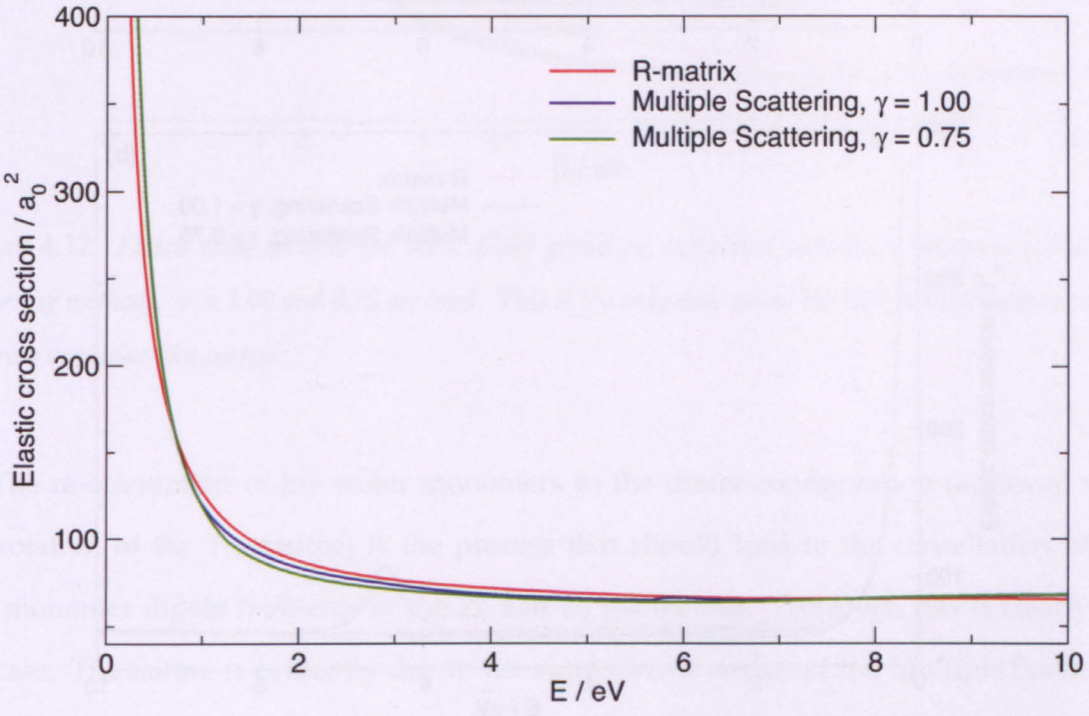

Figure 4.10: *Elastic cross sections for the S dimer geometry, calculated with the R-matrix and Multiple Scattering methods. Both $\gamma = 1.00$ and 0.75 are used.*

In both figures 4.9 and 4.10 the Multiple Scattering cross section is higher than the R-matrix one at lower energies; the crossing happens around the energy of 1 eV. It appears that the effect of the electron – dimer's dipole moment interaction, though never explicitly calculated in the MS programme, is correctly accounted for: the low energy behaviour of the R-matrix cross section is reasonably well reproduced. However, when the comparison is carried out for the two zero-dipole geometries (figure 4.11), the agreement at low energies is much worse: in this case it is evident that the elastic cross section is markedly overestimated

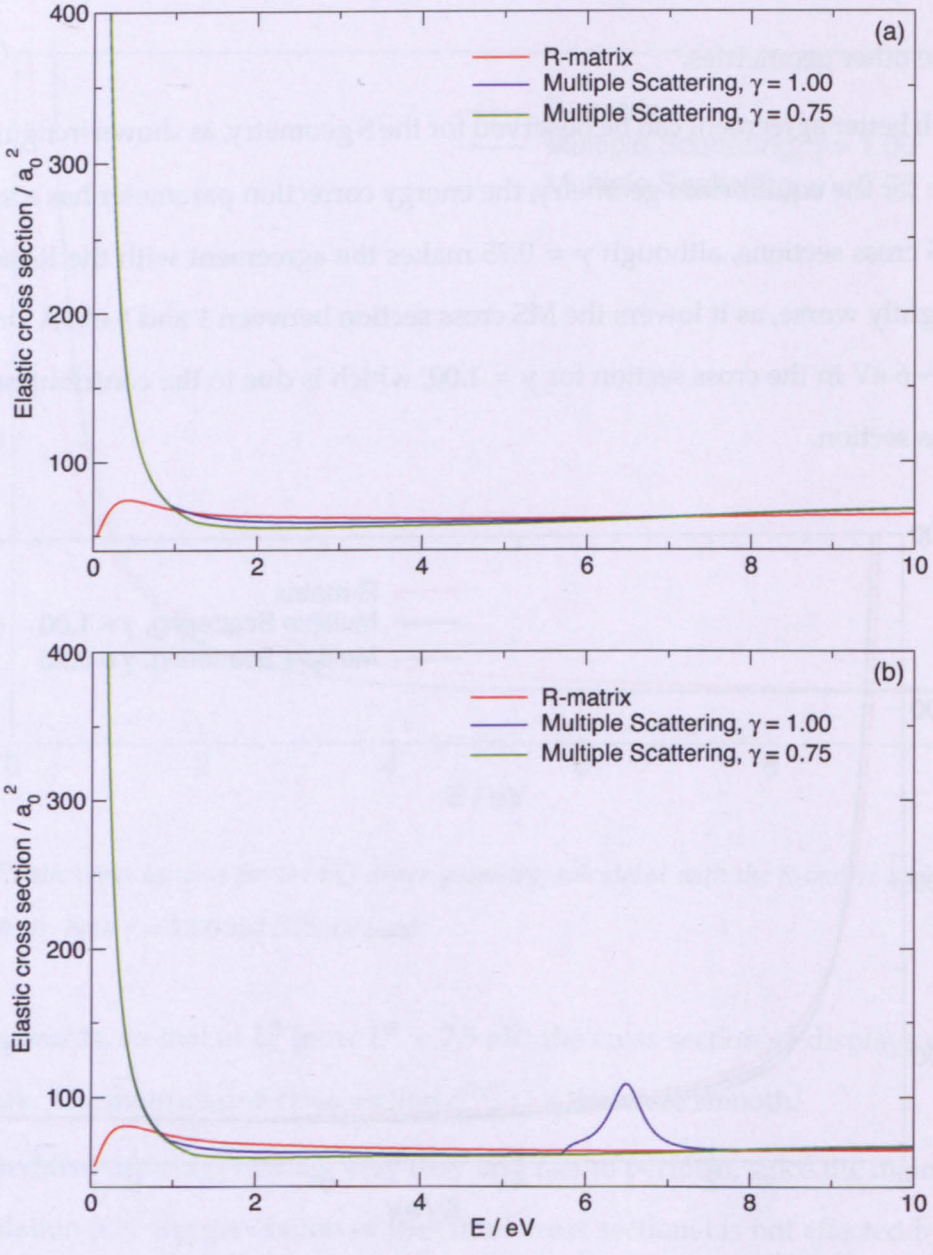

Figure 4.11: *Elastic cross sections for the* (a) Z_1 *and* (b) Z_2 *dimer geometries, calculated with the R-matrix and Multiple Scattering methods. Both* $\gamma = 1.00$ *and 0.75 are used. The* Z_2 *geometry shows a spurious peak for* $\gamma = 1.00$ *that is eliminated by setting* $\gamma = 0.75$.

by the Multiple Scattering method for energies below 1 eV, since it seems to diverge when $E \to 0$. The R-matrix method, on the other hand, correctly predicts the shape of the cross section at low energies which would be expected in a collision with a non-polar target. It would seem that the electron – dimer's dipole moment interaction is not well represented in the MS calculations.

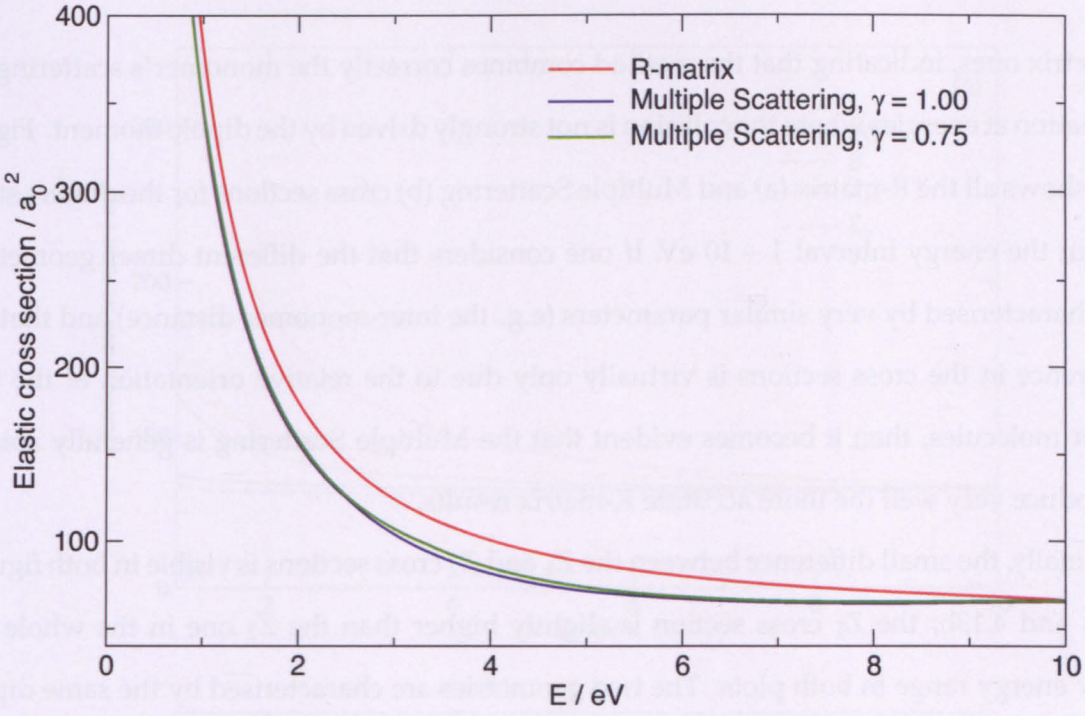

Figure 4.12: *Elastic cross sections for the L dimer geometry, calculated with the R-matrix and Multiple Scattering methods. γ = 1.00 and 0.75 are used. This is the only case where the MS method underestimates the cross section at low energy.*

The re-orientation of the water monomers to the dimer configuration (achieved with the rotation of the T-matrices) is the process that should lead to the cancellation of the two monomer dipole moments in the Z_1 and Z_2 geometries. However, this is clearly not the case. The failure is evidently due to the approximate nature of the Multiple Scattering method, which implicitly constructs the electron – dimer interaction potential from electron – monomer potentials; the limitations of the method when it comes to accounting for the $e^- - (H_2O)_2$ dipole moment interaction are more obvious the more different the monomer and dimer dipole moments are (as the results for the L geometry, displayed in figure 4.12, show).

At energies higher than 1 eV, though, the agreement with the R-matrix results is remarkable for all the geometries.

The comparisons carried out were extremely helpful in starting to understand the limitations and the validity range of the Multiple Scattering method. If one neglects the energies below 1 eV, the Multiple Scattering results are generally in very good agreement with the

R-matrix ones, indicating that the method combines correctly the monomer's scattering information at energies where the collision is not strongly driven by the dipole moment. Figure 4.13 shows all the R-matrix (a) and Multiple Scattering (b) cross sections for the dimers studied, in the energy interval 1 – 10 eV. If one considers that the different dimer geometries are characterised by very similar parameters (e.g. the inter-monomer distance) and that the difference in the cross sections is virtually only due to the relative orientation of the two water molecules, then it becomes evident that the Multiple Scattering is generally able to reproduce very well the more accurate R-matrix results.

Finally, the small difference between the Z_1 and Z_2 cross sections is visible in both figures 4.13a and 4.13b; the Z_1 cross section is slightly higher than the Z_2 one in the whole 1 – 10 eV energy range in both plots. The two geometries are characterised by the same dipole moment and also by very similar orientations and inter-monomer distances, as tables 4.2 and 4.5 show; the main difference is that Z_1 is not planar, while Z_2 is. The extremely good agreement between the R-matrix and Multiple Scattering cross sections indicate that such characteristic is well accounted for by the MS method.

4.2.5 Effect of the dipole moment interaction

The inability of the Multiple Scattering approach to correctly account for the total dipole moment of the cluster has been further analysed. Bouchiha et al. (2008) decided that an extra propagation was needed because the agreement between the R-matrix and MS cross sections was not as good as expected, and the propagation step improved it.

The extra propagation involved converting the global T-matrix $\boldsymbol{T}^{\mathrm{G}}$, obtained with the standard Multiple Scattering method using equation 3.25, into an R-matrix, using the relations:

$$\boldsymbol{K}^{\mathrm{G}} = -\mathrm{i}(2 \cdot \mathbf{1} - \boldsymbol{T}^{\mathrm{G}})^{-1}\boldsymbol{T}^{\mathrm{G}} \tag{4.1}$$

$$\boldsymbol{R}^{\mathrm{G}} = \frac{1}{ka_{\mathrm{III}}}(\boldsymbol{J} - \boldsymbol{N}\boldsymbol{K}^{\mathrm{G}})(\boldsymbol{J}' - \boldsymbol{N}'\boldsymbol{K}^{\mathrm{G}})^{-1}, \tag{4.2}$$

where $k = \sqrt{E}$, a_{III} is the boundary of the sphere labelled III in figure 3.1, $J_{L,L'} = j_l(ka_{\mathrm{III}})\delta_{L,L'}$, $N_{L,L'} = \eta_l(ka_{\mathrm{III}})\delta_{L,L'}$, $J'_{L,L'} = j_l(ka_{\mathrm{III}})\delta_{L,L'}$, $N'_{L,L'} = \eta_l(ka_{\mathrm{III}})\delta_{L,L'}$, j_l and η_l are the spherical Bessel functions of the first and second kind, and $j'_l(z) = \frac{dj_l}{dz}$, $\eta'_l(z) = \frac{d\eta_l}{dz}$.

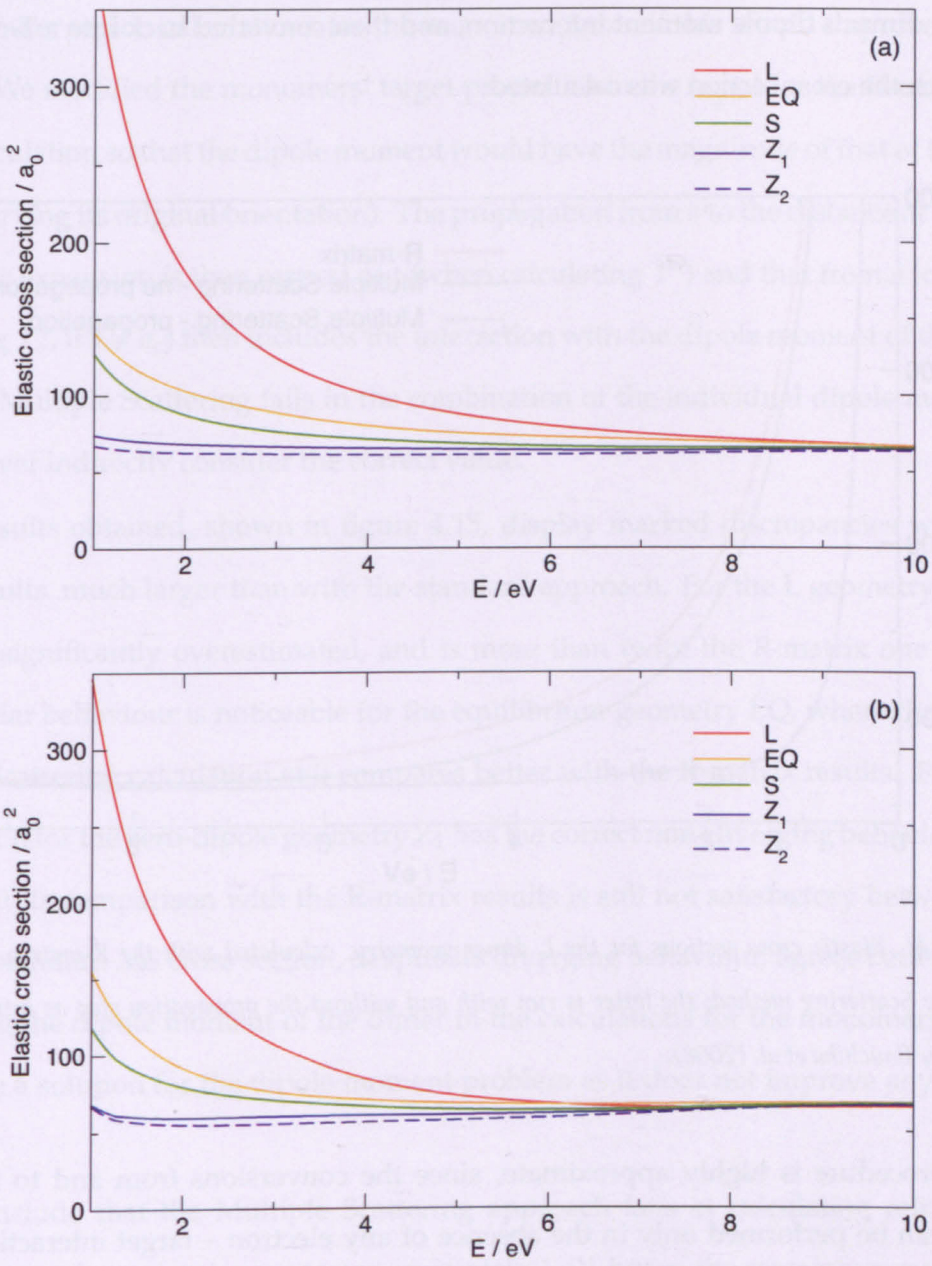

Figure 4.13: *Elastic cross sections for all the dimer geometries, calculated with* (a) *the R-matrix and* (b) *the Multiple Scattering methods.*

While the K- and T-matrices do not depend on the radial distance r, the R-matrix does. a_{III} in equation (4.2) should be set to a distance at which the interaction is negligible, but it was set equal to a (the radius that would be used in an R-matrix calculation for the whole dimer) in Bouchiha et al. (2008). The R-matrix $\boldsymbol{R}^{\mathrm{G}}$ thus obtained was propagated to an asymptotic distance using the standard R-matrix outer region propagation, with the inclusion of the

electron – dimer's dipole moment interaction, and then converted back into a T-matrix T^{∞}, from which the cross section was calculated.

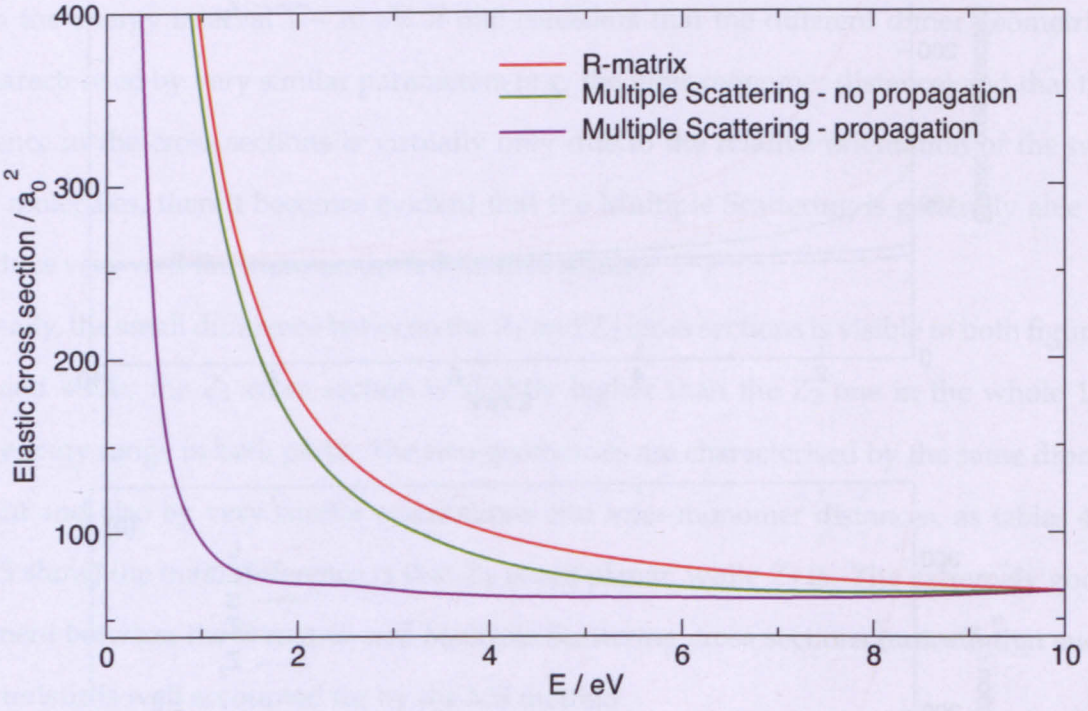

Figure 4.14: *Elastic cross sections for the L dimer geometry, calculated with the R-matrix method and the Multiple Scattering method; the latter is run with and without the propagation step as introduced and performed by Bouchiha et al. (2008).*

This procedure is highly approximate, since the conversions from and to K- and T-matrices can be performed only in the absence of any electron – target interaction; this is clearly not the case at $r = a_{\mathrm{III}} = a_{\mathrm{dim}}$, where the long range interaction with the target is not yet negligible.

When we tried this procedure, we obtained cross sections whose agreement with the R-matrix cross sections was worse than when the propagation was not used. An example for geometry L is shown in figure 4.14, while similarly poor comparisons for the other geometries were observed. We concluded that the approximate conversion $T \rightarrow R$, followed by the propagation, did not lead to a better description of the long-range effect of the electron – dimer's dipole moment interaction. Hence, we chose not to use it.

We then tested a different approach: we used the dipole moment of the dimer in the

R-matrix outer region calculations for the monomer, to see if this would improve the cross sections. We modified the monomers' target properties in the input for the R-matrix outer region calculation so that the dipole moment would have the magnitude of that of the cluster (but conserving its original orientation). The propagation from a to the distance at which the asymptotic expansion is then carried out (when calculating T^n) and that from a to a_c (when calculating T_c^n, if $a \neq a_c$) then includes the interaction with the dipole moment of the cluster; when the Multiple Scattering fails in the combination of the individual dipole moments, it will however indirectly consider the correct value.

The results obtained, shown in figure 4.15, display marked discrepancies with the R-matrix results, much larger than with the standard approach. For the L geometry, the cross section is significantly overestimated, and is more than twice the R-matrix one even at 3 eV. A similar behaviour is noticeable for the equilibrium geometry EQ, where the standard Multiple Scattering calculation still compares better with the R-matrix results. Finally, the cross section for the zero-dipole geometry Z_1 has the correct non-diverging behaviour at low energy, but its comparison with the R-matrix results is still not satisfactory between 0 and 3 eV. The standard MS cross section, despite its diverging behaviour, agrees better down to 1 eV. Using the dipole moment of the dimer in the calculations for the monomers does not seem to be a solution for the dipole moment problem as it does not improve any MS cross section.

We conclude that the Multiple Scattering approach fails at calculating reliable cross sections at very low energies, up to approximately 1 eV, but in the remaining energy range [1 – 10 eV] is able to produce results that are generally in good agreement with the R-matrix ones, with discrepancies of the order of few percent.

4.2.6 Partial waves convergence

The total number of partial waves used in a MS calculation depends on the value of l_{max} used in the monomer R-matrix calculations, where typically $l_{max} = 4$. In order to have converged cross sections that can be compared with experiments, one would have to use a Born-type approximation to add the contribution of the missing partial waves $l > l_{max}$ (see

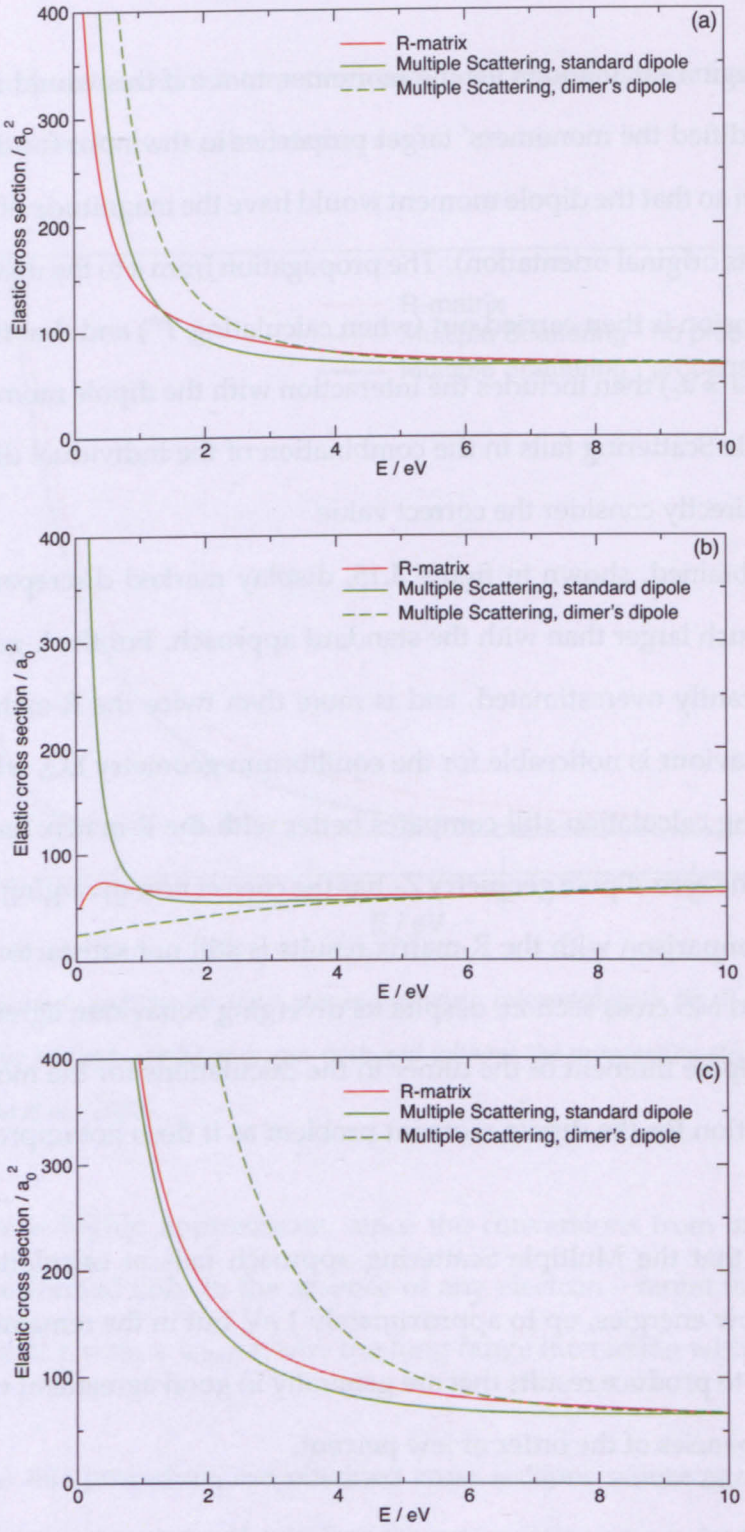

Figure 4.15: *Comparison between the elastic cross sections for the geometries* (a) *EQ*, (b) Z_1, (c) *L, calculated with the R-matrix and Multiple Scattering methods; the MS calculations are run both with the standard procedure and using the dimer's dipole moment in the R-matrix monomer's calculations.*

section 2.5.2). This can be done in an approximate way by adding a quantity to the cross sections (the correction is only energy-dependent); if this is done, the contribution would be the same to the MS and R-matrix cross sections and therefore the comparisons shown and the conclusions drawn so far would not be affected. This type of correction, however, has been recently shown to provide cross sections that are not very good at low energies (Zhang et al. 2009); a better way of completing the partial wave expansion is to correct the T-matrices (Baluja et al. 2007), which could potentially affect the MS and R-matrix cross sections differently.

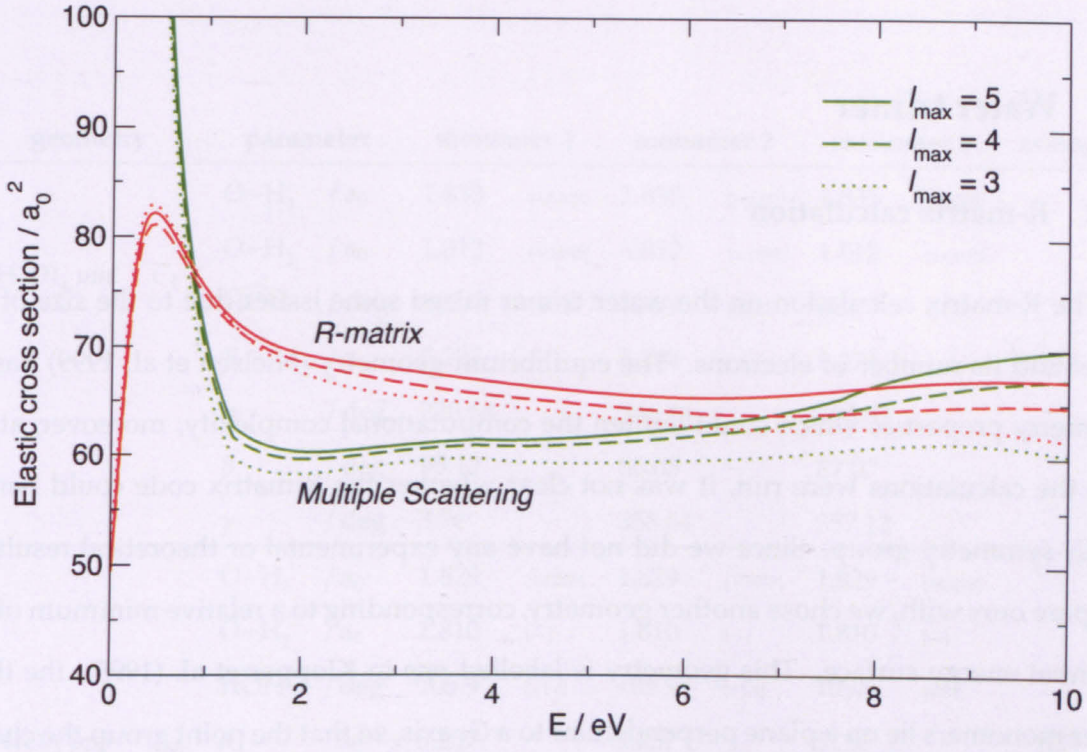

Figure 4.16: *R-matrix and Multiple Scattering elastic cross sections for the Z_2 dimer geometry, where a different number of partial waves was included. The contribution of higher partial waves has a similar effect on both calculations; therefore it does not improve the comparison.*

In order to assess whether the effect would be different in the MS and R-matrix results, we decided to change the number of partial waves l_{max} in the monomer and dimer R-matrix calculations and see how the cross sections change.

We then performed R-matrix calculations on the monomer and on the dimers including

partial waves up to 3 and up to 5. Clearly, the number of cutoff cross sections σ^{l_c} varies, since it depends on l_{max}: the cutoff cross sections calculated for each MS run are from σ^0 to $\sigma^{l_{max}}$. Small differences can be observed between the same cutoff cross sections in calculations where l_{max} is different; they are responsible for the variations observed in the interpolated MS cross section, since the cutoff energies E^{l_c} are not affected by l_{max}.

As figure 4.16 shows for the Z_2 geometry, the partial wave expansion is not convergent in either calculations; however, the effect of adding (or removing) partial waves is very similar for the R-matrix and Multiple Scattering results. Therefore the conclusions drawn so far are not affected by the number of partial waves included and remain valid.

4.3 Water trimer

4.3.1 R-matrix calculation

The R-matrix calculation on the water trimer raised some issues due to the size of the target and its number of electrons. The equilibrium geometry (Nielsen et al. 1999) has no symmetry properties which could lighten the computational complexity; moreover, at the time the calculations were run, it was not clear whether the R-matrix code could handle the C_1 symmetry group. Since we did not have any experimental or theoretical results to compare ours with, we chose another geometry, corresponding to a relative minimum of the potential energy surface. This geometry is labelled *ppp* in Klopper et al. (1995); the three water monomers lie on a plane perpendicular to a C_3 axis, so that the point group the cluster belongs to is C_{3h}.[1] The UK polyatomic R-matrix code is not implemented to treat the C_3 axis, so the molecule was studied as a C_s. Some parameters for this and the equilibrium geometry (labelled *uud*) are reported in table 4.6; bond lengths are generally larger than those of isolated water, and bond angles wider.

Tests were performed to check whether the generation of natural orbitals could improve the calculations. The same basis set used in the dimer calculations was employed; natural

[1] The energy of the *ppp* geometry is only slightly above that of the equilibrium geometry (0.002 E_h, Klopper et al. 1995).

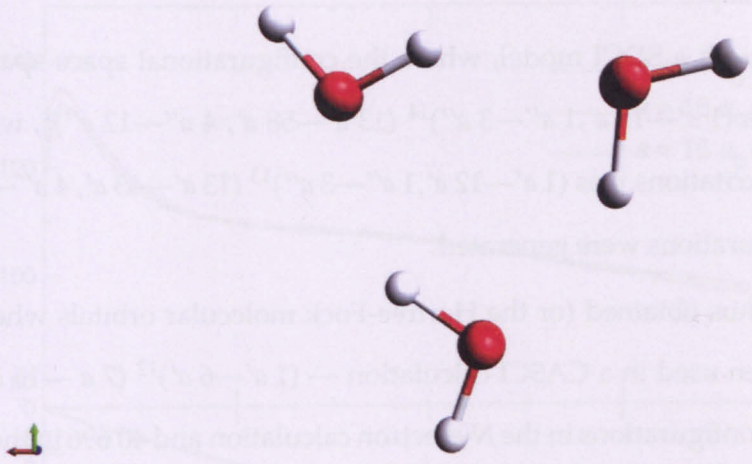

Figure 4.17: *Ball-and-stick models of* $(H_2O)_3$, ppp *geometry.*

geometry		parameter		monomer 1		monomer 2		monomer 3		average
$(H_2O)_3$ *uud*	C_1	O–H_1	/ a_0	1.833	[+0.023]	1.835	[+0.025]	1.835	[+0.025]	
		O–H_2	/ a_0	1.812	[+0.002]	1.812	[+0.002]	1.812	[+0.002]	
		$\widehat{HOH}$	/ deg	105.0	[+0.5]	104.9	[+0.4]	104.7	[+0.2]	
		R	/ a_0	5.297		5.284		5.278		5.287
		α	/ deg	228.64		346.84		108.81		
		β	/ deg	95.12		80.05		87.07		
		γ	/ deg	3.76		358.64		357.12		
$(H_2O)_3$ *ppp*	C_{3h}	O–H_1	/ a_0	1.829	[+0.019]	1.829	[+0.019]	1.829	[+0.019]	
		O–H_2	/ a_0	1.810	[—]	1.810	[—]	1.810	[—]	
		$\widehat{HOH}$	/ deg	105.9	[+1.4]	105.9	[+1.4]	105.9	[+1.4]	
		R	/ a_0	5.287		5.287		5.287		5.287
		α	/ deg	222.64		342.64		102.64		
		β	/ deg	90.00		90.00		90.00		
		γ	/ deg	0.00		0.00		0.00		

Table 4.6: *Geometrical parameters for the two trimer geometries* uud *(equilibrium) and* ppp*, taken from Klopper et al. (1995). The difference between each parameter in the trimer and in the isolated monomer is also shown in square brackets. The set of Euler angles* (α, β, γ) *is also reported. The inter-monomer distances* $R_{n,n'}$ *are listed under the column of monomer n and are referred to the distance between such monomer and the following one.*

orbitals were generated with a SDCI model, where the configurational space spanned by the single excitations was (1 a'—12 a',1 a''—3 a'')^{14} (13 a'—58 a', 4 a''—12 a'')^{1}, while that spanned by the double excitations was (1 a'—12 a',1 a''—3 a'')^{13} (13 a'—43 a', 4 a''—12 a'')^{2}; more than 100 000 configurations were generated.

The natural orbitals thus obtained (or the Hartree-Fock molecular orbitals where these were employed) were then used in a CASCI calculation — (1 a'—6 a')^{12} (7 a'—15 a',1 a''—3 a'')^{18}, generating 8 029 configurations in the N-electron calculation and 40 696 in the $(N+1)$-electron calculation. Such configuration interaction models were chosen after many tests, and are a fair compromise between a good description of the system and the computational capacity of the machines used. The dipole moment obtained was 0.00 D (as predicted by other calculations) and the CI energy −228.2009 2203 E_h. Both a= 14 a_0 and 15 a_0 were tried for the R-matrix radius; the number of continuum orbitals basis functions used is listed in table 4.7 for both the a = 14 and 15 a_0.

radius a	s-type	p-type	d-type	f-type	g-type
14 a_0	14	12	11	8	6
15 a_0	14	13	11	9	7

Table 4.7: *Number of GTOs in the basis sets used to construct the continuum orbitals in the water trimer calculations. The basis set for a = 15 a_0 was taken from Bouchiha et al. (2006); that for a = 14 a_0 was generated with programme GTOBAS (Faure et al. 2002).*

Figure 4.18 shows the elastic cross sections for three tests performed (a = 15 a_0 with both natural and HF-SCF molecular orbitals; a = 14 a_0 with natural orbitals). Firstly, comparing the results for the radius a = 15 a_0, with HF-SCF molecular orbitals and with natural orbitals, it seems that the use of the latter slightly improves the results; this can be concluded analysing the eigenphase sums, shown in panel (b): at higher energies the use of NOs provides slightly higher eigenphase sums. The difference in the cross sections is however very small, amounting to up to 2% at 0.2 eV. As for the R-matrix radius, the results also show that a radius of 14 a_0 is large enough, at least when NOs are employed, since the cross sections agree very well at all energies.

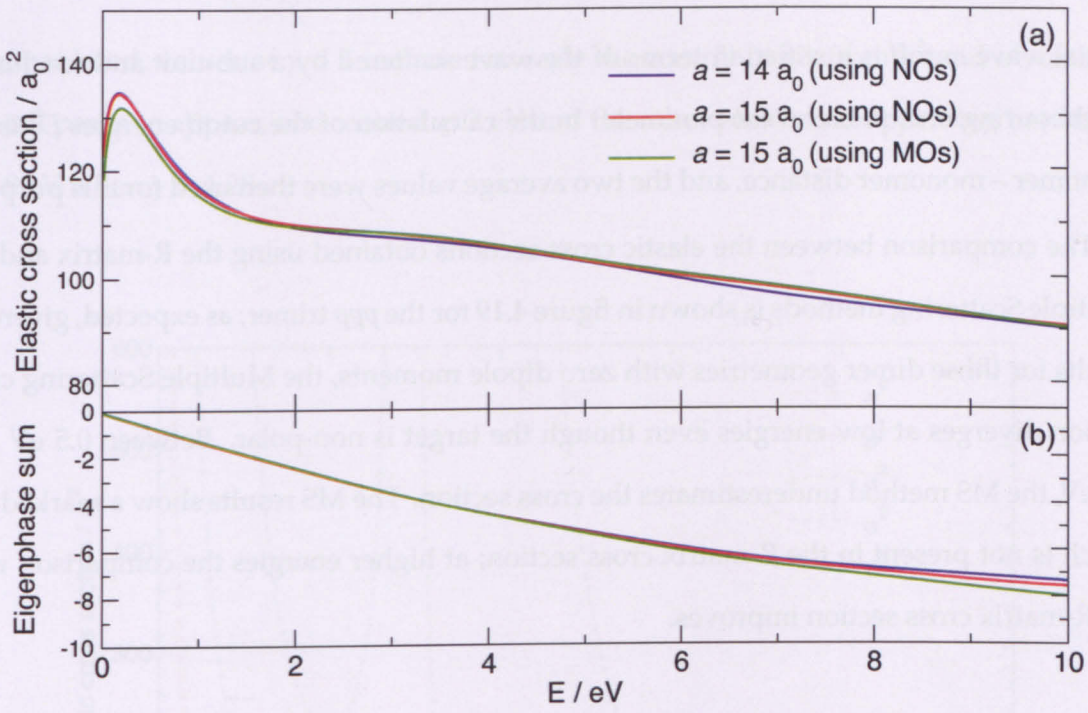

Figure 4.18: (a) *Elastic cross sections and* (b) *eigenphase sum as functions of the energy, for the water trimer from three R-matrix calculations with the parameters indicated in the figure.*

Following these tests, we decided to employ the natural orbitals in the CI expansion and to set the R-matrix radius to 14 a_0.

4.3.2 Multiple Scattering Results

The Multiple Scattering calculations are similar to those described for the water dimers; since the monomers in both *ppp* and *uud* trimers are only slightly distorted, the undistorted gas-phase monomer geometries were employed in the R-matrix calculations run to provide collisional input, as it had been done for all the dimer geometries. We run MS calculations both for the *ppp* and the equilibrium (*uud*) trimers. The former contains monomers with identical parameters, and is completely homogeneous; also, due to the C_3 symmetry axis, the Euler angles (shown in table 4.6) are easy to find. In the equilibrium geometry the monomers differ only slightly.

The inter-monomer distances used were 5.287 a_0 for both *ppp* and *uud* geometries. In the first case, $R_{1,2} = R_{2,3} = R_{1,3}$; in the second case the value 5.287 a_0 is an average of the three inter-monomer distances which however differ by less than 0.4% at most. Since the

partial wave cutoff is justified in terms of the wave scattered by a sub-unit and reaching a neighbouring one, the relevant parameter in the calculation of the cutoff energies E^{l_c} is the monomer – monomer distance, and the two average values were then used for this purpose.

The comparison between the elastic cross sections obtained using the R-matrix and the Multiple Scattering methods is shown in figure 4.19 for the *ppp* trimer; as expected, given the results for those dimer geometries with zero dipole moments, the Multiple Scattering cross section diverges at low energies even though the target is non-polar. Between 0.5 eV and ~ 3 eV, the MS method underestimates the cross section. The MS results show a marked dip which is not present in the R-matrix cross section; at higher energies the comparison with the R-matrix cross section improves.

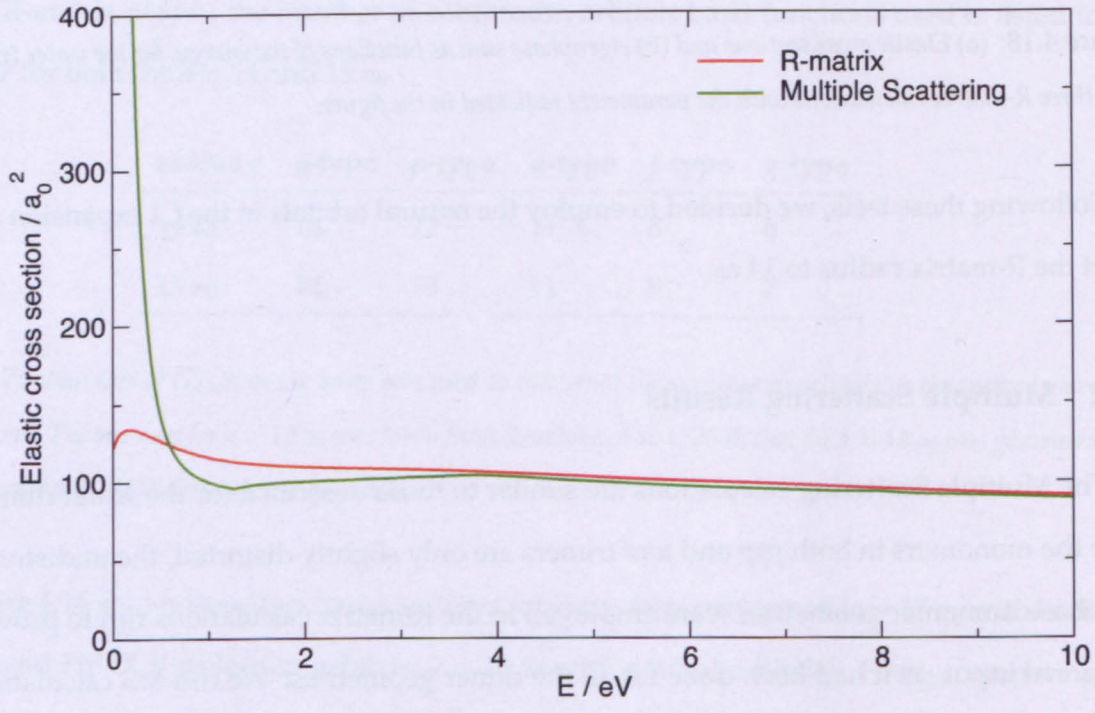

Figure 4.19: *Elastic cross sections for the* ppp *water trimer geometry, produced with the R-matrix (a = 14 a_0, using NOs) and Multiple Scattering methods.*

The Multiple Scattering cross section shown in figure 4.19 is calculated using $\gamma = 0.75$, as for the dimer geometries. A study on the effect of this parameter in the present case, reported in figure 4.20, shows that the dip observed between 0.5 eV and 5 eV is produced by values of $\gamma < 1$, which shift the matching with the σ^2 contribution to higher energies. On

the other hand, values of $\gamma > 1$ include too early the contributions from σ^3 and σ^4, causing two tall peaks to appear, one centred at 3 eV and the other very broad appearing between 5 and 8 eV when $\gamma = 1.25$.

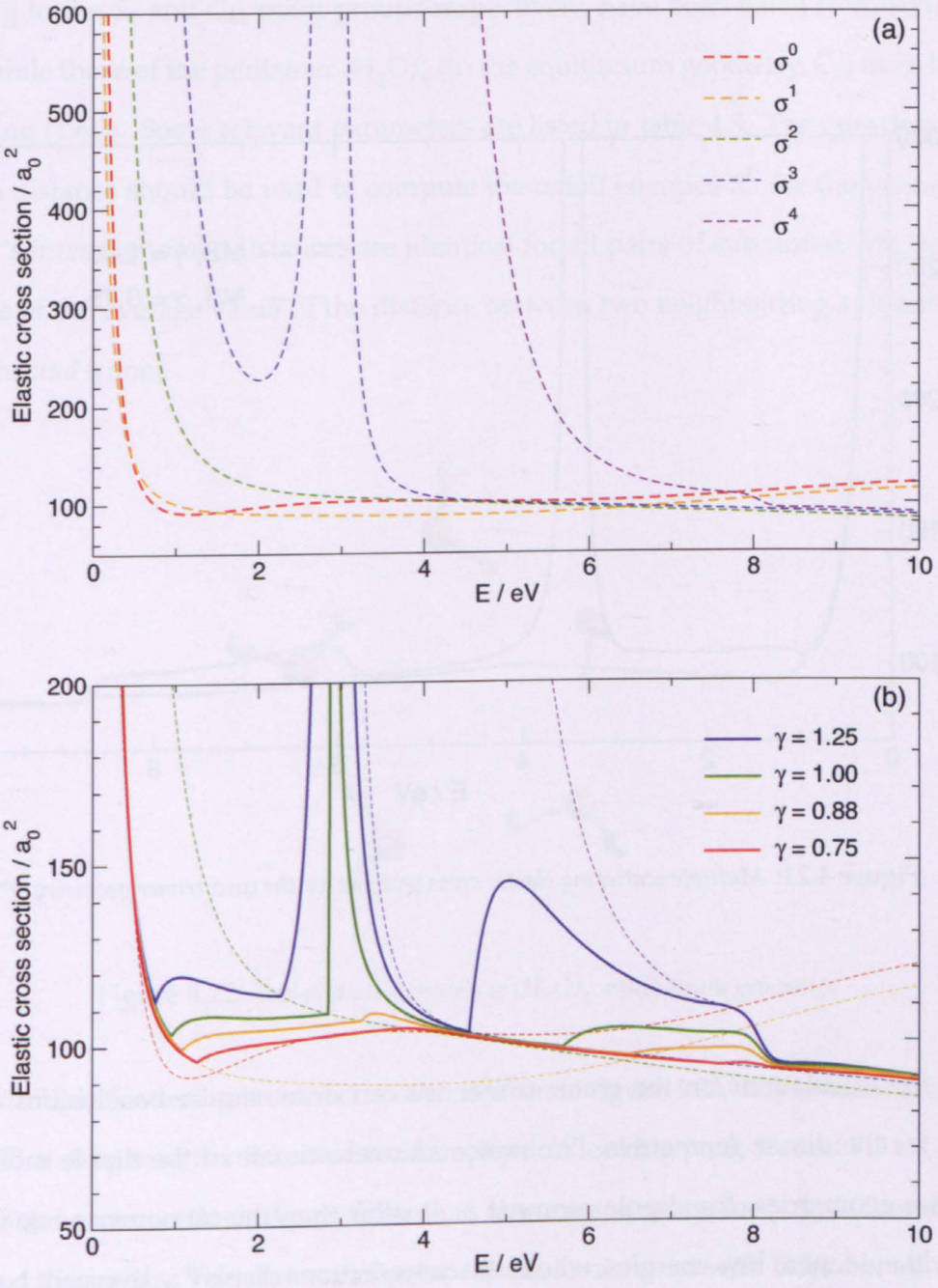

Figure 4.20: (a) *MS cross sections with different numbers of partial waves included, from 0 to* l_{max}, *and* (b) *the interpolated cross section for different values of* γ, *showing the appearance of high peaks when* $\gamma > 0.75$.

Figure 4.21 shows the elastic cross section calculated with the MS method for the C_1 equilibrium trimer geometry (*uud*), whose dipole moment is 1.071 D (Gregory et al. 1997). It is very similar to that obtained for the *ppp* geometry, particularly the low energy divergent behaviour and the presence of two peaks, which are easily washed out by using $\gamma = 0.75$.

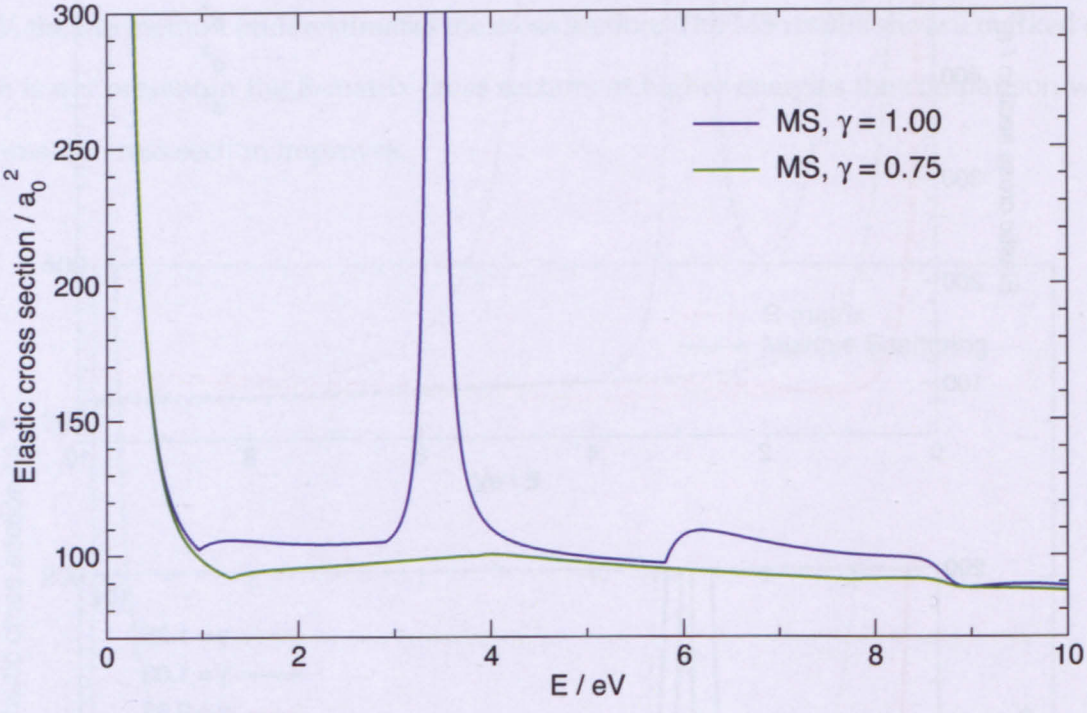

Figure 4.21: *Multiple scattering elastic cross sections for the* uud *trimer geometry.*

From the calculations on the water trimer we can draw similar conclusions to those we drew for the dimer geometries. We notice an overestimate of the dipole moment (in both trimer geometries, the dipole moment is smaller than the monomer one), which is particularly evident at low energies, where the cross sections display a divergent behaviour even for the non-polar *ppp* geometry, unlike the corresponding R-matrix results. Once more, the choice of $\gamma = 0.75$ provides a way to remove non-physical peaks, which arise at the cutoff energies.

4.4 Water tetramer and pentamer and extension to $(H_2O)_n$

This section reports the Multiple Scattering results for the water tetramer (two geometries) and pentamer, for which it has not been possible to perform R-matrix calculations. The geometry parameters of the two tetramer geometries $(H_2O)_4$ labelled *udud* and *pppp*, belonging to the S_4 and C_{4h} point groups respectively, have been taken from Schütz et al. (1995), while those of the pentamer $(H_2O)_5$ (in the equilibrium geometry, C_1) from Xantheas & Dunning (1993). Some relevant parameters are listed in table 4.8. The question arises as to which distance should be used to compute the cutoff energies E^{l_c} for the pentamer (the tetramer's inter-monomer distances are identical for all pairs of sub-units). We decided to make use of the average value of the distance between two neighbouring sub-units, as we did for the *uud* trimer.

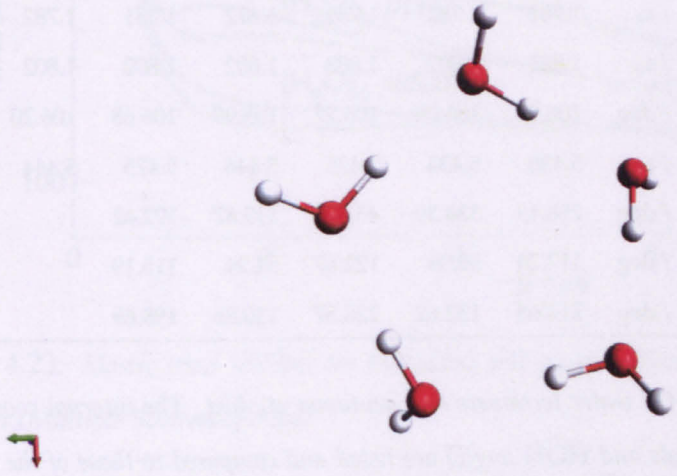

Figure 4.22: *Ball-and-stick models of $(H_2O)_5$, equilibrium geometry.*

The Multiple Scattering cross sections are shown in figure 4.23. It is evident that the use of $\gamma = 0.75$ is necessary to remove a broad unphysical looking peak around 7.5 eV from the *pppp* tetramer cross section. Apart from that, the cross sections for $\gamma = 0.75$ and $\gamma = 1.0$ are not too dissimilar. The absence of prior results to compare with does not allow much discussion on these cross sections. The divergent behaviour below 1 eV characterises all the clusters, although both tetramer geometries are non-polar (the dipole moment of the pentamer is $\sim$ 0.9 D, Toledo et al. 2009).

	geometry	symm	parameter		mon 1	mon 2	mon 3	mon 4	mon 5	average	
			$O-H_1$	/ a_0	1.861	1.861	1.861	1.861		1.861	[+0.051]
			$O-H_2$	/ a_0	1.824	1.824	1.824	1.824		1.824	[+0.014]
			$\widehat{HOH}$	/ deg	105.0	105.0	105.0	105.0		105.0	[+0.5]
(a)	$(H_2O)_4$ *udud*	S_4	R	/ a_0	5.187	5.187	5.187	5.187		5.187	
			α	/ deg	45.52	135.52	225.52	315.52			
			β	/ deg	50.75	129.25	50.75	129.25			
			γ	/ deg	139.23	220.77	139.23	220.77			
			$O-H_1$	/ a_0	1.850	1.850	1.850	1.850		1.850	[+0.040]
			$O-H_2$	/ a_0	1.818	1.818	1.818	1.818		1.818	[+0.008]
			$\widehat{HOH}$	/ deg	106.3	106.3	106.3	106.3		106.3	[+1.8]
(a)	$(H_2O)_4$ *pppp*	C_{4h}	R	/ a_0	5.260	5.260	5.260	5.260		5.260	
			α	/ deg	25.23	115.23	205.23	295.23			
			β	/ deg	90.00	90.00	90.00	90.00			
			γ	/ deg	180.00	180.00	180.00	180.00			
			$O-H_1$	/ a_0	1.783	1.782	1.781	1.872	1.781	1.782	[−0.028]
			$O-H_2$	/ a_0	1.803	1.802	1.803	1.802	1.802	1.802	[−0.008]
			$\widehat{HOH}$	/ deg	106.00	106.08	106.27	105.99	106.68	106.20	[+1.7]
(b)	$(H_2O)_5$	C_1	R	/ a_0	5.436	5.434	5.428	5.446	5.475	5.444	
			α	/ deg	256.49	334.39	45.58	119.87	172.62		
			β	/ deg	117.24	59.98	122.67	52.24	115.19		
			γ	/ deg	214.68	132.62	226.87	130.86	198.69		

Table 4.8: *Geometrical parameters of the water tetramers and pentamer studied. The internal coordinates of each monomeric sub-unit* (O–H *bonds and* $\widehat{HOH}$ *angle) are listed and compared to those of the isolated water. They have been taken from* (a) *Schütz et al. (1995) and* (b) *Xantheas & Dunning (1993). The set of Euler angles* (α, β, γ) *used for the re-orientation of the T-matrices are also reported, together with the distance between nearest neighbours R; the latter is the distance between the sub-unit under whose column the value is listed and the following sub-unit.*

There is a clear tendency of the cross sections for $(H_2O)_n$ to increase as n increases, which was to be expected, although there is no direct proportionality between $\sigma((H_2O)_n)$ and n: the effect of the orientation and position of the monomers is still very important, as our studies on the water dimers also showed. Here, for instance, it is interesting to notice that the two $(H_2O)_4$ geometries are characterised by almost identical parameters (the inter-monomer

distances differ by ~ 1%, both dipole moments are zero); the only geometrical difference is that the *pppp* tetramer is planar, while the *udud* one is not: the monomers alternately point upwards and downwards with respect to the oxygen plane. The effect that this has on the size of the cross sections is very marked, confirming once more that the arrangement of the sub-units is a critical parameter.

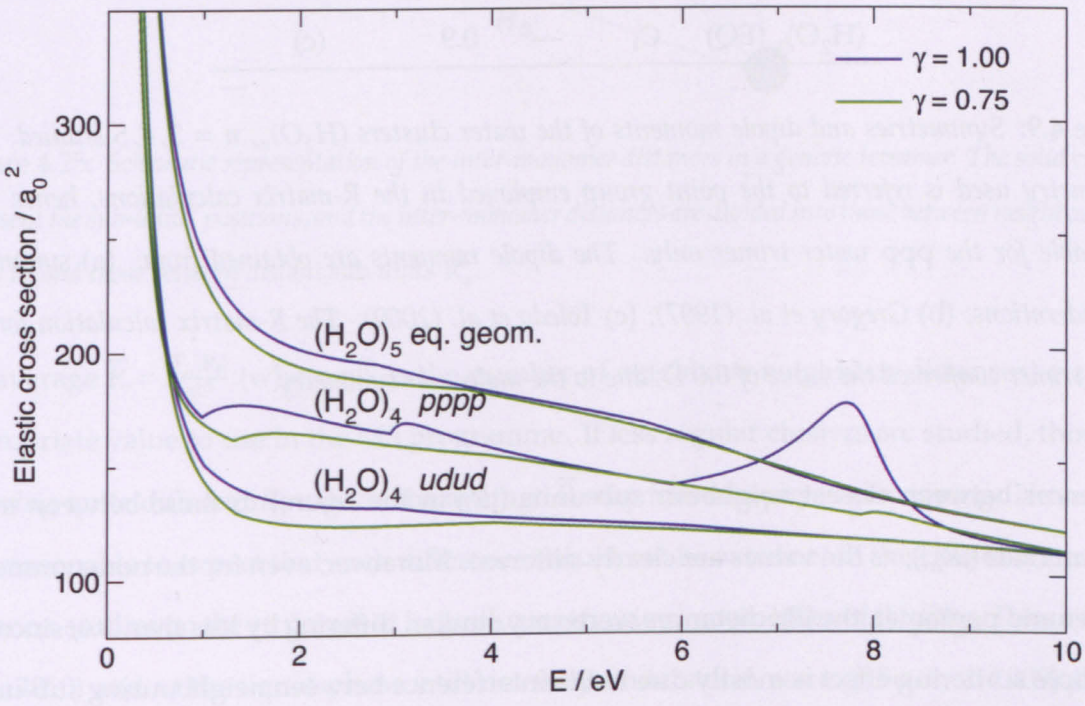

Figure 4.23: *Elastic cross sections for the* udud *and* pppp *tetramer geometries, and for the equilibrium pentamer (Multiple Scattering only).*

Multiple Scattering calculations on larger water clusters can be performed easily once their geometry is known, since all the parameters needed to run can be extracted from it. The atoms forming the clusters must firstly be associated to the different monomers; then the monomers' centres of mass and the inter-monomer distances are calculated. Finally, the Euler angles can be computed using the Fortran programme we have written, *eulerrot*.

There are two remaining issues; the first is: which value must be used as R for the interpolation procedure. This is easily chosen for clusters $(H_2O)_2$ and $(H_2O)_3$, while for $(H_2O)_n$, $n \geqslant 4$, it may be an issue, as figure 4.25 illustrates for a generic cluster made up by four monomers. In the tetramer and pentamer studies, it was easy to distinguish the

geometry	point group		dipole moment / D	
	orig	used		
$(H_2O)_3$ *ppp*	C_{3h}	C_s	0.0	(a)
$(H_2O)_3$ *uud*	C_1	—	1.07	(b)
$(H_2O)_4$ *udud*	S_4	—	0.0	(a)
$(H_2O)_4$ *pppp*	C_{4h}	—	0.0	(a)
$(H_2O)_5$ (EQ)	C_1	—	0.9	(c)

Table 4.9: *Symmetries and dipole moments of the water clusters* $(H_2O)_n$, $n = 3,4,5$ *studied. The symmetry used is referred to the point group employed in the R-matrix calculations, hence it is available for the* ppp *water trimer only. The dipole moments are obtained from:* (a) *symmetry considerations;* (b) *Gregory et al. (1997);* (c) *Toledo et al. (2009). The R-matrix calculation for the* ppp *trimer confirmed the value of 0.0 D, due to the molecular symmetry.*

distances between closest neighbour sub-units ($|\boldsymbol{R}_i|$ in the figure) to those between more distant ones ($|\boldsymbol{R}'_\alpha|$), as the values are clearly different. Moreover, even for the non-symmetric trimer and pentamer, the $|\boldsymbol{R}_i|$ distances were very similar, differing by less than 1%; since the multiple scattering effect is mostly due to the interference between neighbouring sub-units,

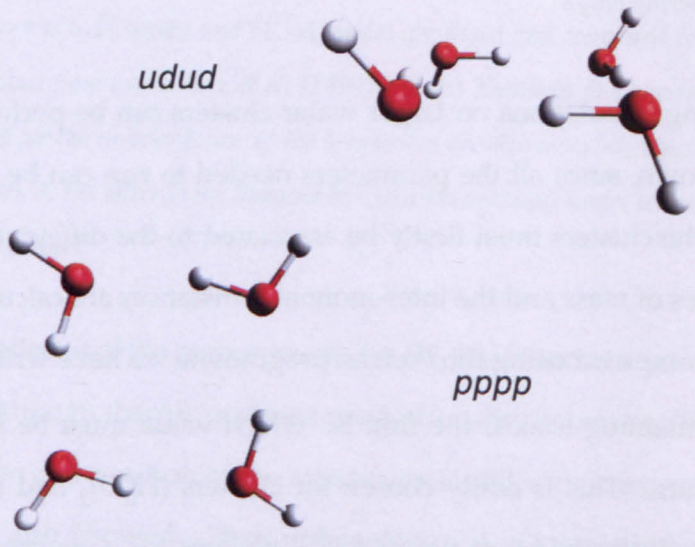

Figure 4.24: *Ball-and-stick models of* $(H_2O)_4$, udud *and* pppp *geometries.*

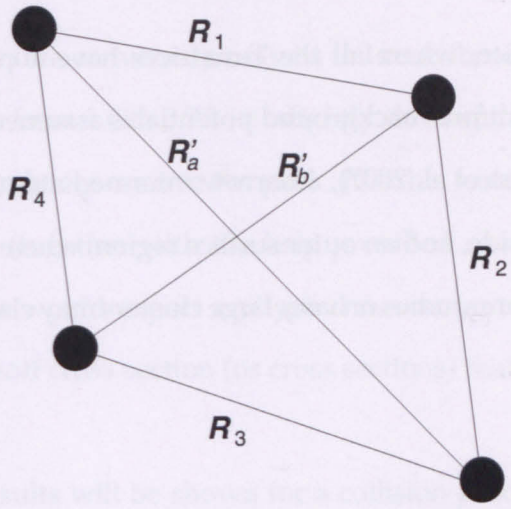

Figure 4.25: *Schematic representation of the inter-monomer distances in a generic tetramer. The solid circles represent the sub-units' positions, and the inter-monomer distances are divided into those between neighbouring units* $\boldsymbol{R}_i$ *and those between distant sub-units* $\boldsymbol{R}'_\alpha$.

the average $\overline{R} = \frac{\sum_i |\boldsymbol{R}_i|}{n^{(i)}}$ (where $n^{(i)}$ is the number of neighbour-neighbour distances) was an appropriate value to use in the MS programme. If less regular clusters are studied, though, showing quite different $\boldsymbol{R}_i$ values, the average $\overline{R}$ may loose its physical meaning. However, it is reasonable to expect that such difference would not be extreme. In the case of water, for instance, studies on the structure of large clusters (various geometries of $(H_2O)_{20}$, Tokmachev et al. 2010) and of the liquid phase (still not fully understood, see e.g. Fu et al. 2009) show that it is meaningful to define *closest neighbours*, since the radial distribution function shows in both cases a first marked peak around 5.3 a_0 (the case of liquid water is more complex, as the position of a second peak at 6.4 a_0 is still not completely clarified).

The second issue may arise when very large clusters are treated; structures of such large aggregates start being available, particularly for water. In this case, it would be possible to distinguish between *internal sub-units* and *surface sub-units*, experiencing different interactions, while in the case of small clusters all the sub-units can be regarded as surface ones, since the surface-to-volume ratio is large. In the work on water dimer by Bouchiha et al. (2008) it is calculated that the surface-to-volume ratio remains larger than 1 for clusters made up by up to ~ 500 molecules (considering an average monomer–monomer distance of 5.5 a_0, as in water); when a cluster is made up by a larger number of monomers, they suggest to partition the physical space into three regions: an inner region treated as a bulk

(as done in the work on ice, where all the T-matrices have a cutoff on the extent of the dipole interaction, and a uniform background potential is assumed in the interstitial regions between sub-regions, Caron et al. 2007), a narrow intermediate region matching the inside of the cluster with the outside, and an outer surface region, where the calculation resembles that on small clusters. Future studies on very large clusters may clarify whether this partition is appropriate.

4.5 Summary

The Multiple Scattering calculations for electron collisions with water clusters for wich an R-matrix comparison is possible show a good agreement with R-matrix results in the energy range [1 eV – 10 eV]. The use of the γ parameter is essential for some clusters, and a value of 0.75 is found to prevent spurious peaks to appear. Its use has however a negligible effect on most of them, so that in general $\gamma = 0.75$ seems to be an appropriate choice in all cases. The cross sections of clusters for which no comparison is available appear sensible.

It is reasonable to wonder whether the peak removal is an acceptable procedure or not, and what the risks are that physically meaningful peaks could be removed, especially when comparisons with other results are not possible. In order to address this problem, we first analyse the cases encountered so far where a peak appeared in the interpolated cross section: namely, geometries Z_2 of $(H_2O)_2$, *ppp* and *uud* of $(H_2O)_3$ and *pppp* of $(H_2O)_4$. We first note that no evident characteristics that could justify the peaks distinguish them from the others: they are characterised by different dipole moments and symmetries. There does not seem to be a particular reason why these geometries should behave differently to the others. In fact, all the water clusters display peaks in the cutoff cross sections, particularly those including high partial waves; these features usually appear at energies where the corresponding partial waves should not contribute to the final cross section, and are therefore cut out during the interpolation. When this does not happen, and a peak appears in σ^{INT}, it is always sufficient to set $\gamma = 0.75$ to avoid the inclusion of the peak. Analysing figures 4.8 and 4.20, it can be observed that the peaks always arise at a cutoff energy E^{l_c}, where a non-peaked cutoff cross section σ^{l_c} is combined with a peaked one, σ^{l_c+1}. We also notice that this peak is never

wholly included in σ^{INT}: quite conversely, only its tail contributes to the interpolated cross section, so that reducing γ from 1.0 to 0.75, i.e. slightly shifting the cutoff energies to higher values, is sufficient to completely remove the peak. It is this feature that leads us to classify the peak as non-physical (together with the help provided comparing with other results eventually available): one would expect a physical resonance to appear fully around the resonant energy in the cutoff cross section (or cross sections) that mostly contribute to σ^{INT} at those energies.

In the next chapter, results will be shown for a collision process whose cross section is known to display peaks associated with shape resonances. This study will allow us to test wheter the MS method is able to reproduce such resonances. In addtion, it will help us ascertain whether the peaks are affected by the interpolation procedure and changes in γ.

Chapter 5

Elastic scattering from formic acid monomer and dimer

Formic acid, HCOOH, is a dipolar molecule that can be found in many different environments, e.g. in the interstellar clouds (Ellder et al. 1980, Irvine et al. 1989), in star forming regions (Hollis et al. 2003, Cazaux et al. 2003), and also in biological environments, where it plays a role in different biochemical processes and is a building block of several compounds. Its gas-phase and dimeric forms have been extensively studied, both experimentally and theoretically, particularly because of the important role they have as key compounds in the formation of small biomolecules in the interstellar medium, where they seem to provide the building blocks of larger molecules of biological significance, especially in the early universe (Irvine et al. 1989, Ban et al. 2000). The resonances observed at low energies in various studies on electron collisions with the formic acid monomer and dimer have been observed to lead to fragmentation; these systems are therefore ideal to analyse dissociation patterns in the biological environment, as both of them are prototypes for larger carboxylic acid monomers and dimers.

In this chapter our results obtained for the LEE collision with these systems are presented; the monomer has been studied using the R-matrix method (section 5.2), and the dimer with the Multiple Scattering one (section 5.3). Section 5.1 reports theoretical and experimental results found in the literature, in particular regarding the position and type of resonances

found at low energies.

5.1 Review of previous work

5.1.1 Formic acid monomer

The majority of the experimental studies on the interaction between low energy electrons and the formic acid monomer have focussed on dissociative electron attachment (DEA). Different resonances have been found, leading to the production of different ions. Pelc et al. (2002) and Pelc et al. (2003) found that the most abundant fragment from the DEA process is the $HCOO^-$ ion, with a resonance peak at 1.25 eV showing a very sharp onset. They also showed that the H loss occurrs from the hydroxyl group O–H, as it was later confirmed by calculations (Gianturco & Lucchese 2004). The production of two other fragments, OH^- and O^-, displays peaks at 6.8 eV and $E > 8.0$ eV respectively. Prabhudesai et al. (2005), using a different apparatus, found ion signals at 1.4 eV ($HCOO^-$), 7.6 eV and 9.3 eV (OH^-/O^-). They also identified a peak due to the production of H^- ion at 7.3 eV, with a shoulder at 9.3 eV (see tables 5.1 and 5.2).

Many different experimental and theoretical studies have focussed on the dissociation process leading to the production of the $HCOO^-$ ion; Pelc and co-workers (Pelc et al. 2002, Pelc et al. 2003) inferred that the formation of this ion comes from an ionic temporary state $(HCOOH^-)^\dagger$ which later either decays by dissociation to $HCOO^-$ or by auto-detachment leaving the parent molecule vibrationally excited. They concluded that a series of closely spaced overlapping shape resonances was involved in the dissociation process (whereas the higher energy ones are core excited resonances).

This notion was later refuted by Gianturco & Lucchese (2004), who used a purely local potential to locate resonant states for the formic acid and found a resonance of A'' symmetry at 3.48 and 3.49 eV (for the neutral molecule in the *cis* and *trans* geometries respectively) with 0.93 eV width, and a broader one of A' symmetry at 11.98 and 12.06 eV. They concluded that the first is a π^* resonance (whose density is entirely on HCOO and has nodes on the O–H bond) which leads to the dissociation of the molecule through vibrational energy redistri-

bution from the carbonyl bond to the dissociative O–H stretching mode; they attribute the discrepancy with other results to their use of several approximations both in the interaction potential and in the quantum dynamics.

Research group	E	Γ	Technique / method used
Tronc et al. (1987)	1.8		Electron transmission spectroscopy
Aflatooni et al. (2001)	1.73	0.82	Electron transmission spectroscopy
Pelc et al. (2003)	1.25	~0.5	DEA
Gianturco & Lucchese (2004)	3.48	0.93	Calculated elastic cross sections
Prabhudesai et al. (2005)	1.4		DEA
Allan (2006)	2.0		Elastic and momentum transfer cross sections
Bettega (2006)	1.9		Differential and momentum transfer cross sections
Rescigno et al. (2006)	1.9	0.2	Calculated DEA cross sections
Trevisan et al. (2006)	1.9	0.2	Calculated momentum transfer cross sections

Table 5.1: *Position and width (in eV) of the π^* resonance in formic acid monomer studies; the determination method is specified in the last column. The values for the ground state geometry only are listed in Gianturco & Lucchese's (2004) case.*

Research group	E	Ion yield / symmetry
Pelc et al. (2003)	6.8	OH^-
	>8.0	O^-
Gianturco & Lucchese (2004)	11.98	A' resonance
	12.06	A' resonance
Prabhudesai et al. (2005)	7.6	OH^- / O^-
	9.3	OH^- / O^-
	7.3	H^-
	9.3	H^-

Table 5.2: *Position (in eV) of the other resonances found in the formic acid monomer studies. The ion observed (experiments) or the symmetry of the resonances (theory) are shown in the last column.*

Rescigno et al. (2006) pointed out two problems in the interpretation given by Gianturco & Lucchese (2004), the main being a symmetry issue; they proposed a different dissociation

pathway passing through the π^* resonance and then proceding to a symmetry breaking, coupling this resonance to a σ^* orbital on the OH bond, leading to the dissociation of the bond itself and the production of the $HCOO^-$ ion. They found the resonance to be at ~ 1.9 eV with a width of ~ 0.2 eV.

Electron transmission spectroscopy experiments (Tronc et al. 1987, Aflatooni et al. 2001) found a resonance at 1.8 eV and 1.73 eV respectively (the latter result confirmed by calculations performed by the same authors) due to the temporary occupation of the first π^* orbital.

More recently, differential and total elastic cross sections and momentum transfer cross sections for the scattering by formic acid have been determined. Allan (2006) presented experimental differential cross sections for the elastic scattering, noticing a π^* resonance around 2 eV which causes strong vibrational excitation; he also stated that the vibrationally inelastic cross section amounts to half of the elastic cross section at that energy.

A similar conclusion was drawn by Trevisan et al. (2006), who presented calculated momentum transfer cross sections showing a very sharp π^* resonance near 1.9 eV; the comparison with the experimental results of Vizcaino et al. (2006) showed that the resonance has a relatively small branching ratio to the vibrationally elastic channel, coupling more strongly to the vibrationally excited and dissociative attachment channels. The calculated differential and momentum transfer cross sections of Bettega (2006) confirm the presence of a π^* shape resonance of A'' symmetry at ~ 1.9 eV. The agreement between the differential cross section for the elastic electron scattering measured by Vizcaino et al. (2006) and those calculated by Trevisan et al. (2006) and Gianturco & Lucchese (2006) is generally good.

Very recently, Gallup et al. (2009*a*) questioned the reaction pathway proposed by Rescigno et al. (2006), leading to dissociation of the O–H bond; employing a one-dimensional model, where the dissociation is assumed to occur along the O–H bond coordinate only, they suggested that a short-lived σ^* resonance, with the additional electron located on the OH bond, is responsible for the break up. The effect of such resonance would not be visible in total electron scattering cross sections but it is in DEA cross sections. Debate followed (Rescigno et al. 2009, Gallup et al. 2009*b*) and is likely to continue.

Table 5.1 summarises the energies at which the various authors mentioned above find the π^* resonance. The theoretical results of Gianturco & Lucchese (2004) find this resonance at higher energy than the other groups; this is due to an underestimate of the target polarisability.

5.1.2 Clustered formic acid

In recent years, numerous studies on aggregates of formic acid have been carried out, particularly because their behaviour, under some conditions, resembles that of aggregates of larger molecules, among which are biologically relevant ones.

In particular, *dimers* of carboxylic acids, $(RCOOH)_2$ are characterised by two hydrogen bonds forming an eight-membered ring (Madeja & Havenith 2002, Chocholousova et al. 2002); this conformation is responsible for reaction pathways which are absent in the monomers. This suggests that the formic acid dimer (and, more generally, its clusters) can serve as a simple model system to study the effect of hydrogen bridges, particularly towards electron attack.

It has been observed that in dimer anions of carboxylic acids (including formic acid) and nucleic acid bases a proton is transferred from the acid to the base in their most stable structures, reached by a barrier-free proton transfer (Dąbkowska, Rak, Gutowski, Nilles, Stokes & Bowen 2004, Dąbkowska, Rak, Gutowski, Nilles, Stokes, Radisic & Bowen 2004). The theoretical study of dissociative electron attachment by Gianturco et al. (2005) also showed that the formic acid dimer behaves quite differently from the monomer: the formation of $HCOOH^-$, $HCOO^-$, $(HCOOH)_2^-$ and $[(HCOOH)\,(HCOO)]^-$ was predicted by their calculations in the Fixed Nuclei approximation (considering the dimer equilibrium geometry) and using an adiabatic potential model. They found several main resonances at low energies, which they linked to possible dissociation pathways leading to $(HCOOH)_2^-$ and $[(HCOOH)\,(HCOO)]^-$ at 2.87 eV (resonance of A_u symmetry), $HCOOH^-$ and $HCOO^-$, both at 3.68 eV (B_g); they also found a resonance at 9.92 eV interpreted as a precursor state to the fragmentation into $(HCOOH)\,(HCOO)$ and H^-, in agreement with the resonance at 9 eV detected by Sedlacko

et al. (2005) for HCOOH film. Further resonances at higher energies were correlated to the observed production of smaller fragments, such as CO_2^- and O^-. Information complementary to that given by DEA was given by Allan's (2007) measurements of the cross section for vibrational excitation and elastic scattering. The A'' shape resonance observed for the monomer at 1.9 eV (resulting from a temporary occupation of a π^* orbital) is split into two A_u and B_g resonances in the dimer, appearing at 1.40 and 1.96 eV respectively. Allan (2007) also showed that the formic acid dimer, unlike the monomer, is subject to a reaction following the vertical electron attachment, proceeding to a lowering of the symmetry and a rapid proton transfer (also confirmed by calculations of Bachorz et al. 2005). The mechanism is a source of slow electrons and is analogous to an electron-driven proton transfer process observed in proteins and other biomolecules by Sobolewski and co-workers (Sobolewski & Domcke 2006, Sobolewski et al. 2002).

Larger aggregates were also studied: DEA experiments performed by Martin et al. (2005) on *formic acid clusters* showed that, while the most common fragment from gas phase formic acid at low electron energies is $HCOO^-$, electron attachment to clusters is strongly enhanced and leads to non-dissociated ions $(HCOOH)_n^-$ ($n \geqslant 11$ in their work) as well as dissociated anionic complexes $(HCOOH)_{n-1}(HCOO)^-$. The most abundant non-dissociated products are $(HCOOH)_2^-$ and $(HCOOH)(HCOO)^-$; the first is the product of electron attachment to a cluster (because this reaction is never observed in the monomer), while the second can be a product from either a monomer or a cluster. Also, various other dissociation reactions are open for clusters, including the formation of $(H_2O)(HCOO-)$, which the authors attributed to a reaction initiated in the cyclic hydrogen bonded dimer. Sedlacko et al. (2005) performed electron stimulated desorption experiments on *formic acid film* deposited on a substrate, that also showed that the main dissociation reaction observed in the gas phase ($HCOOH + e^- \longrightarrow (HCOOH^-)^\dagger \longrightarrow HCOO^- + H$) at ~ 1.25 eV is no longer observed in the condensed phase (it may still be operative but $HCOO^-$ would remain on the surface). Conversely, formation of H^- from the condensed phase HCOOH was observed from the reaction $HCOOH + e^- \longrightarrow (HCOOH^-)^\dagger \longrightarrow HCOOH^* + H^-$, via a core excited resonance appearing around 9 eV. Moreover, the experiments on the clusters detected the $HCOOH^-$

ion which was not present in the electron attachment to gas phase formic acid experiments.

The resonances observed for the formic acid aggregates are summarised in table 5.3.

Research group	target	E	Ion yield / symmetry
Martin et al. (2005)	clusters	~1.0	dissociation into H_2O $(HCOOH)^-$ and HCO
Sedlacko et al. (2005)	film	9.0	formation of H^-
Gianturco et al. (2005)	dimer	2.87	A_u resonance; $[(HCOOH)_2]^-$, $[(HCOOH)\ (HCOO)]^-$
		3.68	B_g resonance; $HCOOH^-$, $HCOO^-$
		9.92	A_g resonance; formation of H^-
		11.71	B_u resonance;
		13.99	B_u resonance; } CO_2^-, O^-, others
		14.05	A_g resonance;
Allan (2007)	dimer	1.40	A_u shape resonance
		1.96	B_g shape resonance

Table 5.3: *Position (in eV) of the resonances observed or calculated for the formic acid aggregates. The kind of aggregate, the type of resonance and the products are also reported.*

5.2 R-matrix calculations for the formic acid monomer

The formic acid monomer may be found in the *cis* or *trans* configurations, depending on the orientation of the O–H bond; the *trans* configuration is the most stable, and its *trans–trans* dimers are also more stable than the *trans-cis* and *cis-cis* ones (Hocking 1976); all the dimers are stabilised by the formation of two hydrogen bonds. For this reason the monomer R-matrix calculation was performed for the *trans* geometry. The geometry parameters have been taken from the NIST Computational Chemistry Comparison and Benchmark DataBase (2010) (obtained from a calculation using MP2 method and cc-pVTZ basis set); the formic acid is a planar molecule belonging to the C_s point group, which consists of two irreducible representations, A' and A''; symmetry properties were used in our R-matrix calculations to lighten the computation process.

Unlike the calculations for the water monomer, for which previous studies were available, the low energy electron collision process with formic acid had not been treated before with

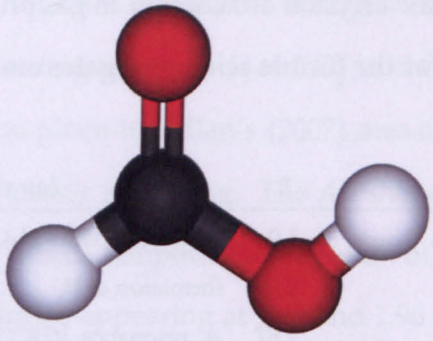

Figure 5.1: *Ball-and-stick model of* trans-*HCOOH.*

the R-matrix method. The tests performed to choose the correct parameters for the target calculations (basis set, choice of HF-SCF molecular or natural orbitals, number of states to include), for the scattering calculations (R-matrix radius, continuum functions basis set) and for the Multiple Scattering input (choice of a_c in the dimer calculation) are described below.

Since the main object of this study was to verify that the Multiple Scattering method is able to reproduce shape resonances, we did not attempt to perform the best R-matrix calculation possible, but one that would reproduce the monomer resonance and provide a reasonable MS input.

5.2.1 Molecular orbital basis set

Three basis sets have been tried: (1) one similar to that employed in the water calculation (referred to as *Dunning*), which included the triple-zeta basis of Dunning (1971) (for H) and double-zeta of Dunning (1970) (for O and C), augmented with diffuse *s* and *p* functions; (2) a *6-31G* basis (Hehre et al. 1972) and (3) a *6-31G*** basis (Hariharan & Pople 1973). The number of functions for each set is listed in table 5.4.

The basis set labelled Dunning and the 6-31G** basis set include diffuse functions which do not cause problems in the water case; since the formic acid is a larger molecule than water, however, they may require a large R-matrix radius *a*; for this reason a less diffuse basis set (6-31G) was also tested.

The CASCI model used includes 6 frozen electrons and 18 active electrons distributed among 12 orbitals $(1a'—3a')^6$ $(4a'—12a', 1a''—3a'')^{18}$, generating a total of 38 896 configura-

basis set	atom	*s*-type	*p*-type	*d*-type
6-31G	H	2		
	C	3	2	
	O	3	2	
6-31G**	H	2	1	
	C	3	2	1
	O	3	2	1
Dunning	H	4	2	
	C	5	2	1
	O	6	3	1

Table 5.4: *Number of atomic orbitals included in the basis sets used for the formic acid monomer calculations.*

tions in the target calculation and 82 175 in the $(N + 1)$ calculation. Our attempts to enlarge further the active space (including 13 orbitals instead of 12) resulted in a very memory demanding $N + 1$ calculation, which was in practice unfeasible. The target energies, at Hartree-Fock and CI levels, together with the dipole moment obtained from the CI calculation, are reported in table 5.5, where they are compared with accurate values. The largest basis set, Dunning, provides the lowest energy, although the differences with the other calculations are almost negligible; the comparison with an accurate energy value (−189.845118 E_h, B3LYP, aug-cc-pVTZ basis set; NIST Computational Chemistry Comparison and Benchmark DataBase 2010) is not very good, since all our energies are at least 1 E_h higher; this may be partly due to the use of different geometries. The 6-31G** basis set provides a dipole moment in agreement with the experimental one (1.41 Debye; Lide 1998), while the other calculations over- and underestimate it (Dunning and 6-31G respectively).

Figure 5.2 shows the electron – HCOOH elastic cross sections from R-matrix calculations, carried out using the three basis sets, with R-matrix radii $a = 10\ a_0$ (when Dunning and 6-31G** basis sets are employed) and $a = 8\ a_0$ (for the 6-31G one), HF-SCF orbitals and including the first 5 states. All cross sections display a resonance of A'' symmetry (better analysed later), whose position, shape and width are strongly influenced by the choice of basis set; the

basis set	HF energy / E_h	CI energy / E_h			dipole moment / Debye		
Dunning	−188.818 959	−188.836 621	+1.008	[+0.53%]	1.52	+0.11	[+7.8%]
6-31G**	−188.767 457	−188.800 967	+1.044	[+0.55%]	1.41	—	[—]
6-31G	−188.662 410	−188.702 743	+1.142	[+0.60%]	1.21	−0.20	[−14.2%]
accurate values		−189.845 118	(a)		1.41	(b)	

Table 5.5: *Hartree-Fock and CI energy and dipole moment for HCOOH, calculated using three different atomic orbital basis sets. The absolute and relative differences with an accurate energy value* (a) *from NIST Computational Chemistry Comparison and Benchmark DataBase (2010) (B3LYP, aug-cc-pVTZ basis set) and with the experimental dipole moment* (b) *by Lide (1998) are shown.*

A' component, conversely, is minimally affected by it and displays a regular behaviour in all three cases, showing a dip at 0.2 eV. The larger basis sets, Dunning and 6-31G**, provide results that agree quite well on the position and shape of the resonance, displayed at about 3.3 eV, although the Dunning peak is slightly wider. The differences with the results obtained employing the 6-31G basis set are more evident, as in the latter calculations the resonance appears at a much lower energy (centred at about 2.6 eV) and its width is smaller. This calculation is therefore in better agreement with the experimental results, which report the resonance at around 2 eV, and the 6-31G basis set seems to be the most appropriate one in this respect, although it provides the highest CI energy and underestimates the dipole moment by 14%. For this reason, we were unable to decide which basis set performed best, and we continued employing all three, both for producing monomer cross sections and for providing the input T-matrices needed in the Multiple Scattering approach.

From a computational perspective, the requirements of the 6-31G** basis set calculations are very similar to those of the Dunning basis set, while the calculations employing the smaller 6-31G basis set are faster and less demanding, due to the smaller number of orbitals involved.

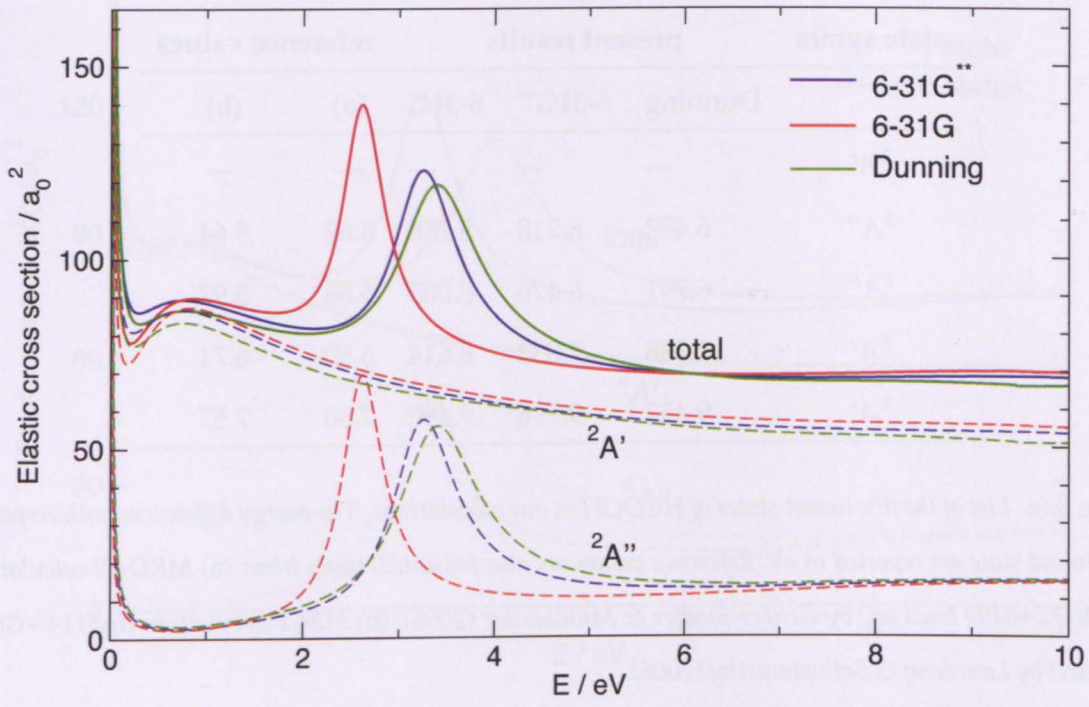

Figure 5.2: *Elastic electron – HCOOH cross section, calculated using different basis sets, with $a = 10\ a_0$ (6-31G** and Dunning) and $a = 8\ a_0$ (6-31G). Five states are included in the close-coupling expansion.*

5.2.2 Number of states in the close-coupling expansion and choice of molecular orbitals

In the energy range where we focused our attention, [0 – 10 eV], five target states are open, as table 5.6 shows; we decided to include all of them (the first two $^1A'$ states, and the first $^1A''$, $^3A'$ and $^3A''$ states) in the scattering calculation, in order to avoid spurious peaks (pseudoresonances), that appear when target states associated with channels that are open in the energy range considered are not included in the close coupling expansion (Tennyson 2010). Table 5.6 also reports the vertical excitation energies calculated by Gruber-Stadler & Muhlhauser (2006) (MRD-CI model, cc-pVDZ+SPD basis set) and Lourderaj & Sathyamurthy (2006) (MRCI model, 6-311++G(p,d) basis set); their energies are lower than ours and hence closer to those we calculated using the smaller 6-31G basis set; the discrepancies are more marked the higher the state, and particularly evident for the $2^1A'$ state.

The number of states included in the close-coupling expansion does not influence the energy of the ground state; however it has effects on some target properties. For instance, it

state symm	present results			reference values	
	Dunning	6-31G**	6-31G	(a)	(b)
$^1A'$	—	—	—	—	—
$^3A''$	6.493	6.218	5.756	5.62	5.64
$^1A''$	6.791	6.476	6.005	5.88	5.97
$^3A'$	7.388	7.033	6.614	6.50	6.71
$^1A'$	9.453	9.796	9.490	7.80	7.57

Table 5.6: *List of the five lowest states of HCOOH in our calculations. The energy differences with respect to the ground state are reported in eV. Reference values are also indicated, taken from:* (a) *MRD-CI calculations (cc-pVDZ+SPD basis set) by Gruber-Stadler & Muhlhauser (2006);* (b) *MRCI calculations (6-311++G(d,p) basis set) by Lourderaj & Sathyamurthy (2006).*

improves the description of the polarisability (discussed later), which is calculated as a sum over states. The polarisability may greatly affect the description of the scattering process, and its effects are particularly evident when resonances are found; the position of the resonance may vary considerably, depending on the value of the polarisability. This effect can be seen in figure 5.3, where the elastic cross sections from R-matrix calculations including 1 and 5 states are shown (6-31G** basis set employed): the $^2A'$ component of the cross section is not heavily influenced by the inclusion of a different number of states, while the $^2A''$ component is, and particularly the resonant peak, which is characterised by a different position and width in each case. The inclusion of a large number of states is therefore to be preferred; however, the requirements of the calculations increase proportionally, especially those for the scattering process, and a compromise must be sought.

A more accurate analysis on the effect that the number of states has on the polarisability is carried out later, when attempts are made to improve its representation.

As for the choice of molecular orbitals, we performed tests where HF-SCF and natural orbitals were employed; the latter were generated from the ground state wavefunction using a SDCI model, that included 19 orbitals available for single and double excitations: $[(1a'—10a',1a'',2a'')^{23}\ (11a'—25a',3a''—6a'')^1]$ (singles), $[(1a'—10a',1a'',2a'')^{22}\ (11a'—$

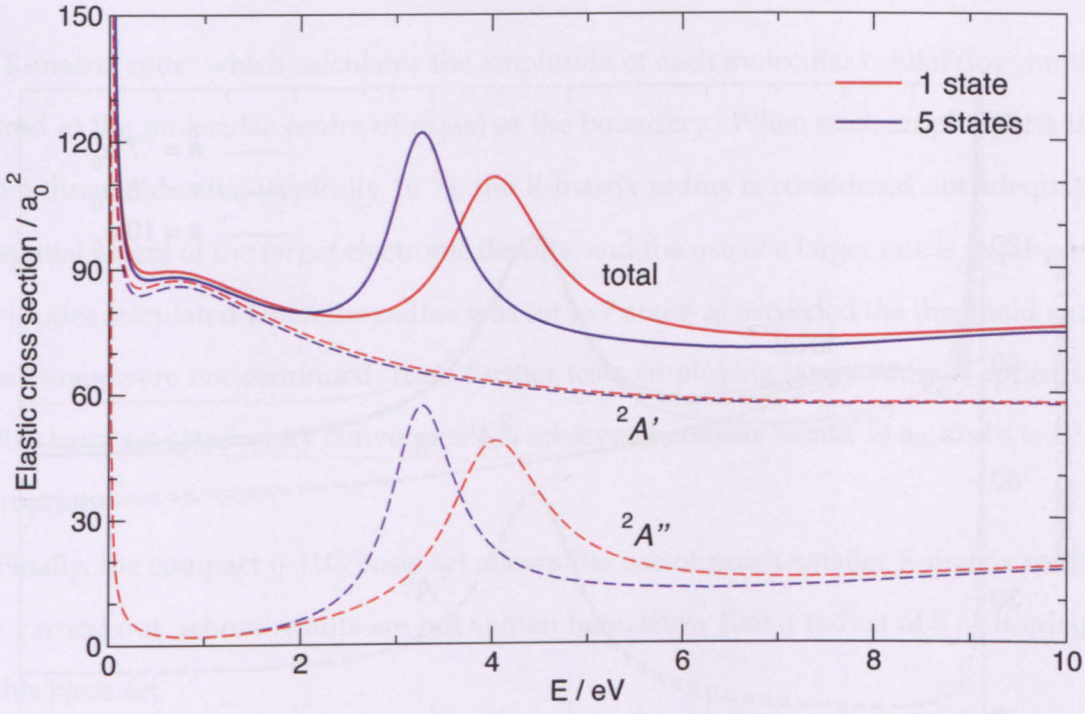

Figure 5.3: *Elastic cross sections for the R-matrix calculations performed using the same basis set (6-31G**) and R-matrix radius ($a = 10\ a_0$), but different number of states; HF-SCF orbitals were employed.*

$25a',3a''$—$6a'')^2$] (doubles). The natural orbitals were then used in a CASCI calculation as described above. When natural orbitals are employed, the CI energy is slightly lower (less than 0.05%) than that obtained with HF-SCF molecular orbitals. Negligible differences are also observed in the values of the dipole moment. We therefore deemed it an unnecessary step to generate and use natural orbitals; HF-SCF molecular orbitals are hence employed throughout the rest of the chapter.

5.2.3 R-matrix radius

In this section the tests carried out to identify the most appropriate R-matrix radius a are presented; since the value of a depends on the spatial extent of the target electronic functions, separate tests needed to be performed for each choice of basis set. As previously done for the water monomer, we carried out calculations at increasing values of a until convergence was reached.[1]

[1]Strictly speaking, it is not correct to call it "convergence", since the results at different radii depend also on other parameters, such as the number of functions in the continuum basis set and its ability to correctly describe the scattering electron in the inner region.

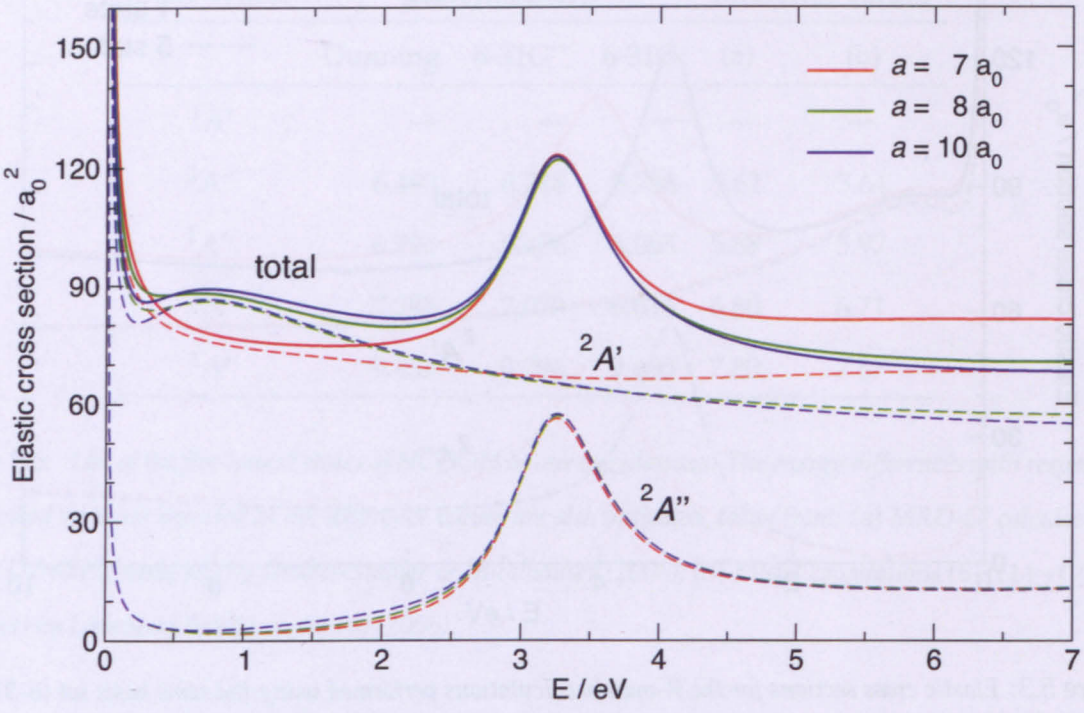

Figure 5.4: *R-matrix elastic cross sections for the electron collision with formic acid, calculated with the 6-31G** basis set and the R-matrix radii indicated in the figure.*

The cross sections shown in figure 5.4 correspond to R-matrix calculations performed using the 6-31G** basis set, with three different values of a. The $^2A''$ contribution (the most influenced in previous tests presented) is here very stable (because the target properties are unchanged): the position and shape of the resonant feature at 3.3 eV are unperturbed. The non-resonant $^2A'$ component is more affected by the choice of a, especially when a changes from 7 to 8 a_0; this probably means that $a = 7$ a_0 is too small a radius for the basis set chosen and does not prevent the target electronic density leaking outside the inner region. The difference between the cross sections calculated with $a = 8$ and 10 a_0 are only slightly different; therefore we decided to use the largest radius in future calculations with the 6-31G** basis set.

Similar tests were performed with the other basis sets. When the more diffuse Dunning basis set was employed, it was not possible to perform R-matrix calculations with radii $a = 7$ and 8 a_0, due to the leaking of the target electron density outside the inner region sphere. As explained in the previous chapter, an approximate test is automatically performed by the

UK R-matrix code, which calculates the amplitude of each molecular orbital (for simplicity centred at the molecular centre of mass) at the boundary. When such amplitude is larger than a threshold value (typically 10^{-3}), the R-matrix radius is considered not adequate for the spatial extent of the target electronic density, and the use of a larger one is required. The amplitudes calculated when the radius was set to 7 and 8 a_0 exceeded the threshold and the calculations were not continued; from further tests employing larger radii, it appears that for this basis set satisfactory convergence is achieved between 10 and 14 a_0, and a = 10 a_0 is appropriate.

Finally, the compact 6-31G basis set allows the use of much smaller R-matrix radii; the tests carried out, whose results are not shown here, show that a radius of 8 a_0 is adequate for this basis set.

5.2.4 Choice of a_c

When R-matrix results are used as input in Multiple Scattering calculations, the radial distance a_c, after which the dipole moment interaction is cut off, must be chosen, in order to correctly build the cutoff T-matrices T_c. Analogous tests carried out for water showed that, although cutting off the dipole moment interaction at a_c has a marked effect on the resulting monomer cross sections, it has a less noticeable one on the Multiple Scattering results.

The tests carried out for HCOOH are characterised by a different behaviour, which is quite unexpected, as figure 5.5 shows. The figure presents the elastic cross sections obtained from R-matrix calculations with the 6-31G** basis set, where a = 10 a_0 and a_c varies over a rather large range (from 6 a_0 to 50 a_0, including a cross section with no dipole cutoff, ideally corresponding to $a_c = \infty$). Similar tests using the two other basis sets, 6-31G and Dunning, are not shown here; they provide similar results to those reported in figure 5.5 and identical conclusions can be drawn in all cases. As mentioned in section 2.4, the cutoff T-matrices are calculated propagating the R-matrix to the corresponding radius a_c, and then matching with Bessel functions, so that the long range interactions are included up to a_c. Conversely, the standard procedure, which is used to calculate the untrimmed T-matrices, includes a propagation up to a large enough distance (typically 50 or 100 a_0), followed by the Gailitis

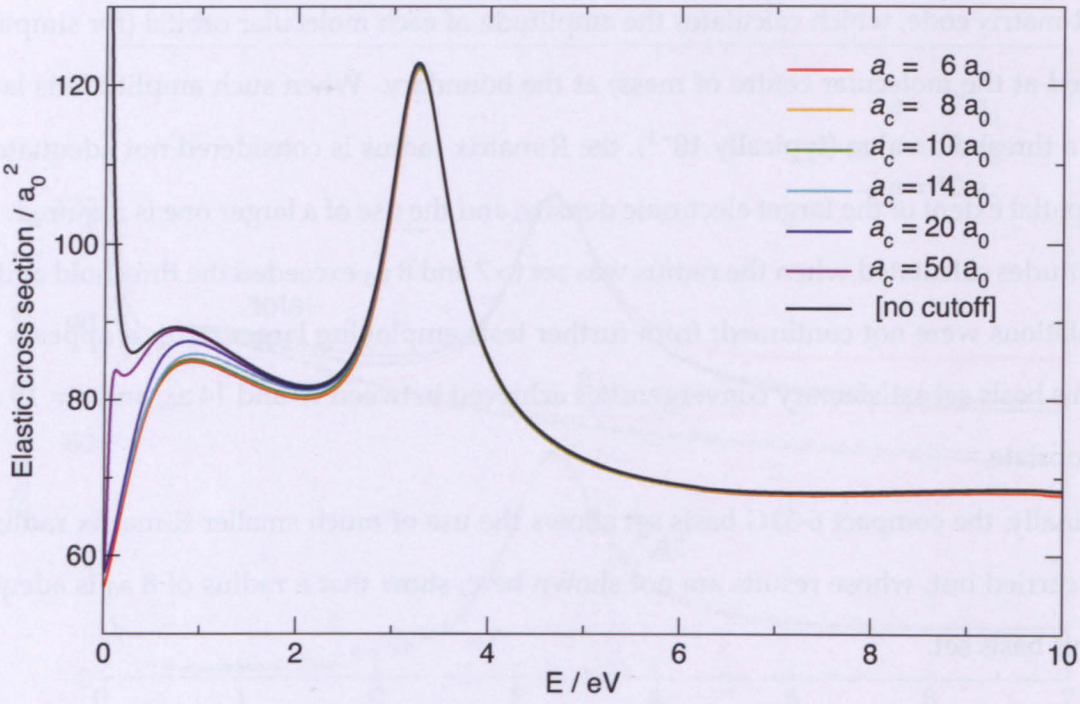

Figure 5.5: *Elastic cross section for the electron – HCOOH scattering, calculated using the 6-31G** basis set and $a = 10\ a_0$; the calculations were performed setting different values for a_c, as indicated in the figure.*

expansion.

The unexpected result is that in the formic acid case, unlike what it had been concluded from the tests on water, the cross sections calculated with different a_c values are remarkably similar. The cross section calculated setting $a_c = 50\ a_0$ differs the most from the others, displaying a slightly dipole-driven behaviour at very low energies, below 1 eV, where minor discrepancies may be also noted between the other cutoff cross sections. However, at energies over 1 eV, all cross sections look very similar, and above 3 eV the differences are in practice negligible. The effect of the inclusion of the dipole moment was also more evident at lower energies in the water case, but the discrepancies were relatively large in the whole energy range studied, and much more marked than here. We expected to observe a similar effect for HCOOH, since its dipole moment is not too different to that of water (1.41 D — Lide (1998) — and 1.855 D — Dyke & Muenter (1973) — respectively). On one hand, it should be pointed out that the propagation from a to a_c is an approximate way to remove or add the dipole interaction, especially for small scattering electron – target distances. However, the same approximate procedure had evident effects on the water cross sections. These results

seem to indicate that for the formic acid the inclusion of the dipole moment in the range [a_c – ∞) is not as significant as it was for water, except at very low energies.

As it is expected, the effect of a_c is even less marked in the Multiple Scattering calculations. The MS cross sections calculated with a_c spanning from 6 a_0 to ∞ differ at most by 0.1 % in the [1 – 10 eV] energy range. The parameter a_c seems therefore to have very little effect and we chose to set it to a, the R-matrix boundary radius, in all our Multiple Scattering calculations.

5.2.5 Results and comparison

Following the tests just described, the R-matrix calculations for HCOOH are performed as described below:

- **basis set**: all three basis sets (Dunning, 6-31G** and 6-31G);
- **max number of partial waves**: $l_{max} = 4$;
- **molecular orbitals**: HF-SCF;
- **CAS model**: CASCI, $(1a'—3a')^6$, $(4a'—12a',1a''—3a'')^{18}$;
- **number of states in the close-coupling expansion**: 5 ($1^1A'$, $2^1A'$, $1^3A'$, $1^1A''$, $1^3A''$);
- **R-matrix radius**: a = 10 a_0 (Dunning and 6-31G**), a = 8 a_0 (6-31G);
- **cutoff radius**: $a_c = a$ [for MS cutoff input].

Figure 5.6 shows the elastic cross sections for the e^- – HCOOH collision process. All our cross sections display a marked resonance of A'' symmetry, centred at 3.4 eV (Dunning), 3.3 eV (6-31G**) and 2.4 eV (6-31G). The symmetry of the resonance is in agreement with the calculations and experiments described in section 5.1, reporting a shape resonance associated with a transient negative ion, with the extra electron occupying a π^* orbital.

Analysing the *position of the resonance*, we can notice that most experimental and theoretical works find it at lower energies than in our results; in the figure, the experimental resonant energies of Allan (2006) and the theoretical ones of Bettega (2006), Rescigno et al. (2006) and Trevisan et al. (2006) are indicated by arrows; comparing with the other results listed in

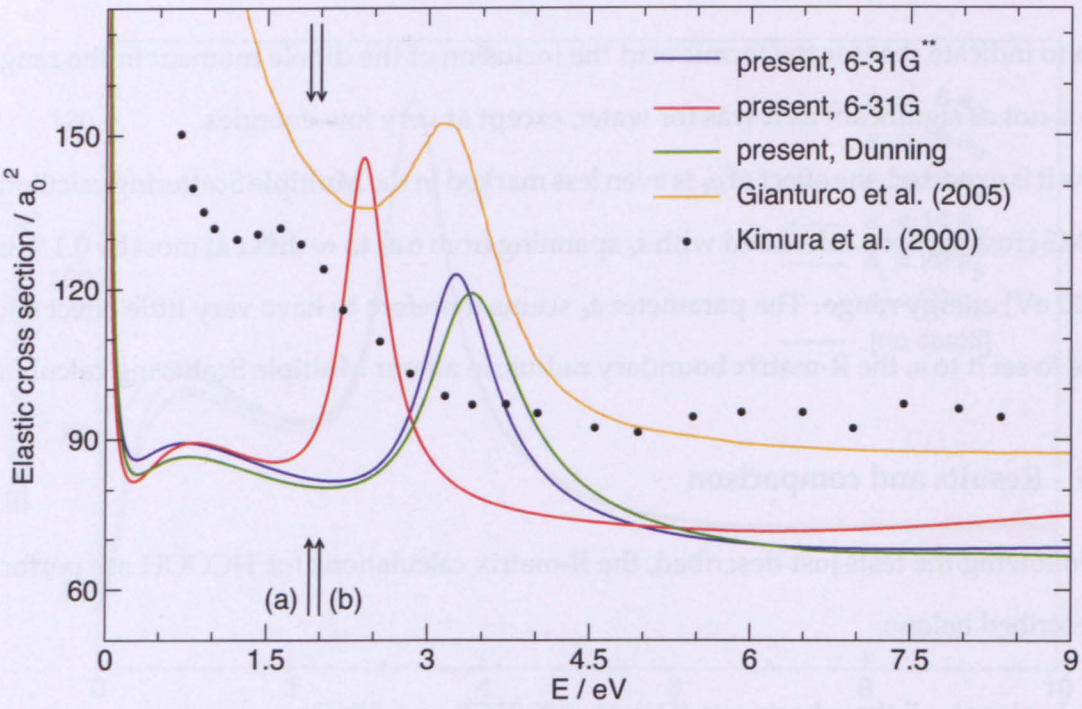

Figure 5.6: *Elastic cross section for the e^- – HCOOH collision, calculated with the R-matrix method as described above, employing different atomic orbital basis sets and R-matrix radii ($a = 10\ a_0$ with 6-31G** and Dunning, $a = 8\ a_0$ with 6-31G). These are the same results shown in figure 5.2. Comparison with earlier theoretical results of Gianturco et al. (2005) and experimental data from Kimura et al. (2000) is provided. Arrows indicate the position of the shape resonance as found by* (a) *Bettega (2006), Rescigno et al. (2006), Trevisan et al. (2006);* (b) *Allan (2006).*

table 5.1, and with the experimental cross section of Kimura et al. (2000),[2] it can be noticed that, with the exception of Gianturco & Lucchese (2004), the resonance is found at $E \leqslant 2$ eV. In this respect, the use of the more compact basis set 6-31G, displaying a peak at 2.4 eV, provides better results than the larger basis sets, even though the former one underestimates the dipole moment by 14 % and is characterised by higher HF and CI ground state energies.

Still analysing the position of the resonances, our cross sections employing larger basis sets are in very good agreement with those of Gianturco & Lucchese (2004): the resonant energies are very close, and also the width of the peaks are comparable. However, Gianturco & Lucchese (2004) were more interested in reproducing the resonant features, analysing the corresponding electron distributions, than in producing realistic elastic cross sections;

[2]Since the typical resolution in electron scattering experiments is of the order of 0.5 eV, much larger than the rotational spacings, the experimental elastic cross sections also include rotationally inelastic contributions.

their calculations greatly underestimate the polarisation effects, focussing mostly on the short range interactions. This can explain why our cross sections display the resonances at higher energies than most of the other experimental and theoretical studies: the values of the mean polarisabilities we obtain, reported in table 5.7, are at least two orders of magnitude lower than the experimental one (22.40 a_0^3, NIST Computational Chemistry Comparison and Benchmark DataBase 2010). It is however unclear why the 6-31G basis set, providing a polarisability not better than those calculated with the other basis sets, produces cross sections which are in better agreement with the experiments.

basis set	$\overline{\alpha}$ / a_0^3
Dunning	0.201
6-31G**	0.045
6-31G	0.061

Table 5.7: *Mean target polarisability, calculated using the three basis sets and including 5 states. The experimental value is 22.40 a_0^3 (NIST Computational Chemistry Comparison and Benchmark DataBase 2010).*

Before addressing the problem of the representation of the polarisability, it is worth noticing that, in absolute values, our cross sections are lower than those of Kimura et al. (2000) and Gianturco & Lucchese (2004) and the shapes also are fairly different, particularly below 3 eV. At low energies, our cross sections are quite flat down to ~ 0.5 eV, where they show a shallow dip and a sharp rise at very low energies. The dip is more marked when the 6-31G basis set is used, and it is due to the A' contribution to the total cross sections. Both cross sections of Kimura et al. (2000) and Gianturco & Lucchese (2004) are characterised by a constant increase as energy decreases, from approximately 4 and 5 eV respectively. Such discrepancy is likely to be due to the contributions from higher partial waves; in all our calculations, l_{max} = 4, while Gianturco & Lucchese (2004) include partial waves up to l_{max} = 16. The UK R-matrix suite does not allow to include partial waves higher than 5, but the contributions from higher ones can be included with a Born-type approximation (section 2.5.2). However, since our primary interest in this chapter is more to analyse the results provided by the Multiple Scattering method when applied to a system

displaying shape resonances, than to reproduce reliable cross sections that can be compared with experimental results, we decided not to make use of the Born-type approximation.

Representation of the polarisability

In the UK R-matrix suite, the polarisability is calculated as a sum over states:

$$\alpha_{v,w} = 2\sum_{n>0} \frac{\langle 0|\mu_v|n\rangle\langle n|\mu_w|0\rangle}{E_n - E_0}, \tag{5.1}$$

where v and w are cartesian components x, y, z, $|0\rangle$ is the state for which the polarisability is calculated (the ground state, in our case), $|n\rangle$ are electronic states included in the close-coupling expansion and $\mu_{v,w}$ the dipole operators. The way the polarisability is calculated in equation (5.1) implies that the more states are added in the close-coupling expansion, the more accurate the result. The failure to obtain reasonable values for the mean polarisability $\overline{\alpha} = \mathrm{tr}(\boldsymbol{\alpha})$ is partly due to the inclusion of a too few states (5, in all our calculations); we therefore studied how $\overline{\alpha}$ varies as a larger number of states is added. We expect that adding more states in the close coupling expansion will improve the description of the polarisability, but it is also known that the latter does not converge if Pseudo-Continuum Orbitals (PCOs) are not used (Gorfinkiel & Tennyson 2004). We therefore performed further calculations including PCOs; before describing these, we will analyse the results obtained without them, where the three basis sets employed so far were used in the CASCI model described above.

Figure 5.7 shows the values of the mean polarisability as functions of the number of states included in the close-coupling expansion. The results from calculations without PCOs clearly show that $\overline{\alpha}$ rises sharply when more states are added. Convergence is achieved, in all cases, when ~100 states are included: the values of the polarisability obtained employing the 6-31G and 6-31G** basis sets are very similar, converging to ~5.5 a_0, while the Dunning basis set (which fared best when 5 states only were included) converges at ~4 a_0; this is also somewhat surprising because the 6-31G** and Dunning basis sets are quite similar and the results obtained with them were always comparable. In general, however, all the basis sets fare very poorly, since they converge to less than a quarter of the experimental polarisability (22.04 a_0^3, NIST Computational Chemistry Comparison and Benchmark DataBase 2010).

In the attempt of improving the description of the polarisability, we introduced a set of pseudo-continuum orbitals (PCOs); the calculations were performed following the procedure first outlined by Gorfinkiel & Tennyson (2005): an extra basis set is added, centred on the centre of mass of the target, in order to represent states which cannot be described using only a basis set centred on the atomic nuclei. The use of PCOs has been found to improve greatly the description of the polarisability, in studies where smaller molecules than HCOOH were studied. The PCO basis set is constituted by even tempered GTOs (Schmidt & Ruedenberg 1979) where the exponents α_i are obtained as:

$$\alpha_i = \alpha_0 \beta^{i-1}, \quad i = 1, 2, ...L. \tag{5.2}$$

We started trying a PCO basis set (henceforth referred to as PCO_1), built with $\alpha_0 = 0.14$ and $\beta = 1.3$; the configurations were built "at Hartree Fock level", i.e. using only occupied MOs, plus the PCOs — $(G.S.)^N + (G.S.)^{N-1}(PCO)^1$. This model, much simpler than a CAS one, and generating a smaller number of configurations, has been found by Jones & Tennyson (2010)

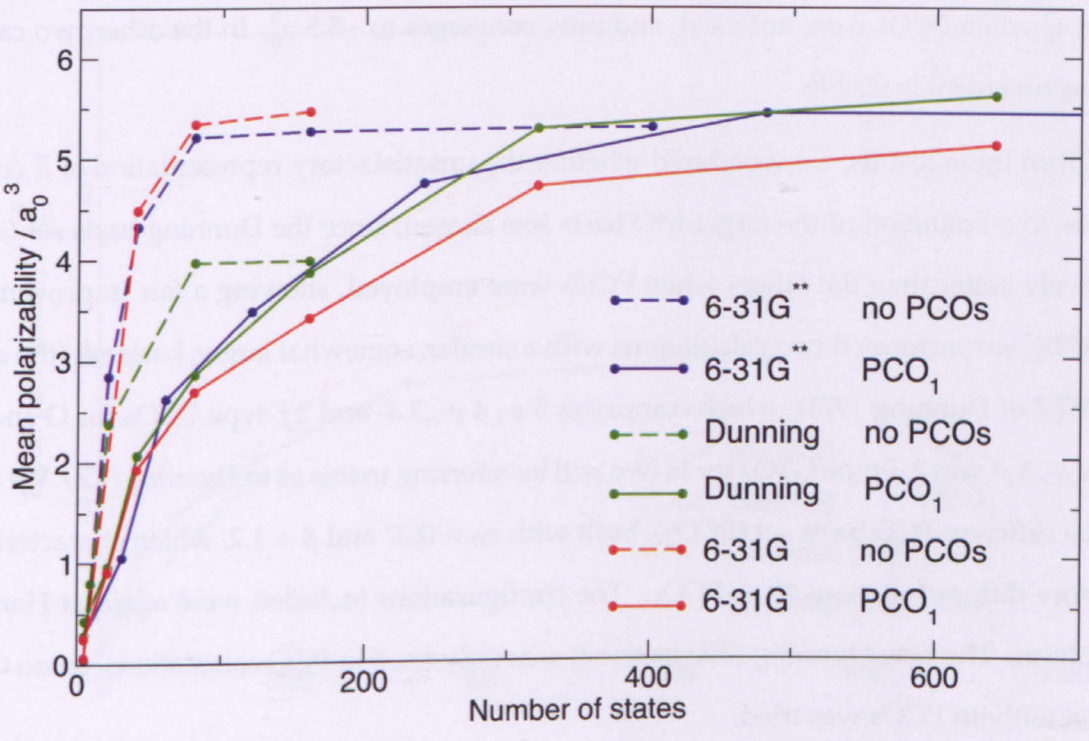

Figure 5.7: *Mean polarisability calculated with different models and basis sets, as a function of the number of states in the close-coupling expansion.*

to provide higher polarisabilities than corresponding CAS models, because the latter include correlation, which reduces the polarisability. The addition of PCOs, and the use of a Hartree Fock model, is then the best possible situation if one wants to increase the polarisability.

Figure 5.7 shows the results obtained for $\overline{\alpha}$ when PCO_1 basis set is used; these are rather disappointing. Firstly, we notice that the convergence of the polarisability is much slower: the polarisability calculated without PCOs converged when ~100 states were included in the close coupling expansion; if PCOs are introduced, $\overline{\alpha}$ is convergent at around 500 states. This is, in general, a great disadvantage: while target calculations can be performed in few hours even if hundreds of states are included, scattering calculations of equivalent accuracy would be in practice unfeasible. Secondly, and most importantly, the inclusion of the PCO basis set does not seem to improve at all the description of the polarisability: for all the MO basis sets shown, $\overline{\alpha}$ converges to approximately 5.5 a_0^3, which is again well below the experimental value. There are no major differences between the results obtained with different MO basis sets, although the 6-31G one provides lower polarisabilities than the others. The PCO basis improves the description of the polarisability for the Dunning basis set only, which converged to ~4 a_0^3 when PCOs were not used, and now converges to ~5.5 a_0^3. In the other two cases, no improvement is visible.

Given these results, we wondered whether the unsatisfactory representation of $\overline{\alpha}$ could be due to a limitation of the target MO basis sets chosen; since the Dunning basis set fared relatively better than the others when PCOs were employed, showing a fair improvement (~+37%), we performed two calculations with a similar, somewhat larger, basis set (the aug-cc-pVTZ of Dunning 1971), which comprises 5 *s*-, 4 *p*-, 3 *d*- and 2 *f*-type GTOs for O and C, and 4 *s*-, 3 *p*- and 2 *d*-type GTOs for H (we will be referring to this as to *Dunning (TZ)*. We also tried a different PCO basis set (PCO_2), built with $\alpha_0 = 0.07$ and $\beta = 1.2$, which characterised by more diffuse functions than PCO_1. The configurations included were again at Hartree Fock level. The new Dunning (TZ) basis set was only used in PCO calculations, so no CAS model without PCOs was tried.

A summary of the models is in table 5.8, while figure 5.8 shows the polarisabilities obtained with both Dunning and Dunning (TZ) MO basis sets, with both PCO basis sets.

name	PCO basis set			model	
	α_0	β	N		
no PCOs	—	—	0	$(CORE)^{n_c}$ $(CAS)^{n_a}$	$(1a'—3a')^6$ $(4a'—12a',1a''—3a'')^{18}$
PCO_1	0.14	1.3	64	$(G.S.)^N$	$(1a'—10a',1a''—2a'')^{24}$
				$(G.S.)^{N-1}$ $(PCO)^1$	$(1a'—10a',1a''—2a'')^{23}$ $(13a'—53a',4a''—26a'')^1$
PCO_2	0.07	1.2	85	$(G.S.)^N$	$(1a'—10a',1a''—2a'')^{24}$
				$(G.S.)^{N-1}$ $(PCO)^1$	$(1a'—10a',1a''—2a'')^{23}$ $(13a'—69a',4a''—31a'')^1$

Table 5.8: *Models employed for the calculation of the polarisability, with and without PCOs. N is the number of PCOs in the basis.*

Firstly, comparing PCO_1 and PCO_2, we conclude that the latter provides worse results, as the polarisabilities are lower than those obtained with the PCO_1 basis set, in both Dunning and Dunning (TZ) MO calculations. Other PCO basis sets have been tried, providing even worse results (not shown here); it seems that the PCO_1 basis set fares best among all the PCO bases tried.

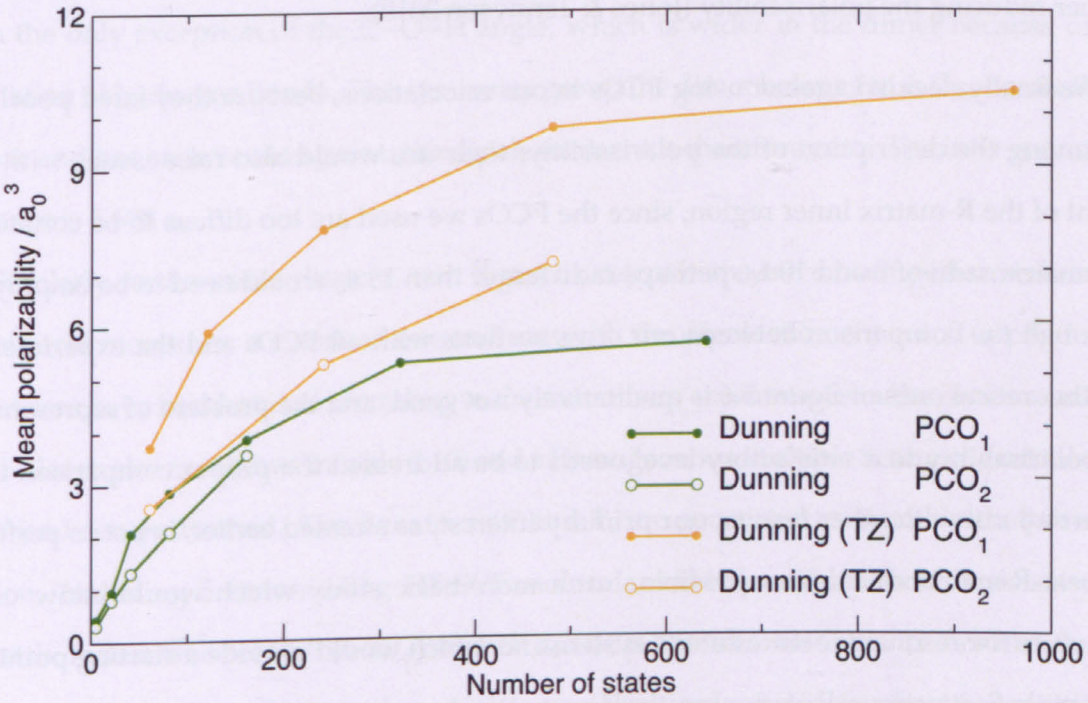

Figure 5.8: *Mean polarisability calculated with different models and basis sets, as a function of the number of states in the close-coupling expansion.*

Comparing the polarisabilities obtained with the Dunning and Dunning (TZ) basis sets, an improvement is noticeable when the latter one is used. On one hand, it can be concluded that the previous unsatisfactory results shown in figure 5.7 were partly due to the MO basis sets, as Jones & Tennyson (2010) also find that a large number of MOs is needed to obtain a good representation of the polarisability. However, the convergence of the polarisabilities provided by the Dunning (TZ) + PCO_1 basis sets is again very slow (more than 1000 states are needed); the final value is almost twice as large as the previous ones obtained (around 10.5 a_0^3, which is still less than half of the experimental value).

These tests seem to indicate that the PCO basis, which was successfully employed in studies on Li_2 (Tarana & Tennyson 2008), LiH, CO (Jones & Tennyson 2010), C_2, H_3^+ (Gorfinkiel & Tennyson 2004), H_2 (Gorfinkiel & Tennyson 2005), does not work so well for larger molecules, where it does not improve the description of the polarisability (a similar problem, for CH_3OH, was experienced by Baker 2010). This may be also due, as we already said, to the too limited number of MOs in our calculations. Attempts to introduce CAS models, in spite of the Hartree Fock level employed so far, had the effect of including correlation, further reducing the polarisability (Jones & Tennyson 2010).

We finally decided against using PCOs in our calculations, because they fared poorly at improving the description of the polarisability; their use would also raise issues with the extent of the R-matrix inner region, since the PCOs we used are too diffuse to be contained in R-matrix radii of 8 and 10 a_0; perhaps radii larger than 15 a_0 would need to be employed. Although the comparison between our cross sections without PCOs and the experimental and theoretical ones of figure 5.6 is qualitatively not good, and the problem of representing the polarisability to a satisfactory level needs to be addressed if a proper comparison is to be carried out with other results, our primary interest, as stressed earlier, is not to perform the best R-matrix calculation possible, but a more basic study which would allow us to reproduce the resonant features of the system and which would provide a starting point for a Multiple Scattering calculation on the dimer. We deem our results, which reproduce the resonance, accurate enough to verify whether the Multiple Scattering method is able to deal with shape resonances or not.

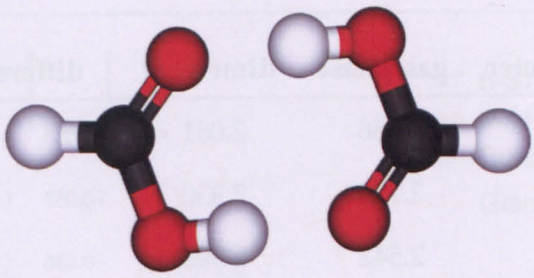

Figure 5.9: *Ball-and-stick model of* $(HCOOH)_2$ *in the equilibrium geometry* (trans–trans).

5.3 Formic acid dimer calculation

5.3.1 Geometry

The dimer geometry was taken from calculations at MP2 level using an aug-cc-pVDZ basis set (Chocholousova et al. 2002). The dimer is made up by 2 monomers in the *trans* configuration, establishing 2 hydrogen bonds which make this structure extremely stable, and is symmetric with respect to an inversion point (therefore the dipole moment is, by construction, zero). Some geometrical parameters are listed in table 5.9, where it is clear that the dimerised monomer geometry is not heavily distorted from that in the gas-phase, with the only exception of the $\widehat{C{-}O{-}H}$ angle, which is wider in the dimer because of the formation of hydrogen bonds. The symmetry group the dimer belongs to is C_{2h}, because it is planar and has an inversion point; the dipole moment is therefore zero. The inter-monomer distance is 5.698 a_0.

Similarly to the water clusters, two R-matrix calculations have been performed on the formic acid monomer: a standard one and one with the dipole moment cutoff applied. The T-matrices have been rotated according to the monomers' orientations in the dimer structure (the Euler angles are shown in table 5.10) and a homogeneous Multiple Scattering calculation has then been performed. The T-matrices $\boldsymbol{T}$ and $\boldsymbol{T}_c$ are generated as stated in the previous section: including 5 states, using HF-SCF molecular orbitals and all three basis sets; the R-matrix radius was set to 8 (6-31G) and 10 a_0 (6-31G** and Dunning). The radius for the dipole cutoff was set to $a_c = a$ (other values were also used, providing almost identical MS results).

The Multiple Scattering cross sections are particularly interesting and need an accurate

parameter	gas-phase	dimerised	difference	
C–H	2.066	2.081	+0.015	(+0.73%)
C=O	2.273	2.330	+0.057	(+2.49%)
C–O	2.542	2.506	−0.036	(−1.41%)
O–H	1.833	1.892	+0.059	(+3.20%)
$\widehat{O{=}C{-}H}$	125.30	122.09	−3.210	(−2.56%)
$\widehat{H{-}C{-}O}$	109.52	111.59	+2.070	(+1.89%)
$\widehat{O{=}C{-}O}$	125.19	126.32	+1.130	(+0.90%)
$\widehat{C{-}O{-}H}$	105.97	109.19	+3.220	(+3.04%)
inter-monomer distance		5.698		

Table 5.9: *Formic acid parameters, in the gas phase (from NIST Computational Chemistry Comparison and Benchmark DataBase (2010)) and in the dimer (from Chocholousova et al. (2002)). Lengths are in a_0 and angles in degrees. The difference between the parameters in the monomer and the dimer are also listed.*

monomer	α	β	γ
1	59.748	180.0	37.326
2	239.748	180.0	37.326

Table 5.10: *Euler angles employed for the $(HCOOH)_2$ Multiple Scattering calculation.*

analysis. In general, our results where larger basis sets (Dunning and 6-31G**) were used have a similar behaviour, as it was also observed in the monomer results of figure 5.6, while the cross sections for the more compact 6-31G basis set differ quite markedly from the other two. All these results are shown in figure 5.10, together with the theoretical cross sections of Gianturco et al. (2005).

We start analysing the cross sections calculated with the Dunning and 6-31G** basis sets. Partial waves up to 4 are included and the energy correction parameter is set to $\gamma = 0.75$, consistently with our water clusters calculations (an analysis of γ is presented later). The most significant features in the MS elastic cross sections are two peaks; the first, at 2.65 eV (6-31G**) and 2.75 eV (Dunning), corresponds in position and width to the first resonances into

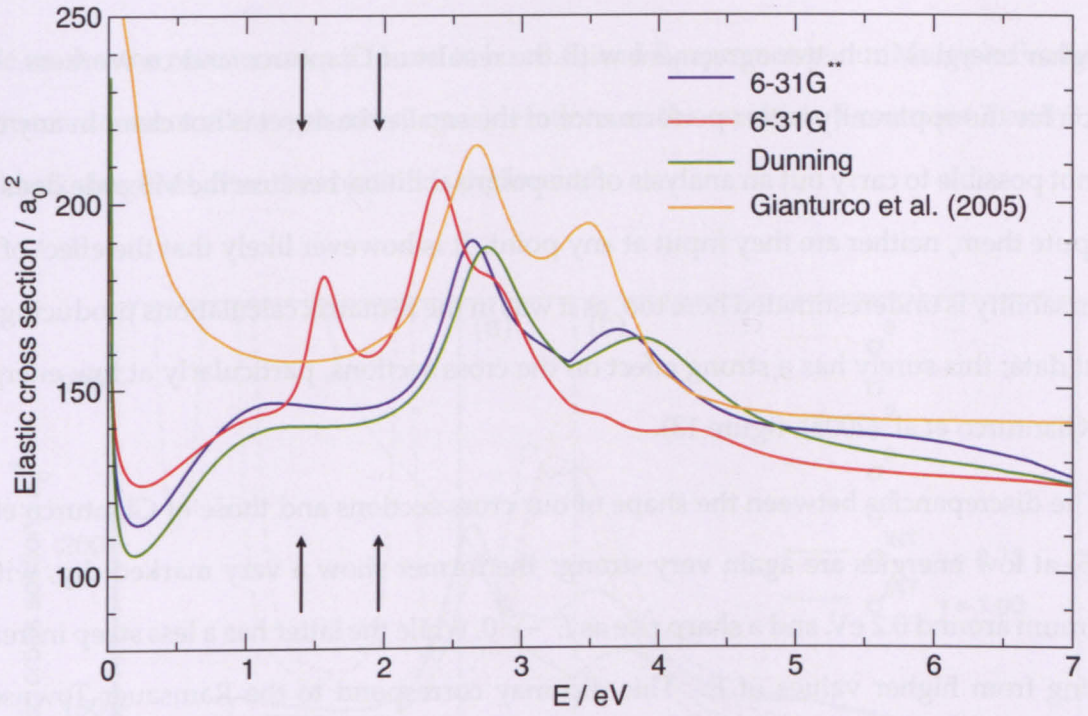

Figure 5.10: *Elastic cross section for the $e^- - (HCOOH)_2$ collision, calculated with the Multiple Scattering method, $\gamma = 0.75$; the monomer R-matrix calculations were performed using the three basis sets discussed earlier and setting $a = 8\,a_0$ (6-31G) and $10\,a_0$ (Dunning, 6-31G**); partial waves up to $l = 4$ were included and $a_c = a$. Comparison with Gianturco et al. (2005) is shown; the arrows indicate where the two shape resonances are found by Allan (2007).*

which the monomer A'' shape resonance is split into, according to Gianturco et al. (2005). The second peak they observe, around 3.5 eV, is narrower than ours, which are broader, characterised by a less defined shape, and displayed at higher energies.

The cross sections we obtain with the 6-31G basis set show a peak at 2.4 eV, with a shoulder at 2.8 eV, and a second peak at lower energy, centred at 1.6 eV. The position of these peaks, at lower energy than the corresponding 6-31G** and Dunning calculations, are in better agreement with the experimental results of Allan (2007), who finds them at 1.40 and 1.96 eV.

These initial observations are very similar to those we made when analysing the monomer results: particularly, the cross section calculated with the 6-31G basis set displays peaks at lower energies, in better agreement with the experimental and most of the theoretical results; those calculated with the 6-31G** and Dunning basis sets are characterised by resonances

at higher energies, in better agreement with the results of Gianturco and co-workers. The reason for the apparently better performance of the smaller basis set is not clear; in any case it is not possible to carry out an analysis of the polarisabilities, because the MS code does not compute them, neither are they input at any point. It is however likely that the effect of the polarisability is underestimated here too, as it was in the R-matrix calculations producing the input data; this surely has a strong effect on the cross sections, particularly at low energies (see Gianturco et al. (2005), figure 13).

The discrepancies between the shape of our cross sections and those of Gianturco et al. (2005) at low energies are again very strong: the former show a very marked dip, with a minimum around 0.2 eV, and a sharp rise as $E \rightarrow 0$, while the latter has a less steep increase, starting from higher values of E. This dip may correspond to the Ramsauer Townsend type minimum predicted by Gianturco et al. (2005) in the A_g component of the cross section (although theirs is at a lower energy, $\sim$ 0.1 eV, and too small to be noticeable in the total cross section), or may just be an artifact due to the incorrect account of the dipole moment effect at low energy, which we have already observed for the water clusters. The low energy behaviour of our MS cross sections, in fact, probably suffers from the same problems encountered when studying the water clusters, related to the construction of the cluster's overall dipole moment; in particular, considering that the formic acid dimer is non-polar, but made up by polar monomers, it is likely that the MS cross sections at low energies are not reliable, as we saw for the Z_1 and Z_2 geometries of $(H_2O)_2$, and for the *ppp* geometry of $(H_2O)_3$.

Finally, our cross sections are generally lower than those of Gianturco et al. (2005) in most of the energy range (apart from the resonant energies); this is again due to contributions from partial waves higher than $l_{max} = 4$, not included in the R-matrix calculations providing the input T-matrices.

Apart from these discrepancies, the features we are mostly interested in are the peaks shown by all our cross sections, approximately separated by 1 eV in all cases; a similar distance in energy is observed in the results by Gianturco et al. (2005), while the experimental resonances of Allan (2007), indicated by arrows in figure 5.10, are slightly closer. In both

these works, the resonances are found to be of A_u and B_g symmetry; our Multiple Scattering approach does not allow symmetry considerations as the resulting T-matrices $\boldsymbol{T}$ and $\boldsymbol{T}_c$ are not block-diagonal after the rotation is performed.

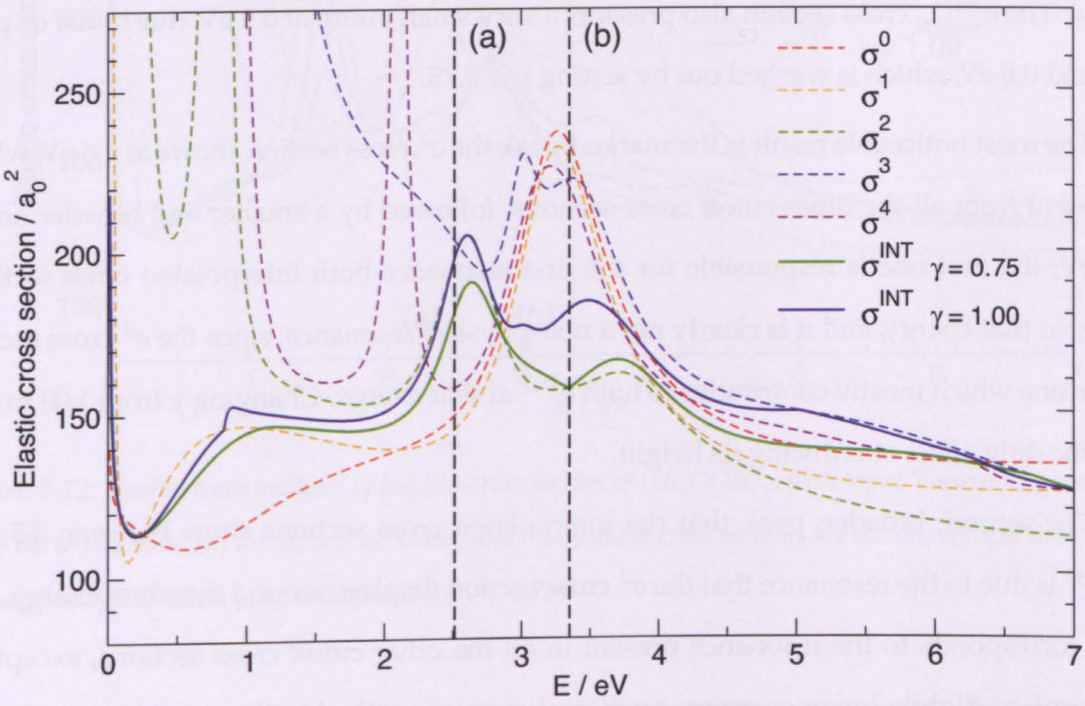

Figure 5.11: *Partial wave analysis of the MS cross section of* $(HCOOH)_2$*, with input T-matrices generated using the 6-31G** basis set,* $a = a_c = 10\ a_0$*. Cutoff and interpolated cross sections are shown; vertical lines mark the cutoff energies* E^2 *(at which* σ^3 *starts being included in* σ^{INT}*) resulting from setting* (a) $\gamma = 1.00$ *and* (b) $\gamma = 0.75$.

We analyse now how the partial wave contribution to $\boldsymbol{T}_c$ affects the Multiple Scattering cross sections. The cutoff cross sections in figure 5.11 have been calculated from T-matrices generated with an R-matrix calculation where $a = a_c = 10\ a_0$, and the 6-31G** basis set was employed. The conclusions drawn here are also valid for the Dunning basis set, which provides similar results. All the cutoff cross sections shown present marked resonances. The σ^0 and σ^1 cross sections, i.e. those including partial waves up to 0 and 1, present a peak at 3.3 eV, while σ^3 and σ^4 present a broader peak around the same energy, looking more like the convolution of two peaks in the σ^3 case. The tall peaks appearing at lower energies (2.1 eV in σ^4, for instance) are evidently due to the incorrect behaviour the high partial waves present

at low energy, as explained in section 3.2.1, and in fact do not contribute to the interpolated cross sections. The double peak of the σ^3 cutoff cross section is marginally included in $\sigma^{\mathrm{INT}}_{\gamma=1.00}$ (where a small bump appears at 3.0 eV), while it is not in $\sigma^{\mathrm{INT}}_{\gamma=0.75}$ because the energy E^2 (after which σ^3 starts contributing to σ^{INT}) is shifted to higher energy, as the vertical dotted lines show. The $\sigma^{\mathrm{INT}}_{\gamma=1.00}$ cross section also presents a very small bump at 0.9 eV, due to the σ^2 peak around 0.8 eV, which is washed out by setting $\gamma = 0.75$.

The most noticeable result is the marked peak the σ^2 cross section shows at 2.6 eV, which is absent from all the other cutoff cross sections, followed by a smaller and broader one at 3.8 eV; the first one is responsible for the first resonance both interpolated cross sections show at that energy, and it is clearly not a non-physical resonance, since the σ^2 cross section is the one which mostly contributes to both σ^{INT} at that energy. Changing γ from 1.00 to 0.75 has the only effect of reducing its height.

The second, broader, peak that the interpolated cross sections show between 3.5 and 3.7 eV is due to the resonance that the σ^3 cross section displays around the same energy, and also corresponds to the resonance present in all the other cutoff cross sections, except σ^2, although at slightly lower energies. Such peak is more marked in the $\gamma = 1.00$ interpolated cross section, because the threshold energy E^2 at which the σ^3 cross section starts being included is lower (2.51 eV when $\gamma = 1.00$, 3.35 eV when $\gamma = 0.75$, indicated in the figure by the vertical lines labelled (a) and (b)).

At very low energies, the minimum discussed before is present in both interpolated cross sections at 0.2 eV.

Comparing the two cross sections for different values of γ, we see that the one with $\gamma = 0.75$ is generally lower than the other, particularly between 2 and 6 eV; as noted above, this cross section does not show the small bumps at 0.9 and 3.0 eV and is generally smoother (for instance at 5 eV). The two peaks are shorter and broader than those in the $\gamma = 1.00$ cross section.

Analysing more closely the cutoff cross sections σ^i, one could wonder whether the peak at 2.6 eV in σ^2 (henceforth referred to as *resonance 1* or R_1) is due to the same resonance the other cross sections display at 3.3 eV (*resonance 2* or R_2), shifted by 0.7 eV, or to a different one

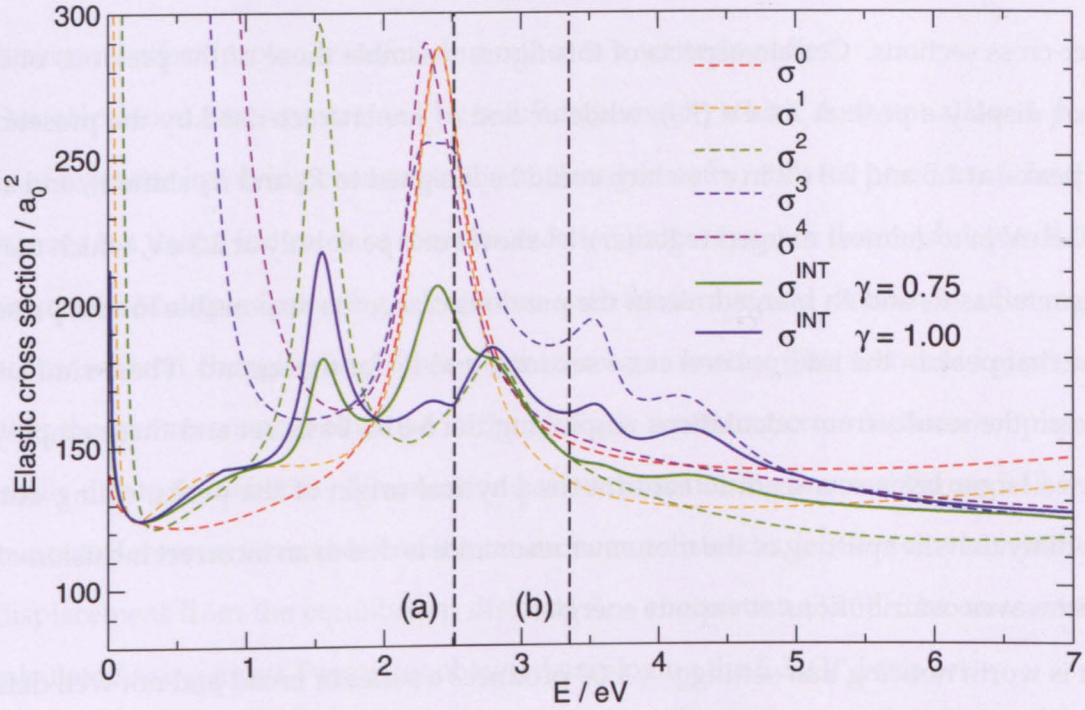

Figure 5.12: *Partial wave analysis of the MS cross section of* $(HCOOH)_2$*, with input T-matrices generated using the 6-31G basis set,* $a = a_c = 8\ a_0$*. Cutoff and interpolated cross sections are shown; vertical lines mark the cutoff energy* E^3 *when* (a) $\gamma = 1.00$ *and* (b) $\gamma = 0.75$.

(that is, whether R_1 and R_2 are the expression of the same resonance or not). In the former case, the interpolation, which produces two peaks, would mistakenly account twice for the same resonance appearing at different energies. On the other hand, at 2.6 eV the major contribution to σ^{INT} must come from σ^2, and it is impossible to remove the peak unless a very large value of γ is used (at least $\gamma = 1.7$), for which there would be no justification.

If R_1 and R_2 were two different resonances, we would however expect that all the cutoff cross sections including the resonant partial wave ($\sigma^l, l \geqslant 2$) would show a peak, so that two peaks would be present in σ^2, σ^3 and σ^4, to account for both R_1 and R_2. Actually, from a closer analysis of the cutoff partial waves, both σ^2 and σ^3 show two peaks, at 2.6 and 3.8 eV in σ^2, and at 3.0 and 3.4 eV in σ^3, which move closer as l increases and possibly merge in σ^4. We therefore conclude that the two peaks visible in the interpolated cross sections correspond to physical resonances.

Figure 5.12 shows the analogous plot resulting from the use of the 6-31G basis set, which presents resonances at lower energies than the other basis sets, both in the monomer and

dimer cross sections. Certain aspects of this figure resemble those of the previous one: σ^0 and σ^1 display a peak at 2.4 eV (R_2), while σ^2 and σ^3 are characterised by the presence of two peaks, at 1.5 and 2.8 eV in σ^2 (which could be assigned to R_1 and R_2 shifted), and at 2.4 and 2.5 eV in σ^3 (almost merged together); σ^4 shows one peak only at 2.3 eV, which may be interpreted as R_1 and R_2 merged. As in the previous case, σ^2 is responsible for the presence of the first peak in the interpolated cross sections, and σ^3 for the second. These similarities between the results from calculations employing the 6-31G basis set and those employing the two larger basis sets seem to confirm the physical origin of the peaks, ruling out the possibility that the splitting of the monomer resonance is due to an incorrect inclusion of the partial waves contributions at various energies.

It is worth noticing that setting $\gamma = 1.00$ produces a series of broad and not well defined peaks, mostly due to the behaviour of the σ^3 cross section at $E > 3.0$ eV; this effect is partly avoided by setting $\gamma = 0.75$, athough a shoulder is visible at 2.8 eV and the behaviour at $E > 3.0$ eV is still irregular. The choice of setting $\gamma = 0.75$ also affects the height and position of the two main resonances.

In general, the peak positions in the cross sections calculated with this basis set agree better with the experiments; unfortunately these cross sections have a less defined shape that seems to depend quite a bit on γ.

5.3.2 Study of the resonance positions as functions of the inter-monomer distance

The splitting of the formic acid monomer's A'' resonance into two dimer resonances is attributed to a spontaneous proton transfer initiated by the attachment of an electron (Bachorz et al. 2005), where the negatively charged formic acid acts as a strong base and attracts a proton via a barrier-free reaction (Dąbkowska, Rak, Gutowski, Nilles, Stokes & Bowen 2004, Dąbkowska, Rak, Gutowski, Nilles, Stokes, Radisic & Bowen 2004). The effect would justify the observed splitting of the O–H stretch frequency in energy loss experiments (Allan 2007). However, the fact that our MS calculations and those of Gianturco et al. (2005), both based on a Fixed Nuclei approximation, reproduce two resonances in the $(HCOOH)_2$ cross sections, indicates that the splitting of the monomer's resonance is not due

to a structural effect (proton transfer), but rather to a scattering effect.

Our calculations are constrained by a fixed geometry, which does not allow a proper study of reactions involving changes in the nuclear geometry; still, the position of the shape resonances is a useful indicator of complex reaction pathways. For this reason, we decided to run various Multiple Scattering calculations with the formic acid monomers at increasing distances, without changing any other geometrical parameter. This test could also clarify whether the two resonances obtained in the Multiple Scattering cross sections are physical, and really due to the effect the dimerisation has on the scattering process. Figure 5.13 shows various cutoff cross sections at different inter-monomer distances, labelled d, which indicates the displacement from the equilibrium distance $R_{1,2}$ of equation (3.26). The cross sections are calculated using input T-matrices obtained employing the 6-31G** basis set.

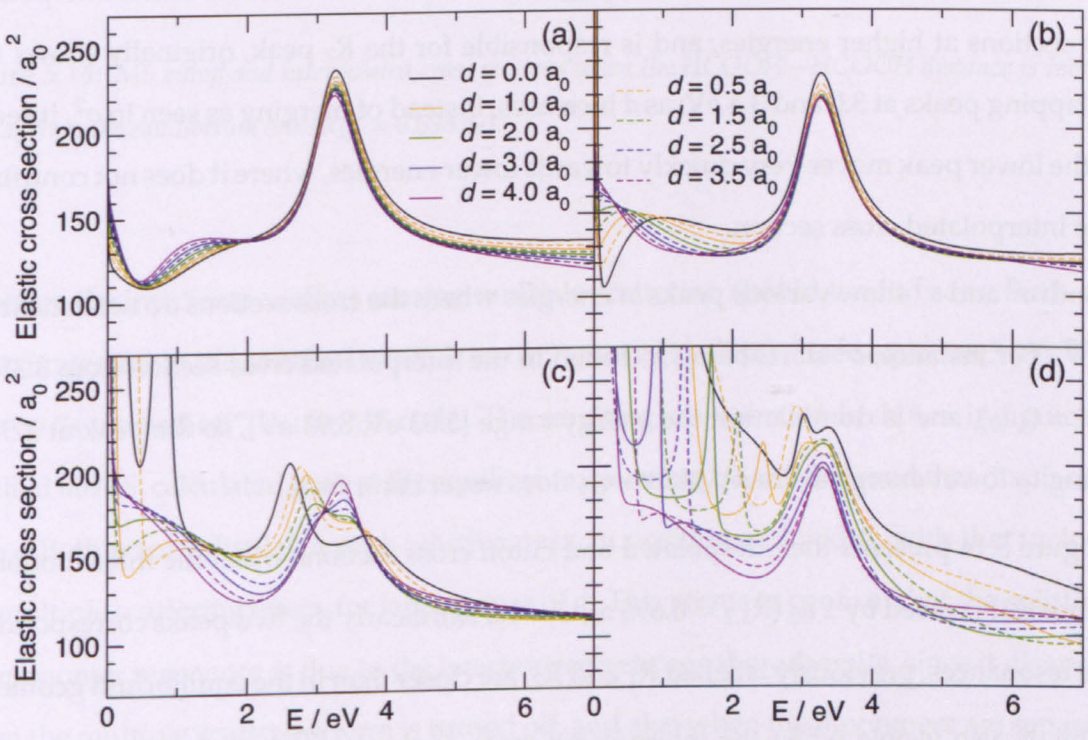

Figure 5.13: *Cutoff cross sections as functions of the inter-monomer distance, from the equilibrium one (R = 5.698 a_0, d = 0.0). Integer and half-integer displacements d are plotted. The different panels show different cutoff cross sections:* (a) σ^0, (b) σ^1, (c) σ^2, (d) σ^3. *The last cutoff cross section, σ^4, is not shown. These cross sections are calculated from R-matrix input employing the 6-31G** basis set.*

Figure 5.13a, displaying the σ^0 cutoff cross section, shows that the position of the peak

at 3.3 eV does not change when the distance between the monomers is increased; at low energies it is visible how the dip becomes more visible as d increases (although the MS results in this energy range are most likely not reliable); at higher energies the cross section tends to get smaller with increasing d.

The σ^1 cross section, depicted in figure 5.13b, displays a more limited variation at high energies, although the marked minimum at 0.2 eV disappears as d is increased.

The σ^2 cross section (figure 5.13c), which was responsible for the appearance of the first peak in the interpolated cross section at the equilibrium geometry, clearly shows the two peaks originally at 2.6 and 3.8 eV moving closer and completely merging at 3.35 eV when d = 4.0 a_0. Such behaviour causes the two resonances R_1 and R_2 in σ^{INT} to merge as the separation between monomers increases, as it will be discussed later.

Finally, the σ^3 cross section, shown in figure 5.13d, which contributes to the interpolated cross sections at higher energies, and is responsible for the R_2 peak, originally shows two overlapping peaks at 3.0 and 3.4 eV; as d increases, instead of merging as seen in σ^2, it seems that the lower peak moves very quickly towards lower energies, where it does not contribute to the interpolated cross section.

Both σ^2 and σ^3 show various peaks at energies where the cross sections do not contribute to σ^{INT}. For instance, σ^3 starts being included in the interpolated cross section from 3.35 eV (for d = 0 a_0), and is dominant in the energy range [5.03 eV, 8.93 eV], so the peak at 2.5 eV, moving to lower energies when d increases, does never contribute.

Figure 5.14 presents the interpolated and cutoff cross sections when the inter-monomer distance is increased by 1 a_0 ($R_{1,2}$ = 6.698 a_0, d = 1.0 a_0); clearly the two peaks corresponding to the resonances, previously labelled R_1 and R_2, are closer than in the equilibrium geometry.

This is also visible when the interpolated cross sections σ^{INT} (γ = 0.75), calculated at different values of the displacement coordinate d, are plotted together, as shown in figure 5.15. As d increases, i.e. as the monomers move apart, the two peaks observed at 2.6 and 3.7 eV move closer and finally merge at 3.3 eV (when d = 5.0 a_0). The two resonances may then be explained in terms of the splitting of the original shape resonance in the monomer as an effect of the dimerisation. As the monomers move apart, they become more isolated, and

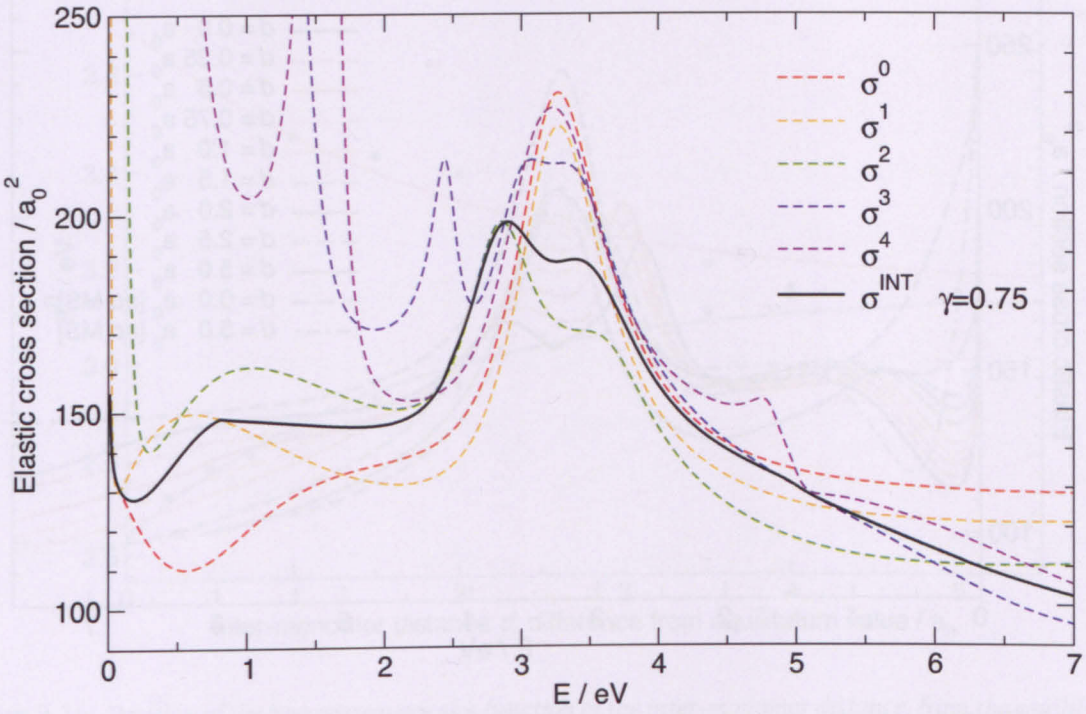

Figure 5.14: *MS cutoff and interpolated cross sections when the HCOOH—HCOOH distance is increased by 1 a_0 from the equilibrium one ($R_{1,2}$ = 6.698 a_0).*

therefore the interference effect causing multiple scattering should tend to zero. Such effect is accounted for in the so called *multiple scattering term* $(\mathbb{1} - \mathbb{X}\mathbb{T})^{-1}$ (see equation 3.25), which may be "switched off" in our MS code. The resulting cross section is shown in figure 5.15, labelled *no MS*, calculated both at the equilibrium geometry (d = 0.0 a_0) and that displaced by 5.0 a_0. Both results display a peak which agrees, in position and width, with that including the multiple scattering effect, for large values of d. This seems to confirm that the splitting of the monomer resonance is due to the interference between the sub-units, since it disappears when the multiple scattering term is turned off, and also when the monomers are separated.

Discrepancies between the cross section at d = 5 a_0 (with MS) and those without MS and are however visible, particularly at low energies. As the inter-monomer distance increases, the parameter $R_{1,2}$ in the interpolation procedure, which defines the cutoff energies E^i, increases as well, so that the cutoff energies decrease and the cross sections for larger displacements need partial waves higher than l = 4 to be included. This is shown in the figure

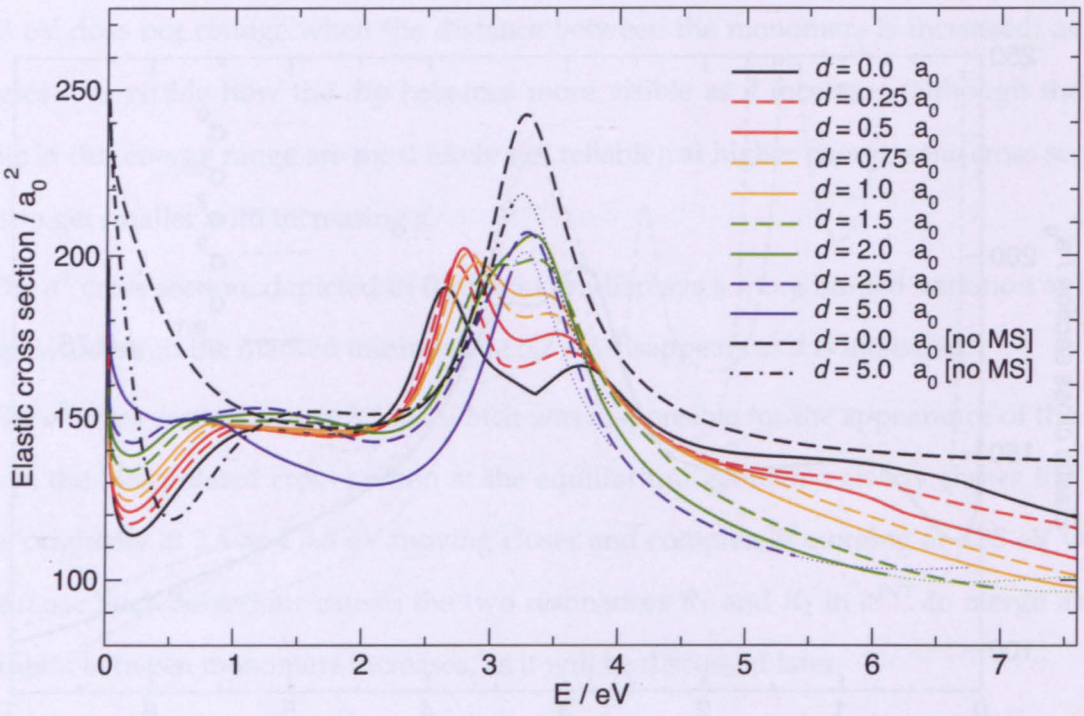

Figure 5.15: *MS interpolated cross section ($\gamma = 0.75$) as a function of the inter-monomer distance, from the equilibrium value ($R = 5.698\ a_0$, $d = 0.0\ a_0$) to that displaced by 5 a_0 ($d = 5.0\ a_0$). The cross sections where the multiple scattering term is switched off are shown at two values of d. When $\sigma^l, l > 4$ should start being included, the curves' thickness is reduced, and they are eventually discontinued when such partial waves' contribution becomes dominant.*

by reducing the width of the lines where partial wave $l = 5$ should start being included, and interrupting them when the contribution from higher partial waves is dominant.

At each value of the intermonomer distance, the MS elastic cross section with $\gamma = 0.75$ was analysed and the resonances were fitted to Lorentzian functions in order to determine their position and width. The resonance energies are plotted against the value of d in figure 5.16 and fitted with exponential functions of the form $E = c_1 + c_2 e^{c_3 d}$. The functions shown in figure fit better the resonances at lower values of d than at higher ones: at $d = 4\ a_0$ the difference between the resonant energies is about 0.5 eV, and they merge at $d = 5\ a_0$ (at an energy of ~ 3.2 eV), while the fitting functions seem to join at higer values of d.

In our tests, we also tried reducing the inter-monomer distance; for small displacements, $0 > d > -0.5\ a_0$, the cross sections do not vary considerably, displaying the two resonances slightly more spaced than for $d = 0$. When the distance is further reduced, the non-physical

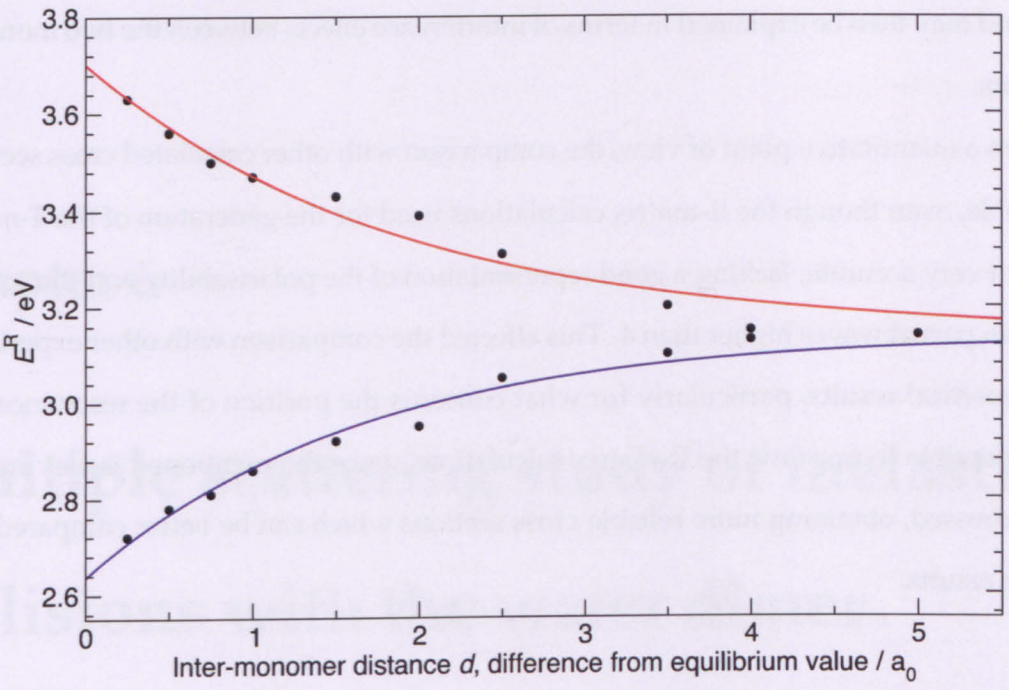

Figure 5.16: *Position of the two resonances as a function of the inter-monomer distance, from the equilibrium one ($R = 5.698\ a_0$, $d = 0.0\ a_0$) to that displaced by 5 a_0 ($d = 5.0\ a_0$). The fitting functions are exponential of the form $y = c_1 + c_2 e^{c_3 x}$.*

peaks characterising the cutoff cross sections at low energies (particularly those including the higher partial waves) move to higher energy, and get included in the interpolated cross section instead of being cut out. The latter hence displays several peaks of non-physical origin, which can no longer be eliminated by reducing γ. This effect can be explained considering that the electronic densities of the monomers overlap to such extent that the assumptions underpinning the Multiple Scattering approach are no longer valid.

5.4 Summary

The formic acid dimer was studied to verify whether the Multiple Scattering method is able to reproduce the presence of shape resonances; the features we aimed at reproducing were two shape resonances produced by the splitting of the monomer's A'' shape resonance because of dimerisation effects. The Multiple Scattering method succeeded at reproducing the two peaks; we also showed that these are merged when the formic acid monomers move

apart and may then be explained in terms of interference effects between the two monomeric sub-units.

From a quantitative point of view, the comparison with other calculated cross sections is acceptable, even though the R-matrix calculations used for the generation of the T-matrices were not very accurate, lacking a good representation of the polarisability and the contribution from partial waves higher than 4. This affected the comparison with other experimental and theoretical results, particularly for what concerns the position of the resonances. It is surely possible to improve the R-matrix calculations, once the mentioned issues are properly addressed, obtaining more reliable cross sections which can be better compared to the existing results.

Chapter 6

Multiple scattering study of inelastic collisions with the water dimer

The Multiple Scattering method has been adapted to treat electronically inelastic collisions; the theory, as described below, does not apply to every inelastic process, but relies on some assumptions that limit its validity to certain specific cases. The extension to a wider range of electronic excitation processes, not included in this treatment, may be undertaken by further modifying the theoretical approach; for the moment, however, we focus on verifying whether inelastic cross sections may be calculated within said limitations. It is understood that all the assumptions made for the elastic treatment (mainly, the non-overlap of the sub-units' potentials) still hold here.

We assume that, during the collision, only one excitation process may take place, i.e. one sub-unit undergoes electronic excitation while the others are limited to elastic scattering only; the case in which all the sub-units scatter elastically is also taken into account. This assumption drastically limits the cases that can be treated, since it rules out the possibility of studying excitations to states of the cluster which are located on more than one sub-unit. This is however unavoidable, given the general assumption the MS method is subject to, even in the elastic case, i.e. that the interaction potential of the cluster may be approximated as a linear combination of the potentials of the subunits. However, since clusters are not strongly bonded, it is not unreasonable to expect that the lowest excited states are strongly

localised on one sub-unit, and roughly correspond to a configuration where that sub-unit is in an excited state (has undergone electronic excitation), while the others only scatter elastically.

The theory developed, illustrated in the following section, has been applied to the inelastic scattering with the water dimer, and its results compared with R-matrix ones. From the comparisons it is clear that the results are not good and this work is still regarded as a work in progress.

6.1 Multiple Scattering inelastic treatment

In order to simplify the following treatment, we also assume that the sub-units forming the clusters may be divided into three ensembles, E, P and Q. Sub-units in E can only undergo elastic scattering, while sub-units in P and Q can be excited to states $|p\rangle$ and $|q\rangle$ respectively, at different energies. Here, by $|p\rangle$ and $|q\rangle$ we refer to *monomer states*. As explained above, in order to comply with the assumptions underpinning the multiple scattering theory, we can only consider excitations into cluster states that can be approximated as one monomer in an excited state and all the other monomers in the ground state (disregarding for the moment multiple excitations). We therefore define *cluster states* $|P\rangle$ and $|Q\rangle$ as:

$$|P\rangle = |0\ldots0\rangle_E|0\ldots p\ldots0\rangle_P|0\ldots0\rangle_Q; \tag{6.1}$$

$$|Q\rangle = |0\ldots0\rangle_E|0\ldots0\rangle_P|0\ldots q\ldots0\rangle_Q, \tag{6.2}$$

where the kets $|\,\rangle_E$, $|\,\rangle_P$ and $|\,\rangle_Q$ define the states of the monomers belonging to the E, P and Q ensembles respectively (including all the possible permutations). Given this definition, it follows that the energy needed to excite the cluster from the ground state to, for instance, $|P\rangle$ is equal to that needed to excite an isolated monomer belonging to the ensemble P to its excited state $|p\rangle$. However, when we study the electron collision with each monomer separately, in order to provide the collisional information needed by the MS code, it should be expected that the electronic density of the monomer states (and therefore their energies) is different when the molecule is isolated or clusterised. We refer to the effects caused by the presence of surrounding molecules on the electronic density as to *clusterisation effects*; these

are disregarded in the MS approach, but they can be partially accounted for, at least for what concerns the energy levels, by artificially shifting upwards or downwards the thresholds of the monomers' electronic states in order to match them to the cluster ones; this issue is addressed in section 6.1.8.

For the moment, let us assume that the threshold of the dimer state $|P\rangle$ is identical to that of the monomer state $|p\rangle$, and that the same holds for states $|Q\rangle$ and $|q\rangle$. At a certain scattering energy, here referred to as E_0, we define E_P and E_Q as:

$$E_{P,Q} = E_0 - \Delta E_{P,Q}, \tag{6.3}$$

where ΔE_C is the threshold energy at which channel C opens for the cluster and E_C is the energy available after the excitation of one sub-unit has taken place. Let us also assume that the thresholds ΔE_P and ΔE_Q are related as in figure (6.1), i.e. $\Delta E_P < \Delta E_Q$.

We now divide the collision problem into three energy ranges: (1) when $E_0 < \Delta E_P$ (elastic scattering only); (2) when $\Delta E_P < E_0 < \Delta E_Q$ (sub-units belonging to P may undergo inelastic scattering — not simultaneously); (3) when $E_0 > \Delta E_Q$ (sub-units belonging to P and Q may undergo inelastic scattering — again, not simultaneously). The first case has been already studied in the previous section, whose conclusion can be written mathematically as:

$$\boldsymbol{T}^{\mathrm{G}} = \mathbb{N}\mathbb{T}\left(\mathbb{1} - \mathbb{X}\mathbb{T}\right)^{-1}\mathbb{M}. \tag{6.4}$$

In order to obtain such equation, we derived an expression for the vector amplitudes $\boldsymbol{g}^n$ of equation (3.8), collectively written $\mathbb{G}$: $\mathbb{G} = \left(\mathbb{1} - \mathbb{X}\mathbb{T}\right)^{-1}\widehat{\mathbb{G}}$.

In the second case, when the impinging electron energy E_0 satisfies the relation $\Delta E_P < E_0 < \Delta E_Q$, the sub-units belonging to the ensemble P can undergo inelastic scattering. Recalling the definition of cluster state $|P\rangle$ as in equation (6.1), the asymptotic wavefunction $\psi(\boldsymbol{r})$, relative to the scattering of an electron off the whole cluster, may be written as:

$$\psi(\boldsymbol{r}) = \sum_{L,L'} Y_{L'}(\hat{\boldsymbol{r}})\left[j_{l'}(k_0 r)\delta_{L,L'} + \frac{1}{2}h^+_{l'}(k_0 r)T^{\mathrm{G,EL}}_{L',L} + \frac{1}{2}h^+_{l'}(k_P r)T^{\mathrm{G},P}_{L',L}\right]\widehat{f_L}, \tag{6.5}$$

where both $\boldsymbol{T}^{\mathrm{G,EL}}$ and $\boldsymbol{T}^{\mathrm{G},P}$ are *global* T-matrices (elastic and inelastic respectively), i.e. they refer to the cluster as a whole. The first term in brackets describes the plane wave representing the incoming electron; the second and third terms account for the wavefunction of the

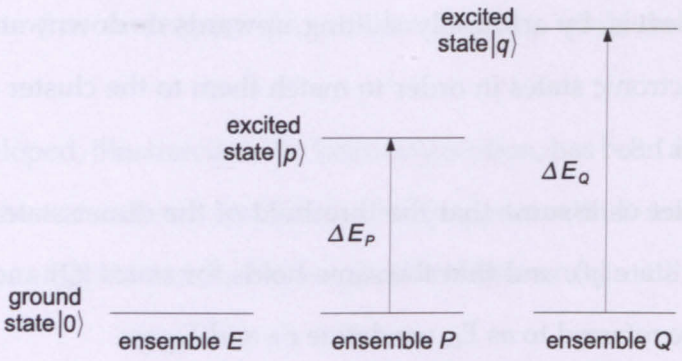

Figure 6.1: *Schematic representation of the electronic states of the sub-units forming a cluster, which are available to excitation. Higher electronic states are not shown.*

electron scattered elastically with energy E_0 ($k_0 = \sqrt{E_0}$) and inelastically with energy E_P from equation (6.3) ($k_P = \sqrt{E_P}$).

We can now follow the steps introduced in the elastic treatment: firstly we write the incoming wavefunction on each sub-unit, as a function of quantities g; then we calculate the wavefunction scattered from each, which will be summed together in order to obtain the total incoming wave on each sub-unit. This allows to express g in terms of the known amplitudes $\widehat{g}$. Finally, the total scattered wavefunction is matched with equation (6.5) and the global T-matrices $\boldsymbol{T}^{\mathrm{G,EL}}$ and $\boldsymbol{T}^{\mathrm{G},P}$ are obtained.

6.1.1 Step [1]: incoming wavefunction on each monomer

The re-expansion of the incoming plane wave, as described in equation (3.5), is still valid here; however, the total incoming wave on each scatterer, previously written as in equation (3.8), needs now to be changed to:

$$\psi_{\mathrm{in},n}(\boldsymbol{r}_n) = \sum_{L_1} Y_{L_1}(\hat{r}_n)\left[j_{l_1}(k_0 r_n)\ \overset{(0)}{g}{}^{n}_{L_1} + j_{l_1}(k_P r_n)\ \overset{(P)}{g}{}^{n}_{L_1}\right], \tag{6.6}$$

in order to account for the possibility of having scattered functions of energy E_P.

6.1.2 Step [2]: wavefunction scattered from each monomer

At this point, a distinction needs to be made: sub-units belonging to ensembles E and Q can only scatter elastically, while sub-units belonging to P can scatter inelastically the wavefunction with energy E_0 (since we are still analysing the case $\Delta E_P < E_0 < \Delta E_Q$). No inelastic scattering of the wavefunction with energy E_P is allowed because of the initial assumption that the cluster may undergo one inelastic process only; such wavefunction in fact has already been scattered inelastically (losing part of its energy).

Then:

$$\psi_{sc,n\in P}(\boldsymbol{r}_n) = \frac{1}{2}\sum_{L,L'} Y_{L'}(\hat{r}_n)\ \left[\left(h^+_{l'}(k_0 r_n)\ \overset{00}{T}{}^n_{L',L}(E_0) + h^+_{l'}(k_P r_n)\ \overset{0p}{T}{}^n_{L',L}(E_0)\right)\overset{(0)}{g}{}^n_L + \right.$$
$$\left. + \left(h^+_{l'}(k_P r_n)\ \overset{00}{T}{}^n_{L',L}(E_P)\right)\overset{(P)}{g}{}^n_L\right]; \tag{6.7a}$$

$$\psi_{sc,n\notin P}(\boldsymbol{r}_n) = \frac{1}{2}\sum_{L,L'} Y_{L'}(\hat{r}_n)\ \left[\left(h^+_{l'}(k_0 r_n)\ \overset{00}{T}{}^n_{L',L}(E_0)\right)\overset{(0)}{g}{}^n_L + \left(h^+_{l'}(k_P r_n)\ \overset{00}{T}{}^n_{L',L}(E_P)\right)\overset{(P)}{g}{}^n_L\right]. \tag{6.7b}$$

In the last two equations, matrices $\overset{00}{T}{}^n(E_C)$ and $\overset{0p}{T}{}^n(E_C)$ are the elastic and inelastic T-matrices of sub-units n, calculated at the scattering electron energy E_C. The two terms in the first brackets of equation (6.7a) describe the response of sub-units belonging to ensemble P to the incoming wavefunction having energy E_0: the first accounts for the elastic scattering (the scattered wave is still characterised by energy E_0), while the second accounts for the inelastic scattering (outgoing wave of energy E_P), following the excitation of sub-unit n from the ground state $|0\rangle$ to state $|p\rangle$. The second brackets contain the term describing the elastic scattering of the wavefunction of energy E_P (which has already undergone an inelastic scattering). Equation (6.7b) is similar but does not contain the inelastic term.

Both equations can now be re-expanded around n', which stands for a generic sub-unit,

different from n:

$$\psi_{\mathrm{sc},n\in P}(\boldsymbol{r}_{n'}) = \sum_{L,L',L_1} Y_{L_1}(\hat{r}_{n'}) \left[\left(j_{l_1}(k_0 r_{n'}) \overset{(0)}{X}{}^{n',n}_{L_1,L'} \overset{00}{T}{}^{n}_{L',L}(E_0) + j_{l_1}(k_P r_{n'}) \overset{(P)}{X}{}^{n',n}_{L_1,L'} \overset{0p}{T}{}^{n}_{L',L}(E_0)\right) \overset{(0)}{g}{}^{n}_{L} + \right.$$
$$\left. + \left(j_{l_1}(k_P r_{n'}) \overset{(P)}{X}{}^{n',n}_{L_1,L'} \overset{00}{T}{}^{n}_{L',L}(E_P)\right) \overset{(P)}{g}{}^{n}_{L}\right]; \tag{6.8a}$$

$$\psi_{\mathrm{sc},n\notin P}(\boldsymbol{r}_{n'}) = \sum_{L,L',L_1} Y_{L_1}(\hat{r}_{n'}) \left[\left(j_{l_1}(k_0 r_{n'}) \overset{(0)}{X}{}^{n',n}_{L_1,L'} \overset{00}{T}{}^{n}_{L',L}(E_0)\right) \overset{(0)}{g}{}^{n}_{L} + \right.$$
$$\left. + \left(j_{l_1}(k_P r_{n'}) \overset{(P)}{X}{}^{n',n}_{L_1,L'} \overset{00}{T}{}^{n}_{L',L}(E_P)\right) \overset{(P)}{g}{}^{n}_{L}\right], \tag{6.8b}$$

where matrices $\overset{(0)}{X}{}^{n',n}$ and $\overset{(P)}{X}{}^{n',n}$ are consistent with definition (3.11):

$$\overset{(C)}{X}{}^{n',n}_{L_2,L'} \equiv \frac{1}{2} \sum_{L_1} \mathrm{i}^{l_1+l_2-l'} (-)^{m'} F^{l_1,l_2,l'}_{m_1,m_2,-m'} Y_{L_1}(\hat{R}_{n',n}) h^{+}_{l_1}(k_C R_{n',n}),\ C = \{0, P\}. \tag{6.9}$$

6.1.3 Step [3]: total incoming wavefunction and derivation of g

The total incoming wavefunction on each scatterer can be derived as follows:

$$\psi_{\mathrm{in},n\in P}(\boldsymbol{r}_n) = \psi_{\mathrm{in,PW}}(\boldsymbol{r}_n) + \sum_{\substack{n'\neq n \\ n'\in P}} \psi_{\mathrm{sc},n'}(\boldsymbol{r}_n) + \sum_{n''\notin P} \psi_{\mathrm{sc},n''}(\boldsymbol{r}_n); \tag{6.10a}$$

$$\psi_{\mathrm{in},n\notin P}(\boldsymbol{r}_n) = \psi_{\mathrm{in,PW}}(\boldsymbol{r}_n) + \sum_{n'\in P} \psi_{\mathrm{sc},n'}(\boldsymbol{r}_n) + \sum_{\substack{n''\neq n \\ n''\notin P}} \psi_{\mathrm{sc},n''}(\boldsymbol{r}_n), \tag{6.10b}$$

obtaining:

$$\psi_{\mathrm{in},n\in P}(\boldsymbol{r}_n) = \sum_{L_1} Y_{L_1}(\boldsymbol{r}_n) \left[j_{l_1}(k_0 r_n) \left(\widetilde{g}^{n}_{L_1} + \sum_{\substack{n'\neq n \\ n'\in P}} \sum_{L,L'} \overset{(0)}{X}{}^{n,n'}_{L_1,L'} \overset{00}{T}{}^{n'}_{L',L}(E_0) \overset{(0)}{g}{}^{n'}_{L} + \sum_{n''\notin P} \sum_{L,L'} \overset{(0)}{X}{}^{n,n''}_{L_1,L'} \overset{00}{T}{}^{n''}_{L',L}(E_0) \overset{(0)}{g}{}^{n''}_{L} \right) + \right.$$
$$+ j_{l_1}(k_P r_n) \left(\sum_{\substack{n'\neq n \\ n'\in P}} \sum_{L,L'} \overset{(P)}{X}{}^{n,n'}_{L_1,L'} \overset{00}{T}{}^{n'}_{L',L}(E_P) \overset{(P)}{g}{}^{n'}_{L} + \sum_{n''\notin P} \sum_{L,L'} \overset{(P)}{X}{}^{n,n''}_{L_1,L'} \overset{00}{T}{}^{n''}_{L',L}(E_P) \overset{(P)}{g}{}^{n''}_{L} \right) +$$
$$\left. + j_{l_1}(k_P r_n) \left(\sum_{\substack{n'\neq n \\ n'\in P}} \sum_{L,L'} \overset{(P)}{X}{}^{n,n'}_{L_1,L'} \overset{0p}{T}{}^{n'}_{L',L}(E_0) \overset{(0)}{g}{}^{n'}_{L} \right) \right]. \tag{6.11}$$

In this equation, the first line accounts for the terms with energy E_0, which include the plane wave and the waves scattered elastically; the expressions for sub-units $n' \in P$ and that for the $n'' \notin P$ are identical, and the only sub-unit left out is n itself, which does not self-scatter. However, taking advantage of the property of matrices $\boldsymbol{X}^{n,n'}$ ($\boldsymbol{X}^{n,n} = \boldsymbol{0}$), sub-unit

n can be formally introduced in the summation, so that the first line of equation (6.11) may be rewritten as:

$$j_{l_1}(k_0 r_n)\left(\widehat{g}^n_{L_1} + \sum_{n'}\sum_{L,L'} \overset{(0)}{X}{}^{n,n'}_{L_1,L'}\ \overset{00}{T}{}^{n'}_{L',L}(E_0)\ \overset{(0)}{g}{}^{n'}_{L}\right). \tag{6.12}$$

The same may be done on the second line, which accounts for the elastic scattering of waves having energy E_p; it may then be rewritten as:

$$j_{l_1}(k_P r_n)\left(\sum_{n'}\sum_{L,L'} \overset{(P)}{X}{}^{n,n'}_{L_1,L'}\ \overset{00}{T}{}^{n'}_{L',L}(E_P)\ \overset{(P)}{g}{}^{n'}_{L}\right). \tag{6.13}$$

The third line of equation (6.11) accounts for the inelastic scattering of the wave with energy E_0, which is performed by sub-units in ensemble P only and depends on the monomers' inelastic T-matrices $\overset{0p}{T}{}^{n'}(E_0)$. Such matrices are not defined for sub-units $n'' \notin P$, but we may easily extend the definition assuming that $\overset{0p}{T}{}^{n''}(E_0) = \mathbf{0}, n'' \notin P$. With such assumption, the third line too may be formally written as a sum over all the sub-units:

$$j_{l_1}(k_P r_n)\left(\sum_{n'}\sum_{L,L'} \overset{(P)}{X}{}^{n,n'}_{L_1,L'}\ \overset{0p}{T}{}^{n'}_{L',L}(E_0)\ \overset{(0)}{g}{}^{n'}_{L}\right). \tag{6.14}$$

Finally, writing the equation equivalent to (6.11), for sub-units $n \notin P$, and making the same assumptions as above, we obtain an identical result, so that it is possible to write, for all sub-units:

$$\begin{aligned}\psi_{\mathrm{in},n}(\boldsymbol{r}_n) = \sum_{L_1} Y_{L_1}(\hat{r}_n)\ \Bigg[& j_{l_1}(k_0 r_n)\left(\widehat{g}^n_{L_1} + \sum_{n'}\sum_{L,L'} \overset{(0)}{X}{}^{n,n'}_{L_1,L'}\ \overset{00}{T}{}^{n'}_{L',L}(E_0)\ \overset{(0)}{g}{}^{n'}_{L}\right) + \\ & + j_{l_1}(k_P r_n) \sum_{n'}\sum_{L,L'} \overset{(P)}{X}{}^{n,n'}_{L_1,L'}\left(\overset{00}{T}{}^{n'}_{L',L}(E_P)\ \overset{(P)}{g}{}^{n'}_{L} + \overset{0p}{T}{}^{n'}_{L',L}(E_0)\ \overset{(0)}{g}{}^{n'}_{L}\right)\Bigg]. \end{aligned} \tag{6.15}$$

Comparing this result with equation(6.6) and defining vectors $\overset{(0)}{\mathbb{G}}$ and $\overset{(P)}{\mathbb{G}}$ consistently with definition (3.15), it is now possible to write:

$$\overset{(0)}{\mathbb{G}} = \widehat{\mathbb{G}} + \overset{(0)00}{\mathbb{XT}}(E_0)\ \overset{(0)}{\mathbb{G}}; \tag{6.16a}$$

$$\overset{(P)}{\mathbb{G}} = \overset{(P)00}{\mathbb{XT}}(E_P)\ \overset{(P)}{\mathbb{G}} + \overset{(P)0p}{\mathbb{XT}}(E_0)\ \overset{(0)}{\mathbb{G}}, \tag{6.16b}$$

which can be solved to obtain:

$$\overset{(0)}{\mathbb{G}} = \left(\mathbb{1} - \overset{(0)00}{\mathbb{XT}}(E_0)\right)^{-1} \widehat{\mathbb{G}}; \tag{6.17a}$$

$$\overset{(P)}{\mathbb{G}} = \left(\mathbb{1} - \overset{(P)00}{\mathbb{XT}}(E_P)\right)^{-1} \overset{(P)0p}{\mathbb{XT}}(E_0)\left(\mathbb{1} - \overset{(0)00}{\mathbb{XT}}(E_0)\right)^{-1} \widehat{\mathbb{G}}. \tag{6.17b}$$

It is important to notice that expression (6.17a), accounting for the elastic scattering, is identical to that obtained in the elastic treatment (equation 3.18).

6.1.4 Step [4]: total scattered wavefunction

Now that vectors $\overset{(0)}{\mathbb{G}}$ and $\overset{(P)}{\mathbb{G}}$ are known, equations (6.7a) and (6.7b) may be used to express the scattered wavefunction from each monomer. Summing the contributions from all the sub-units, and re-expanding them around $\boldsymbol{r}$, it is possible to obtain an expression for the total scattered wavefunction, which will be later compared to equation (6.5).

$$\psi_{sc,n\in P}(\boldsymbol{r}) = \frac{1}{2}\sum_{L,L',L_1} Y_{L_1}(\hat{r}) \left[h_{l_1}^{+}(k_0 r)\, \overset{(0)}{N}{}^{n}_{L_1,L'}\, \overset{00}{T}{}^{n}_{L',L}(E_0)\, \overset{(0)}{g}{}^{n}_{L} + \right.$$
$$\left. + h_{l_1}^{+}(k_P r) \left(\overset{(P)}{N}{}^{n}_{L_1,L'}\, \overset{0p}{T}{}^{n}_{L',L}(E_0)\, \overset{(0)}{g}{}^{n}_{L} + \overset{(P)}{N}{}^{n}_{L_1,L'}\, \overset{00}{T}{}^{n}_{L',L}(E_P)\, \overset{(P)}{g}{}^{n}_{L} \right) \right] \quad (6.18a)$$

$$\psi_{sc,n\notin P}(\boldsymbol{r}) = \frac{1}{2}\sum_{L,L',L_1} Y_{L_1}(\hat{r}) \left[h_{l_1}^{+}(k_0 r)\, \overset{(0)}{N}{}^{n}_{L_1,L'}\, \overset{00}{T}{}^{n}_{L',L}(E_0)\, \overset{(0)}{g}{}^{n}_{L} + \right.$$
$$\left. + h_{l_1}^{+}(k_P r)\, \overset{(P)}{N}{}^{n}_{L_1,L'}\, \overset{00}{T}{}^{n}_{L',L}(E_P)\, \overset{(P)}{g}{}^{n}_{L} \right], \quad (6.18b)$$

where matrices $\overset{(0)}{\boldsymbol{N}}{}^{n}$ and $\overset{(P)}{\boldsymbol{N}}{}^{n}$ are consistent with definition (3.20):

$$\overset{(C)}{N}{}^{n}_{L_1,L'} \equiv \sum_{L_1} \mathrm{i}^{l_1+l_2-l'}(-)^{m'} F^{l_1,l_2,l'}_{m_1,m_2,-m'} Y_{L_2}(-\hat{R}_n) j_{l_2}(k_C R_n),\ C = \{0, P\}. \quad (6.19)$$

Again, from our previous extension of inelastic T-matrices ($\overset{0p}{\boldsymbol{T}}{}^{n''}(E_0) = \boldsymbol{0}, n'' \notin P$), the missing term $h_{l_1}^{+}(k_P r)\, \overset{(P)}{N}{}^{n}_{L_1,L'}\, \overset{0p}{T}{}^{n}_{L',L}(E_0)\, \overset{(0)}{g}{}^{n}_{L}$ (which is zero for $n \notin P$) can be added to equation (6.18b), so that the same equation can be written to express the wave scattered off any sub-unit, whether belonging to P or not. Hence:

$$\psi_{sc,TOT}(\boldsymbol{r}) = \sum_{n} \psi_{sc,n} = \quad (6.20)$$
$$= \frac{1}{2}\sum_{L_1} Y_{L_1}(\hat{r}) \left[h_{l_1}^{+}(k_0 r) \left(\overset{(0)00}{\mathbb{NT}}(E_0)\, \overset{(0)}{\mathbb{G}} \right)_{L_1} + h_{l_1}^{+}(k_P r) \left(\overset{(P)0p}{\mathbb{NT}}(E_0)\, \overset{(0)}{\mathbb{G}} + \overset{(P)00}{\mathbb{NT}}(E_P)\, \overset{(P)}{\mathbb{G}} \right)_{L_1} \right].$$

Comparing this with equation (6.5), it is possible to obtain relations between the cluster and sub-units' T-matrices:

$$\boldsymbol{T}^{G,EL} = \overset{(0)00}{\mathbb{NT}}(E_0) \left(\mathbb{1} - \overset{(0)00}{\mathbb{XT}}(E_0) \right)^{-1} \mathbb{M}; \quad (6.21a)$$

$$\boldsymbol{T}^{G,P} = \overset{(P)}{\mathbb{N}} \left[\mathbb{1} + \overset{00}{\mathbb{T}}(E_P) \left(\mathbb{1} - \overset{(P)00}{\mathbb{XT}}(E_P) \right)^{-1} \overset{(P)}{\mathbb{X}} \right] \overset{0p}{\mathbb{T}}(E_0) \left(\mathbb{1} - \overset{(0)00}{\mathbb{XT}}(E_0) \right)^{-1} \mathbb{M}. \quad (6.21b)$$

Here, matrix $\mathbb{M}$ is defined as in equations (3.21) and (3.6); unlike matrices $\mathbb{N}$, it does not depend on the channel (0, P or Q). Again, the result obtained for the elastic T-matrix $T^{G,EL}$ is identical to that resulting from the elastic treatment (equation 3.24).

Finally, when the energy overcomes the second threshold ΔE_Q, both sub-units belonging to P and Q are allowed to undergo inelastic scattering (but not simultaneously). The resulting equations (6.21a) and (6.21b) do not change; a third relation must be added for the inelastic T-matrix relative to the excitation to the state $|Q\rangle$:

$$T^{G,Q} = \overset{(Q)}{\mathbb{N}} \left[\mathbb{1} + \overset{00}{\mathbb{T}}(E_Q) \left(\mathbb{1} - \overset{(Q)00}{\mathbb{X}\mathbb{T}}(E_Q) \right)^{-1} \overset{(Q)}{\mathbb{X}} \right] \overset{0q}{\mathbb{T}}(E_0) \left(\mathbb{1} - \overset{(0)00}{\mathbb{X}\mathbb{T}}(E_0) \right)^{-1} \mathbb{M}, \tag{6.22}$$

where matrices $\overset{(Q)}{\mathbb{N}}$, $\overset{0q}{\mathbb{T}}$ and $\overset{(Q)}{\mathbb{X}}$ are defined in an analogous way to $\overset{(P)}{\mathbb{N}}$, $\overset{0p}{\mathbb{T}}$ and $\overset{(P)}{\mathbb{X}}$.

6.1.5 Extension to more general cases

The results presented above, obtained in the assumption that the sub-units belong to the ensembles E, P and Q, can be easily extended to more general cases, where, mantaining the restriction that no multiple excitations are allowed, the number of ensembles is not limited to these three. The elastic T-matrix always assumes the form of equation (6.21a), while the inelastic channels, regardless of the number of sub-units contributing to them, are used to build the inelastic T-matrices in the following way:

$$T^{G,C} = \overset{(C)}{\mathbb{N}} \left[\mathbb{1} + \overset{00}{\mathbb{T}}(E_C) \left(\mathbb{1} - \overset{(C)00}{\mathbb{X}\mathbb{T}}(E_C) \right)^{-1} \overset{(C)}{\mathbb{X}} \right] \overset{0c}{\mathbb{T}}(E_0) \left(\mathbb{1} - \overset{(0)00}{\mathbb{X}\mathbb{T}}(E_0) \right)^{-1} \mathbb{M}. \tag{6.23}$$

Here, $k_C = \sqrt{E_C}$ and $E_C = E_0 - \Delta E_C$, and the sub-units' inelastic T-matrices are defined as:

$$\overset{0c}{T^n} = \begin{cases} \overset{0c}{T^n}, & n \in C \\ \mathbf{0}, & n \notin C \end{cases} \tag{6.24}$$

where C contains sub-units with the same excitation threshold ΔE_c.

A further extension is needed if more than one state is available to one ensemble for excitation, as illustrated in figure 6.2. It turns out that the equations obtained so far are valid in this case too: i.e. state $|p'\rangle$ is regarded as a new state, whose contribution comes from

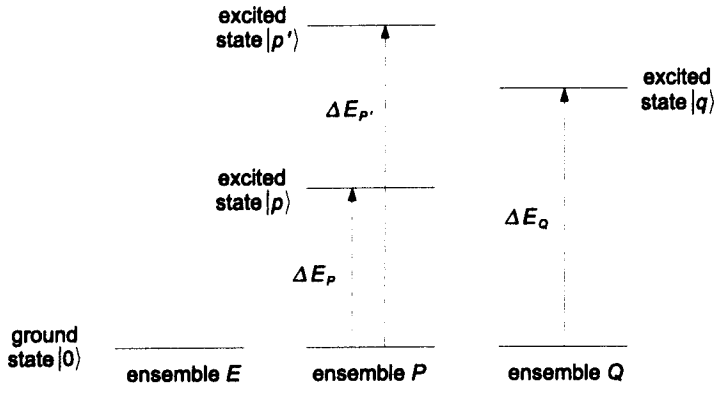

Figure 6.2: *Schematic representation of the electronic states of the sub-units forming a cluster, which are available to excitation. Two electronic states are available for excitation of sub-units belonging to ensemble P.*

sub-units in ensemble P only:

$$\overset{0p'}{\boldsymbol{T}}{}^n = \begin{cases} \overset{0p'}{\boldsymbol{T}}{}^n, & n \in P \\ \mathbf{0}, & n \notin P \end{cases} \tag{6.25}$$

6.1.6 Terms contributing to the global T-matrices

As for the elastic case, one can identify *re-expansion terms* $\mathbb{M}$ (from $\boldsymbol{r}$ to $\boldsymbol{r}_n$) and $\overset{(C)}{\mathbb{N}}$ (from $\boldsymbol{r}_n$ to $\boldsymbol{r}$); the latter depends on the threshold energy ΔE_C. There are also *multiple scattering terms*, of which one is related to the elastic scattering of a wavefunction that did not loose energy, $\left(\mathbb{1} - \overset{(C)00}{\mathbb{X}}\mathbb{T}\,(E_0)\right)^{-1}$, and one to the elastic scattering of a wavefunction that underwent inelastic scattering from the other sub-units, with a consequent energy loss, $\left(\mathbb{1} - \overset{(C)00}{\mathbb{X}}\mathbb{T}\,(E_C)\right)^{-1}$.

In the absence of any multiple scattering effect, matrices $\overset{(C)}{\mathbb{X}}$ and $\overset{(0)}{\mathbb{X}}$ become null (i.e. a zero matrix), and equations (6.21a) and (6.23) reduce, as expected, to:

$$\boldsymbol{T}^{G,EL}(E_0) = \overset{(0)00}{\mathbb{N}}\mathbb{T}\,(E_0)\mathbb{M}, \tag{6.26a}$$

$$\boldsymbol{T}^{G,C}(E_0) = \overset{(C)0c}{\mathbb{N}}\mathbb{T}\,(E_0)\mathbb{M}, \tag{6.26b}$$

i.e. they revert to the sub-units' T-matrices, although rotated and re-expanded.

In general, it is important to stress that, at each scattering energy E_0, matrices $T^{G,EL}(E_0)$ and $T^{G,C}(E_0)$ are calculated using monomers' T-matrices for different energies.

6.1.7 Cutoff

The reasons why two cutoffs were applied on the multiple scattering T-matrix in the elastic treatment still hold here. The T-matrices appearing in the terms accounting for the interference between sub-units must have the cutoffs applied on the number of partial waves and on the extent of the dipole interaction. As stated above, the two terms $\left(\mathbb{1} - \overset{(C)00}{\mathbb{X}\mathbb{T}}(E_0)\right)^{-1}$ and $\left(\mathbb{1} - \overset{(C)00}{\mathbb{X}\mathbb{T}}(E_C)\right)^{-1}$ clearly introduce multiple scattering effects; the value of a_c, defining the radial distance from which the dipole interaction is disregarded, assumes the same value in both cases, as it only depends on the distance between sub-units. On the other hand, the partial wave cutoff depends on the energy of the incoming wavefunction, which is different in the two cases (E_0 and E_C). Therefore, the number of partial waves included in the elastic T-matrices $\overset{00}{\mathbb{T}}(E_0)$ and $\overset{00}{\mathbb{T}}(E_C)$ is in general different at a certain scattering energy E_0. Equation (3.27) should be rewritten in more general terms as:

$$\frac{l(l+1)}{R^2_{n,n'}} \leqslant \gamma E_C, \tag{6.27}$$

where E_C is, as defined before, the energy of the scattered wavefunction. Such modification is justified by the interpretation given to the cutoff.

As for the other T-matrices in equation (6.23), the inelastic one, $\overset{0c}{\mathbb{T}}(E_0)$, does not account for the multiple scattering, as it is the only term left if the interference is turned off (i.e. all X-matrices are set to zero — see equation 6.26b) and should therefore reproduce the correct behaviour of the inelastic channel of a single sub-unit.

In practice, it is not clear whether the cutoff should be applied to the remaining term, $\overset{00}{\mathbb{T}}(E_C)$. In our attempt to apply the inelastic treatment to water clusters we will analyse different solutions.

6.1.8 Computational implementation

The inelastic model has been implemented by significantly modifying the elastic Multiple Scattering code, although the programme outline, described in section 3.2.5, is substantially unchanged. The modifications increased the memory requirements and also affected the computational time. Minor modifications included the reading of the inelastic T-matrices and the computation of matrices $\overset{(C)}{\mathbb{X}}$ and $\overset{(C)}{\mathbb{N}}$; the most memory consuming modification, however, is the storage of all the elastic T-matrices at the same time, since at each energy step E_0, the elastic T-matrices calculated at the various E_C must be read. The most straightforward solution, although certainly not the most economical, was to store all the elastic and inelastic T-matrices for all the energy steps into a single vector; the memory requirements are however easily manageable on a desktop machine.

The issue of how to include in the inelastic treatment the effect that the clusterisation has on the channel threshold energies was also addressed. As stated before, the code is able to treat those excitations which can be approximated as the excitation of a single sub-unit; however, the neighbouring sub-units often have an effect on the energy at which a channel opens, shifting it to higher or lower energies. This in practice means that the energy of the isolated monomer state $|p\rangle$ does not equal the energy of the cluster state $|P\rangle$. In order to address this problem, the code allows a customisable energy shift of the inelastic T-matrices, so that the threshold energies can be easily modified.

The interpolation procedure, illustrated in section 3.2.1, involves an interpolation of the cutoff cross sections, each of which is calculated in the whole energy range. The inelastic theory introduces a second cutoff on the $\overset{00}{T}$ (E_C) matrices, which is independent to that applied to the $\overset{00}{T}$ (E_0) matrices; the cutoff cross sections will therefore be identified by two indices and henceforth referred to as σ^{l_1,l_2}, where l_1 refers to E_0 and l_2 to E_C. The interpolation procedure has not been changed substantially: a first run interpolates in the usual way the cross sections σ^{l_1,l_2} having the same value of l_2, generating cross sections $\sigma^{\mathrm{INT},l_2}$. The latter are then interpolated with respect to l_2. There is no reason why l_1 should be interpolated before l_2, and the opposite procedure may be followed instead.

Under certain aspects, it may be argued that the inelastic treatment lacks most of the

self-sufficiency that the elastic one had; the Multiple Scattering theory has been developed in such a way that it is able to produce a cluster's scattering data from virtually only sub-units' information; the only input relative to the cluster are the geometrical parameters. The inelastic treatment, on the other hand, needs a good prior knowledge of the cluster's properties, which can be obtained from previous theoretical or experimental studies. In particular, it is necessary to know the spatial distribution of the unoccupied orbitals, in order to assign each excited state to a sub-unit, when possible, and also the cluster excitation energies. Without such information, it is very difficult to produce reliable results and therefore the treatment is highly dependent on previous studies.

6.2 Application to the water dimer

We applied the Inelastic Multiple Scattering code to the water dimer cluster in the equilibrium geometry. For this target, a recent theoretical study by Chipman (2005) provides the information required as input, i.e. the localisation of the first two excited states of the dimer on different monomers. The first singlet and triplet excited states of A'' symmetry are localised on the bond donor molecule (i.e. the *in plane* one), while those of A' symmetry, at higher energy, are localised on the bond acceptor molecule (the *out of plane* one) — see figure 6.3. They both correspond to an excitation to the first excited state of the monomer, of B_1 symmetry (A'' if C_s point group is used instead of C_{2v} and the reflection plane is chosen as that containing the molecule). In Chipman (2005), the first excited states of H_2O and $(H_2O)_2$ in the equilibrium geometry were calculated with a CIS (Configuration Interaction Singles, Del Bene et al. 1971) and a EOM-CCSD (Equations-of-motion coupled-cluster with singles and doubles, Dalgaard & Monkhorst 1983) models and aug-cc-pVTZ basis set. The vertical excitation energies are reported in tables 6.1 and 6.2, along with ours. A more comprehensive report for the monomer may be found in Gorfinkiel et al. (2002).

As in chapter 4, we performed R-matrix calculations both on the water monomer (to provide collisional input for the MS code) and on the water dimer. The latter served both to provide cross sections to use as a comparison (as in the elastic case) and also to produce excitation energies for the dimer's states, which are an additional input required by the

inelastic MS code.

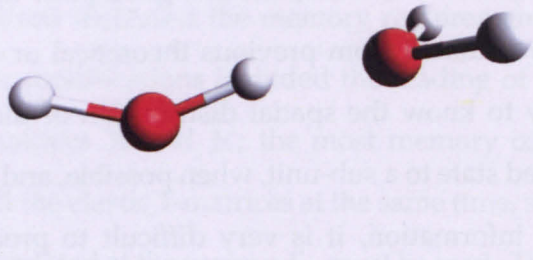

Figure 6.3: *Ball-and-stick model of $(H_2O)_2$, equilibrium geometry. The monomer on the left is the bond donor,* in plane, *while the other is the bond acceptor,* out of plane.

	method	$^1B_1$ / eV	$^3B_1$ / eV
Cheng et al. (1999)	photoabsorption cross section	7.4	
Chipman (2005)	calc. EOM-CCSD/aug-cc-pVTZ	7.54	7.13
Chipman (2005)	calc. CIS/aug-cc-pVTZ	8.62	7.92
present	calc. CASCI/Dunning	7.51	7.04

Table 6.1: *Vertical excitation thresholds for H_2O. Also see Gorfinkiel et al. (2002). The EOM-CCSD model of Chipman (2005) stands for Equations-of-motion coupled cluster with singles and doubles (Dalgaard & Monkhorst 1983, Stanton & Bartlett 1993, Purvis & Bartlett 1982).*

6.2.1 Inelastic R-matrix calculations for H_2O

R-matrix calculations on H_2O were performed as in the work of Gorfinkiel et al. (2002), as for our elastic calculations. The basis set employed (Dunning) was the DZP Gaussian basis set of Dunning (1970), augmented with two *s*-type and one *p*-type functions, for O, and the TZ basis of Dunning (1971), augmented with two *p*-type functions, for H. Natural orbitals were employed. The R-matrix sphere was extended to 10 a_0 to allow the more diffuse excited states to be contained in the inner region, and the first 9 states were included in the calculation (the vertical excitation energies of the first two excited states are listed in table 6.1). The

	method	$^1A''$ / eV	$^3A''$ / eV
Valenzano et al. (2005)	MRCI/TZVP	7.29	6.99
Chipman (2005)	EOM-CCSD/6-311(2+)G*	7.13	6.81
Chipman (2005)	CIS/aug-cc-pVTZ	8.66	8.05
present	CASCI/Dunning	8.25	7.66

Table 6.2: *Calculated vertical excitation energies for* $(H_2O)_2$.

continuum basis optimised for $a = 10\ a_0$ (Faure et al. 2002) comprised 9 *s*-type, 7 *p*-type, 7 *d*-type, 7*f*-type and 6 *g*-type gaussian functions. The CAS model employed included 2 frozen electrons in the lowest a_1 orbital and 8 electrons in the active space, defined as ($2a_1$—$4a_1$, $1b_1$—$2b_1$, $1b_2$—$2b_2$), generating ~ 1 100 (target) and ~ 9 100 (scattering) configurations.

The inelastic cross sections for the first two excited states (the singlet and triplet states of symmetry B_1) are shown in figure 6.4 up to 13 eV, because the ionisation threshold is 12.6 eV (NIST Computational Chemistry Comparison and Benchmark DataBase 2010) and at higher energies this process must therefore be included. The most noticeable features are the peaks at 9.15 eV, present in both cross sections, which are due to a $^2A_1$ Feshbach resonance whose parent state is the first $^3A_1$ state (Gorfinkiel et al. 2002). A very narrow Feshbach resonance at an energy slightly below the first excitation threshold has also been observed by Gorfinkiel et al. (2002) and others, and appears in our elastic cross section (not shown here) at 6.96 eV.

The excitation energies for the $^1B_1$ and $^3B_1$ states, reported in table 6.1, are in good agreement with those calculated by Chipman (2005).

6.2.2 Inelastic R-matrix calculations for $(H_2O)_2$

The dimer R-matrix calculation was performed as in Gorfinkiel (2007); the same basis sets of Dunning (1970) and Dunning (1971), used in the monomer calculation, were employed. An arithmetic average of the natural orbitals from the ground state $^1A_1$, and the lowest $^1A_1$ and $^1B_1$ states produced a set of natural orbitals for the target and scattering calculations. A CAS model with 8 electrons frozen and an active space defined as ($5a'$—$11a'$,$1a''$—$3a''$) was employed, producing ~ 34 600 and ~ 152 500 configurations respectively. The first 8 states

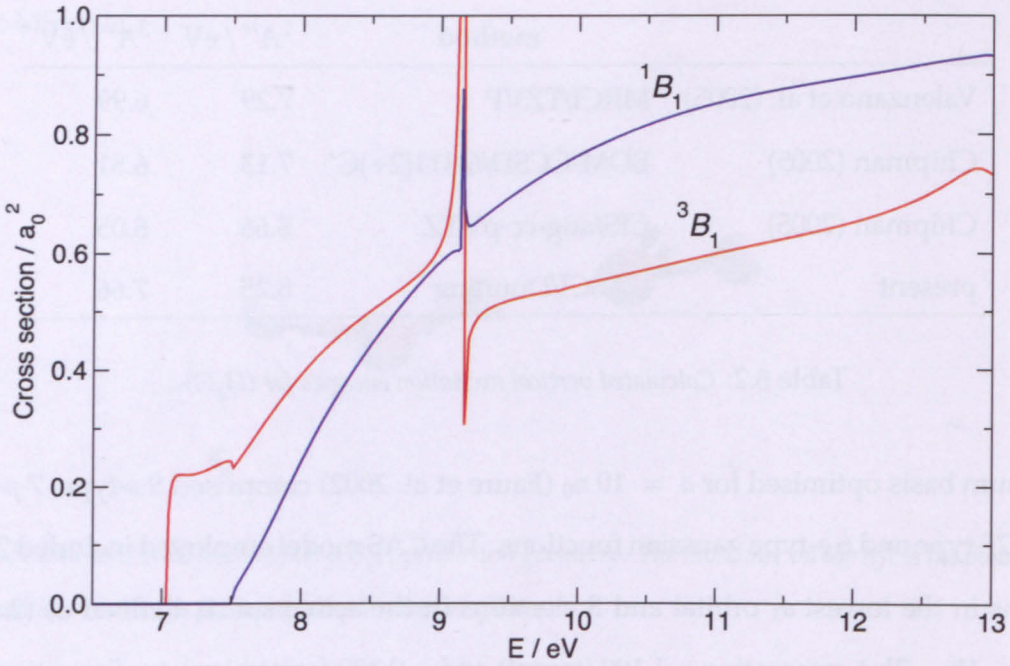

Figure 6.4: *Inelastic R-matrix cross sections for the electronic excitation into the first two states of H_2O, indicated in the figure.*

were included in the close-coupling expansion; the excitation energies of the two lowest ones (triplet and singlet belonging to symmetry A'') are listed in table 6.2. The inelastic cross sections for the excitation into the first four states of $(H_2O)_2$ are shown in figure 6.5; the elastic cross section, not shown here, display two very narrow resonances originating from the splitting of the first Feshbach resonance of the monomer, at 7.63 and 7.82 eV, as shown in Gorfinkiel (2007); the latter resonance is also visible as a little spike on the $^3A''$ cross section.

6.2.3 Inelastic Multiple Scattering calculations for $(H_2O)_2$

The Multiple Scattering calculations were run inputting the geometrical parameters employed in the elastic calculation, listed in tables 4.2 and 4.5; the additional input required by the inelastic code consists in the energy shifts, by which the excitation energies of the monomer must be shifted in order to match those of the dimer. The way such shifts have been calculated is illustrated in table 6.3, where each dimer state is associated to a monomer one: the A'' states of the dimer (both singlet and triplet) are associated to the in plane monomer (monomer 1), since Chipman (2005) found that the LUMO is localised there. The lowest A'

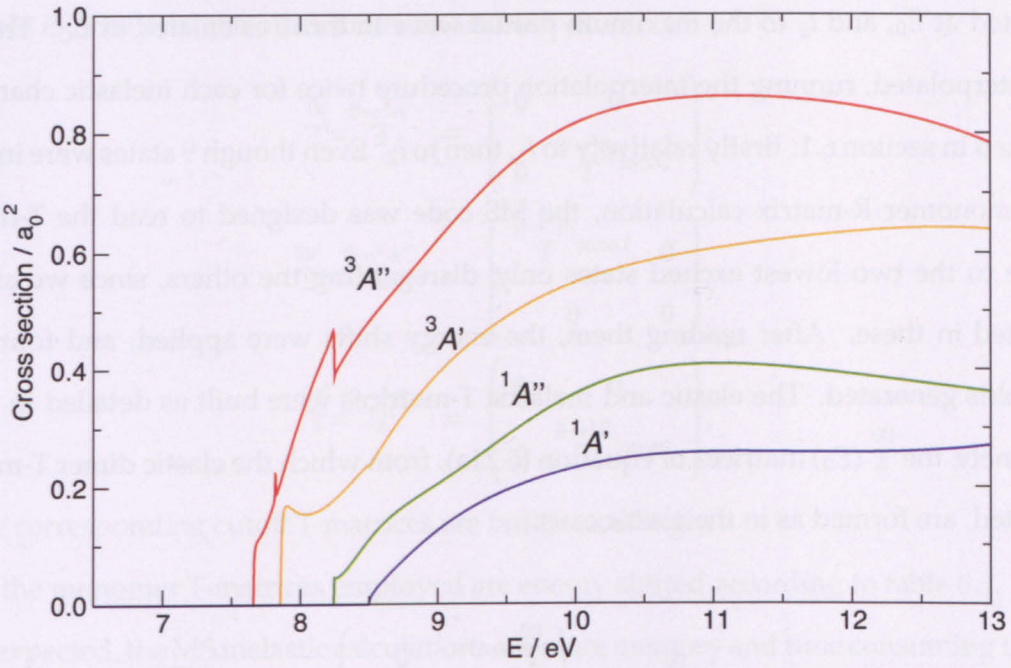

Figure 6.5: *Inelastic R-matrix cross sections for the electronic excitation into the four lowest states of $(H_2O)_2$, indicated in the figure.*

molecular orbital of the dimer, on the other hand, is localised on the out of plane monomer (monomer 2). For the calculation of the energy shifts, we chose to use the dimer energies calculated with the R-matrix method, since we will be comparing the MS cross sections with the R-matrix ones.

$(H_2O)_2$ states		corresponding H_2O states			shift
sym	exc.thr.	sym	exc.thr.	excited mon.	
$^3A''$	(7.665)	$^3B_1$	(7.035)	monomer 1	+0.630
$^3A'$	(7.860)	$^3B_1$	(7.035)	monomer 2	+0.825
$^1A''$	(8.250)	$^1B_1$	(7.508)	monomer 1	+0.742
$^1A'$	(8.505)	$^1B_1$	(7.508)	monomer 2	+0.997

Table 6.3: *Shift required to match the monomer and dimer states. All the energies are in eV, calculated with the R-matrix method both for H_2O and $(H_2O)_2$.*

Once the input is constructed, the programme is run several times, obtaining the cutoff cross sections σ^{l_1,l_2}, where l_1 refers to the maximum partial wave included in the T-matrices

calculated at E_0, and l_2 to the maximum partial wave in those calculated at E_C. These are then interpolated, running the interpolation procedure twice for each inelastic channel, as explained in section 6.1: firstly relatively to l_1, then to l_2. Even though 9 states were included in the monomer R-matrix calculation, the MS code was designed to read the T-matrices relative to the two lowest excited states only, disregarding the others, since we are only interested in these. After reading them, the energy shifts were applied, and four dimer thresholds generated. The elastic and inelastic T-matrices were built as detailed in section 6.1, namely, the $\overset{00}{\mathbb{T}}(E_0)$ matrices of equation (6.21a), from which the elastic dimer T-matrix is calculated, are formed as in the elastic case:

$$\overset{00}{\mathbb{T}}(E_0) = \begin{pmatrix} \overset{00}{T}^{\text{mon1}} & \mathbf{0} \\ \mathbf{0} & \overset{00}{T}^{\text{mon2}} \end{pmatrix}, \tag{6.28}$$

where both monomer T-matrices $\overset{00}{T}^{n}$ are calculated at E_0; cutoff T-matrix $\overset{00}{\mathbb{T}}_c(E_0)$ is computed in a similar way, using the trimmed monomer T-matrices.

For what concerns the inelastic dimer T-matrices $T^{G,C}$ of equation 6.23, they need three different T-matrices: $\overset{00}{\mathbb{T}}(E_0)$, $\overset{00}{\mathbb{T}}(E_C)$ and $\overset{0c}{\mathbb{T}}(E_0)$; the first two are calculated as in equation 6.28, from elastic monomer T-matrices at the scattering energy E_0 and at $E_C = E_0 - \Delta E_C$, respectively. As for the inelastic T-matrices $\overset{0c}{T}(E_0)$, they are formed in the following way. Firstly, we recall that there are four inelastic channels (in energy order, $|P\rangle = |^3A''\rangle$, $|Q\rangle = |^3A'\rangle$, $|P'\rangle = |^1A''\rangle$, $|Q'\rangle = |^1A'\rangle$) and two ensembles ($P$, formed by monomer 1 only — responsible for the excitations into the singlet and triplet A'' states — and Q, formed by monomer 2 — responsible for the states of symmetry A'). Therefore matrix $\overset{0p}{\mathbb{T}} = \overset{0\to^3A''}{\mathbb{T}}$ is built as:

$$\overset{0p}{\mathbb{T}} = \overset{0\to^3A''}{\mathbb{T}} = \begin{pmatrix} \overset{0\to^3B_1}{T}{}^{\text{mon1}} & \mathbf{0} \\ \mathbf{0} & \mathbf{0} \end{pmatrix}; \tag{6.29}$$

the element $\overset{0p}{\mathbb{T}}_{2,2}$ is 0 because, following equation (6.24), monomer 2 does not belong to

ensemble P. Similarly, the other matrices are built as:

$$\overset{0q}{\mathbb{T}} = \overset{0\rightarrow{}^3A'}{\mathbb{T}} = \begin{pmatrix} \mathbf{0} & \mathbf{0} \\ \mathbf{0} & \overset{0\rightarrow{}^3B_1}{T}{}_{\text{mon2}} \end{pmatrix}; \tag{6.30}$$

$$\overset{0p'}{\mathbb{T}} = \overset{0\rightarrow{}^1A''}{\mathbb{T}} = \begin{pmatrix} \overset{0\rightarrow{}^1B_1}{T}{}_{\text{mon1}} & \mathbf{0} \\ \mathbf{0} & \mathbf{0} \end{pmatrix}; \tag{6.31}$$

$$\overset{0q'}{\mathbb{T}} = \overset{0\rightarrow{}^1A'}{\mathbb{T}} = \begin{pmatrix} \mathbf{0} & \mathbf{0} \\ \mathbf{0} & \overset{0\rightarrow{}^1B_1}{T}{}_{\text{mon2}} \end{pmatrix}, \tag{6.32}$$

and the corresponding cutoff T-matrices are built accordingly.

All the monomer T-matrices employed are energy shifted according to table 6.3.

As expected, the MS inelastic calculations are more memory and time consuming than the corresponding elastic ones, taking up to 50% longer; the running time is however reasonable, even on an average desktop computer, and the whole set of calculations with all the cutoff values is executed in less than one hour, provided the monomer collisional input is available.

6.3 Results

As mentioned in section 6.1, the two T-matrices $\overset{00}{\mathbb{T}}(E_0)$ and $\overset{00}{\mathbb{T}}(E_C)$ appearing in brackets in equation (6.23) clearly account for the interference between sub-units and therefore both dipole and partial wave cutoffs need to be aplied to them. In particular, the number of partial waves to be included at each energy in the two terms is different, since the energy of the incoming wave is E_0 in one case and E_C in the other.

The inelastic T-matrix $\overset{0c}{\mathbb{T}}(E_0)$, on the other hand, needs no cutoff. As for the remaining one, $\overset{00}{\mathbb{T}}(E_C)$, it is not clear whether either of the two cutoffs should be applied; we therefore run two different calculations, where such T-matrix has been built, in one case applying the cutoffs on the monomer's T-matrices, and in the other case applying no cutoff. When the cutoff on the number of partial waves to be included is employed, equation (6.27) was followed (i.e. the number of partial wave contributions is calculated according to the energy of the incoming wave, E_0 or E_C). It would be possible to study the effect of the cutoffs separately (i.e. applying each one independently), since, as explained, their use is justified

by considerations of a different kind (the cutoff on the number of partial waves eliminates those which cannot overcome the centrifugal barrier at a certain energy; the cutoff on the extent of the long range interaction, which in our case is limited to the dipole moment, on the other hand, is applied to comply with the assumption that the sub-units' potentials do not overlap). However, the underlying justification in both cases is that the sub-units whose T-matrices are cut off take part in the multiple scattering process; therefore we have applied both cutoffs at the same time.

Figure 6.6 presents inelastic cross sections for the first excited state of the dimer ($^3A''$) produced with the Inelastic Multiple Scattering code; in one case the cutoffs have been applied to $\overset{00}{\mathbb{T}}(E_C)$, in the other case they have not. The figure also presents a MS inelastic cross section (labelled 2) obtained applying the cutoffs on l_2, but keeping $l_1 = 0$. This in practice means that $\overset{00}{\mathbb{T}}(E_0)$ and $\overset{0c}{\mathbb{T}}(E_0)$ are formed with a contribution from the $l = 0$ partial wave only, while $\overset{00}{\mathbb{T}}(E_C)$ includes the correct number of partial waves required at each energy, following equation (6.27). The R-matrix cross section is also shown in the figure. Apart from the shape of the MS cross sections, which will be discussed later, it is clear that applying the cutoffs brings the MS cross section closer to the R-matrix one, used as reference; the size of the untrimmed MS cross section is much larger by several orders of magnitude, and very different in shape. Only at high energies (around 13 eV) it becomes comparable with the R-matrix cross section. We then conclude that the cutoffs need to be applied to $\overset{00}{\mathbb{T}}(E_C)$.

The difference between cross sections (1) and (2) is more marked at low energies, where the inclusion of all the l_1 partial waves in the T-matrices calculated at E_0 has the effect of significantly increasing the cross section near the threshold for the excitation into the first state. Cross section (2) therefore resembles the R-matrix one in both shape and size.

The difference between these cross sections is more evident in figure 6.7, where the results for the excitation into the $^1A''$ dimer state are shown. The "no cutoff" cross section (not visible in the figure) is again too high in the whole energy range, and from now on we will not plot it anymore, concluding that the cutoffs need to be applied to $\overset{0c}{\mathbb{T}}(E_0)$. Comparing cross sections (1) (including all the partial waves needed at each energy in $\mathbb{T}(E_0)$) and (2) (where only $l_1 = 0$ is kept, and the interpolation is carried out on l_2 only), we can see that in the second case

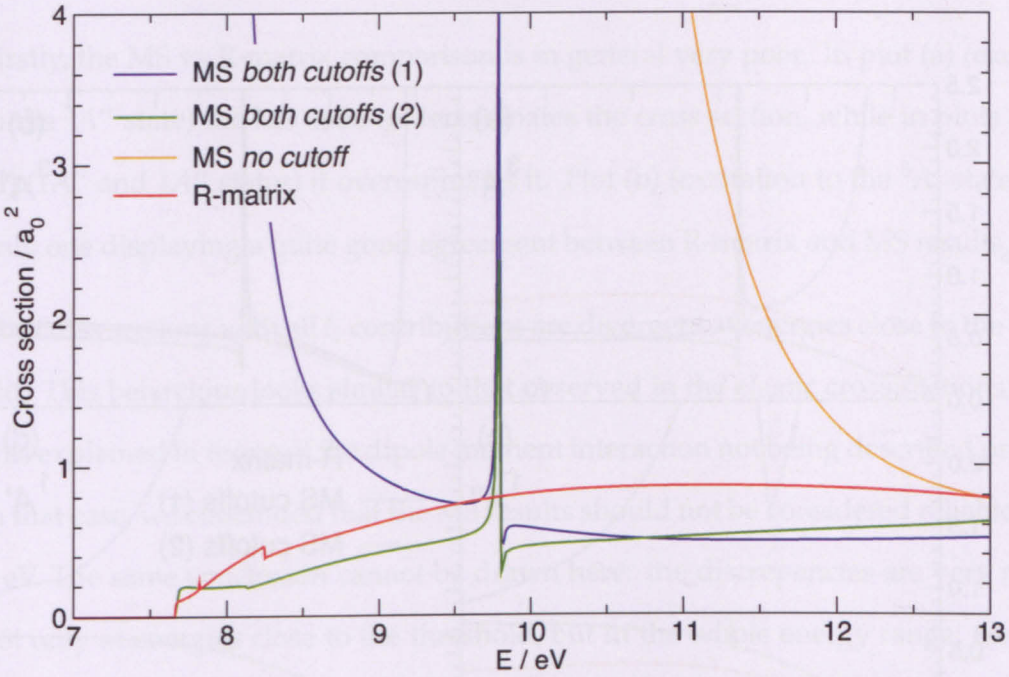

Figure 6.6: *Inelastic cross sections for the excitation to the dimer $^3A''$ state; comparison between R-matrix and MS results (obtained applying different cutoffs). In cross section labelled (1) all the partial waves needed at each energy, calculated with equation (6.27), are included in $\overset{00}{\mathbb{T}}(E_c)$ (see text for details). In cross section labelled (2), equation (6.27) is applied only for the interpolation over l_2, while the l_1 partial wave is only 0.*

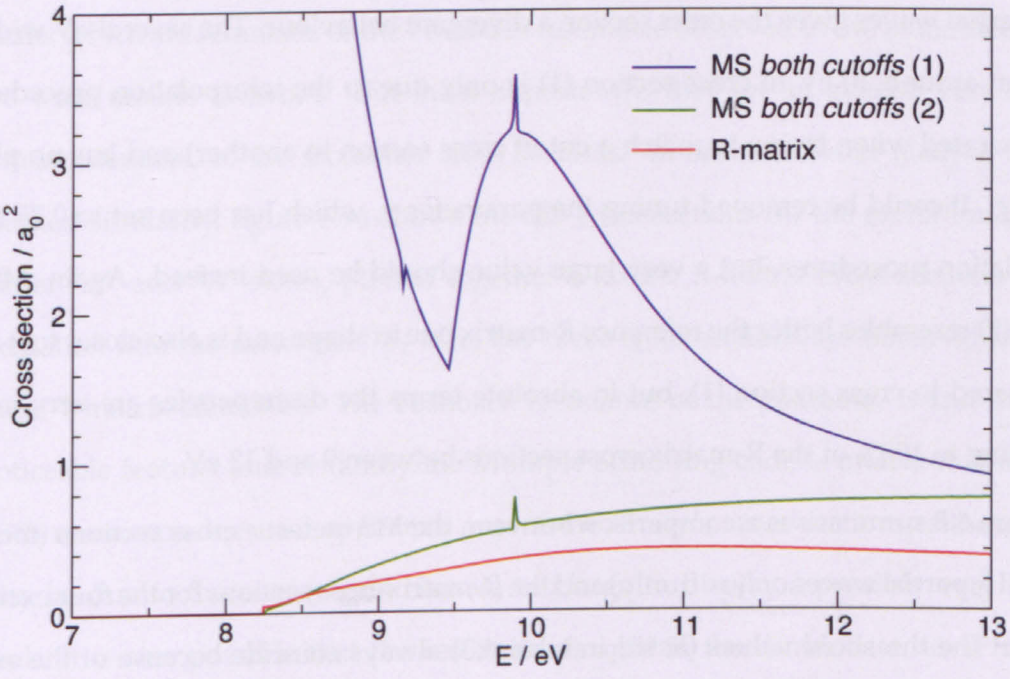

Figure 6.7: *Inelastic cross sections relative to the excitation to the dimer $^1A''$ state: comparison between R-matrix and MS results. The cross section without cutoff is not visible in the plot, lying well above the others.*

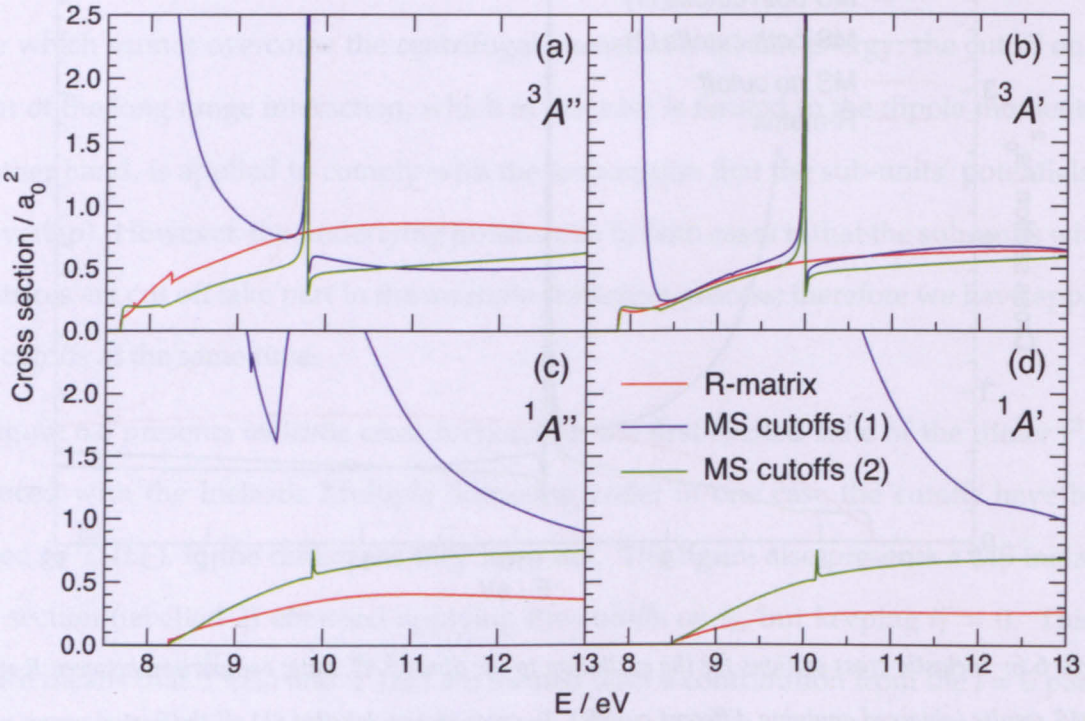

Figure 6.8: *R-matrix and MS inelastic cross sections for the excitation into the lowest four states of* $(H_2O)_2$. *The symmetry of the states is specified in the figure.*

the cross section displays a correct behaviour at the threshold, while the inclusion of the other partial waves gives the cross section a divergent behaviour. The several-eV wide peak visible at around 10 eV in cross section (1) is only due to the interpolation procedure (i.e. it is generated when trying to match a cutoff cross section to another) and has no physical meaning. It could be removed tuning the parameter γ, which has been set to 0.75 in both interpolation procedures, but a very large value should be used instead. Again, MS cross section (2) resembles better the reference R-matrix one in shape and is also closer to it in size, if compared to cross section (1), but in absolute terms the discrepancies are very marked, amounting to 100% of the R-matrix cross sections between 9 and 13 eV.

Figure 6.8 summarises a comparison between the MS inelastic cross sections (including either all l_1 partial waves or $l_1 = 0$ only) and the R-matrix cross sections for the four excitations studied. The threshold values (listed in table 6.3) always coincide because of the artificial shifting carried out in the MS calculation. Several conclusions can be drawn from the analysis of figure 6.8.

i. Firstly, the MS vs R-matrix comparison is in general very poor. In plot (a) (excitation to the $^3A''$ state) the MS code underestimates the cross section, while in plots (c) and (d) ($1A''$ and $1A''$ states) it overestimates it. Plot (b) (excitation to the $^3A'$ state) is the only one displaying a quite good agreement between R-matrix and MS results.

ii. The cross sections with all l_1 contributions are divergent at energies close to the threshold. This behaviour looks similar to that observed in the elastic cross sections, which was explained in terms of the dipole moment interaction not being described properly; in that case, we concluded that the MS results should not be considered reliable below 1 eV. The same conclusion cannot be drawn here: the discrepancies are very marked not only at energies close to the threshold, but in the whole energy range; the extent of the divergence is different in the various plots: the $^3A'$ cross sections (plot b) are in good agreement about 1 eV after the threshold, while the singlet cross sections (plots c and d) show large discrepancies up to high energies (outside our range).

iii. The MS cross sections including l_1 partial wave 0 only, labelled (2), generally in better agreement with the R-matrix ones than those labelled (1), are characterised by a good behaviour at the threshold, but the comparison is still poor. They all display marked peaks which are remnants of the Feshbach resonance observed in the monomer, which we were unable to avoid. But most importantly, they are in general very similar, almost identical, to the monomer cross sections. In order to better analyse this too marked similarity, figure 6.9a shows the MS cross sections for the excitation into the dimer $^3A''$ and $^3A'$ states, plotted together with the R-matrix cross sections for the excitation into the monomer $^3B_1$ state (all these cross sections are obtained from the same T-matrix elements). The Feshbach resonance of the monomer is still the most noticeable feature, and evidently the Multiple Scattering code is unable to remove it. Such resonance does not appear in any of the dimer's cross sections, although this may be due to the energy grid chosen, too large to display a possibly very narrow peak; it is also possible that the resonance is split in the dimer case, as it happens for the first Feshbach resonance (of $^2B_1$ symmetry). However, this would be due to dimerisation effects (i.e. structural interaction between sub-units); we already noted

how the MS inelastic code is unable to account for these (e.g. the shift of the energy thresholds), since it relies on the assumption that the only interaction between sub-units is limited to the multiple scattering effects during the collision process. Even disregarding the Feshbach resonances it is still evident that the MS dimer cross sections resemble the monomer cross sections more than they resemble the R-matrix dimer ones. The same conclusions can be drawn for figure 6.9b, where the MS cross sections for the excitation into the dimer $^1A''$ and $^1A'$ states are plotted together with the R-matrix cross sections for the excitation into the monomer $^1B_1$ state. This behaviour can be expressed mathematically as $T^{G,C} \approx \overset{0c}{T}$, where $T^{G,C}$ is the global MS T-matrix for the excitation into the dimer state $|C\rangle$ and $\overset{0c}{T}$ is the monomer T-matrix for the excitation into the monomer state $|c\rangle$. Recalling equation (6.23) and also that $\overset{0c}{\mathbb{T}}(E_0)$ is formed by the monomer $\overset{0c}{T}(E_0)$ from sub-units belonging to ensemble C only, we can conclude that, including partial wave $l_1 = 0$ only (producing the MS cross section labelled 2), the term in square brackets in (6.23) (i.e. the multiple scattering term) is almost negligible, affecting minimally the final cross section. If, on the other hand, higher partial waves are included in $\overset{00}{T}(E_0)$ according to the standard procedure (producing cross sections labelled 1), the term in brackets contributes more to the final T-matrix, increasing by several orders of magnitude the cross section. In particular, the term $\left(\mathbb{1} - \overset{(C)00}{\mathbb{X}\mathbb{T}}(E_C)\right)^{-1}$ was responsible for the divergence observed in the elastic cross section, which was in that case limited to $E < 1$ eV. Here the effect is much more noticeable even for $E_C > 1$ eV ($E_0 > \Delta E_C + 1$ eV), because the inelastic cross sections are in general more than one order of magnitude lower than the elastic ones. Therefore, in one case we underestimate the interference effects (hence cross sections (2) are almost identical to the monomer R-matrix ones, as seen in figure 6.9), in the other case the incorrect low energy behaviour of the interference term is dominant and suppresses all other contributions.

As a final remark, the main difference between $^3A''$ and $^3A'$ cross sections, as well as that between $^1A''$ and $^1A'$ ones, is due to the localisation of the excited states they refer to on two different water molecules (the *in plane* and *out of plane* ones). The effect of such localisation can be analysed looking at figure 6.10, where the cross sections for the

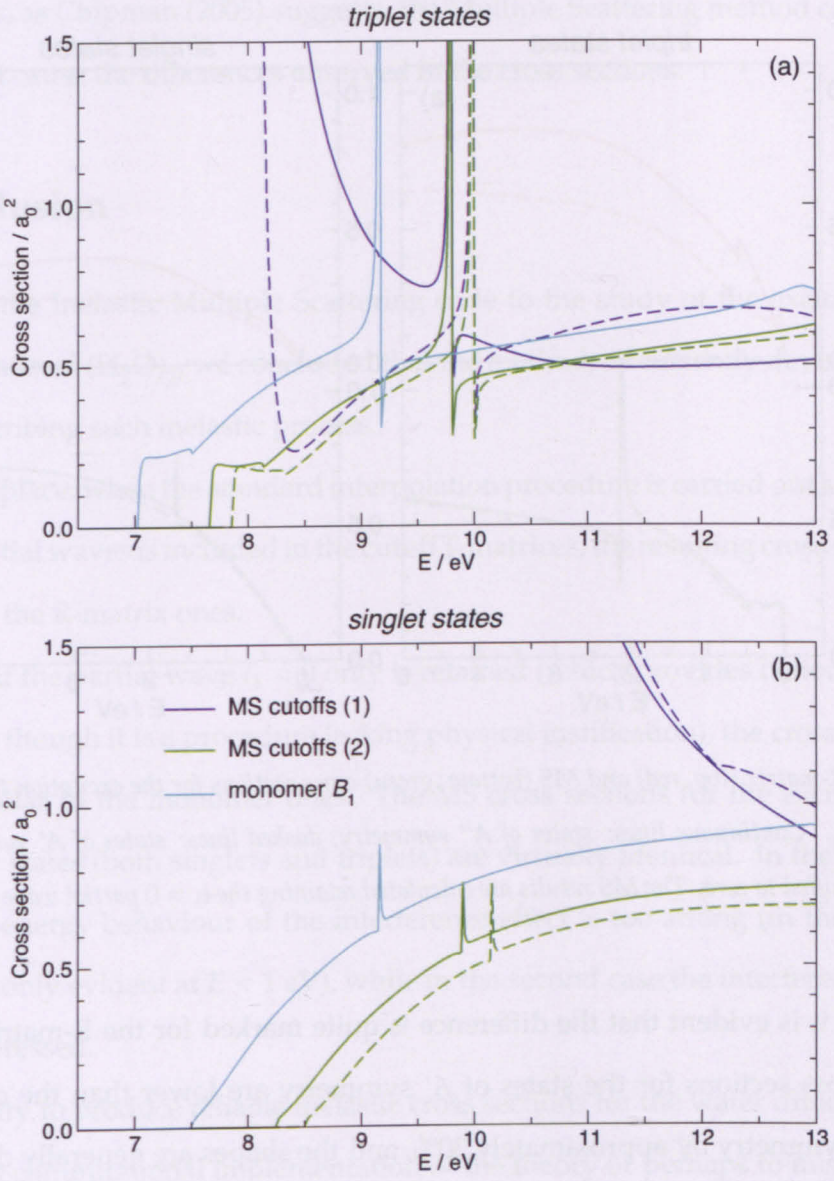

Figure 6.9: *Comparison between the monomer R-matrix cross sections and the corresponding dimer MS cross sections, which are calculated using the same T-matrix elements:* (a) *excitation into triplet states: R-matrix cross section for monomer state* $^3B_1$ *and MS cross sections for dimer states* $^3A'$ *and* $^3A''$*;* (b) *excitation into singlet states: R-matrix cross section for monomer state* $^1B_1$ *and MS cross sections for dimer states* $^1A'$ *and* $^1A''$*. For the dimer cross sections in both panels, continuous lines refer to states of* A'' *symmetry, dashed lines to states of* A' *symmetry.*

excitation into the triplet ($^3A''$ and $^3A'$) and the singlets states ($^1A''$ and $^1A'$) are shown; the thresholds have all been shifted to zero. Comparing each couple of lines at the top of both figures, showing the cross sections of A'' and A' symmetry (continuous and dashed lines

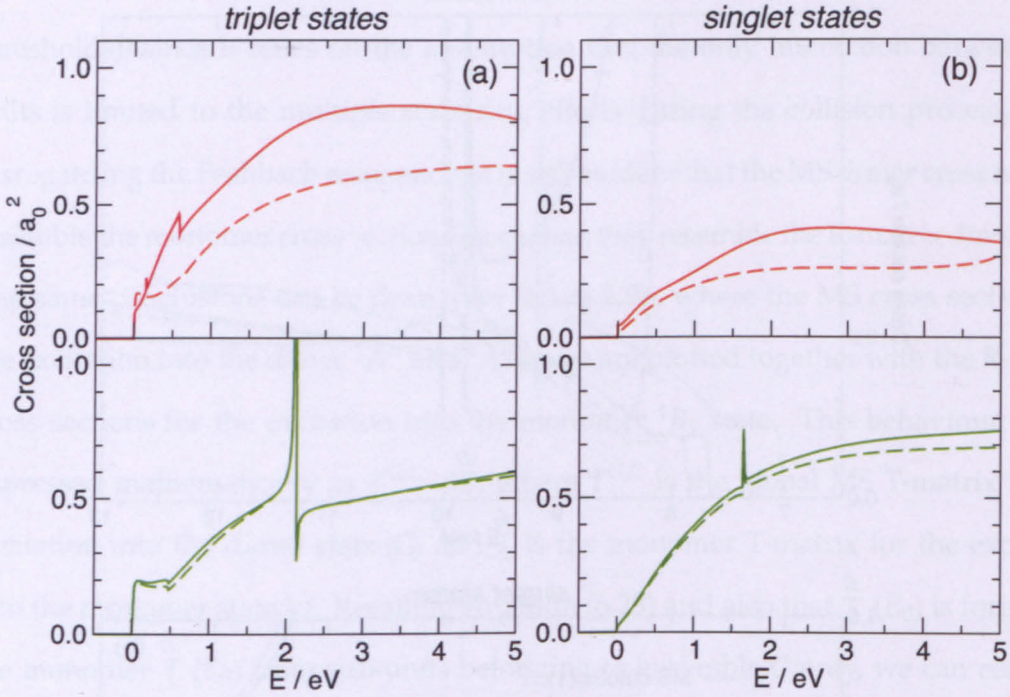

Figure 6.10: *R-matrix (top, red) and MS (bottom, green) cross sections for the excitation to the lowest four states of $(H_2O)_2$. Continuous lines: states of A'' symmetry; dashed lines: states of A' symmetry. All the thresholds are shifted to zero. The MS results are calculated retaining the $l_1 = 0$ partial wave only.*

respectively), it is evident that the difference is quite marked for the R-matrix results (top plots); the cross sections for the states of A' symmetry are lower than the corresponding states of A'' symmetry by approximately 30%, and the shapes are generally different. Such differences are approximately only due to the localisation of the same state on different monomers, since all states correspond to a monomer excitation into B_1 (singlet or triplet) states.

The effect of the localisation is much less evident in the Multiple Scattering results (bottom plots), where the difference amounts to ~ 5% at most, and the shapes are almost identical. This, again, is due to the fact that the MS cross sections (2) are virtually identical to the monomer R-matrix ones, as we noticed before, and that the interference effects are almost completely negligible. To very little extent, the MS code accounts for the localisation, since the dashed lines are lower than the corresponding continuous ones, but certainly the effect is not properly included. Perhaps, even in clusters where the excited states are well localised on

the monomers, as Chipman (2005) suggests, the Multiple Scattering method cannot include the effects that cause the differences observed in the cross sections.

6.4 Conclusion

Applying the Inelastic Multiple Scattering code to the study of the excitation into the lowest four states of $(H_2O)_2$, we concluded that the method, as currently devised, fares very poorly in describing such inelastic process.

In the first place, when the standard interpolation procedure is carried out and the correct number of partial waves is included in the cutoff T-matrices, the resulting cross sections differ strongly from the R-matrix ones.

Secondly, if the partial wave $l_1 = 0$ only is retained (which provides better shaped cross sections, even though it is a procedure lacking physical justification), the cross sections look extremely similar to the monomer ones. The MS cross sections for the excitation into A' and A'' dimer states (both singlets and triplets) are virtually identical. In the first case, the incorrect low energy behaviour of the interference effect is too strong (in the elastic cross section it was only evident at $E < 1$ eV), while in the second case the interference effects are virtually suppressed.

Our inability to produce reliable inelastic cross sections for the water dimer may be due to an incorrect computational implementation of the theory or perhaps to mistakes or bugs in the code that we have been unable to find. But the discrepancies may also indicate that the excited states of the cluster cannot be correctly described as [$\text{monomer}_{\text{g.s.}}$ monomer*] in a scattering study, even if a prior calculation on $(H_2O)_2$ seems to indicate that this is a good approximation. It is also possible that, as one sub-unit undergoes an electronic excitation and scatters the electron inelastically, the effect that the sudden change of electronic distribution has on the other sub-units is not negligible (even though time considerations would suggest this is an unlikely explanation); in such a case, the treatment developed here would be too simplistic and should be perhaps modified to include one sub-units' response to the excitation of the other.

More generally, even if the code worked for $(H_2O)_2$, the method would still be less general

than the elastic version, which only requires geometrical parameters to run; before applying it to other systems, prior information would be needed about the electronic structure of the target.

In conclusion, the study presented in this chapter is still regarded as a work in progress, and the inelastic MS approach as still incomplete. Future studies may help clarify the issues encountered.

Chapter 7

Conclusions

7.1 Outline of the work done

The research presented in this thesis has been focused on the development of a novel theoretical method, derived from the Multiple Scattering theory of Dill & Dehmer (1974) and making use of *ab initio* scattering data, which has been employed to calculate cross sections for the collision process between a low energy electron and a molecular cluster. The primary aim of the method is to provide reliable results without making use of semiempirical parameters, and overcoming the strong dependence on the size and number of electrons of the target which is typical of standard *ab initio* methods. In order to achieve this, several assumptions, implicit in the basis of the MS method, needed to be made, which limit the number of targets that can be studied, and which may be summarised as: *the method only accounts for the multiple scattering of the impinging electron's wavefunction; any other interaction between the sub-units, and its effect on the collision, are totally disregarded.*

The research carried out consisted in applying the method developed to the study of collisions with various cluster systems, in order to assess its validity, identify the application range and establish its limitations; the results of these studies were compared to others obtained with other theoretical methods (particularly the R-matrix one) whenever possible.

The Multiple Scattering method was firstly applied to calculating elastic cross sections for several geometries of the water dimer, mostly differing by their dipole moments; from

the very encouraging results it was concluded that the method is able to account well for the effect of the relative orientation of the monomers, and, in a more limited energy range, for the effect of the overall dipole moment, producing good results at energies higher than ~1 eV. At lower enegies the effect of the dipole moment of the cluster, which is not correctly accounted for by the combination of differently oriented T-matrices, is very important; its poor description leads to an incorrect estimate of the cross sections. Larger water clusters were then studied, and a good agreement with R-matrix results was observed for $(H_2O)_3$. The MS code was also applied to larger water clusters ($(H_2O)_4$ and $(H_2O)_5$), for which geometrical parameters were known, producing reasonable cross sections (R-matrix calculations could not be performed) in a very efficient way, without the drastical increase in the computational and time requirements that would characterise other *ab initio* methods. The mentioned requirements depend only on the size of the monomers' T-matrices (i.e. on the number of partial waves included) and on the number of sub-units forming the cluster; matrix operations only are involved. The most time consuming operations are the R-matrix calculations for the monomers that generate the T-matrices which serve as input.

In order to test whether the method would correctly reproduce cross sections for systems characterised by shape resonances, a study was carried out on the formic acid dimer, whose elastic cross sections display two marked shape resonances below 7 eV. The MS results successfully reproduced these features, which appeared at different energies depending on the basis sets employed in the monomer R-matrix calculations; the qualitative comparison with existing theoretical and experimental results proved quite good, although since the R-matrix calculations for the monomers were not of excellent quality (partly because of the poor description of the polarisability), the agreement with experimental data (resonance positions) was not so good. It was however established that the method is able to reproduce shape resonances.

An attempt to modify the MS treatment in order to describe inelastic processes did not succeed; a limitation of the method is that the calculations require a very accurate prior knowledge of the cluster excited states (particularly their energies and their exact localisation on the monomers). Even when such information is available, the results we obtained for the

excitation into the lowest four states of $(H_2O)_2$ in the equilibrium geometry (employing two partial wave cutoff methods) either showed marked discrepancies with the R-matrix cross sections, or were very similar to the monomer ones. This indicates that there is something incorrect in the derivation or implementation of the technique.

The conclusions reported in the next sections refer to the elastic calculations only.

7.2 Effect of the parameters

Apart from the geometrical and collisional input (cluster geometry parameters and monomer T-matrices), the MS code requires the use of two parameters, γ and a_c, which must be chosen independently. The additional parameter a, which determines the radius of the R-matrix inner region, is employed when the collisional input for the sub-units is generated with the R-matrix code, and it is not intrinsic in the MS technique. In the studies carried out in this thesis, it was observed that the choice of a is uninfluential, and it must be based on considerations relative to the R-matrix method alone. In general, larger values of a ensure that the target electron density is negligible in the outer region, hence ensuring correct R-matrix results.

The parameter a_c is introduced to limit the extent of the long range interaction when calculations on the cutoff T-matrices T_c are performed. It is required because of the assumption that the sub-units' potentials do not overlap. Different values of a_c may have a very marked effect on the sub-units' cross sections, as it was observed in the case of water. However, such effect is drastically reduced when MS cross sections are calculated. In both kinds of clusters analysed (water and formic acid ones) it was concluded that the effect of a_c is hardly noticeable (provided it is within a reasonable range), and in all cases we decided to set $a_c = a$. The possibility cannot be excluded, however, that a_c may have a more marked effect when other types of clusters are studied.

Finally, it was noted that the interpolation procedure, which builds the final MS cross section combining cutoff cross sections σ^l, according to the cutoff energies E^l, may be tuned by means of an ad hoc energy correction parameter γ. Its effect is to shift the cutoff energies to higher or lower values. Setting γ to 0.75 (instead of the "natural" choice of 1) provided

better cross sections in some cases, avoiding the appearance of spurious peaks which were due to the "jump" from one cutoff cross section to another. In other cases, when spurious peaks did not appear, its effect was negligible. The same value $\gamma = 0.75$ was used in both water and formic acid clusters, and therefore seems to be independent on the nature of the cluster. Further studies should be carried out on other types of clusters in order to assess its general validity.

7.3 Range of application and limitations

For the targets treated in this thesis, all of which comprise monomers with a non zero dipole moment, the MS method produces reliable elastic cross sections for energies of the scattering electron higher than $\sim$ 1 eV; although the effect of the monomers positions and relative orientations seem to be correctly accounted for, the cluster's dipole moment is not always described correctly; at low energies, where such effect is critical, the cross sections are not reliable. The application to clusters of non-polar molecules should potentially be easier.

The most important limitation of the MS treatment is that it cannot account for any mutual interaction between sub-units, other than that due to the multiple scattering of the impinging electron's wavefunction. Distortions of the sub-units' electron densities, due to covalent or hydrogen bonds, or more generally to van-der-Waals interaction, are completely neglected. In some cases such effects may be partially introduced in the calculation, e.g. modifying the sub-units' geometries in order to account for the distortion, but in general these issues cannot be properly addressed. For this reason the method gives the best results with molecular clusters where the monomeric sub-units are minimally influenced by the others, and there is virtually no electron density between them (although dipole–dipole interactions are still present when polar sub-units are treated).

7.4 Final remarks and future work

In conclusion, within the limitations addressed above, the Multiple Scattering method provides reliable elastic cross sections with little memory and computing time requirements;

it correctly reproduces shape resonances. It requires a minimal input, which is limited to geometrical parameters and can make use of collisional information obtained with any theoretical method, although the R-matrix one is particularly suitable for the task due to some of its characteristics.

If issues related to surface effects are addressed, it can be successfully applied in the future to the study of very large clusters, potentially describing the solid or liquid phases in a realistical way, although a static description of the targets may in these cases be incomplete. The method can be applied just as easily to heterogeneous clusters, and therefore an ensemble of sub-units may be built up in such a way to describe realistical biological environments. Its application to the study of LEE scattering from biomolecules (e.g. the recent works of Caron and co-workers) may be further investigated, and will likely be extended to include the effect of a biologically significant environment.

Finally, the MS method developed here may be easily applied to positron scattering with no modification of the code.

In general, its application is likely to lead in the near future to new theoretical research on low energy electron collisions with macromolecules and clusters, particularly biological ones but not necessarily limited to them, mainly because of the method's limited computational requirements, which absolutely distinguish it from the *ab initio* methods available today.

Acknowledgments

The first person I would like to thank is my supervisor Jimena Gorfinkiel, who is responsible for my coming to the OU in the first place, and who guided me through the PhD with enthusiasm and competence, introducing me to the world of scientific research. She has not only been a professional guide, though, but also a kind and understanding person, helping during difficult moments and incredibly patient in many occasions when other people would (rightly) get furious. I believe I owe her my gratitude for much of my professional and human growth.

I would also like to thank our collaborators from the University of Sherbrooke, Canada, Dorra Bouchiha and Laurent Caron, who firstly applied the Multiple Scattering theory to the study of low energy electron collisions with molecular clusters and wrote a first version of the code. Dorra's help has been very useful in several occasions. This research has also been made possible by the EPSRC support.

I feel grateful to many professors at the Open University, who contributed to my scientific development with encouragements and suggestions, particularly my second supervisor, Nigel Mason, E. Krishnakumar, Ray Mackintosh, Mark Bowden, Nick Braithwaite and Stephen Sergeant. Particular thanks go to our very busy computer manager Geoff Bradshaw, who helped me with technical support and provided me with a new shiny keyboard, which improved drastically both my programming and writing-up speed[1] (although not as much as I had firstly foreseen).

Among the many people I met in Milton Keynes, I cannot help remembering my office mates Jonty, Michał and Vladimir, with whom I have shared not just an office, but also

[1] People often underestimate the power of good keyboards.

discussions, arguments, experiences, drinks and laughs, that will always be the fingerprint of my stay at the OU. In particular, I thank Jonty for his priceless classes on how-to-insult-people-in-a-very-British-way; Michał for his music suggestions — especially for introducing me to the *Strachy na Lachy* band —; and Vladimir for his extremely funny Serbian / Bosnian jokes, which I have noticed do not work in Italy at all[2]. I will always feel alone without them, and without my glorious ex-housemates Katarina and Andres, who made me feel part of the big Marshworth family, and dragged me out to places as different as *The Cannon* and *Pink Punters*. Also, I cannot forget thanking Gosia, who has been a skillful guide during my first crossing of the two-pints-threshold (and during most of the following thresholds). Discussions with other postgraduates of the Physics & Astronomy department provided useful information on other fields of Physics which I would not be aware of otherwise (I particularly recall an interesting chat on exoplanets).

Finally, I would like to thank all the people I have met during my stay in the UK,[3] whom I will not try to list lest I forget some (with the exception of Chiara, Mattia, Mauro, Camilla, Panayiota, Steve, the über-helpful Paula Piggott, Paul, Aga[4], *Panna Anna*, Zdeněk, the Andys and Jon). British people, BBC shows, car trips and regular visits to *The Plough* in Simpson helped me fall in love with this Country and understand some of its cultural and sociological aspects. Moreover, in the UK I have experienced an open multicultural environment, which deeply contributed to my personal development and to my understanding and esteem of cultures, habits and ideas different from my own.

A final thought goes to Francesca who managed to put up with me during stressful times for longer than anyone should ever be asked to. My family has been very understanding as well; I would like to dedicate this thesis to my great-grandmother Anita, few days before her 102nd birthday.

[2]Or maybe I am the only one who finds them funny. Who knows.

[3]With the only exception of the guy who punched me in May 2007.

[4]Who had already been acknowledged in my Master's thesis. Twice is enough.

PAGES
NOT SCANNED
AT THE REQUEST OF
THE UNIVERSITY

SEE ORIGINAL COPY
OF THE THESIS FOR
THIS MATERIAL

Bibliography

Abdoul-Carime H & Sanche L 2002 *Int. J. Radiat. Biol.* **78**, 89.

Aflatooni K, Hitt B, Gallup G A & Burrow P D 2001 *Journal of Chemical Physics* **115**, 6489.

Agassi D & Gal A 1973 *Ann. Phys.* **75**, 561.

Allan M 2006 *J. Phys. B* **39**, 2939–2947.

Allan M 2007 *Phys. Rev. Lett.* **98**, 123201.

Aloisio S, Hintze P E & Vaida V 2002 *J. Phys. Chem. A* **106**, 363.

Aplin K L & McPheat R A 2005 *J. Atmos. Sol-Terr. Phy.* **67**, 775.

Arai S, Chatake T, Ohhara T, Kurihara K, Tanaka I, Suzuki N, Fujimoto Z, Mizuno H & Niimura N 2005 *Nucleic Acids Res.* **33**, 3017.

Atkins P W & Friedman R S 1997 *Molecular quantum mechanics* Oxford University Press Oxford.

Baccarelli I, Sebastianelli F, Gianturco F A & Sanna N 2009 *Eur. Phys. J. D* **51**, 131.

Bachorz R A, Haranczyk M, Dąbkowska I, Rak J & Gutowski M 2005 *J. Chem. Phys.* **122**, 204304.

Baker A 2010. *Private communication.*

Balog R, Langer J, Gohlke S, Stano M, Abdoul-Carime H & Illenberger E 2004 *Int. J. Mass Spectr.* **233**, 267.

Baluja K L, Burke P G & Morgan L A 1982 *Comput. Phys. Commun.* **27**, 299.

Baluja K L, Zhang R, Franz J & Tennyson J 2007 *J. Phys. B* **40**, 3515.

Ban F, Gould J W & Boyd R J 2000 *J. Phys. Chem. A* **104**, 10159.

Benedict W S, Gailar N & Plyer E K 1956 *J. Chem. Phys.* **24**, 1139.

Bettega M H F 2006 *Phys. Rev. A* **74**, 054701.

Blanco F & García G 2007 *Phys. Lett. A* **360**, 707.

Bloch C 1957 *Nucl. Phys.* **4**, 503.

Bouchiha D, Caron L G, Gorfinkiel J D & Sanche L 2008 *J. Phys. B* **41**, 045204.

Bouchiha D, Gorfinkiel J D, Caron L G & Sanche L 2006 *J. Phys. B* **39**, 975.

Boudaïffa B, Cloutier P, Hunting D, Huels M A & Sanche L 2000 *Science* **287**, 1658–1660.

Burke P G 1976 *Proc. 5th Int. Conf. At. Phys* Plenum New York.

Burke P G & Berrington K A 1993 *Atomic and Molecular processes: an R-matrix Approach* Institute of Physics Publishing Bristol and Philadelphia.

Burke P G, Hibbert A & Robb W D 1971 *J. Phys. B* **4**, 153.

Burke P G, Mackey I & Shimamura I 1977 *J. Phys. B* **10**, 2497.

Burke P G & Robb W D 1975 *Adv. Atom. Mol. Phys.* **11**, 143.

Butler W H, Gonis A & Zhang X G 1992 *Phys. Rev. B* **45**, 11527–11541.

Butler W H, Gonis A & Zhang X G 1993 *Phys. Rev. B* **48**, 2118–2130.

Butler W H & Nesbet R K 1990 *Phys. Rev. B* **42**, 1518–1525.

Cai Z, Dextraze M, Cloutier P, Hunting D & Sanche L 2006 *J. Chem. Phys.* **124**, 024705.

Caprasecca S, Gorfinkiel J D, Bouchiha D & Caron L G 2009 *J. Phys. B* **42**, 095205.

Caron L, Bouchiha D, Gorfinkiel J D & Sanche L 2007 *Phys. Rev. A* **76**, 032716.

Caron L G & Sanche L 2003 *Phys. Rev. Lett.* **91**, 113201.

Caron L & Sanche L 2004 *Phys. Rev. A* **70**, 032719.

Caron L & Sanche L 2005 *Phys. Rev. A* **72**, 032726.

Caron L & Sanche L 2006 *Phys. Rev. A* **73**, 062707.

Caron L, Sanche L, Tonzani S & Greene C H 2008 *Phys. Rev. A* **78**, 042710.

Caron L, Sanche L, Tonzani S & Greene C H 2009 *Phys. Rev. A* **80**, 012705.

Case D A 1982 *Ann. Rev. Phys. Chem.* **33**, 151.

Castleman, Jr A W & Jena P 2006 *P. Natl. Acad. Sci. USA* **103**, 10554.

Cazaux S, Tielens A G G M, Ceccarelli C, Castets A, Wakelam V, Caux E, Parise B & Teyssier D 2003 *Astrophys. J. Lett.* **593**, L51.

Charlson R J, Seinfeld J H, Nenes A, Kulmala M, Laaksonen A & Facchini M C 2001 *Science* **292**, 2025.

Chatgilialoglu C & O'Neill P 2001 *Exp. Gerontol.* **36**, 1459.

Cheng B, Chew E P, Liu C, Bahou M, Lee Y, Yung Y L & Gerstell M F 1999 *Geophys. Res. Lett.* **26**, 3657.

Chipman D M 2005 *J. Chem. Phys.* **122**, 044111.

Chocholousova J, Vacek J & Hobza P 2002 *Phys. Chem. Chem. Phys.* **4**, 2119.

Chu S & Dalgarno A 1974 *Phys. Rev. A* **10**, 788.

Coe J V, Lee G H, Eaton J G, Arnold S T, Sarkas H W, Bowen K H, Ludewigt C, Haberland H & Worsnop D R 1990 *J. Chem. Phys.* **92**, 3980.

da Costa R F, Bettega M H F, Varella M T d N & Lima M A P 2010 *J. Chem. Phys.* **132**, 124309.

Dalgaard E & Monkhorst H 1983 *Phys. Rev. A* **28**, 1217.

Daly M J 2009 *Nature Rev. Microbiol.* **7**, 237.

Danos M & Maximon L C 1965 *J. Math. Phys.* **6**, 766.

Dehmer J L & Dill D 1975 *Phys. Rev. Lett.* **35**, 213.

Dehmer J L, Dill D & Wallace S 1979 *Phys. Rev. Lett.* **43**, 1005.

Del Bene J E, Ditchfield R & Pople J A 1971 *J. Chem. Phys.* **55**, 2236.

Dill D & Dehmer J L 1974 *J. Chem. Phys.* **61**, 692.

Dixon-Warren S, Jensen E T & Polanyi J C 1991 *Phys. Rev. Lett.* **67**, 2395.

Dąbkowska I, Rak J, Gutowski M, Nilles J M, Stokes S T & Bowen K H 2004 *J. Chem. Phys.* **120**, 6064.

Dąbkowska I, Rak J, Gutowski M, Nilles J M, Stokes S T, Radisic D & Bowen K H 2004 *Phys. Chem. Chem. Phys.* **6**, 4351.

Dora A, Tennyson J, Bryjko L & van Mourik T 2009 *J. Chem. Phys.* **130**, 164307.

Dragan A I, Russell D J & Privalov P L 2008 *Biopolymers* **91**, 95.

Duley W W 1996 *Astrophys. J.* **471**, L57.

Dunning, Jr T H 1970 *J. Chem. Phys.* **53**, 2823.

Dunning, Jr T H 1971 *J. Chem. Phys.* **55**, 716.

Dyke T R & Muenter J S 1973 *J. Chem. Phys.* **59**, 3125.

Ellder J, Friberg P, Hjalmarson A, Hoeglund B, Irvine W M, Johansson L E B, Olofsson H, Rydbeck G & Rydbeck O E H 1980 *Astrophys. J.* **242**, L93.

Faulkner J S 1979 *Phys. Rev. B* **19**, 6186–6206.

Faure A, Gorfinkiel J D, Morgan L A & Tennyson J 2002 *Comput. Phys. Commun.* **144**, 224.

Fliflet A W & McKoy V 1980 *Phys. Rev. A* **21**, 1863.

Freitas T C, Lima M A P, Canuto S & Bettega M H F 2009 *Phys. Rev. A* **80**, 062710.

Fu L, Bienenstock A & Brennan S 2009 *J. Chem. Phys.* **131**, 234702.

Gailitis M 1976 *J. Phys. B* **9**, 843.

Gallup G A, Burrow P D & Fabrikant I I 2009*a* *Phys. Rev. A* **79**, 042701.

Gallup G A, Burrow P D & Fabrikant I I 2009*b* *Phys. Rev. A* **80**, 046702.

Garrett B C, Dixon D A, Camaioni D M, Chipman D M, Johnson M A, Jonah C D, Kimmel G A, Miller J H, Rescigno T N, Rossky P J, Xantheas S S, Colson S D, Laufer A H, Ray D, Barbara P F, Bartels D M, Becker K H, Bowen K H, Bradforth S E, Carmichael I, Coe J V, Corrales L R, Cowin J P, Dupuis M, Eisenthal K B, Franz J A, Gutowski M S, Jordan K D, Kay B D, LaVerne J A, Lymar S V, Madey T E, McCurdy C W, Meisel D, Mukamel S, Nilsson A R, Orlando T M, Petrik N G, Pimblott S M, Rustad J R, Schenter G K, Singer S J, Tokmakoff A, Wang L S & Zwier T S 2005 *Chem. Rev.* **105**, 355.

Gianturco F A & Lucchese R R 2004 *New J. Phys.* **6**, 66.

Gianturco F A & Lucchese R R 2006 *Eur. Phys. J. D* **39**, 399–405.

Gianturco F A, Lucchese R R, Langer J, Martin I, Stano M, Karwasz G & Illenberger E 2005 *Eur. Phys. J. D* **35**, 417–428.

Gianturco F A, Sebastianelli F, Lucchese R R, Baccarelli I & Sanna N 2008 *J. Chem. Phys.* **128**, 174302.

Gibson T L, Lima M A P, McKoy V & Huo W M 1987 *Phys. Rev. A* **35**, 2473.

Gil T J, Rescigno T N, McCurdy C W & Lengsfield B H I 1994 *Phys. Rev. A* **49**, 2642.

Gorfinkiel J 2007 *in* 'Abstract of contributed papers, XXVth International Conference on Photonic, Electronic and Atomic Collisions' Freiburg, Germany.

Gorfinkiel J D, Morgan L A & Tennyson J 2002 *J. Phys. B* **35**, 543.

Gorfinkiel J D & Tennyson J 2004 *J. Phys. B* **37**, L343.

Gorfinkiel J D & Tennyson J 2005 *J. Phys. B* **38**, 1607.

Goumans T P M, Gianturco F A, Sebastianelli F, Baccarelli I & Rivail J L 2009 *J. Chem. Theory Comput.* **5**, 217.

Gregory J K, Clary D C, Liu K, Brown M G & Saykally R J 1997 *Science* **275**, 814.

Gruber-Stadler M & Muhlhauser M 2006 *J. Phys. Chem. A* **110**, 6157.

Haberland H 1994 *Clusters of Atoms and Molecules* Springer New York.

Hanel G, Fiegele T, Stamatovic A & Märk T D 2001 *Int. J. Mass Spectrom.* **205**(1-3), 65 – 75.

Hariharan P C & Pople J A 1973 *Theoret. Chimica Acta* **28**, 213.

Harrison R G & Carslaw K S 2003 *Rev. Geophys.* **41**, 2–1.

Hehre W J, Ditchfield R & Pople J A 1972 *J. Chem. Phys.* **56**, 2257.

Hocking W H Z 1976 *Naturforsch. A* **31a**, 1113.

Hollis J M, Pedelty J A, Synder L E, Jewell P R, Lovas F J, Palmer P & Liu S 2003 *Astrophys. J.* **588**, 353.

Huang X, Braams B J & Bowman J M 2006 *J. Phys. Chem.* **110**, 445.

Inokuti M 1971 *Rev. Mod. Phys.* **43**, 297.

Irvine W M, Friberg P, Kaifu N, Kitamura Y & Kawaguchi K 1989 *Astrophys. J.* **342**, 871.

Jones M & Tennyson J 2010 *J. Phys. B* **43**, 045101.

Kabeláč M & Hobza P 2007 *Phys. Chem. Chem. Phys.* **9**, 903.

Khakoo M A, Lima M A P & Tennyson J 2006 *Phys. Scripta* **74**, C7.

Kim S K, Lee W & Herschbach D R 1996 *J. Phys. Chem.* **100**, 7933.

Kimura M, Sueoka O, Hamada A & Itikawa Y 2000 *Adv. Chem. Phys.* **111**, 537.

Kjaergaard H G, Robinson T W, Howard D L, Daniel J S, Headrick J E & Vaida V 2003 *J. Phys. Chem. A* **107**, 10680.

Klopper W, Schütz M, Lüthi H P & Leutwyler S 1995 *J. Chem. Phys.* **103**, 1085 –.

Kohn W & Rostoker N 1954 *Phys. Rev.* **94**, 1111.

Korringa J 1947 *Physica* **13**, 392.

Kosztin D, Gumport R I & Schulten K 1999 *Nucleic Acids Res.* **27**, 3550.

Kreil J, Ruf M, Hotop H, Ettischer I & Buck U 1998 *Chem. Phys.* **239**, 459.

Landman U, Barnett R N, Cleveland C L, Scharf D & Jortner J 1987 *J. Phys. Chem.* **91**, 4890.

Lemke K H & Seward T M 2008 *J. Geophys. Res.* **113**, D19304.

Lide D R, ed. 1998 *CRC Handbook of Chemistry and Physics* 79th edn CRC, Boca Raton.

Light J C & Walker R B 1976 *J. Chem. Phys.* **65**, 4272.

Lourderaj U & Sathyamurthy N 2006 *J. Phys. Chem. A* **110**, 2709.

Madeja F & Havenith M M 2002 *J. Chem. Phys.* **117**, 7162.

Makochekanwa C, Kajita R, Kato H, Kitajima M, Cho H, Kimura M & Tanaka H 2005 *J. Chem. Phys.* **122**, 014314.

Märk T D 1991 *Int. J. Mass Spectrom. Ion Process.* **107**, 143.

Martin I, Skalicky T, Langer J, Abdoul-Carime H, Karwasz G, Illenberger E, Stano M & Matejcik S 2005 *Phys. Chem. Chem. Phys.* **7**, 2212.

Matejcik S, Kiendler A, Stampfli P, Stamatovic A & Märk T D 1996 *Phys. Rev. Lett.* **77**, 3771.

Messiah A 1962 *Quantum Mechanics* Wiley New York.

Milosavljević A R, Blanco F, Maljković J B, Šević D, García G & Marinković B R 2008 *New J. Phys.* **10**, 103005.

Mores P M 1956 *P. Natl. Acad. Sci. USA* **42**, 276.

Morgan L A 1984 *Comput. Phys. Commun.* **31**, 419.

Morgan L A, Gillan C J, Tennyson J & Chen X 1997 *J. Phys. B* **30**, 4087.

Morrell T E & Shields G C 2010 *J. Phys. Chem.* **114**, 4266.

Mott N F & Massey H S W 1965 *Theory of Atomic Collisions* Clarendon Oxford.

Nam S H, Park H S, Song J K & Park S M 2007 *J. Phys. Chem. A* **111**, 3480.

Nestmann B M, Nesbet R K & Peyerimhoff S D 1991 *J. Phys. B* **24**, 5133.

Nestmann B M & Peyerimhoff S 1990 *J. Phys. B* **23**, L773.

Nielsen I M B, Seidl E T & Janssen C L 1999 *J. Chem. Phys.* **110**, 9435.

NIST Computational Chemistry Comparison and Benchmark DataBase 2010. *National Institute of Standards and Technology — USA.*
URL: *http://cccbdb.nist.gov/*

Noble C J & Nesbet R K 1984 *Comput. Phys. Commun.* **33**, 399.

P.-O. Löwdin 1955 *Phys. Rev.* **97**, 1474.

Pan X, Cloutier P, Hunting D & Sanche L 2003 *Phys. Rev. Lett.* **90**, 208102.

Pan X & Sanche L 2005 *Phys. Rev. Lett.* **94**, 198104.

Park C Y, Kim Y & Kim Y 2001 *J. Chem. Phys.* **115**, 2926.

Pelc A, Sailer W, Scheier P, Mason N J, Illenberger E & Märk T D 2003 *Vacuum* **70**, 429.

Pelc A, Sailer W, Scheier P, Probst M, Mason N J, Illenberger E & Märk T D 2002 *Chem. Phys. Lett.* **361**, 277.

Prabhudesai V S, Nandi D, Kelkar A H, Parajuli R & Krishnakumar E 2005 *Chem. Phys. Lett.* **405**, 172 – 176.

Privalov P L, Dragan A I, Crane-Robinson C, Breslauer K J, Remeta D P & Minetti C A S A 2007 *J. Mol. Biol.* **365**, 1.

Ptasińska S & Sanche L 2007 *Phys. Rev. E* **75**, 031915.

Purvis G D & Bartlett R J 1982 *J. Chem. Phys.* **76**, 1910.

Rescigno T N, Trevisan C S & Orel A E 2006 *Phys. Rev. Lett.* **96**, 213201.

Rescigno T N, Trevisan C S & Orel A E 2009 *Phys. Rev. A* **80**, 046701.

Rueda M, Kalko S G, Luque F J & Orozco M 2003 *J. Am. Chem. Soc.* **125**, 8007.

Rueda M, Kalko S G, Luque F J & Orozco M 2006 *J. Am. Chem. Soc.* **128**, 3608.

Saenger W 1984 *Principles of Nucleic Acid Structure* Springer-Verlag New York.

Sanche L 2005 *Eur. Phys. J. D* **35**, 367.

Schlathölter T, Alvarado F, Bari S, Lecointre A, Hoekstra R, Bernigaud V, Manil B, Rangama J & Huber B 2006 *ChemPhysChem* **7**, 2339.

Schmidt M W & Ruedenberg K 1979 *J. Chem. Phys.* **71**, 3951.

Schneider B I 1975 *Chem. Phys. Lett.* **31**, 237.

Schneider B I & Hay P J 1976 *Phys. Rev. A* **13**, 2049.

Schütz M, Klopper W, Lüthi H & Leutwyler S 1995 *J. Chem. Phys.* **103**, 6114.

Sedlacko T, Balog R, Lafosse A, Stano M, Matejcik S, Azria R & Illenberger E 2005 *Phys. Chem. Chem. Phys.* **7**, 1277.

Sen S, Andreatta D, Ponomarev S Y, Beveridge D L & Berg M A 2009 *J. Am. Chem. Soc.* **131**, 1724.

Senn G, Muigg D, Denifl G, Stamatovic A, Scheier P & Märk T D 1999 *Eur. Phys. J. D* **9**, 159.

Sennikov P G, Ignatov S K & Schrems O 2006 *ChemPhysChem* **6**, 392.

Shimamura I 1977 *J. Phys. B* **10**, 2597.

Siegel J, Dehmer J L & Dill D 1980 *Phys. Rev. A* **21**, 85.

Siegel J, Dehmer J L & Dill D 1981 *Phys. Rev. A* **23**, 632.

Siegel J, Dill D & Dehmer J L 1976 *J. Chem. Phys.* **64**, 8.

Sobolewski A L & Domcke W 2006 *Chem. Phys. Chem.* **7**, 561.

Sobolewski A L, Domcke W, Dedonder-Lardeux C & Jouvet C 2002 *Phys. Chem. Chem. Phys.* **4**, 1093.

Stamatovic A 1988 *Electronic and Atomic collisions* Elsevier Amsterdam.

Stanton J F & Bartlett R J 1993 *J. Chem. Phys.* **98**, 7029.

Stibbe D T & Tennyson J 1998 *Comp. Phys. Comm.* **114**, 236.

Sugano S 1991 *Microcluster Physics* Springer New York.

Szabo A & Ostlund N S 1996 *Modern Quantum Chemistry* Dover New York.

Tarana M & Tennyson J 2008 *J. Phys. B* **41**, 205204.

Taylor J R 2006 *Scattering Theory: The Quantum Theory of Nonrelativistic Collisions* Dover New York.

Tennyson J 1996 *J. Phys. B* **29**, 6185.

Tennyson J 2010 *Phys. Rep.* **491**, 29.

Tokmachev A M, Tchougréeff A L & Dronskowski R 2010 *ChemPhysChem* **11**, 384.

Toledo E J L, Custodio R, Ramalho T C, Garcia Porto M E & Magriotis Z M 2009 *Theochem* **915**, 170.

Trevisan C S, Orel A E & Rescigno T N 2006 *Phys. Rev. A* **74**, 042716.

Tronc M, Allan M & Edard F 1987 *in* 'Abstract of contributed papers, XVth International Conference on Photonic, Electronic and Atomic Collisions' Brighton, UK p. 335.

Tschumper G S, Leininger M L, Hoffman B C, Valeev E F, Schaefer H F & Quack M 2002 *J. Chem. Phys.* **116**, 690.

Valenzano L, van Hemert M C & Kroes G 2005 *J. Chem. Phys.* **123**, 034303.

van Harrevelt R & van Hemert M C 2000 *J. Chem. Phys.* **112**, 5777.

Vizcaino V, Jelisavcic M, Sullivan J P & Buckman S J 2006 *New J. Phys.* **8**, 85.

Ward J F, Blakely W F & Joner E I 1985 *Radiat. Res.* **103**, 383.

Watson D K & McKoy V 1979 *Phys. Rev. A* **20**, 1474.

Wigner E P 1946 *Phys. Rev.* **70**, 606.

Wigner E P & Eisenbud L 1947 *Phys. Rev.* **72**, 29.

Williams A R & Morgan J 1974 *J. Phys. C* **7**, 37–60.

Winstead C & McKoy V 2008 *Radiat. Phys. Chem.* **77**, 1258.

Winstead C, McKoy V & d'Almeida Sanchez S 2007 *J. Chem. Phys.* **127**, 085105.

Xantheas S S & Dunning, Jr T H 1993 *J. Chem. Phys.* **99**, 8774.

xkcd.com 2010.

URL: *http://xkcd.com/722/*

Yokoya A, Cunniffe S M T, Watanabe R, Kobayashi K & O'Neill P 2009 *Radiat. Res.* **172**, 296.

Yonetani Y, Maruyama Y, Hirata F & Kono H 2008 *J. Chem. Phys.* **128**, 185102.

Zhang R, Faure A & Tennyson J 2009 *Phys. Scr.* **80**, 015301.

Zheng Y, Cloutier P, Hunting D, Wagner R & Sanche L 2005 *J. Am. Chem. Soc.* **127**, 16592.

Ziesche P 1974 *J. Phys. C* **7**, 1085–1097.